Deparment of Physics

Nanomaterials doped with lanthanide ions under extreme conditions for sensor and photonics applications

PhD Thesis submitted by Miguel Andrés Hernández Rodríguez

February 2018

DIRECTOR: Dr. Ulises Ruymán Rodríguez Mendoza

TUTOR: Dr. Inocencio Rafael Martín Benenzuela

El Dr. Ulises Ruymán Rodríguez Mendoza, Profesor Titular de la Universidad y el Dr. Inocencio Martín Benenzuela, Profesor Titular de Universidad, del Departamento de Física de la Universidad de La Laguna

CERTIFICAN:

Que la Tesis Doctoral que presenta el estudiante de Tercer Ciclo D. Miguel Andrés Hernández Rodríguez, titulada **"*Nanomaterials doped with lanthanide ions under extreme conditions for sensor and photonics applications*"**, ha sido realizado bajo nuestra dirección y tutela respectivamente, y

AUTORIZAN:

La presentación del trabajo de D. Miguel Andrés Hernández Rodríguez para que sea defendido en sesión pública ante el tribunal correspondiente y en cumplimiento de la legislación vigente para optar al Grado de Doctor en Astrofísica, especialidad en Estructura de la Materia.

Y para que así conste, expedimos la presente que firmamos en San Cristóbal de La Laguna a 31 de enero de 2018.

Dr. Ulises Ruymán Rodríguez Mendoza — **Director**

Dr. Inocencio Martín Benenzuela — **Tutor**

Acknowledgements

En primer lugar, quiero agredecer a mi director y tutor de tesis, el Dr. Ulises Rodríguez Mendoza y el Dr. Inocencio Martín Benenzuela, sin olvidar al Dr. Víctor Lavín della Ventura por ofrecerme esta indispensable y gran oportunidad de seguir formándome como científico, ayudándome a salir de la mala época que estaba pasando, poco antes de empezar a trabajar con ustedes. Los tres me han ayudado y asistido bastante durante mi etapa doctoral, resolviendo cualquier duda o problema que tuviese dentro y fuera del laboratorio. Por otro lado, destacar que he aprendido bastante en lo que se refiere al fundamento físico de los experimentos que he realizado, así como en el manejo de los equipos (muchas gracias por esto, Inocencio), aunque soy conciente de que me falta un largo camino. En definitiva, ya no los veo únicamente como los "jefes" que tengo, sino también como personas con las que puedo conversar y hablar de cualquier cosa. Espero mantener el contacto con ustedes.

Por otra parte, pese a que he pasado estos tres años prácticamente solo sin compañeros de laboratorio, en lo que se refiere a otros doctorandos, sí que tengo que mencionar la agradable compañía del Dr. Antonio Diego Lozano que hacía de mis días en laboratorio un lugar todavía más ameno. También agradecerle por lo que me ha enseñado respecto a la síntesis de los materiales de la tesis como de conocimientos indispensables de cristalografía. Por supuesto, agradecerle también su ayuda a la hora de corregir el inglés de los trabajos publicados. Eres una gran persona con la que agradezco haber conocido. Espero seguir manteniendo el contacto y desearte mucha suerte con lo del puesto de profesor en la Universidad, ¡ésta es la tuya!

To Dr. Marcin Runowski who I spent more than two month with him during his stay in the ULL. It was nice to have you here and, of course met you. Pleasurable conversations about several things and pretty nice company for me in this laboratory. Hope to keep in touch with you!

Al Dr. Alfonso Muñoz y la Dr^{a}. Plácida Rodríguez Hernández por su inestimable y valiosa ayuda en los cálculos ab-initio y simulaciones aportadas en dos de los trabajos de esta tesis, que sin ellos no hubiera sido posible. ¡Muchas gracias!

Al Dr. Javier González Platas por las medidas de difracción de rayos-X de mi muestra bajo condiciones extremas de presión, fundamentales en uno de los trabajos de esta tesis.

Durante esta época de doctorado también he tenido la oportunidad de viajar y conocer a otras personas, en especial al Dr. Javier Manjón, el cual me ayudó y enseñó bastante sobre la Espectroscopía Raman durante mi estancia en Valencia. También le agradezco enormemente su paciencia para explicarme las cosas. No debo olvidarme tampoco del Dr. Juan Ángel Sans, el cual me ayudó los primeros días con las medidas Raman de mis muestras, además de consejos valiosos en todo el procedimiento referente a la carga de las celdas de diamante. ¡Muchas gracias a los dos!

Al Dr. Luis Carlos por haberme permitido pasar tres meses muy amenos y agradables en Aveiro (Portugal) trabajando y aprendiendo en el laboratorio que conforman su grupo, y todo el apoyo brindado por su parte. Un fuerte agradecimiento al Dr. Carlos Brites porque estuvo ayudándome durante los tres meses que estuve allí, por no dejar de mencionar que se movió hasta el último día de mi llegada para conseguirme sitio donde residir. Obrigado!

Al Dr. Alfredo Segura por su tiempo y enseñarme a reparar una celda de diamantes a la que uno de sus diamantes se había roto.

Ya fuera del entorno laboral, no puedo olvidarme de mis amigos con los que llevo ya mucho tiempo compartiendo diferentes hobbys, y que con el paso del tiempo eso no haya cambiado me alegra. Vayamos por partes, como diría Jack el Destripador:

Zebenzui, que decirte, te conozco ya desde 2010, y que gracias al BlazBlue se haya consolidado una amistad para la posteridad. Espero seguir manteniendo el contacto contigo y ahora que “El Goku” está con nosotros podamos repetir como antaño con el BlazBlue.

Alan, desde 2011 te veo el careto y desde ese entonces me has demostrado con creces lo buena persona que eres, y que las “kdds” en tu casa, junto a los demás, me ha brindado momentos para el recuerdo. ¡Espero asistir más a esas “kdds” de las montañas de Icod!

Liam, te conozco prácticamente desde 2013-2014, y desde ese entonces te integraste en nuestro grupito. Eres muy buena persona, con la que junto a los demás he pasado grandes momentos. ¡Espero que también le des al Goku!

Samuel Kim, mi coreano preferido, eres una persona de gran corazón, y desde que te conocimos no has dejado de sorprendernos con gestos nobles y desinteresados. Te has convertido en una persona entrañable, que ahora que no estás en Tenerife, te echamos en falta. ¡Espero que todo te vaya bien por tierras inglesas, y que pronto nos visites!

A mi buen amigo Raúl, que desde la época del instituto que nos conocemos, me has demostrado ser una persona muy legal con la que puedo hablar de lo que sea y cuando sea. ¡Espero que todo te vaya bien y nos veamos más a menudo!

A Kevin Soler que, aunque no estés de doctorando, prácticamente te has comportado como uno, el cual ha sido una agradable compañía durante mis días por este sitio. Tío diez ciertamente. Espero que te vaya todo bien y estemos en contacto.

A mis compañeros de la Facultad de Química, Lucho, Rubén Rizo y Olmedo Guillén que, durante mi corta etapa en ese lugar, me echaron un cable en todo momento. Espero que os vaya todo a pedir de boca.

A todos los colegas y amigos de la península, con los cuales he pasado también momentos muy agradables tanto dentro como fuera de los torneos y eventos. Destaco al grupo "skypers", Sergio por echarme siempre el guante con temas relacionados con las tesis doctorales, así como el tour que me diste durante mi visita por Lisboa (eres un tío diez de diez). Carlos el isleño de las Baleares, Led, Luis alias "crucius" y su talento innato de ser humorista sin quererlo, David Palau por ser el mejor anfitrión en todo lo que organiza preocupándose de que la gente se lo pase bien, Guillermo, y en general a toda la gente de Mollerussa y Barna (Adrián, Jose, Jordi alias "elmestre"…).

No puedo olvidarme del "Cónclave", el Guille el cual considero un tío "top tier", Iván Prats el llorón de la comunidad, pero entrañable en el fondo, Frankbottle y Tohno. Al fiscal de Huelva el Joselón, Luismi con el que siempre compartí asiento en los viajes desde Málaga a Granada con risas aseguradas por el camino, y en general a todos los andaluces con los que me he cruzado a lo largo de estos años.

Finalmente, y en especial sobre todo lo demás a mi querida familia, que ha estado siempre allí cuando la necesito. Mi madre Yanitza por su gran apoyo, para las buenas y animándome para las no tan buenas en todo momento. Mi padre Juan Miguel, la persona más honesta y humilde que conozco, y que es capaz de quitarse el pan de la boca para dárselo a los demás. A mi hermano Juan Andrés, que está siempre al pie del cañón para lo que sea, ya sea en las buenas o en las malas, al cual admiro bastante. A mi hermana Geor que siempre ha tenido un detalle conmigo. Aunque yo no sea muy dado de expresar las cosas, te admiro bastante, sister. A mi abuela Georgina que siempre se preocupó y preguntó por mí hasta el final. Te echamos de menos. A Carlos, que es prácticamente como uno más de la familia. Soy muy afortunado de tener una familia así.

Contents

1. INTRODUCTION

This PhD thesis is focused on the characterization of lanthanide ions-doped nano-perovskites under extreme conditions of pressure or temperature for potential applications in photonics and optical sensors. It was performed bewteen April 2015 and April 2018 at Departamento de Física of Universidad de La Laguna in order to achieved Doctor degree in "Astrofisica especialidad en Estructura de la Materia". This thesis was carried out under supervision of Dr. Ulises Ruymán Rodríguez Mendoza and the tutelage of Dr. Inocencio Rafael Martín Benenzuela, and was supported by *Ministerio de Economía y Competitividad* (MINECO) of Spain under National Program of Materials (MAT2013-46649-C4-3-P, MAT2013-46649-C4-4-P, MAT2015-71070-REDC, MAT2016-75586-C4-3-P, and MAT2016-75586-C4-4-P) and by the EU-FEDER fundes. I want to thank MINECO for the FPI (Formación de Personal Investigador) grant (BES-2014-068666).

The present thesis has been written in the "compendium of published articles" format, and it is formed by five parts. Firstly, a general introduction about the state of the art and objectives of this work. Secondly, a theoretical background of the techniques used during the thesis period. Thirdly, all experimental methods needed to carry out this study. In the fourth place, the article compendium with an explanation of each paper developed in this thesis. Finally, the conclusions.

The papers which compose the *compedium*, with the position of each journal within its field, are listed below:

I. M.A. Hernández-Rodríguez, A.D. Lozano-Gorrín, I.R. Martín, U.R. Rodríguez-Mendoza and V. Lavín "*Spectroscopic properties of Nd^{3+} ions in YAP nano-perovskites*", Journal of Luminescence **188** (2017) 204-208. (OPTICS, Q2 (25/92)).

II. M.A. Hernández-Rodríguez, V. Monteseguro, A.D. Lozano-Gorrín, F.J. Manjón, J. González-Platas, P. Rodríguez-Hernández, A. Muñoz, V. Lavín, I.R. Martín and U.R. Rodríguez-Mendoza "*Structural, Vibrational, and Elastic Porperties of Yttrium Orthoaluminate Nanoperovskite at High Pressures*" Journal of Physical Chemistry C **128** (2017) 15353-15367. (CHEMISTRY, PHYSICAL, Q1 (31/146); NANOSCIENCE & NANOTECHNOLOGY, Q2 (25/86); MATERIALS SCIENCE, MULTIDISCIPLINARY, Q1 (43/274)).

III. M.A. Hernández-Rodríguez, A.D. Lozano-Gorrín, I.R. Martín, U.R. Rodríguez-Mendoza and V. Lavín *"Comparison of the sensitivity as optical temperature sensor of nano-perovskite doped with Nd^{3+} ions in the first and second biological windows"* Sensors & Actuators B: Chemical **255** (2018) 970-976. (CHEMISTRY, ANALYTICAL, Q1 (6/76); ELECTROCHEMISTRY, Q1 (3/28); INSTRUMENTS & INSTRUMENTATION Q1 (2/58)).

IV. M.A. Hernández-Rodríguez, A.D. Lozano-Gorrín, V. Lavín, U.R. Rodríguez-Mendoza and I.R. Martín *"Yttrium orthoaluminate nanoperovskite doped with Tm^{3+} ions as upconversion optical temperature sensor in the near-infrared"* Optics Express **25** (2017) 27845-27856. (OPTICS, Q1 (17/92)).

V. Miguel A. Hernández-Rodríguez, Juan E. Muñoz-Santiuste, Víctor Lavín, Antonio D. Lozano-Gorrín, Plácida Rodríguez-Hernández, Alfonso Muñoz, Vemula Venkatramu, Inocencio R. Martín and Ulises R. Rodríguez-Mendoza *"High pressure luminescence of Nd^{3+} in $YAlO_3$ nano-perovskites. A crystal-field analysis"* Journal of Chemical Physics **in press** (2018). (CHEMISTRY, PHYSICAL, Q2 (65/146); PHYSICS, ATOMIC, MOLECULAR & CHEMICAL, Q2 (10/36)).

VI. M.A. Hernández-Rodríguez, U. R. Rodríguez-Mendoza, V. Lavín, J.E. Muñoz-Santiuste, I. R. Martín and A.D. Lozano-Gorrín *"High pressure sensitivity of anti-Stokes fluorescence in Nd^{3+} doped yttrium orthoaluminate nano-perovskites"* Journal of Luminescence **196** (2017) 20-24. (OPTICS, Q2 (25/92)).

The main goal of these papers is the complete characterization of lanthanide ions-doped nano-perovskites at ambient conditions and extreme conditions of temperature or pressure. The two first papers represent the first steps regarding the initial characterization of undoped nano-perovskites and doped nanoperovskites. The article I allowed to define the optimal thermal treament during sol-gel synthesis of nano-perovskites, by means of optical measurements in order to obtain pure chemical perovskite phase, and the article II includes an extensive structural, vibrational and elastic properties characterization of undoped nano-perovskites from ambient to extreme conditions of pressure. Articles III and IV comprise one of the main part of this thesis (PhD) regarding the analysis of the viability of nano-perovskites doped with lanthanide ions, specifically in Tm^{3+} and Nd^{3+} ions as optical temperature sensors working in the NIR. Finally, the fifth and sixth papers suppose the last part of the experimental results of this thesis, focusing on the analysis of

the viability of nano-perovskites doped with Nd^{3+} ions, i.e. $YAlO_3$ nano-perovskite doped with 1 mol % Nd^{3+} ions as optical pressure sensors working in the NIR. In addition, a detailed crystal-field analysis was also performed in article V.

The combination of the outstanding luminescence properties of lanthanide ions doped nano-perovskite and the mechanical and chemical stability of the nano-perovskites makes them useful for a variety of applications, such as, optical applications, optical pressure sensors and optical nano-thermometers.

1.1. State of the art

1.1.1. What is an optical sensor?

A sensor is defined as "*a device that detects and responds to some type of input from the physical environment*", in the case of optical sensors, optical properties of a certain material, which can be, for instance, its absorption or emission spectra, lifetimes…, depend strongly on the environment conditions of temperature, pressure, pH, etc. Hence, when these parameters undergo changes, then the optical response of the material is automatically altered. This peculiar behaviour leads to the well-known optical sensors, which are being developed for their application as probes to detect physical or chemical fluctuations, when the environment conditions changes respect to their initial ones.

Generally, two elements are required to develop an optical sensor (see Fig. 1.1):

i) An optically active material that acts as a probe which is place at the place of interest.

ii) A measuring system, usually composed by a low pump power laser source for the excitation and an optical detector which is attached to a spectrometer.

As opposed to other similar devices, such as thermocouples or pH-meters, an optical sensor does not need any physical connections such as wires between the optically active material and the detector, since the electromagnetic radiation does not need any specific guiding system for its propagation. Nonetheless, the optically active material luminescence can be focused on an optical fiber in order to guarantee a better measurement, being this the third element that can be considered in the development of optical sensors [1].

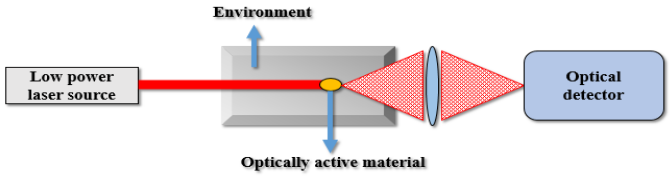

Fig. 1.1. Simple diagram of an optical sensor and its elements.

In these devices, the fluctuation of a physical or chemical magnitude from an initial condition to a final one is recorded as a variation of the luminescence response. This response can be translated into in different ways, such as changes in the spectral position, band shape, intensity, bandwith and even lifetime [2] (see Fig. 1.2).

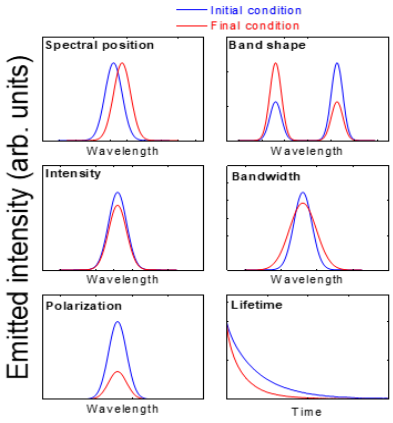

Fig. 1.2. Different luminescent responses of an optical sensor due to fluctuations of physical or chemical magnitudes of the environment.

1.1.2. Optical pressure sensors

Matter under extreme conditions of pressure is a subject that gathers many fields of science, such physics, geology, biology, chemistry and even material science with a common objetive which is mimicking and understanding the processes and phenomena that happen in the interior of the planet Earth and any other planetary object. These phenomena usually involve phase transitions, chemical reactions or microbioligal activities. In this sense, high pressure technique results to be a really powerful tool that allows the scientist to control in a reversible way, the volume of a sample and, thus, controlling also its chemical, magnetic and optical properties.

Generally, the pressure on a certain material is induced by using a pressure cell, whose design differs depending on the working pressure range to be achieved [3].

In order to achieve the highest posible pressures without shattering the anvils, diamond was used. This is not only the hardest material in the Earth, it also presents unique features for high pressure experiments as is its transparency in the optical UV-VIS-NIR and in the range of hard X-rays. In addition, diamond has an extraordinary thermal conductivity which allows experiment with temperature and pressure simultaneously. The principles of the current diamond anvil cells (DAC) are similar to the Bridgman's anvils [4], i.e. a sample placed between the flat parallel faces of two opposed diamond anvils (see Fig. 1.3) is undergone to pressure when a mechanical force pushes these two anvils together. Besides, the versatility to generate pressure due to new devices, including the possibility as well of observing the properties of a material under pressure just by using a microscope as main features of DACs, allow performing a wide variety of studies in a wide pressure and temperature ranges, such as, structural characterization by X-ray diffraction, absorption and fluorescence; as well as vibrational experiments using Raman spectroscopy, etc. Accordingly, DACs have become the most useful ultra-high-pressure device which allow scientists discovering of new states of matter and understand the basic physics linked to ultra-high-pressure phenomena.

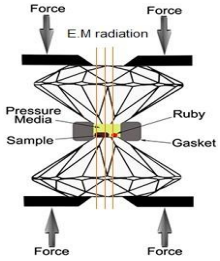

Fig. 1.3. Scheme of a current pressure DAC with its components.

In general, current DACs setup is very straightforward. Briefly, a thin metal sheet (gasket), with a thickness size around 200-250 μm, pre-indented by own anvils with a centered drilled hole together with the diamons themselves constitutes what is called the hydrostatic chamber or cavity (see Fig. 1.3). The sample is introduced in this cavity along with the pressure transmitting medium (PTM) and the pressure sensor. The hydrostatic chamber size is conditioned by the pressure range that is going to be achieved, so that a high pressure on the order of tons of GPa, the size must be very small around of 100 μm diameter and 50 μm high.

Concerning the PTM, its choice depends on its chemical reactivity with the sample and its structural behavior. Usually, a solution of methanol: ethanol: water (16:3:1) is the most commonly used as PTM, which a hydrostaticity limit around 10 GPa. However, pressures that exceed 10 GPa another kind of PTM is required, such as argon, nitrogen, hydrogen, etc [3].

The determination of the pressure inside the hydrostatic sample chamber of the cell, requires a calibrated standard. The transparency of the anvils in the optical range allows to estimate the working pressure via an in-situ, indirect measurement of the calibrated pressure-sensitive luminescence of an optically ion, i.e. transition metal or lanthanide, in a micro-sized or nano-sized crystalline host located in the sample chamber. These sensors are called as optical pressure sensors.

Regarding the ideal pressure sensor, there are some requirements that have to be satisfied in order to be used in high pressure experiments, described by Barnett et al. [5]. These requirements are:

i) Optical pressure sensor must have a single and isolated emission line from the whole spectrum.
ii) The broadening of the emission line must be neglectable small.
iii) The emission line shift must be strongly-dependant with the pressure.
iv) Simultaneously, its temperature dependence must be neglectable or very small.
v) For higher sensitivity or accuracy, line width must be insignificant compared with the displacement of the latter.
vi) Host matrix must be very stable at high pressures and temperature.

The most employed optical pressure sensor since its discovery in 1973, is the Cr^{3+}: Al_2O_3 (ruby), in which pressure is determinate by monitoring the redshift of the R_1 (692.7 nm) and R_2 (694.2 nm) bands ($^2E \rightarrow {}^4A_2$). The main advantage of this sensor are its fluorescence efficiency and large shift of the emission bands compared with its width when the pressure increases. On the other hand, chromium (Cr^{3+}) ion fluorescence can be obtained by exciting with conventional lasers (Ar+, diode laser or solid state) and recording it with straightforward detection equipments.

Nonetheless, ruby has several drawbacks which are:

i) Notably temperature induced broadening which leads to the overlap between R_1 and R_2 emission lines.

ii) Large inhibition of the emission above 500 ºC.

iii) Low sensitivity below 1 GPa, a range specifically relevant for biologic systems.

iv) Possible overlap of its emission with the sample fluorescence [6].

Considering the requirements for the ideal optical pressure sensor, the search of the viability of lanthanide ions fluorescence in different host materials as alternative have become in a relevant issue.

The main feature of the lanthanide (Ln^{3+}) ions is the 4f-electrons shielding which leads to lesser sensitivity to the environment and thus sharper absorption and emission covering UV-Visible-NIR than those of the 3d-electrons Cr^{3+}.

The first detailed study in which the Ln^{3+} ions fluorescence was used as optical pressure sensor was performed by Barnett et al. [5] in 1973, who studied the luminescence of neodymium (Nd^{3+}) ion in yttrium aluminium perovskite crystal ($YAlO_3$ or YAP) matrix, object of study of this PhD. The pressure and temperature dependence were measured and compared with those obtained for the $YAlO_3$ and $Y_3Al_5O_{12}$ doped with Cr^{3+}. The results of the study stated that Nd^{3+} ion emission lines shift with pressure were smaller than those obtained for Cr^{3+} ions. However, temperature broadening of Nd^{3+} lines were notably lesser than Cr^{3+} ones.

Later, in 1989 an alternative to ruby was considered and studied by Lacam *et.al* whose work focused on the SrB_4O_7 doped with Sm^{2+} ions [7]. The advantage of employing the former ion is that it has a narrowed, isolated and intense emission singlet line associated to the $^5D_0 \rightarrow {}^7F_0$ transition. In addition, the pressure shift of this singlet is similar to ruby's. With these features many other works were possible, extending the calibration of this sensor up to megabar range in 1990 [8] and also calibrated above 120 GPa in 1997 [9] and more recently in 2013 [10].

Following years, other host materials doped with Sm^{3+} ions were investigated, for instance, YAG: Sm^{3+} under extreme condition of pressure and/or temperature. The evolution of the doublet Y_1 (618 nm) and Y_2 (616 nm) of Sm^{3+} with pressure at room temperature up to 180 GPa [11] was analyzed and it was found that the pressure-induced shift peak was comparable to the ruby's. Simultaneously, it was found that the temperature-induced shift was notably smaller than ruby's. In fact, experiments above 673 K (400 ºC) at 25 GPa stated that was possible determinate the pressure from Sm^{3+} without any temperature correction in this range [12]. Calibration up to 338 GPa at room

temperature [13,14] and more recently, up to 120 GPa at 1246 K (973 ºC) were carried out [15].

Interesting experiments in high-pressure conditions were carried out in yttrium Nd^{3+}-doped gadolinium (YGG) and gadolinium gallium (GGG) and especially gadolinium scandium gallium (GSGG) garnet co-doped with Cr^{3+} in which the $R_{1,2}(^4F_{3/2}) \rightarrow Z_1(^4I_{9/2})$ emission lines associated to the transition $^4F_{3/2} \rightarrow {}^4I_{9/2}$ for their use as optical pressure sensor working in the NIR [16,17].

So far, many studies in different crystal garnets doped with Nd^{3+} ions at high pressure have also been performed, such as $La_3Lu_2Ga_5O_{12}$ (LLGG) [18], YAG [19] and GGG [20], paying special attention to the emission lines associated to the $R_{1,2}(^4F_{3/2}) \rightarrow Z_5(^4I_{9/2})$ Stark transition.

However, few works have been done concerning the perovskite-based materials doped with Ln^{3+} working as optical pressure sensor, beyond the studies done by Barnett and Hua [5,21]. Not to mention the overall lackness of studies focused on Ln^{3+} doped-nanostructured materials at high pressure conditions. To the best of my knowledge, there are not many studies focused on nanoperovskites doped with Ln^{3+} working as optical pressure sensor [22,23].

1.1.3. Optical temperature sensors

Temperature is probably the most relevant parameter in all kinds of science. Futhermore, the accurate measurement of this parameter is an issue that must be considered. Sensors in general are widely employed in daily life, metrology, climate and marine research, medicine, biology, air condition, in practicaly all devices for heating and cooling, in production plants and the storage of food, etc. Statistically, the share of sensors for temperature amounts almost the 70-80% of the world sensor market [24]. There are many types of thermometers, such as: i) liquid-filled glass thermometers based on the materials thermal expansion [25]; ii) thermocouples based on the Seebeck's effect [26]; iii) optical sensors [27].

In the sense of environmental and health issues, there is a tendency to substitute classic liquid-filled thermometers by another alternative, the thermocouples.

The former ones are non-toxic, very straightforward to use and have a vast analytical range (3 to 3300 K approximately) with good accuracy. In addition, the signals can be easily digitized [24]. Considering these feature, they have become the most often used industrial sensors. However, they are not exempt of many drawbacks, such as

thermocouples and related systems require an electrical link to the sensor at the sampling site. They also have limitations if applied in corrosive environments, and are strongly affected by interference from electromagnetic fields. Not to mention that contact measurements require convective heat transfer and thus need to reach equilibrium between the sensor and the object. This can alter the sample temperature during the measurement, especially if the size of the sample is small compared to the sensor head. Classic bimetallic and liquid-filled thermometers, pyrometers, thermocouples and thermistor are not suitable for temperature measurement with small spatial resolution below ~10 μm, whose dimension is common in cellular systems, for instance.

Optical sensors for temperature, in contrast to other thermometers, do not need any physical connections such as wires between the optically active material and the detector, since the electromagnetic radiation does not need any specific guiding system for its propagation as it was mentioned in the section 1.1 of this thesis.

The characterization of these devices is a relative novel field of research with potential applications in different disciplines such as chemistry, biomedicine or electromagnetism, in which limitations such as the working range, a slow response or a high sensitivity to electromagnetic interferences of conventional sensors, such as thermocouples or pyrometers, need to be overcome [28–30].

Temperature determination in these devices are based on the existence of two emitting levels of an optically active ion which are close enough each other in energy to be considered in quasi-thermal equilibrium. One of the most employed technique to calibrate an optical temperature sensor is known as the fluorescence intensity ratio technique (FIR), *R*, which calculates the ratio of the areas under the emission bands of these two close energy thermalized levels as a function of the temperature, which is proportional to their transition energies, emission cross-sections and population distributions, and follows a Boltzmann-type distribution [28–30]. The former technique possesses the advantage of reducing the influence of the measurement conditions leading to a relative simple experimental setup. In order to develop an optical temperature sensor, two requirements should be considered:

i) Selection of a suitable optically active ion.
ii) The host material in which the optically active ion is embedded.

Concerning the optically active ion, the first option would be the transition metal ions due to their high temperature sensitivity. Nonetheless, their luminescence decreases notably

with the temperature [31]. An alternative option to metal transition ions is the used of Ln^{3+} ions, which present high efficient luminescence and rich energy level diagrams that show in most of the cases, small energy gaps between two levels, enough to be populated by these ions following a Boltzmann's distribution [28–30]. However, from the practical point of view, not all of Ln^{3+} ions are suitble to be used to calibrate the optical response. Futhermore, some general requirements must be fullfiled in order to considere the use of a certain Ln^{3+} ion:

i) The energy gap between the thermalized levels must be large enough to avoid overlapping of two nearby emissions.
ii) At the same time, this energy gap must be short enough to ensure a minimum population of the upper level in the temperature range of interest.
iii) The radiative probabilities of the thermalized levels must be high enough to show large emission intensities.

Ln^{3+} ions such as praseodimium (Pr^{3+}), Nd^{3+}, Sm^{3+}, thulium (Tm^{3+}), europium (Eu^{3+}), holmium (Ho^{3+}) and erbium (Er^{3+}) have energy level pairs which satisfy these criteria and have been employed as optically active ion for optical temperature sensors [1,30,32–36]. The first study in 1990 performed by Jörgensen et al. [37] in which the $^2H_{11/2}$, $^4S_{3/2}$ thermalized levels of Er^{3+} in fluorindate fibers was analyzed using the FIR technique in the temperature range between 293 K (20 ºC) and 473 K (200 ºC) with an experimental deviation around 2 K (2 ºC). However, these fibers showed limitations above 523 K (250 ºC), due to the presence of fluorides in their structure.

Later, other works with different host materials and Ln^{+} ions as optical temperature sensors have been arousen, for instance, analysis of Er^{3+}-doped and Er^{3+}/Yb^{3+}-codoped fluorindate and chalcogenide fibers [38,39]. A fiber optic sensors based on silica doped with ytterbium (Yb^{3+}) and Nd^{3+} were reported to be especifically useful on temperature sensing in the ranges of 303-883 K (30-610 ºC) and 223-1773 K (-50-1500 ºC) with a resolution of ±1 K (±1 ºC) and ±2.5 K (±2.5 ºC) [40] respectively, and the last one improved to ~1.3 K (~1.3 ºC) [41].

VK. Rai et al. published many works focused on different host materials doped with Ln^{3+} ions. One of these works studied the dependence of the Pr^{3+} ion luminescence in tellurite glass from 273 K (0 ºC) up to 443 K (170 ºC), showing a very high experimental deviation around 8 K (8 ºC) [42]. Another one, but focused on an oxyfluoroborate glass doped with Sm^{3+} reported its possible application for ratiometric luminescent up to 500 K (227 ºC)

with a thermal sensitivity around 0.00126% K^{-1} [32]. Also, the first study of the invidual behavior of the Er^{3+} emission associated to $^2H_{11/2}$,$^4S_{3/2}$ transition in a tellurite glass host matrix with the temperature was carried out [43].

Particularly interesting are the temperature influence on the luminescence of Eu^{3+} and terbium (Tb^{3+})-doped host materials. These materials can be excited using UV light which results in a sharp emission band at 611 nm that corresponds to the $^5D_0 \rightarrow ^7F_2$ Eu^{3+} ions transition. For example, the host Sr_2CeO_4 doped with different concentration of Eu^{3+} in which the thermal quenching happens allowing the use of this feature for sensing in the temperature range from 273 K up to 523 K [44]. On the other hand, it is found that the life time of Y_2O_3: Eu^{3+} (4.52% w/w) and YAG: Tb^{3+} (5% w/w) drops from 1000 to 0.4 μs on going from 823 K (550 ºC) to 1273 K (1000 ºC) with an accuracy around of ± 5% [45].

Also, host materials doped with dysprosium ions (Dy^{3+}) to be used as optical temperature sensors were reported, such as YAG: Dy^{3+}[46].

In the last decade, the nanostructured materials have become a hot topic due to their possible application in several fields, which cannot be contemplate by using the bulk counterparts, especially in biomedicine and nanomedicine. Nanomaterials have been evaluated as efficient tools for diagnostic and therapy for in-vitro and in-vivo applications. In particular, the nanomaterials doped with Ln^{3+}.

The first paper on intracellular sensing of temperature using upconverting nanoparticles (UCNPs) was published by Vetrone et at. in which $NaYF_4$: Er^{3+}/Yb^{3+} upconverting nanoparticles was usded to monitorize the temperature inside a cell [2] with a temperature resolution of 0.5 K. More recent study, reports the temperature evolution of the luminescence of various UCNPs of the type $NaYF_4$ codoped with Yb^{3+} and X (X= Er^{3+}, Ho^{3+} and Tm^{3+}) [47], especially $NaYF_4$: Er^{3+}/Yb^{3+} showing a very high temperature response within the physiological range of temperature from 293 (20 ºC) up to 318 K (45 ºC).

From the point of view of biological applications, nanomaterials doped with Nd^{3+} ions have become very interesting, because their absorption and emission lie in the well-known “near infrared biological windows” (NIR-BW) of human (see Fig. 1.4). These windows are not more than the infrared spectral region where the scattering of the light due to water and hemoglobin is almost negligible [48]. This feature allows the possible application of these materials in biological systems.

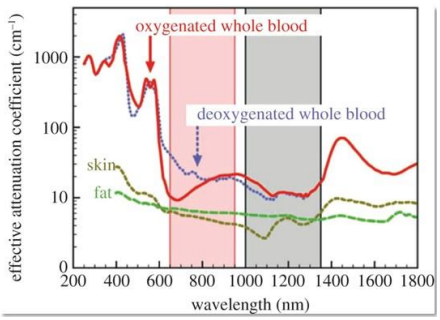

Fig. 1.4. Optical windows in biological tissues.

The ratio of the luminescence centered at 863 and 870 nm which correspond to the Stark levels of the $^4F_{3/2} \rightarrow {}^4I_{9/2}$ transition was studied in $NaYF_4$ doped with Nd^{3+}, finding a strongly dependency of the former ratio with the temperature and governed by the Boltzmman law [49]. This sensor works in the temperature range of 273 K (0 ºC) to 423 K (150 ºC), being particularly useful for deeper tissue penetration because of the two emissions in the NIR.

U. Rocha et al. published an interesting work focused on the LaF_3 nanoparticles doped with large concentration of Nd^{3+} which can simulteneously operate as biologically compatible nanoheaters and optical temperature sensor [50,51].

Other type of nanomaterials doped with Nd^{3+} for biomedical application have been reported, for instance YAG: Nd^{3+} nanoparticles [52] whose water dispersibility allowed to test their performance as temperature sensing in microelectronic systems and optofluidic devices. Also, these nanoparticles showed their operability in the biological windows, being successfuly employed for subtissue thermal sensing with potential use for early detection and controlloed thermal treaments. The both heating and sensing capabilities of YVO_4 nanoparticles doped with Nd^{3+} for photothermal therapy application was tested and reported this year by Kolesnikov et al. [53].

1.1.4. Perovskites

Oxide perovskites with general stoichiometry ABO_3 are simple structures formed by corner-linked BO_6 cation-centred octahedra with larger *A* cations occupying the voids within the three-dimensional framework of octahedra. In the ideal cubic perovskite structure, the *A* cations are surrounded by twelve equidistant oxygen ions. Most of the ABO_3 compounds crystallize with the orthorhombic distortion of the perovskite structure.

The orthorhombic structures are originated from the ideal cubic structure via the titling and distortion of the BO_6 octahedra [54–56]. Perovskites are of great interest in materials science because the relatively simple crystal structure displays many diverse electric, magnetic, piezoelectric, optical, catalytic and magnetoresistive properties. In addition, perovskites are of interest in Earth sciences because (Mg, Fe)SiO_3 transforms to a perovskite structure with *Pbnm* symmetry at high pressures and temperatures and is believed to form the bulk of the Earth's lower mantle [57].

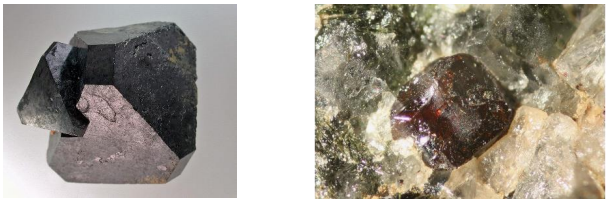

Fig. 1.5. $CaTiO_3$ (left) and (right) $SrTiO_3$ oxide perovskites.

1.1.5. Ln^{3+}-doped perovskites

Perovskites have been intensively studied due to their importance from both the viewpoint of fundamental physics and device applications. In particular, ABO_3-type perovskites oxides, where *A* and *B* denote two different cations, have gained interest for their potential application in oxide-based electronics, due to their fascinating and multifunctional electronic properties beyond conventional semiconductors. Most perovskites are wide band gap semiconductors and show exceptional optical properties, which are used for optoelectronic devices as nonlinear optical crystals [58,59], scintillators [60], photoluminescence and electroluminescence materials [61,62] and solar cells [63]. In particular, perovskite doped with Ln^{3+} ion can be found in several applications as optical sensors, for instance $Na_{0.5}Bi_{0.5}TiO_3$ doped with Er^{3+} or codoped with Er^{3+}-Yb^{3+} and $BaTiO_3$ doped with Er^{3+} [64,65] as optical temperature sensor and Nd^{3+}-doped with $YAlO_3$ as optical pressure sensor [21]. Among all perovskites, yttrium orthoaluminate perovskite ($YAlO_3$) has shown excellent physical and chemical properties, such as high hardness, good structural stability, and large mechanical strength, which make it an excellent candidate as a laser host material for Ln^{3+} [66–69].

However, the research in nanomaterials has attracted the interest of scientists from several fields due to their unique properties [70], being one of their main advantages that they

keep the bulk counterpart properties for sizes larger than 10−20 nm. The interest in rare-earth-doped nanoperovskites is based on the fact that the chemistry and optical spectroscopy of the analogous perovskite bulk crystals are well-known, opening the possibility to establish meaningful comparisons between the properties of the nanosized and bulk materials. In this regard, several works focused on studies of the properties of Ln^{3+} doped nanoperovskites have been carried out. [71–75] Among interesting applications of nanoperovskites, it can be cited their use as optical temperature sensors [64,65,76,77], CO sensors [78] and single photon emitters [79].

1.2. Justification and objectives

The study of the nano-sized materials is currently in trending topic, because it allows new approaches to many field of science, from developing new materials nanoscale dimensions to direct control of the matter on the atomic scale. Such fields which can be nano-electronics, nano-mechanics and even nano-photonics have been constantly evolving during the last few decades in order to give a solid basis of the nanotechnology. Many phenomena become relevant as the system dimensions decrease. Along these phenomena, it is particularly interesting the one associated to quantum size effects, in which the physical, mechanical, electrical and optical properties among other of a nanometric (typically at distances between 1 to 10 nm) changes notably compared with its macroscopic counterpart. Not to mention that these nanoscale materials can be used eventually as bulk, because it can shows the same properties that their macroscopic counterparts exhibit.

One of the objetives of this thesis is to synthesize undoped and lanthanide ions doped nano-perovskites via sol-gel synthesis method for several applications in the nano-technology field, especially, in sensing, biomedicine, bioimaging, nano-optoelectronics, as optical sensors in extreme condition of pressure or temperature experiments. These nano-perovskites are mainly characterized and studied by experimental techniques. Orthoaluminate nano-perovskite ($YAlO_3$) was selected to be studied in this thesis. Firsly, by optical techniques, especially, the site selection spectroscopy, the optimal thermal treatment during sol-gel synthesis of nano-perovskites was defined. In the second place, an extensive structural, vibrational and elastic properties characterization of undoped nano-perovskites at ambient to extreme conditions of pressure was perfomed and compared with theoretical results. This study includes X-ray diffraction and Raman

scattering measurements both ambient and extreme condition of pressure. Thirdly, the viability of Nd^{3+}-doped $YAlO_3$ and Tm^{3+}-doped $YAlO_3$ nanoperovskites as optical temperature sensor working in NIR for biological applications was performed. In addition, the potential application of Nd^{3+}-doped $YAlO_3$ nano-perovskite in sub-tissue luminescence imaging. Finally, the last part of the experimental results of this thesis, focusing on the analysis of the viability of nano-perovskites doped with Nd^{3+} ions, as optical pressure sensors working in the NIR. In addition, a detailed crystal-field analysis was also carried out.

2. THEORETICAL BACKGROUND

2.1. Lanthanide ions

Lanthanides ions (Ln^{3+}) are a group of 15 elements from lanthanum (Z=57) to lutetium (Z=71) (see Fig. 2.1). The main difference of these atoms compared to the rest of elements is that the outer shells do not get filled as the atomic number increases, but the inner shell 4f does. Lanthanum has the former shell empty, while the lutenium one is full.

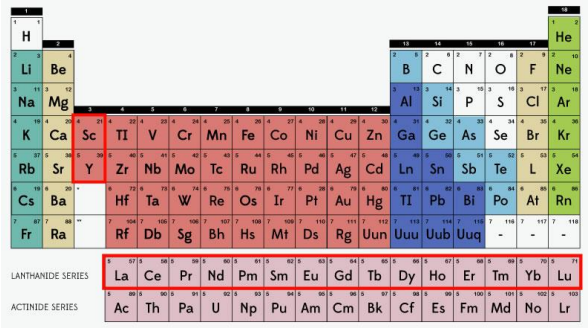

Fig. 2.1. Periodic table of elements. Lanthanide elements are highlighted (red).

Regarding the spectroscopy, the electrons that lodge in 4f incomplete shell are distributed in accordance with the Pauli Exclusion Principle. This distribution leads to unpaired electrons which can be interact with the UV, visible or IR radiation. In contrast to transition metals, 4f electrons of the lanthanides cannot create any bond with the environment. This phenomenon is due to the called lanthanide contraction [80–82] in which the 5d and 6s electrons are attracted toward the nucleus, resulting in a smaller atomic radius, i.e. the lanthanide contraction describes the ionic radii reduction of the lanthanide series from lanthanum (1.16 Å) to the luthenum (0.97 Å). This leads to a shielding of the 4f shell electrons that unable their interaction with the environment. The former feature can be translated to in many of Ln^{3+} properties that can be studied by optical spectroscopy. The effect of the environment over the 4f shell electrons can be treated as a perturbation, which are small enough compared to the electrostactic and spin-

orbit interactions between 4f electrons themselves, from the point of view of atomic physics.

The determination of the Ln^{3+} energy levels is described in the mark of the atomic theory formalism. In this sense, the electrostatic Hamiltonian that describes a Ln^{3+} ion composed by *N* electrons and *Ze* nuclear charge is:

$$H_{electrostatic} = H_0 + H_{re} + H_{SO} + H_{terms} \tag{2.1}$$

where H_0 are the kinetic energy and potential interaction between the *N* electrons and the field created by the point nucleus of infinite mass, H_{re} is the Coulumb interaction between electron pairs, H_{SO} is the spin-orbit interaction and H_{terms} other weakers electrostatic and magnetic interactions such as spin-spin, spin-other orbits, etc.

The non-relativistic part of the Hamiltonian of a free ion with *N* electrons and point nucleus with infinite mass is described as follow [82]:

$$H_{electrostatic} = H_0 + H_{re} = \sum_{i=1}^{N}\left[-\frac{\hbar^2}{2m}\nabla_i^2 - \frac{Ze^2}{r_i}\right] + \sum_{i>j}\left[\frac{e^2}{r_{ij}}\right] \tag{2.2}$$

where $\hbar$, *e*, *m* and r_{ij} are the Planck constant, electron charge, mass and the electron-electron distance respectively.

Since the 4f electrons are more relevant from the point of view of optic spectroscopy, the central field approximation can be applied. The former approximation considers that 4f electrons move independently each other within a total field, which is the sum of fields created by the ion's nucleus and the central field symmetric created by the electrons potential from filled shells and the rest of 4f electrons. In this sense, eq. (2) is rewritten as follow:

$$H'_{electrostatic} = H'_0 + H'_{re} = \sum_{i=1}^{N}\left[-\frac{\hbar^2}{2m}\nabla_i^2 - V(r_i)\right] + \sum_{i>j}\left[\frac{e^2}{r_{ij}}\right] \tag{2.3}$$

This new Hamiltonian only takes into account the 4f electrons contribution to the energy. The eigenvectors of H'_0, are provided by the Slater determinant and the energy of each final state only depends on on the set values known as the electronic configuration, $(n_1\ l_1)\ldots(n_N\ l_N)$. The parity of these states is given by $(-1)^{l_1}\ldots(-1)^{l_n}$ while the degeneration is given by the Pauli Exclusion Principle [83]:

$$\frac{(4l+2)!}{N!(4l+2-N)!} \tag{2.4}$$

By this way, L^2, L_z, S^2 and S_z form a complete set of commuting of observables where the eigenvectors of the former system are given by the quantum numbers L, S, m_l, m_S and are a linear combination of Slater determinants.

Coulomb interaction, H'_{re} between 4f electrons leads to the splitting of the electronic configuration in a *LS* coupling, i.e. Russel-Saunders coupling, ^{2S+1}L terms. The *LS* terms are associated to $(2L+1)(2S+1)$ eigenstates. Nonetheless, the number of total levels is the same from the electronic configuration:

$$\sum_{LS}(2L+1)\cdot(2S+1)=\frac{(4l+2)!}{N!(4l+2-N)!} \tag{2.5}$$

Concerning the spin-orbit interaction, H_{SO}, it breaks partially the degeneration of the *LS* multiplets:

$$H_{SO}=\sum_{i=1}^{N}\xi(r_i)\cdot\vec{s}_l\cdot\vec{l}_l \tag{2.6}$$

$$\xi(r_i)=\frac{\hbar^2}{2(mc)^2}\cdot\frac{1}{r}\cdot\frac{dU(r)}{dr} \tag{2.7}$$

where r_i is the radial coordinate, s_i is the spin, l_i is the *i*-th electron angular momentum and $\xi(r_i)$ is a term that depends on the central field potential and distance between electron-nucleus.

H_{SO} commutes with the total angular momentum $J=L+S=\sum s_i+\sum l_i$. Futhermore, the Hamiltonian, $H=H'_{electrostatic}+H_{SO}$, eigenstates can be expresses as eigenstates of the operators *J* and *Jz* [83].

Since the excited LS coupling levels of the configuration $4f^N$ are very close, the Russel-Saunders coupling is not longer valid. Hence, the spin-orbit coupling is comparable to the electrostatic interaction, i.e. $H'_{electrostatic}\approx H_{SO}$ giving rise to the *Intermediate coupling*. In this case, the energy levels of free ion will be a linear combination of Russel-Saunders states:

$$\left|l^N\alpha\left[LS\right]JM\right\rangle=\sum_{L'S'}\sum_{\alpha'}c(\alpha'L'S'J)\cdot\left|l^N\alpha'L'S'JM\right\rangle \tag{2.8}$$

where the *c(α'L'S'J')* coefficients are obtained in the calculus and the sum in *α'* is extended to all quantum numbers to distinguish two states with the same value of *L* and *S*. Figure 2.2 shows the Dieke diagram of Er^{3+} in $LaCl_3$ host matrix [84].

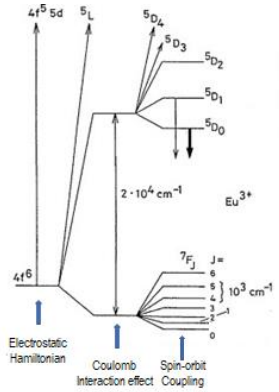

Fig. 2.2. Energy level diagram of free Eu^{3+} ion. The sucesive splitting of the levels associated to the non-relativistic electrostatic Hamiltonian, due to the Coulomb interaction and the spin-orbit coupling are shown.

2.1.1. Crystal field interaction: Ln^{3+} ion in a host matrix

When a Ln^{3+} ion is introduced in a solid matrix, the influence of such material upon the ion is reflected in an inhomogeneous electric field that weakly interacts with its 4f electrons. This interaction provokes the degeneracy breakdown of the free ion levels leading to a splitting of these levels, which depends strongly on the point symmetry of the ion.

The former field, which will be responsible of the degeneracy breakdown of the free ion levels (and thus, the splitting of these levels), presents the same point symmetry as the Ln^{3+} ion, so that the observed splitting in the absorption and emission of the ion will be strongly related to this symmetry (see Fig. 2.3). In other words, the fine structure levels and the intensities of the radiative transitions between levels of the same ion could be different in distinct host material.

The Hamiltonian that describes the influence of the host matrix ligands (optically inert) upon an Ln^{3+} ion (optically active) is:

$$H_{ion+matrix} = H_{free\ ion} + H_{electron-static\ matrix} + H_{electron-dynamical\ matrix} + H_{dynamical-matrix} \qquad (2.9)$$

a) $H_{free\ ion}$: is the Hamiltonian that describes the isolated ion.

b) $H_{electron-static\ matrix}$: describes the host matrix effect upon the Ln^{3+} ion. This effect is characterized by a electrostatic filed with a specific symmetry that interacts with the 4f electron. It also known as the static crystal field interaction.

c) $H_{electron-dynamical\ matrix}$: describes the effect's degree of the ligand ions vibrational modes upon the Ln^{3+} ion, through the 4f electron-phonon coupling.

d) $H_{dynamical-matrix}$: represents the vibrational energy of the host matrix atoms which is responsible of the non-radiative dexecitation between Ln^{3+} ion levels.

Since the last two interactions are weaker than the static crystal field, perturbation theory can be applied upon the Ln^{3+} ion levels. These two interactions have a relevant role in optical transitions between the mentioned level, altering the shape and intensity of an electronic transition, leading to vibronic bands or inducing non-radiative transitions.

The interaction of the crystal field is described in the mark of one-electron model in which the ligand ions interacts with each 4f electron of the Ln^{3+} individually [85]. This provokes a total perturbation that can be expressed as the summation of the each electron ones. The electrostatic field upon 4f electrons is originated by indivual set of point charges, thus both Ln^{3+} and resultant crystal field present the same point symmetry and as it was mentioned before, the splitting of the absorption and emission bands will be strongly related to this symmetry.

The static crystal field interaction, can be obtained from the classic expression of the electrostatic potential, with the origin of coordinates in the Ln^{3+} nucleus and considering an electrostatic distribution $\rho(\vec{R})$ due to the environment ligands. On the other hand, the potential energy considering the Ln^{3+} ion charge $q_i = -|e|$ in the points $(r_i, \theta_i, \varphi_i)$ is:

$$W_c = \sum_i q_i V(\vec{r}_i) = -|e| \sum_i V(\vec{r}_i) = -|e| \sum_i \int \frac{\rho(\vec{R})}{|\vec{R} - \vec{r}|} \tag{2.10}$$

where $\vec{r}$ is the 4f electron position and $\vec{R}$ is the ligand ion position in the environment. The summation is over the 4f electrons and the integral sweeps upon the variables $(r_i, \theta_i, \varphi_i)$ in the whole solid volume.

By expanding the integral of eq. 2.10 using the multipole expansion, it is possible to separate the radial and angular part of it:

$$\sum_{i<j}\frac{1}{\left|\vec{r_1}-\vec{r_2}\right|}=\sum_{i<j}\sum_{k=0}^{\infty}\frac{r_<^k}{r_>^{k+1}}P_k\left(\mathrm{Cos}\,\gamma_{ij}\right)$$
$$P_k\left(\mathrm{Cos}\,\gamma_{ij}\right)=\sum_{q=-k}^{k}(-1)^q\cdot C_{k,-q}(j)\cdot C_{kq}(i) \qquad (2.11)$$

where the $P_k\left(\mathrm{Cos}\,\gamma_{ij}\right)$ are the Legendre polynomials which are expressed in terms of the irreducible tensors $C_q^{(k)}$.

Taking into account eq. (11), the potential energy is expressed as follow:

$$W_c=\sum_{k,q,i}B_q^k C_{kq}(\theta_i,\varphi_i)$$
$$B_q^k=-|e|\int\rho(\vec{R})\frac{r_<^k}{r_>^{k+1}}(-1)^q C_{k,-q}(\alpha,\beta)\,d\tau \qquad (2.12)$$

where B_q^k are the crystal parameters in the Wybourne notation [82]

2.1.2. Crystal field interaction. Symmetry

The Hamiltonian that represents the crystal field interaction in the Wybourne notation is:

$$H_{CF}=\sum_{k,q,i}B_q^k C_q^{(k)}(i) \qquad (2.13)$$

where the irreducible tensor operator $C_q^{(k)}$ acts upon the 4f electron and the B_q^k crystal field parameters satifistifies the condition $B_{-q}^k=(-1)^q\cdot\left(B_q^k\right)^*$ with $q<0$, because H_{CF} is hermitian. Futhermore, the relation of these coefficients is:

$$B_0^k=\left(B_{k0}\right)$$
$$B_q^k=(-1)^q\cdot\left(B_{kq}-iS_{kq}\right)$$
$$B_{-q}^k=(-1)^q\cdot\left(B_q^k\right)^*=B_{kq}+iS_{kq} \qquad (2.14)$$

and H_{CF} can be rewritten as follow:

$$H_{CF} = \sum_{k=0}^{\infty}\sum_{i}\left[B_{k0}C_0^{(k)}(i) + \sum_{q=1}^{k}\left(B_{kq}\left(C_{-q}^{(k)}(i) + (-1)^q C_q^{(k)}(i)\right)\right) + iS_{kq}\left(\left(C_{-q}^{(k)}(i) - (-1)^q C_q^{(k)}(i)\right)\right)\right] \quad (2.15)$$

This Hamiltonian is a general expresion of the crystal field interaction in which B_{kq} and S_{kq} can be adjusted by experimental results. In addition, the H_{CF} presents an even and odd part which are responsible of the splitting of the free ion levels and the intensity of intraconfigurational transitions f-f respectively (see Fig. 2.3).

i) The splitting magnitude depends on the intensity of the interaction of the host matrix ion (ligands ions).

ii) The resulting number of levels due to the splitting depends on the crystal symmetry.

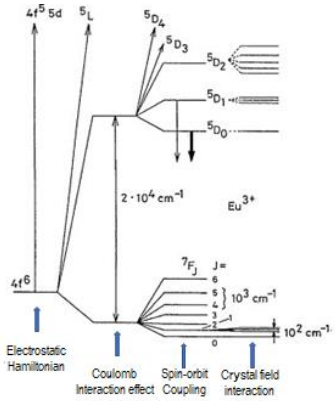

Fig. 2.3. Energy level diagram of free Eu^{3+} ion. The sucesive splitting of the levels associated to the non-relativistic electrostatic Hamiltonian, due to the Coulomb interaction, the spin-orbit coupling are shown and the crystal field interaction.

2.2. Optical spectroscopy

When a Ln^{3+} ion is in an excited state, eventually it tries to return to its ground state. During this process, Ln^{3+} ion budges the energy previously absorbed to the environment as photons, phonons, combination of both or even by interaction with other optically active ion.

2.2.1. Radiative emission

Radiative emission is the most direct channel in which a Ln^{3+} ion can return to the ground state, releasing photons during the process. This proccess is associated to a certain probability which is specific to each electronic level. Usually, this probability is denoted by W_{RAD} and it is the inverse of the time that Ln^{3+} ion takes to return to its ground state only considering the spontaneous emission as the unique possible de-excitation:

$$\tau_{RAD} = \frac{1}{W_{RAD}} \tag{2.16}$$

If the rest of probabilities were considered then, the experimental time would be:

$$\frac{1}{\tau_{EXP}} = W_{RAD} + W_{MP} + W_{ET} = \frac{1}{\tau_{RAD}} + W_{MP} + W_{ET} \tag{2.17}$$

where W_{MP} and W_{ET} are the multiphonon and energy transfer processess probabilities respectively.

2.2.2. Multiphonon relaxation process

Multiphonon relaxation processess transform totally or partially the electronic excitation into vibrational energy (phonons). These processess are typically of picoseconds order, so they happen inmmediately after the electronic excitation. In the case of Ln^{3+}, these processess are less competitive than the ones in transition metal ions, due to the nature of the 4f inner electrons. Thus, it is possible to observe luminescence from many excited states [86]. The transition between two states with emission of p phonons, having the same energy for simplicity, according to the perturbation theory is:

$$W_P(T) = W_o\left[1+n\right]^p \tag{2.18}$$

where n is the occupation number of a phonon mode and W_o is the multiphonon de-excitation rate at T=0 when n=0 and the phonon modes are all initially in their ground stated. As the temperature increases W_P rate increases because of larger phonons emission.

W_P rate can be related to the energy gap ΔE between two consecutive level by the "energy gap law":

$$W_P(T) = W_o \exp[-\alpha \Delta E] \tag{2.19}$$

where $\alpha=\ln(R)/\hbar\omega$ and $R=W_P/W_{P-1}$. W_o and α are constants which are specific to each host material and any Ln^{3+} within it.

2.2.3. Energy transfer processes

Energy transfer occurs when the absorption and emission does not take place whitin the same optically active ion (center). There are radiative and non-radiative energy transfer processes depending on if photons participate in the transfer process or not, and between renosant and phonon-assisted energy transfer (see Fig. 2.4)

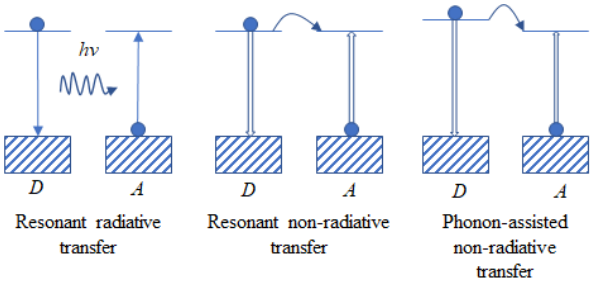

Fig. 2.4. Several basic energy transfer processes between two ions. Aceptor ion (*A*), which is initially in the ground state, receives the energy from the donor ion (*D*).

I. Radiative energy transfer process

The radiative energy transfer rate is defined as the product of the *D* ion and the absorption probability of the *A* ion (ref 14 virginia):

$$W_{DA}(\nu) = A_{21D} g_D(\nu) B_{12A} g_A(\nu) \frac{h\nu}{c4\pi R^2} \tag{2.20}$$

where $g_D(\nu)$ and $g_A(\nu)$ are the line profile of *D* and *A* respectively, A_{21D}, B_{12A} and *R* are the Einstein's coefficient for the spontaneous emission, induced absorption and the distance between *D* and *A* ions (see Fig 2.5).

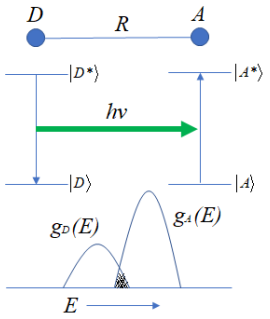

Fig. 2.5. Resonant energy transfer from D to A an the optical transition line shapes $g_D(E)$ and $g_A(E)$.

Equation 2.20 can be rewritten in a different way, considering the definition of absorption cross section σ as follow:

$$W_{DA}(\nu) = \frac{A_{21D} g_D(\nu) \sigma_A g_A(\nu)}{4\pi R^2} = \frac{C_{DA-RAD}}{R^2}$$
$$C_{DA-RAD} = \frac{A_{21D}\sigma_A}{4\pi} = \int g_D(\nu) g_A(\nu) d\nu \qquad (2.21)$$

where σ_A is the acceptor integrated absorption cross section.

The former process has some features that need to be mentioned. First at all, the position of the sample will affect the experiment results. Secondly, the dependence on the line profiles changes in the emission spectrum of *D* ion. Thirdly, *D* ion lifetime does not depend on the concentration of the acceptors, although this lifetime will decreases if the transfer process is between the same type of ions.

II. Non-radiative energy transfer processes

In these kind of processess, there are two different statistical treament, being the first the one, which neglects the migration between donors contribution and the second one, which considers the former contribution.

In the first case, when *D* ion is excited by a pulsed radiation at t = 0 in absence of *A* ions, the probability of finding a *D* ion in the excited state at time *t*, is described by:

$$\rho_i(t) = \exp(-t/\tau_o)$$
$$\tau_o = 1/(W_{RAD} + W_{MP}) \qquad (2.22)$$

Following the pulsed excitation of the *D* ions system, the probability of a *D* ion at a position R_i is excited at time *t* is given by:

$$\frac{d\rho_i(t)}{dt} = \left[-\frac{t}{\tau} - \sum_{j=1}^{N_A} W_{DA}\left(\left|\vec{R}_i - \vec{R}_j\right|\right) \right] \rho_i(t) \tag{2.23}$$

where R_j is the position of *A* ion *j* and W_{DA} is the energy transfer probability between *D* and *A* ions.

The solution of this equation, with $\rho_i(0) = 1$ and considering, from the macroscopic point of view, $\Phi(t)$ as the average of $\rho_i(t)$ upon an infinitive large number of *D* ions:

$$\phi(t) = \exp\left[-\frac{t}{\tau} - \frac{4\pi}{3} C_A \Gamma\left(1 - \frac{3}{S}\right) \left(C_{DA}\tau\right)^{3/S} \right] \tag{2.24}$$

where S = 6,8,10 correspond to the different type of multipolar interactions (dipole-dipole, dipole-quadrupole and quadrupole-quadrupole, respectively), C_{DA} is the energy transfer parameter which depends on the type of multipolar interaction between *D* and *A* ions. $\Gamma(x)$ is the gamma function.

On the other hand, the temporal evolution of the emission of the *D* ions, $I(t)$ after the pulsed radiation is given by Inokuti-Hirayama's expression [87]:

$$\begin{aligned} I(t) &= I(0) \exp\left[-\frac{t}{\tau} - Q\left(\frac{t}{\tau}\right)^{3/S} \right] \\ Q &= \frac{4\pi}{3} C_A \Gamma\left(1 - \frac{3}{S}\right) \left(C_{DA}\tau\right)^{3/S} \end{aligned} \tag{2.25}$$

When the *A* ions inside the matrix are different each other, then a slightly modification of the former equation must be considered.

$$\begin{aligned} I(t) &= I(0) \exp\left[-\frac{t}{\tau} - Q'\left(\frac{t}{\tau}\right)^{3/S} \right] \\ Q' &= \frac{4\pi}{3} \Gamma\left(1 - \frac{3}{S}\right) \sum_{\alpha=1}^{A} C_{A\alpha} \left(C_{DA\alpha}\tau\right)^{3/S} \end{aligned} \tag{2.26}$$

Concerning the case in which the migration between *D* ion is considered, there are two ways to approach this problem, the first one, the energy migration is considered as a diffusion process [88] and the second one, as a random process in which the excitation is

jumping between *D* ions ("hopping") until it is transferred to an *A* ion [89,90] (see Fig. 2.6).

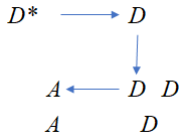

Fig. 2.6. Energy transfer with migration.

2.2.4. Upconversion processes

Upconversion (UC) is a proccess in which the absorption of two or more photons leads to the emission of light at higher energy than the excitation radiation. UC is a non-linear anti-Stokes type emission. There are different mechanisms that give rise to the conversion of the infrared energy into visible one:

i) Energy transfer upconversion (ETU) mechanism consists in a sequential energy transfer from an excited *D* ions to another nearby *A* ion. Therefore, two excited ion can eventually transfer their energy to an *A* ion promoting it to a higher energy state (see Fig. 2.7 left)

ii) Excited state absorption (ESA) mechanism consists in a consecutive absorption of the incident photons by the same ion, so that, the former ion absorbs one photon, promoting it to an excited state. Eventually, this ion in its excited state, absorbs another photon, causing a second excitation.

iii) The cooperative luminescence proccess consists in a sequential absorption of two photons by two different active ions, causing their promotion to their excited states. After that, both ions decay at the same time to their ground states, creating a single photon whose energy comes from of both ions.

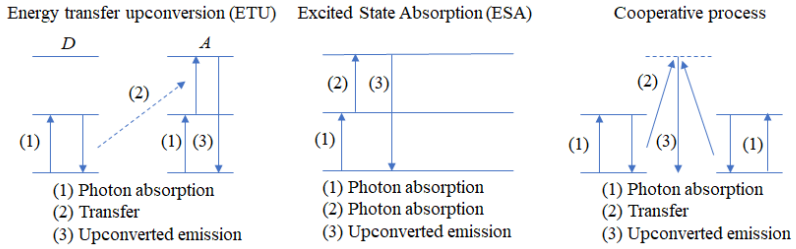

Fig. 2.7. Diagrams of different upconversion process: (left) ETU; (center) ESA and (right) Cooperative. Dashed line on the Cooperative process diagram represents a virtual energy state.

UC processess do not happen with the same probability, in fact, a certain UC mechanism could be predominat in a specific system but not in other one. In any case, four steps should be taken into account in order to know what is the predominant UC mechanism:

i) Relative positions of the different energy levels involved

ii) Upconverted emission intensity dependence with the pump power of the excitation source

iii) Upconverted emission intensity dependence with with the D ions concentration

iv) Temporal evolution of the upconverted emission

2.2.5. Temperature dependence of the Ln^{3+}-doped host material optical properties. Fluorescence Intensity Ratio (FIR)

The emission radiation from an excited ion tends to reach a less energetic level or even the fundamental state. This occurs dependending on the radiative probability respect to the total probability, i.e. radiative, multiphonon and energy transfer.

Nonetheless, when both initial and final states are known, the transition intensity is constant, unless the temperature of the sample changes. This temperature dependence of the intensity is due to the phonon emission probability. In general, the luminescence tends to decrease as the temperature increases, while decreasing the temperature leads to an increment of the luminescence. This dependence of the luminescence with temperature allows to determinate the sample temperature.

The intensity ratio between two transitions associated to *i*-th and *j*-th level, which radiatively decay to a *k*-th level is usually considered in order to remove any experimental

errors due to the temperature influence. In this case, the fluorescence intensity ratio (FIR) is [91,92]:

$$R = \frac{I_{ik}}{I_{jk}} = \frac{N_i(T)}{N_j(T)} \cdot \frac{A_i \beta_{ik} h\nu_{ik} g_i}{A_j \beta_{jk} h\nu_{jk} g_j} \tag{2.27}$$

where N_i, A_i β_{ik} and $h\nu_{ik}$ are the ions population of the *i*-th excited state, the radiative probability, branching ratio related to the phonon emission from level *i* to level *k* and the energy of the emitted phonon respectively. However, thermalized levels are more sensitivity to temprature changes, these levels are electronic multiplets $^{2S+1}L_J$ multiplets, which are very close each other in energy, around hundred of cm^{-1} energy separation ΔE and thermally coupled. As it was briefly mentioned in section 1.1.3, there are some requirements that must be fulfilled in order to consider a pair of thermally coupled level for optical temperature sensors:

i) The energy gap between the thermalized levels must be large enough to avoid overlapping of two nearby emissions (~300 cm^{-1} < ΔE < 2000 cm^{-1}).

ii) At the same time, this energy gap must be short enough to ensure a minimum population of the upper level in the temperature range of interest.

iii) The radiative probabilities of the thermalized levels must be high enough to show large emission intensities.

iv) Sample luminescence must be obtained by conventional lasers

v) Emission sample must be in a spectral region where detectors are more efficient

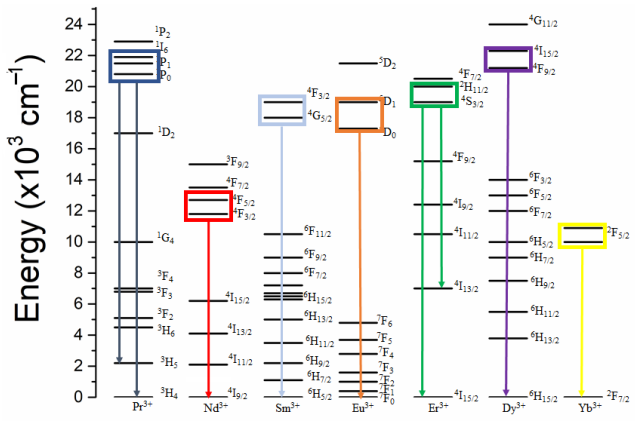

Fig. 2.8. Dieken's diagram of some lanthanide ions. Thermalized levels are also indicated.

Equation 2.27 represents the fluorescence intensity ratio with the temperature. However, it is necessary to rewrite the former equation in order to show an expression that describes the temperature dependence of the *i*-th level population $N_i(T)$. In the case of thermalized system, the ions population of each excited level is well described by the Boltzmann distribution [93,94]. Then, the population of ions found in a certain excited level (N_i) respect to the ground stated population (N_1) is:

$$\frac{N_i}{N_1} = \frac{g_i}{g_1} e^{\left(\frac{-E_{i1}}{K_B T}\right)} \tag{2.28}$$

where K_B, g_i and E_{i1} are the Boltzmann's constant, the degeneracy (2J+1) of the *i*-th level and the energy gap between the ground state and the *i*-th excited state respectively. From the former relationship, the population ratio thermalized level is:

$$\frac{N_{ij}(T)}{N_{jk}(T)} = \frac{g_i}{g_j} e^{\left(\frac{-E_{ij}}{K_B T}\right)} \tag{2.29}$$

This expression is valid if the Ln^{3+}-doped host material (optical temperature sensor) is in thermal equilibrium. In this sense, the optical temperature sensor interacts with two radiation sources at the same time: the thermal radiation of its environtment and the laser radiation source which leads to the emission of the sample. Thus, equation 2.29 must be satisfied in these conditions.

I. Ln^{3+}-doped host matrix into contact with a thermal radiation without laser radiation

In spite of there is not pumping laser, thermal radiation from the environment could promote a small amount of ions to an excited state.

For a simple three-level scheme of a certain Ln^{3+} ion, in which N_1, N_2 and N_3 are the populations of the ground state and thermalized levels respectively. The intensity ratio between level 2 and 3 will be used as $R = I_3/I_2$ (see Fig. 2.9).

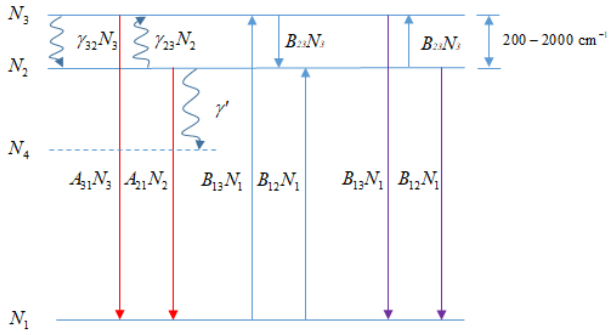

Fig. 2.9. Excitation and de-excitation probabilities between Ln^{3+} ions energy levels which interacts with a thermal radiation source.

For this system, the rate equation are given by:

$$\begin{aligned}
\frac{dN_1}{dt} &= -B_{12}\rho_V N_1 - B_{13}\rho_V N_1 + A_{21}N_2 + A_{31}N_3 + B_{12}\rho_V N_2 + B_{13}\rho_V N_3 + \gamma' N_2 \\
\frac{dN_2}{dt} &= -A_{21}N_2 - \gamma_{23}N_2 - B_{12}\rho_V N_2 - \gamma' N_2 - B_{23}\rho_V N_2 + A_{32}N_3 + B_{23}\rho_V N_3 + \gamma_{32}N_3 + B_{12}\rho_V N_1 \\
\frac{dN_3}{dt} &= -A_{31}N_3 - A_{32}N_3 - \gamma_{32}N_3 - B_{13}\rho_V N_3 - B_{23}\rho_V N_3 + \gamma_{23}N_2 + B_{13}\rho_V N_1 - B_{23}\rho_V N_2
\end{aligned} \quad (2.30)$$

where A_{ij}, $B_{1j}\rho_V$, $B_{ij}\rho_V$ are the photon emission probability calculated by Judd-Ofelt theory, the photon absorption and emission probabilities induced by thermal radiation ρ_V (T) and B_{1j} and B_{ij} are the Einstein's coefficients for induced absorption and emission respectively, and γ_{ij} is the phonon emission or absorption probability. γ' is the probability that N_2 ions level have in order to return to the fundamental level by emitting phonons. The phonon decay to a lower level N_5 should not be neglected as it will be discussed later.

For a system which interacts with the black body radiation, the relation between the Einstein's coeffiecients for all pair of levels B_{ik}=B_{ki}, then the system will evolve until reaching an equilibrium, veryfing Boltzmann's law [91,95](ref 22 y 23):

$$\frac{N_2}{N_1}=\frac{P(E_2)}{P(E_1)}=e^{\frac{-E_{21}}{K_BT}} \qquad \frac{N_3}{N_1}=\frac{P(E_3)}{P(E_1)}=e^{\frac{-E_{31}}{K_BT}} \tag{2.31}$$

From former expression:

$$\frac{N_3}{N_2}=\frac{P(E_3)}{P(E_2)}=e^{\frac{-E_{32}}{K_BT}} \tag{2.32}$$

This last expression represents the total probability and population ratios $P(E_3)/P(E_2)$ and N_3/N_2 in a regime of thermal equilibrium.

II. Ln^{3+}-doped matrix interacting with thermal and laser radiations

When a laser excitation is considered, it is possible to promote ions from N_1 level to N_4 level (see Fig 2.10). In the former case, a term which represents the effect of the laser ΦN_1 is added in first and third equations:

$$\begin{aligned}
\frac{dN_1^*}{dt}&=-\phi N_1-B_{12}\rho_V N_1-B_{13}\rho_V N_1+A_{21}N_2+A_{31}N_3+B_{12}\rho_V N_2+B_{13}\rho_V N_3+\gamma' N_2\\
\frac{dN_2^*}{dt}&=-A_{21}N_2-\gamma_{23}N_2-B_{12}\rho_V N_2-\gamma' N_2-B_{23}\rho_V N_2+A_{32}N_3+B_{23}\rho_V N_3+\gamma_{32}N_3+B_{12}\rho_V N_1\\
\frac{dN_3^*}{dt}&=-A_{31}N_3-A_{32}N_3-\gamma_{32}N_3-B_{13}\rho_V N_3-B_{23}\rho_V N_3+\gamma_{23}N_2+B_{13}\rho_V N_1-B_{23}\rho_V N_2+\phi N_1
\end{aligned} \tag{2.33}$$

The superscript (*) emphatizes the interaction with the laser.

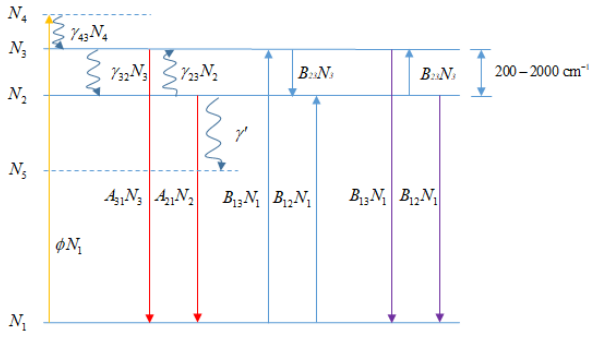

Fig. 2.10. Excitation and de-excitation probabilities between Ln^{3+} ions energy levels which interacts with a thermal radiation and low laser sources.

In this system, the thermal equilibrium is not totally reached, being the population ratio in this case:

$$\frac{N_3^*}{N_2^*} = \frac{P(E_3) + \phi(A_{21} + B_{12}\rho_V + B_{23}\rho_V + \gamma_{23} + \gamma')}{P(E_2) + \phi(A_{13} + B_{23}\rho_V + \gamma_{32})} \neq \frac{N_3}{N_2} = e^{\frac{-E_{32}}{K_B T}} \tag{2.34}$$

In spite of total thermal equilibrium is not reached, it can be assumed that the values for population ratio of N_3/N_2 are more or less similar than the ones from eq. (2.34):

$$\frac{N_3^*}{N_2^*} = \frac{P(E_3) + \phi(A_{21} + B_{12}\rho_V + B_{23}\rho_V + \gamma_{23} + \gamma')}{P(E_2) + \phi(A_{13} + B_{23}\rho_V + \gamma_{32})} \approx \frac{\phi\gamma_{23}}{\phi\gamma_{32}} = e^{\frac{-E_{32}}{K_B T}} = \frac{N_3}{N_2} \tag{2.35}$$

This result can be extended to any Ln^{3+} in a host matrix, since all terms, both numerator and denominator are negligible compared to the products of the multiphonon probabilities, whose ration is the Boltzmann's law.

The calibration procedure for the optical temperature can be obtained by combining eqs. 2.27 and 2.35:

$$R = \frac{I_{31}(T)}{I_{21}(T)} = \frac{N_3(T)}{N_2(T)} \cdot \frac{A_3\beta_{31}h\nu_{31}g_3}{A_2\beta_{21}h\nu_{21}g_2} e^{\frac{-E_{32}}{K_B T}} \tag{2.36}$$

The former equation can be rewritten in a more convenience way, considering the study of the intensity ratio between Stark levels associated to the same or different electronic levels of a certain Ln^{3+} in a crystal, as follow:

$$\begin{aligned} R_{Stark} &= \frac{I_3}{I_2} = Ce^{\frac{-E_{32}}{K_B T}} \\ C &= \frac{A_3\beta_{31}A_{3S}h\nu_3}{A_2\beta_{21}A_{2S}h\nu_2} \end{aligned} \tag{2.37}$$

where A_{iS} and E_{32} is the radiative probability associated to each Stark level involved, and E_{32} is the energetic separation between these levels. Equations 2.36 and 2.37 allow to study the temperature evolution of the intensity ratio between two electronic levels or thermalized Stark levels.

The use of thermally coupled levels in fluorescence intensity ratio (FIR) technique presents several advantages over the use of two noncoupled levels. First, the theory of the relative changes in the fluorescence intensity originating from thermally coupled levels is well understood and therefore, their behaviour is easier to predict. Second, the

population of the individual thermally coupled levels is directly proportional to the total population, thus, any changes in the total population due to changes in the excitation laser source power, will affect the individual levels to the same extent. This feature allows to reduce the dependence of the measurement technique on the excitation power, which is relevant for the stability of the sensor. Last but not least, the employment of relative closely spaced energy levels suggests that the fluorescence wavelengths will be close.

For sensing application, it is relevant to know the rate at which th fluorescence intensity ration changes for a certain change in temperature. This magnitude, known as relative sensitivity S_{REL}, is defined as:

$$S_{REL} = \frac{1}{R}\left|\frac{dR}{dT}\right| = \frac{\Delta E}{K_B T^2} \tag{2.38}$$

From the last equation, it is clear the using pairs of energy levels with larger differences, increasesd the sensitivity. However, this is true only to some extend, because if the energy gap between two levels is higher enough, then the population and hence the fluorescence intensity from the upper thermilizing level will decrease.

2.3. Raman spectroscopy

Raman scattering is a spectroscopic technique used to observe vibrational, rotational, and other low-frequency modes in a system. Raman spectroscopy is widely used in chemistry to provide a structural fingerprint by which molecules can be identified.

The Raman effect takes place when electromagnetic radiation interacts with a solid, liquid, or gaseous molecule's polarizable electron density and bonds. The spontaneous effect is a type of inelastic light scattering, where a photon (ν_0) excites the molecule in either the ground (lowest energy) or excited rovibronic state (a rotational and vibrational energy level within an electronic state). The former excitation puts the molecule into a virtual energy state for a very short time before the inelastic photon scattering proccess takes place. The former scattered photon can be of either lower (Stokes) or higher (anti-Stokes) energy than the incoming photon, compared to elastic, or Rayleigh, scattering where the scattered photon has the same energy as the incoming photon.

For the total energy of the system to keep constant after the molecule moves to a new rovibronic state, the scattered photon shifts to a different energy, and thus a different frequency. This energy difference is equal to that between the initial and final rovibronic

states of the molecule. If the final state is higher in energy than the initial state, the scattered photon will be shifted to a lower frequency (lower energy) so that the total energy remains the same. This shift in frequency is called a Stokes shift ($\nu_0 - \nu_m$), or downshift. If the final state is lower in energy, the scattered photon will be shifted to a higher frequency, which is called an anti-Stokes ($\nu_0 + \nu_m$) shift, or upshift.

Raman scattering is a typical example of inelastic scattering, due to the energy and momentum transfer between the photons and the molecules during the interaction. On the other hand, Rayleigh scattering is a elastic scattering, i.e. the energy of the scattered light has the same frequency as the incoming electronic radiation, as shown in Fig. 2.11. It worth to mention that Raman scattering is a proccess with an order of magnitude around 10^{-6} weaker than the Rayleigh's one.

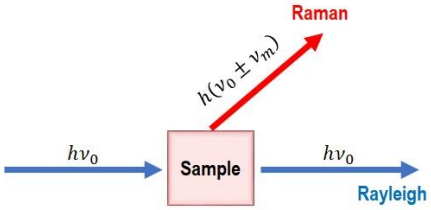

Fig. 2.11. Raman effect mechanism.

Usually, radiation is characterized by its wavelength (λ). Nonetheless, in spectroscopy, the frequency (ν) or wavenumber ($\bar{\nu}$) are more commonly used, which also are linearly related with the energy:

$$\begin{aligned} \lambda &= c/\nu \\ \Delta E &= h\nu \\ \bar{\nu} &= 1/\lambda = h/\nu \end{aligned} \qquad (2.39)$$

where ΔE is the difference between two energy levels, h is the Planck's and c is the velocity of light.

According to classical assumptions, Raman scattering can be explained as follows:

When a diatomic molecule is irradiated by a electric field E of the electronic magnetic field (laser beam) that fluctuates with time t:

$$E = E_0 C\mathrm{os}\left(2\pi\nu_0 t\right) \qquad (2.40)$$

where E_0 is the vibrational amplitude and ν_0 is the laser frequency, an electric dipole moment *P* is induced:

$$P = \mu + \alpha E = \mu_0 + \alpha E_0 \mathrm{Cos}\left(2\pi\nu_0 t\right) \tag{2.41}$$

where μ and αE are the permanent dipolar moment ann the induced dipolar moment respectively. Constant α is the polarizability. When the diatomic molecule is vibrating with a certain frequency ν_m, the nuclear displament *q* is defined as:

$$q = q_0 \mathrm{Cos}\left(2\pi\nu_m t\right) \tag{2.42}$$

where q_0 is the vibrational amplitude. When these amplitudes are small enough, then α is a linear function of *q*:

$$\alpha = \alpha_0 + \left(\frac{\partial\alpha}{\partial q}\right) q_0 + \ldots \tag{2.43}$$

where α_0 and $\left(\partial\alpha/\partial q\right)$ are the polarizability at the equilibrium configuration and the rate of change of α respect to *q*, evaluated at the equilibrium position. Combining eqs. 2.41, 2.42 and 2.43, *P* can be expressed as:

$$\begin{aligned} P = {} & \mu_0 + \alpha E_0 \mathrm{Cos}\left(2\pi\nu_0 t\right) + \left(\frac{\partial\mu}{\partial q}\right) q_0 \mathrm{Cos}\left(2\pi\nu_m t\right) \\ & + \frac{1}{2} E_0 \left(\frac{\partial\mu}{\partial q}\right)_0 q_0 \left[\mathrm{Cos}\left\{2\pi\left(\nu_0 + \nu_m\right)t\right\} + \mathrm{Cos}\left\{2\pi\left(\nu_0 - \nu_m\right)t\right\}\right] \end{aligned} \tag{2.44}$$

Second term of the former equation is the Rayleigh scattering contribution, which describes the oscilaltion of a dipole that radiates light of frequency ν_0. The third one is related to the infrarred absorption and the fourth one is the Raman scattering contribution. Figure 2.12 shows Raman scattering in terms of a diatomic energy level scheme.

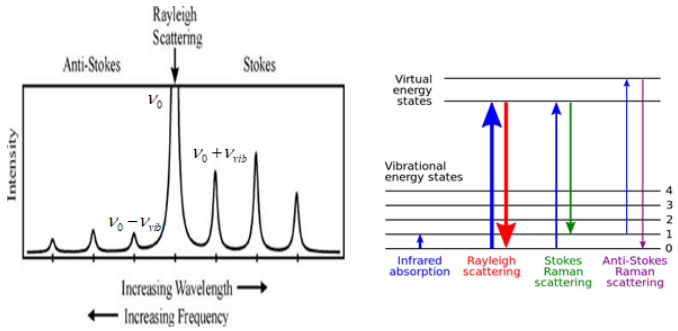

Fig. 2.12. Raman spectrum showing the Rayleigh, Stokes and anti-Stokes lines (on the left). Diagram of vibrational and electronic levels of a molecule comparising infrared absorption, Rayleigh and Raman scattering.

2.3.1. Vibrations in molecules

In the case of a molecule consisting in a N atoms, the problem is the same to the diatomic molecule, but it also more complicate. N atoms means that there is going to be 3N degrees of freedom in order to describe the molecular system. Nonetheless, for a free and non-linear molecule, only three coordinates (Euler's angles) are required to describe completely the orientation of this molecule in the space. For a linear molecule, just two oriental coordinates are needed.

Taking into account these arguments, it is possible to establish the following statements regarding the total degrees of freedom to describe a non-linear and linear molecule:

i) 3N(total)-3(translational)-3(orientational) = 3N-6 vibrational degrees of freedom.

ii) 3N(total)-2(translational)-3(orientational) = 3N-5 vibrational degrees of freedom.

Ignoring any dynamics considerations, the normal vibration of a molecule can be described in terms of its geometry, i.e. the molecule symmetry by certain symmetry operations in its equilibrium configuration. These operations or more especifically, coordinate transformations, leave the energy of the molecule invariant to the former operations. In addition, this set of coordinate transformations forms a group in the mathematical sense. This application of the group theory permits the classification of normal modes according to the symmetry species for each group [96]. It is worth to mention that there are two types of symmetry classification of the molecular vibrations:

i) There is always one symmetry species in a group which conserve the molecule equilibrium configuration, i.e. symmetric and asymmetric vibrational modes.

ii) The symmetry operation called inversion, which consists in a exchange of equivalent atoms (or coordinates) with respect to a center of inversion.

A molecule that posses a inversion center, all normal modes of vibration are either symmetric or antisymmetric, i.e. “g” or “u” with respect to the inversion operation. In such case, symmetrical vibration modes under inversion will be Raman-active. On the opposite case, they will be infrared-active.

In general, the classification of vibration normal modes in symmetry species does not give rise to certain description of the nature of molecular vibrations [97], but, more relevant, to direct information of the selection rules that govern infrared and Raman spectral activity (see Fig. 2.13).

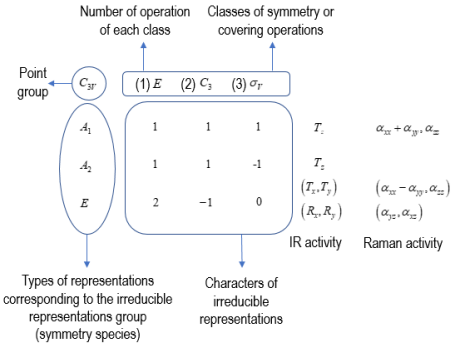

Fig. 2.13. Diagrammatic interpretation of the character table associated to the C_{3V} point group.

2.3.2. Selection rules

Selection rules must be applied on each normal vibration in order to determine if such vibration is active in the IR or Raman spectra. According to quantum mechanics, a vibration is Raman-active and IR-active if the dipole moment and polarizability changes during the vibration respectively.

Concerning the Raman activity, the plarizability is considered. When a molecule is irradiated by a laser beam, it suffers distortions, because the positively charged nuclei are attracted toward the negative pole, and electros toward the positive pole. This charge separation leads to an induced dipole moment *P* given by:

$$P \approx \alpha E \tag{2.45}$$

Due to the vectorial nature of P and E of three components, eq.22 must be rewritten in matrix form as follows:

$$\begin{bmatrix} P_x \\ P_y \\ P_z \end{bmatrix} = \begin{bmatrix} \alpha_{xx} & \alpha_{xy} & \alpha_{xz} \\ \alpha_{yx} & \alpha_{yy} & \alpha_{yz} \\ \alpha_{zx} & \alpha_{zy} & \alpha_{zz} \end{bmatrix} \begin{bmatrix} E_x \\ E_y \\ E_z \end{bmatrix} \tag{2.46}$$

First matrix in the right side of the former equation is called the polarizability tensor. According to quantum mechanics, a vibration is Raman-active if one of the polarizability tensor components changes during the vibration.

3. METHODS

3.1. Sol-gel synthesis method

The sol-gel method is a wet-chemical technique, also known as chemical solution deposition, which is commonly employed in a variety of fields, such as, material science and even ceramic engineering. This method is used for the fabrication of materials, usually a metal oxide, beginning from a chemical solution (called “sol”) that acts as the precursor for discrete particles or polymer networks (“gel”) [98]. Typical precursors use to be nitrates or chlorides/alkoxides metal.

In this chemical process, the 'sol' (or solution) gradually evolves towards the formation of a gel-like diphasic system containing both a liquid and solid phases whose morphologies range from discrete particles to continuous polymer networks. In the case of the colloid, the particle density could be so low that a significant amount of fluid could need to be removed previously for the gel-like properties to be recognized. This can be managed in many ways. The simplest method is to permit time for sedimentation to happen, and then pour off the remaining liquid. Centrifugation can also be used to accelerate the process of phase separation.

Removal of the remaining liquid (solvent) phase requires a drying process, which is typically accompanied by a significant amount of shrinkage and densification. The rate at which the solvent can be removed is ultimately determined by the distribution of porosity in the gel. The ultimate microstructure of the final component will clearly be strongly influenced by changes imposed upon the structural template during this phase of processing.

Afterwards, a thermal treatment, or firing process, is often necessary in order to favor further polycondensation and enhance mechanical properties and structural stability via final sintering, densification and grain growth. One of the distinct advantages of using this methodology as opposed to the more traditional processing techniques is that densification is often achieved at a much lower temperature.

The precursor sol can be either deposited on a substrate to form a film (e.g., by dip coating or spin coating), cast into a suitable container with the desired shape (e.g., to obtain monolithic ceramics, glasses, fibers, membranes, aerogels), or used to synthesize

powders (e.g., microspheres, nanospheres) [99]. The sol-gel approach is a cheap and low-temperature technique that permits for the fine control of chemical composition of the product. Even small quantities of dopants, such as organic dyes and lanthanide elements, can be introduced in the sol and end up uniformly dispersed in the final product. It can be used in ceramics processing and manufacturing as an investment casting material, or as a means of producing very thin films of metal oxides for various purposes.

Sol-gel derived materials have many applications in optics, electronics, energy, space, (bio) sensors, medicine (e.g., controlled drug release), reactive material and separation (e.g., chromatography) technology.

In this thesis, the former method was employed in order to synthesize pure undoped and lanthanide doped nano-perovskites. The average main size achieved by this method was around 40 nm. A large number of nano-perovskites was prepared, however some of them, such as, Nd^{3+} -doped $YAlO_3$ with different mol % concentration of the former ion (0.1, 0.5, 1.0 and 2.5 mol %), Tm^{3+}-doped $YAlO_3$ (2.5 mol %) and undoped $YAlO_3$ were studied.

3.1.1. Sol-gel synthesis method. Steps

Sol-gel is a really straigthforward synthesis method which steps are summarized in the diagram of Fig. 3.1. Briefly:

1) Nitric acid (HNO_3) was used as a solvent in which the precursor materials, nitrates $X(NO_3)_3\_yH_2O$, where X site is associated to the transition metals and/or lanthanide ions and "y" corresponds to the water molecules number and the citric acid ($C_6H_8O_7$) as complexing agent. The former agent lead to a better distribution of the different metals in the resulting precursor, giving rise to a more efficient reaction at high temperature and a proper dwelling time.

2) Nitrates compounds in a stoichiometric molar ratio were dissolved in 25 mL of 1 M HNO_3 under stirring at 353 K (80 ºC) for 3 h.

3) Then citrid acid, with a 1:2 molar ratio of metal ions to citrid acid, was added to the solution. Such solution was stirred and heated at 363 K (90 ºC), until reaching the transparency of the solution.

4) Then, 4 mg of polyethylene glycol was added to the solution, leading to the formation of a gel.

5) A first thermal treatment upon the former gel was carried out at 673 K (400 ºC) for 6 h in order to remove the residual nitrates and organic compounds.

6) A second thermal treatment was performed at 1823 K (1550 ºC) to achieve the nano-crystalline powder sample.

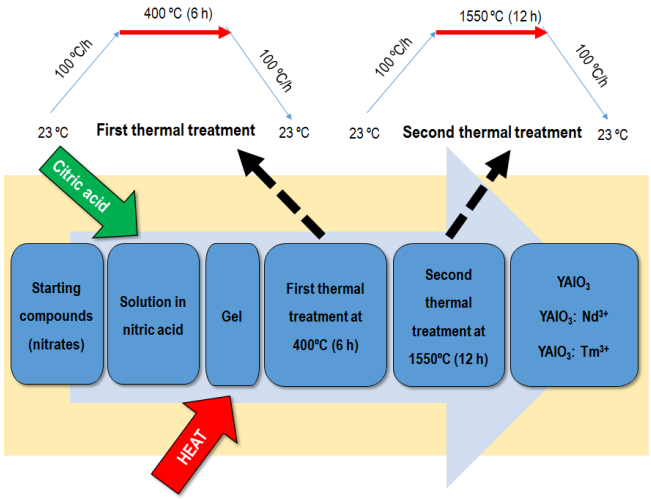

Fig. 3.1. Sol-gel synthesis method steps diagram.

3.1.2. Perovskite structural characterization

The perovskite crystallographic structure has been extended to other compounds with the general formula ABO_3. Perovskites present four formula units per unit cell with the formula ABO_3. The structure is formed by corner linked octahedra containing the *B* cation (BO_6) with dodecahedral interstices containing the *A* cation (AO_{12}) (see Fig. 3.2).

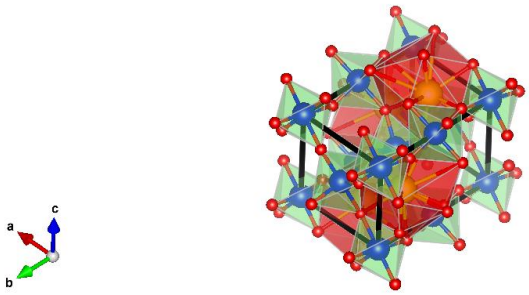

Fig. 3.2. $YAlO_3$ perovskite unit cell. YO_{12} dodecahedra (red) and AlO_6 octahedra (green) are highlighted.

Generally, perovskites are characterized by a orthorhombic structure, in particular, $YAlO_3$ crystallizes in the orthorhombic *Pnma* structure (see Fig. 3.3), i.e. *Pbnm* with a different setting [100]. However, they can crystallize in a variety number of space groups depending on the ratio of the cation sizes, which causes various tilts and twists of the octahedra. With no tilts, twists, or distortions, the structure is cubic ($Pm\bar{3}m$).

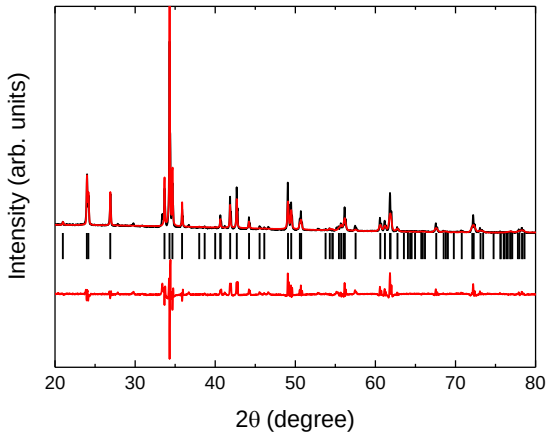

Fig. 3.3. X-ray diffraction pattern of the $YAlO_3$ nano-perovskite. Rietveld refinements including the difference between calculated and observed patterns are also shown (red)

According to theoretical considerations, the *Pnma* structure of ABO_3 perovskite with four formula units per primitive cell, has 60 vibrational modes distributed in 24 Raman-active

modes (Γ_R), 25 infrared-active modes (Γ_{IR}), 8 silent modes (Γ_S) and 3 acoustic modes (Γ_{AC}):

$$\begin{aligned}\Gamma_R &= 7A_g + 5B_{1g} + 7B_{2g} + 5B_{3g}\\ \Gamma_{IR} &= 9B_{1u} + 7B_{2u} + 9B_{3u}\\ \Gamma_S &= 8A_u\\ \Gamma_{AC} &= B_{1u} + B_{2u} + B_{3u}\end{aligned} \quad (3.1)$$

The Raman spectrum of perovskites can be interpreted, in a first approximation, considering that the different Raman modes could be related to the vibrational modes of dodecahedra (AO_{12}) and octahedra (BO_6) units. However, the attribution of each Raman mode to an indivual unit is not easy, becasue these vibrational modes are coupled each other.

There are a huge variety of perovskites crystal with different compositions, such as, $GdFeO_3$, $GdAlO_3$, $LaAlO_3$, etc

3.2. Experimental setups and techniques

Since the experimental procedures are well described on the corresponding experimental section of each paper, only a brief covering of the equipment and techniques employed in this thesis will be exposed here.

3.2.1. Ambient condition characterization

I. X-ray diffraction and TEM setups

Powder X-ray diffraction data were collected on a PANalytical X'Pert PRO diffractometer (Bragg-Brentano geometry) with an X'Celerator detector employing the Cu $K\alpha_1$ radiation (λ=1.5405 Å) in the angular range $5^o < 2\theta < 80^o$, by continuous scanning with a step size of 0.02º (see Fig 3.4 left). TEM measurements were performed in a JEOL JEM 2100 equipment operanting at 200 Kv (see Fig 3.4 center). Dynamic light scattering (DLS) measurements were carried out on a Mastersizer 2000/E (see Fig 3.4 right).

Fig. 3.4. **(left)** PANalytical X'Pert PRO diffractometer (Bragg-Brentano geometry), **(center)** JEOL JEM 2100 and **(right)** Mastersizer 2000/E equipments.

II. Absorption

When the energy of an incident radiation on a sample is higher enough to ensure the transition between two energy levels of the 4f electrons, the absorption of the former incident radiation occurs. Lambert-Beer allows the relationship between the attenuation of light and the properties of the material through which the light is travelling:

$$I(d) = I_0 e^{-\alpha d} \tag{3.2}$$

where d, I_0 and I are the sample thickness, radiation intensity before and after through the sample respectively. α is the absorption coefficient which depends on the wavelength and the polarization of the incident light. Experimentally, absorption measurements are function of the transmitance T or the optical density, DO. Both magnitudes can be related as follow:

$$DO = \log \frac{I_0(\lambda)}{I(\lambda)} = \log \frac{1}{T} = \frac{\alpha d}{2.303} \tag{3.3}$$

Since the nano-perovskites that have been studied in this thesis are powders, the absorption only could be obtained by diffuse reflectance measurements.

Diffuse reflection is the reflection of light or other waves or particles from a surface such that a ray incident on the surface is scattered at many angles rather than at just one angle as in the case of specular reflection (see Fig 3.5). An *ideal* diffuse reflecting surface is said to exhibit Lambertian reflection, meaning that there is equal luminance when viewed from all directions lying in the half-space adjacent to the surface.

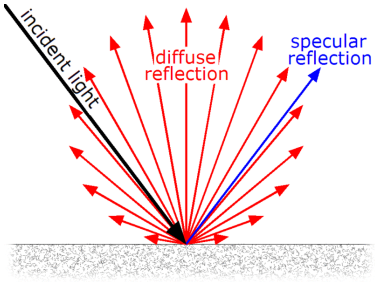

Fig. 3.5. Diffuse and specular reflection from a surface. The rays represent luminous intensity, which varies according to Lambert's cosine law for an ideal diffuse reflector.

The diffuse reflectance spectrum is defined as the relation between the reflexed flux of the powder sample and the flux of a reference sample in the same geometrical and spectral conditions. This relation can be monitored in two ways: i) specular reflectance and ii) diffuse reflectance. The last one requires and integrating sphere which collects the reflectance diffuse on the incident light on the powder sample Incident light wavelength is varied in the study range.

In order to measure the diffuse reflectance spectra whitin the study range, a Cary 5000 spectrometer (Varian) was employed (see Fig 3.6). This equipment possesses two lamps, one halogen quartz lamp for VIS-NIR range and another deuterium lamp for ultraviolet range. In addition, it has two detectors, one is the PMT (Hamamatsu R928) for the UV-VIS range and a InGaAs detector for NIR.

Fig. 3.6. Cary 5000 (Varian).

Reflectance diffuse measurments were carried out using an integrating sphere. Background was taken from a reference sample and after that, the powder samples were placed and measured. These measurements were performed at Universidad de La Laguna

III. Luminescence

Luminescence allows to study the radiative desexcitation channel of each excited level of the 4f electrons. Photon emissions is not the unique mechanism, in fact, it competes witrh other ones such as, non-radiative proccess and energy transfer between ions.

Luminescence measurements were carried out by using different diode-pumped solid state lasers and optical parametric oscillator OPO (EKSPLA/NT342/3/UVE) laser (see Fig 3.7)

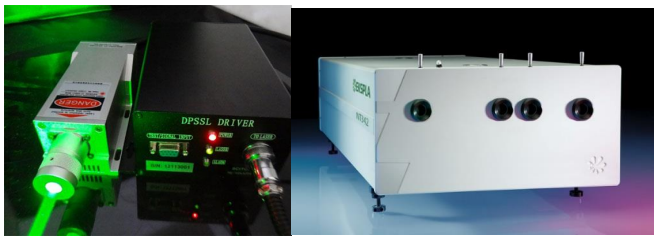

Fig. 3.7. **(left)** diode-pumped solid laser and **(right)** and optical parametric oscillator OPO (EKSPLA/NT342/3/UVE) laser

The experimental setup employed for the luminescence measurements of the samples, was set to a "90º configuration", i.e. the CCD spectrometer is placed perpendicularly respect to the incident laser beam, in order to avoid direct incidence of the former laser on CCD, as it is shown in Fig. 3.8.

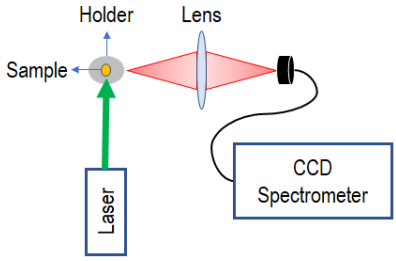

Fig. 3.8. Experimental setup diagram of luminescence measurement in 90º configuration set.

Some of monochromators, CCDs and detectors that were used during the optical characterization of the samples are depicted in Fig. 3.9.

Fig. 3.9. CCD cameras, detectors and monochromators.

IV. Luminescence dynamics. Life time

The experimental measurement of the life time is employed to study the temporal dynamics of each excited level. This technique allows to determine the population and depopulation mechanism of each level.

The experimental setup of luminescence dynamics measurement is shown in Fig 3.10. In this case, a 90º configuration was also applied. Nano-perovskite samples were excited. Briefly, the sample is excited by a OPO laser, whose working range is from 210 up to 2300 nm. Laser pulses have bandwiths and periods around of 5 cm^{-1} and 10 ns respectively. The energy output of each pulse depends on the selected excitation wavelength and varies between 20 to 100 mW. Since the sample emission could be associated to the desexcitation from several levels, it has to be descomposed using a monochromator (TRIAX 320), which selects the wavelength that will pass to the detector (photomultiplier). The temporal evolution of the detected luminescence is recorded by a digital LeCroy (WS424) oscilloscope, as it is shown in the diagram of the Fig. 3.10.

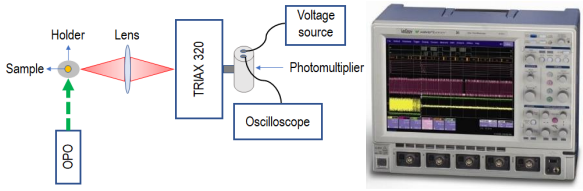

Fig. 3.10. **(left)** Experimental setup diagram of luminescence lifetime measurement and **(right)** LeCroy (WS424) oscilloscope.

3.2.2. High pressure characterization

In this thesis, two type of DACs were used. For XRD, Raman scattering and luminescence measurements at high-pressure conditions, a Merrill-Basset type DAC and a membrane-DAC were employed respectively (see Fig 3.11).

Fig. 3.11. **(left)** Merril-Basset type DAC for XRD experiments and **(right)** membrane-type DAC for Raman scattering and luminescence experiments.

The preparation of one of these DACs for a specific measurement, follows the next steps.

i) The pre-indentation process, applying pressure with the diamonds of DACs on a tungsten gasket placed between these diamonds, in order to make a mark on it, with a thikness around of 55 μm.

ii) In the center of the former mark, a hole of 100-150 μm of diameter is performed using a drill (Boehler microDriller) (see Fig. 3.12). This hole is called the hydrostatic chamber.

iii) The sample, ruby chips as reference to measure the pressure inside the cavity, and a 16:3:1 solution of methanol:ethanol:water as pressure transmitting medium, are placed in the former hole.

Fig. 3.12. Spark erosion system for gasket drilling.

I. Pressure calibration with ruby fluorescence

At the beginning, pressure was estimated by force over area, high-pressure XRD studies by internal markers, for instance NaCl, KCl, Au or by phase transition of a certain sample by XRD. In 1972, Forman et at. [101] showed that the R lines of Cr^{3+}-doped Al_2O_3 shifted following a linear behaviour as the pressure increased from 0.1 GPa to 2.2 GPa, ansd showing a noticeable broadening of these lines as well in non-hydrostatic conditions. Afterwards, a published work by Barnet et at. [102] showed a very straigthforward way to measure the pressure inside the hydrostatic chamber of the DAC using the ruby fluorescence technique. Piermarini et al. [103] showed that the ruby R lines shift, follows a linear behaviour as pressure increases up to 20 GPa, which later, a positive small non-linear trend was observed by Mao et al. [104] on R lines, monitoring the pressure evolution of R_1 line up to 80 GPa. Finally, Carter et al [105] proposed the most commonly used equation for pressure calibration so far, which is defined as:

$$P = \frac{A}{B}\left[\left(1+\frac{\lambda}{\lambda_0}\right)^{B} - 1\right] \tag{3.4}$$

where A=1871 GPa, B= 10.06 and λ_0 = 694.24 nm [106].

The former equation along with the one proposed by Syassen [106] were employed in this thesis.

II. Raman scattering and optical pressure calibration sensor setup

For ambient to high-pressure condition experiments, a Raman microscopy setup was employed. Figure 3.13 shows a diagram of some Raman microscopy components.

Briefly, the excitation laser source (solid state laser) beam passes through an interference filter which removes the undesired lines present in the emited light of the former laser, in order to ensure its monochromaticy. Afterwards, it pass through a lens which focuses it towards a first pinhole. This pinhole ensures the filtering of the laser beam. One face of the first beamsplitter lets the transmission of the laser beam through it, towards a second beamsplitter which reflects it to the microscope. The laser is focused on the sample by the microscope objectives. The signal from the sample (could be Raman or luminescence, depending on the measurement which is carried out to) comes back and passes through a filter, which is placed between the first and second beamsplitters. The former filter blocks the impure signals, which can be the Rayleigh scattering contribution, if it is about of Raman scattering measurement or undesired signal that does not come from the sample, in the case of luminescence measurement. Finally, once the emission of the sample is filtered from any impure signal, it sent to the spectrometer, passing through before a second pinhole, which works as the entry slits of the CCD spectrometer, where the emission is recorded.

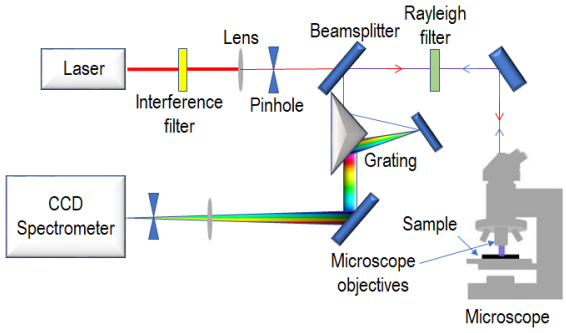

Fig. 3.13. Raman microscope experimental setup diagram for ambient to high-pressure condition measurement.

The Raman scattering at ambient to high-pressure conditions were performed at Universitat Politècnica de València, using a HORIBA Jobin Yvon LabRAM HR UV spectrometer in combination with a thermoelectrically cooled multichannel Synapse CCD detector (see Fig 3.14 left).

On the other hand, the ambient and high-pressure luminescence experiments were carried out at Universidad de La Laguna, using a Reninshaw inVia Raman Microscope (see Fig 3.14 right).

Fig. 3.14. **(left)** HORIBA Jobin Yvon LabRAM HR UV spectrometer and **(right)** Renishaw inVia Raman Microscope.

3.2.3. High temperature luminescence

For the optical temperature calibration experiments, a tubular electric furnace where the samples were placed at the center of it and heated at a rate of 1.77 K/min, was employed. Briefly, the excitation laser source excited the sample from one side of the furnace, while the emission was collimated by a lens located on the other exit side, and then focalized with another lens into an optical fiber coupled to a 0.3 m single grating spectrometer (Andor SR-500i-B2-R). Finally, the detection was carried on with a cooled CCD detector (Newton DU490A-1.7) with a resolution of 0.7 nm (~25 cm^{-1}) and an integration time of 1 s (see Fig. 3.15).

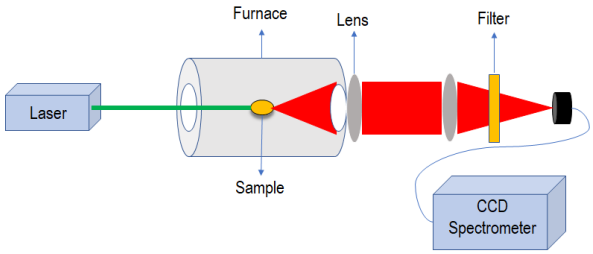

Fig. 3.15. Temperature calibration experimental setup.

III. Optical temperature calibration. Fluorescence Intensity Ratio technique (FIR)

For the optical temperature calibration of the samples, the FIR technique was considered. As it was discussed in the section 2.2.5 of this thesis, FIR seeks the determination of the temperature analyzing the changes in the band shape of RE^{3+} emissions. This technique studies the relative emission intensities of two nearby energy levels, close enough in energy to allow the thermal redistribution of the population from the lower level (E_2) to

the upper one (E_3) (see Fig. 3.16). Therefore, the intensity ratio of these levels depends on the temperature *T*, but at the same time, this ratio is independent of the source power excitation, because the population of each level is proportional to the pump power used. Under low pump power excitation, the intensity ratio between the emitting E_2 and E_3 levels, *R*, is described by Boltzmann's law, given by:

$$R = \frac{I_{31}}{I_{21}} = \frac{\omega_{31}^R g_3 h\nu_3}{\omega_{21}^R g_2 h\nu_2} e^{\frac{-\Delta E}{K_B T}} = Ce^{\frac{-\Delta E}{K_B T}} \tag{3.5}$$

where K_B is the Boltzmann constant, $\Delta E = E_3 - E_2$ is the energy gap between E_3 and E_2 excited thermalized levels, g_3 and g_2 are the degeneracies *(2J+1)* of the levels, and ω_{31}^R and ω_{21}^R are the spontaneous emission rates of the E_3 and E_2 levels to the ground level (E_1), respectively.

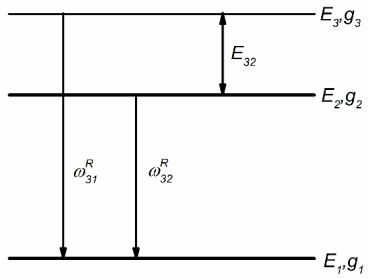

Fig. 3.16. Simplified diagram for three levels particularized to Tm^{3+} ion. ΔE is the energy gap between the two excited levels (E_2 and E_3), g_i is the degeneracy of the *i-th*-level and ω_{ij}^R is the spontaneous emission rate between the *i-th* and *j-th* levels.

The sensor sensitivity *S* can be defined as the rate at which *R* changes with temperature:

$$S = \left|\frac{dR}{dT}\right| = R\left(\frac{\Delta E}{k_B T^2}\right) \tag{3.6}$$

However, it is necessary to introduce another parameter, the relative sensor sensitivity S_{REL}, which is defined as follows:

$$S_{REL} = \frac{1}{R}\left|\frac{dR}{dT}\right| = \left(\frac{\Delta E}{k_B T^2}\right) \tag{3.7}$$

that only depends on the temperature. Hence, it allows the comparison with other optical temperature sensors.

From the last equation, the larger the energy gap between two thermalized levels the larger the sensitivity. Nevertheless, as the energy gap between these levels increases, the population and the intensity from the upper thermalized level decreases.

The temperature uncertainty, δT, is the smallest temperature change that can be achieved in a given measurement and can be estimated by the equation [107]

$$\delta T = \frac{1}{S_{REL}} \frac{\delta R}{R} \tag{3.8}$$

where S_{REL} is the relative sensitivity and the $\delta R/R$ is the relative uncertainty on R.

3.2.4. Subtissue penetration depth setup

For the depth penetration studies, the sample was excited at 895 nm, using the laser line of a Ti: sapphire laser (3900S Spectra Physics) pumped by Millenia Prime laser (Millenia 15sJSPG) along with a vertical setup.

Briefly, the sample was placed into a holder which was located under a 1 mm size cuvette filled with a solution of Intralipid 10% (phantom tissue). The sample was optically excited with a continuous laser source at around 895 nm. Part of this laser was reflected to the sample by a filter and then was focused on the sample. After that, the NIR emission of the sample passed through the former filter and then was focused on the spectrometer by a second lens. The phantom tissue thickness was varying just filling a specific volume of the cuvette with a solution of Intralipid. This setup allowed to measure the NIR emission as a function of the tissue thickness by simply filling the cuvette with a specific volume of the phantom tissue as it is shown in Fig. 3.17.

The NIR emission of the sample, was detected through a solution of Intralipid®, which is an intravenous nutrient consisting of an emulsion of phospholipid miceless and water [108] as phantom tissue. The phantom tissue consists in an absorbing and scattering medium that has been extensively employed in the past to mimic the optical properties of human skin in the I-*BW* and II-*BW* [109–112] as a function of the depth penetration was recorded by using the same grating spectrometer with a NIR extended photomultiplier (HAMATSU H10330B-75). The concentration of Intralipid® used in this experiment was the equivalent to 0.025 mol of it in a volume of solution of 24.85 mL.

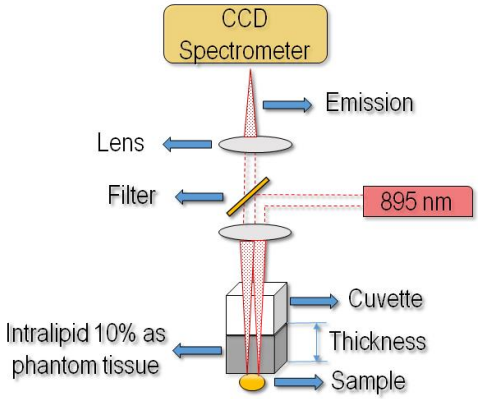

Fig. 3.17. Schematic diagram showing the experimental procedure to determine the penetration depth.

4. ARTICLES COMPENDIUM

In this section, the six papers that have been published during the thesis period are presented.

4.1. Structural and optical characterization of the $YAlO_3$ nanoperovskites

In this section, the first and second of the six papers are included and represent the first steps regarding the initial characterization of undoped and Nd^{3+}-doped $YAlO_3$ nano-perovskites.

The first paper, the effects of two different thermal treaments, during the sol-gel synthesis procedure on the structural and optical properties of $YAlO_3$ doped with different concentration of Nd^{3+} ions, were studied. This paper was the starting point in terms of the optimization of the employed synthesis method during this thesis.

The second paper, an extensive experimental and theoretical study concerning the structural, vibrational and elastic properties of undoped $YAlO_3$ nano-perovskite at ambient and high-pressure conditions was performed.

4.1.1. Spectroscopic properties of Nd^{3+} ions in YAP nano-perovskites

Authors: **M.A. Hernández-Rodríguez**, A.D. Lozano-Gorrín, I.R. Martín, U.R. Rodríguez-Mendoza and V. Lavín

Published in: **Journal of Luminescence;** Volume: **188;** Pages: **204-208;** DOI: 10.1016/j.jlumin.2017.04.031; Accepted **21, April 2017**

In this article, $YAlO_3$ nano-perovskites doped with different concentrations of Nd^{3+}, i.e, nano-crystalline perovskites of composition $Y_{(1-x)}Nd_xAlO_3$ with x = 0.001, 0.005, 0.01 and 0.025 (in mol %) (from now, YAP: Nd^{3+} 0.1% YAP: Nd^{3+} 0.5% YAP: Nd^{3+} 1.0% and YAP: Nd^{3+} 2.5%) were successfully synthesized by sol-gel method with two different thermal treatments at 1200 ºC and 1550 ºC.
X-ray diffraction (XRD) patterns of these nano-perovskites confirmed two different profiles between the ones annealed at 1200 ºC and those treated at 1550 ºC during the synthesis procedure. XRD patterns confirmed the monoclinic structure space group *P2/m* with a comparable double contribution of the perovskite (YAP) and garnet-type (YAG)

profiles, as it is shown in Fig 1a. of this article. On the other hand, XRD spectra of the nano-perovskites treated at 1550 ºC confirmed the orthorhombic structure space group *Pnma* with a predominant YAP phase with a minor YAG phase as impurity as it is shown in the Fig. 1b of this article.

Since XRD measurements confirmed the existence of two possible environmets for Nd^{3+} ions in these nano-perovskites, site selection spectroscopy was performed exciting the samples at 529.5 and 531 nm with a pulsed laser excitation source. Site excitation spectroscopy, indeed confirmed two different environments for Nd^{3+} in nano-perovskites annealed at 1200 ºC, whose emission spectra showed two different profiles exciting with one or another wavelength, being a mixture of both environments where YAP phase (site I) was clearly predominant compared to YAG phase (site II) and site II was predominat compared to site I, when the excitation wavelength was set to 529.5 and 531 nm respectively as it is shown in Fig. 3 in the article. Concerning the samples treated at 1550 ºC, site selection spectroscopy did not distinguish clearly the former phases, only a predominant profile which is related to site I, which means that YAP phase was predominant against YAG one as it is shown in Fig. 4 in the article. These results were in agreement with the XRD predictions. In addition, luminescence dynamics studies confirmed only the existence of energy transfer between Nd^{3+} ions in the samples.

Time resolved spectroscopy allowed to confirm that the thermal treatment at 1550 °C was the proper one in order to obtain nano-perovskites with crystallite sizes around 40 nm.

Journal of Luminescence 188 (2017) 204–208

Contents lists available at ScienceDirect

Journal of Luminescence

journal homepage: www.elsevier.com/locate/jlumin

Spectroscopic properties of Nd^{3+} ions in YAP nano-perovskites

M.A. Hernández-Rodríguez[a,*], A.D. Lozano-Gorrín[a], I.R. Martín[a,b,d], U.R. Rodríguez-Mendoza[a,b,d], V. Lavín[a,b,c]

[a] Departamento de Física, Universidad de La Laguna, E-38200 San Cristóbal de La Laguna, Santa Cruz de Tenerife, Spain
[b] MALTA Consolider Team, Universidad de La Laguna, E-38200 San Cristóbal de La Laguna, Santa Cruz de Tenerife, Spain
[c] Instituto Universitario de Estudios Avanzados en Física Atómica, Molecular y Fotónica (IUdEA), Universidad de La Laguna, E-38200 San Cristóbal de La Laguna, Santa Cruz de Tenerife, Spain
[d] Instituto Universitario de Materiales y Nanotecnología (IMN), Universidad de La Laguna, E-38200 San Cristóbal de La Laguna, Santa Cruz de Tenerife, Spain

ARTICLE INFO

Keywords:
Pechini method
Thermal treatment
YAP nano-perovskites
X-ray diffraction
Site selection spectroscopy

ABSTRACT

Yttrium aluminium nano-perovskite doped with different concentrations of Nd^{3+} (YAP: Nd^{3+}) were successfully synthesized by the Pechini sol-gel method at 1200 °C and 1550 °C. X-ray powder diffraction patterns confirmed the monoclinic and orthorhombic structure space group *P2/m* and *Pnma* for the samples treated at 1200 °C and 1550 °C respectively. Yttrium aluminium garnet phase was detected in both treatments, being more noticeable at 1200 °C treated samples. The non-equivalent center nature of these samples was observed performing site selection spectroscopy, confirming the presence of two different sites for the Nd^{3+} ions in the samples, associated with perovskite and garnet phases, previously detected in XRD measurements. The study of the luminescence dynamics of YAP: Nd^{3+} nano-perovskites treated at 1550 °C for all concentrations was carried out, confirming the existence of the energy transfer between Nd^{3+} ions. Time resolved spectroscopy allowed to confirm that the thermal treatment at 1550 °C was the proper one in order to obtain nano-perovskites.

1. Introduction

The research in the nanomaterials field has become of relevant importance for the industrial applications. New developments in electronics, optics or biology imply the evolution of new phosphors whose properties can be enhanced by reaching the nanometric scale. Nano-crystallites possess unique properties, which are not observed for their bulk samples counterparts, their size, shape and large surface to volume ratio influence the material properties, such as the electronic energy levels, optical transitions, conductivity and phase transition temperatures [1].

In the last years, research works in perovskites have gained interest because of their relevance in several technological applications, such as hydrogen sensors, SOFC electrodes, multilayer capacitors, and solar cells [2]. Among them, the most used one is the $CaTiO_3$ perovskite, due to its thermal and chemical stabilities [3]. On the other hand, some of its features makes this perovskite a promising candidate for a new host material for powder lasers as well as host lattice for efficient luminiscence of lanthanide ions [4–7] and biomedical applications [8]. In addition to this, it is possible to find works focused on others types of perovskites, such as $BaTiO_3$ which it is reconigzed because its ferroelectric properties [9–11] or $LaAlO_3$ as a host material for lanthanide ions [7].

The $YAlO_3$ perovskite (YAP) doped with different lanthanide ions in bulk crystal and nano-powder has been extensively studied due to its optical properties. It has been successfully used as scintillators [12–14], phosphors [15–18], and for solid-state lasers [19,20]. Focusing on laser applications, the YAP: Nd^{3+} presents good mechanical and thermal properties as well as a high emission cross section and a long fluorescence lifetime (180 μs), similar to those of the well-known YAG: Nd^{3+} laser crystal [21]. Additionally, the incorporation of Nd^{3+} ions in YAP crystals is about four times higher than that of YAG: Nd^{3+} crystals, which would allow a more efficient pumping. Another interesting feature of the YAP in contrast to YAG, is its anisotropy [22–24] which allows to select crystallographic orientations in order to optimize specific laser performances. In this paper, the spectroscopic properties of the YAP: Nd^{3+} nano-perovskite are presented and the influence of the Nd^{3+} concentration and the thermal treatment during synthesis processes in the luminescent properties is discussed.

2. Experimental details

Nano-crystalline YAP perovskites of composition $Y_{(1-x)}Nd_xAlO_3$, with x = 0.001, 0.005, 0.01 and 0.025 (in mol%) (YAP: Nd^{3+} 0.1%, YAP:

* Corresponding author.
E-mail address: miguelandreshr@gmail.com (M.A. Hernández-Rodríguez).

http://dx.doi.org/10.1016/j.jlumin.2017.04.031
Received 3 February 2017; Received in revised form 13 March 2017; Accepted 20 April 2017
Available online 21 April 2017

Nd^{3+}0.5%, YAP: Nd^{3+}1.0% and YAP: Nd^{3+}2.5%) were successfully synthesized by the Pechini citrate sol–gel method in an air atmosphere. Stoichiometric molar ratios of high-purity $Y(NO_3)_3{\cdot}4H_2O$ (ALDRICH, 99.9%), $Al(NO_3)_3{\cdot}9H_2O$ (ALDRICH, 99.9%) and $Nd(NO_3)_3{\cdot}H_2O$ (ALDRICH, 99.9%) materials were dissolved in 25 ml of 1 M HNO_3 under stirring at 80 ºC for 3 h. Then citric acid, with a molar ratio of metal ions to citric acid of 1:2, was added to the solution, which was stirred and heated at 90 ºC until reaching the transparency of the solution. Then, 4 mg of polyethylene glycol was added to the solution. This last step created a gel that was fired at 400 °C for 6 h in order to remove the residual nitrates and organic compounds and the subsequently obtained powder sample was finally burnt out at 1200 °C for 20 h. The second thermal treatment was performed at 1550 °C for 12 h.

X-ray diffraction (XRD) patterns were measured on a diffractometer (PANalytical X'Pert Pro) using CuKα1 radiation.

The visible and NIR diffuse reflectance spectrum in the range from 200 to 1800 nm was measured using an integrating sphere with a Cary 5000 (Varian).

Site selection spectroscopy of the YAP: Nd^{3+} nano-perovskites were measured by exciting at 529.5 and 531 nm with a 10 ns pulsed optical parametric oscillator OPO (EKSPLA/NT342/3/UVE). The emission of the samples was focused on the entrance slit of a CCD spectrograph. The luminescence decay curves were measured by exciting the Nd^{3+} ions with the OPO laser and using an analogic storage oscilloscope (LeCroy WS424) coupled to the detection system. All spectra were corrected for the spectral response of the equipment.

3. Results and discussion

3.1. Structural characterization

All diffraction patterns of powder samples were well indexed to a monoclinic structure space group *P2/m* phase at the stage of having been thermally treated at 1200 °C, having found a mixture of perovskite and garnet phases and therefore finding a monoclinic space group always suitable to match the number of peaks found on the pattern (Fig. 1*a*).

However, after heating at 1550 °C, the new profile shows the presence of two phases, but a predominant perovskite-type one and a residual garnet-type one (Fig. 1*b*). The diffraction patterns are well indexed in the orthorhombic space group *Pnma* (phase 1) and in the cubic *Ia-3d* (phase 2). Thus, X-ray diffraction (XRD) confirms the YAP: Nd^{3+} structure to be that as perovskite-type one. The inset of the Fig. 1*b* shows the YAP: Nd^{3+} unit cell. Crystal structure parameters have been obtained after fitting the profiles of the nano-perovskites by the Rietveld method using FULLPROF program [25].

Table 1
Cell Parameters and Reliability Factors Obtained from the Rietveld Refinement.

Compound	a (Å)	b (Å)	c (Å)	X^2	R_p	R_{wp}	R_{exp}
$YAlO_3$: Nd^{3+} 1.0%	5.33	7.38	5.18	3.66	7.21	10.8	1.78

For simplicity, only the Rietveld refinement for the $YAlO_3$: Nd^{3+}1.0% nano-perovskite treated at 1550 °C is shown in Table 1 and Fig. 1*b* because the obtained data from it were practically the same for all YAP: Nd^{3+} nano-perovskites treated at 1550 °C.

The average grains size "*D*" was determined from Scherrer formula:

$$D = \frac{0.89\lambda}{\beta \, \mathrm{Cos}\, \theta} \quad (1)$$

where λ = 1.5406 Å, β is the full width at half maximum of the peaks and θ is the angle of diffraction. The average grains size value was around 30–40 nm. No amorphous phase was found in the samples.

3.2. Absorption and luminescence

From the point of view of the optical applications, it is relevant to know the local structure around the RE^{3+} ions inside the host matrix, because it establishes the fine structure splitting of the free-ion multiplets and the forced intra-configurational 4f–4f electric-dipole transition probabilities in the optical range (UV–VIS–NIR). In the particular case the of the yttrium-aluminium based perovskite structures, the Nd^{3+} ion predominantly enter into the octahedral interstice sites occupied by the Y^{3+} ions [26]. As a result, the crystal field interaction implies a complete breakdown of the degeneracy of the $^{2S+1}L_J$ mutiplets of the free Nd^{3+} ion, resulting in (2 J + 1)/2 Stark levels, which are labeled according the irreducible representations obtained from group theory [27]. This crystal field splitting of the electronic levels can be identified from the absorption and emission spectra. The first step in this section is the measurement of the diffuse reflectance spectum of the YAP nano-perovskite doped with 2.5 mol% of Nd^{3+} in the visible-NIR range, which is shown in Fig. 2. The most concentrated sample was chosen for this measure because the absorption was more noticeable. The peaks observed correspond to the intra-configurational $4f^3$-$4f^3$ electronic transitions beginning from the $^4I_{9/2}$ ground state to

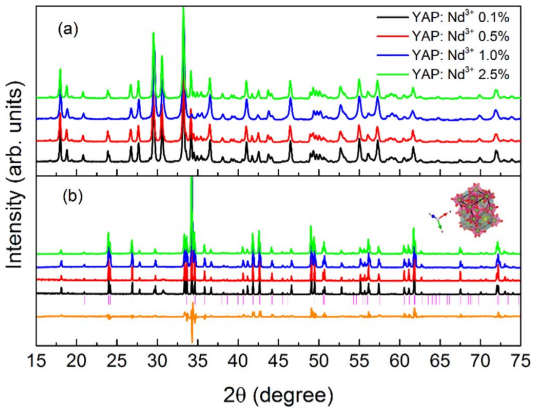

Fig. 1. XRD patterns of the YAP doped with 0.1%, 0.5%, 1% and 2.5% mol of Nd^{3+} at (a) 1200 °C and (b) 1550 °C and the *Pnma* symmetry Rietveld refinement including difference between calculated and observed patterns for the YAP: 1.0% Nd^{3+} nano-perovskite. The unit cell of the *Pnma* YAP nano-perovskite structure is also shown.

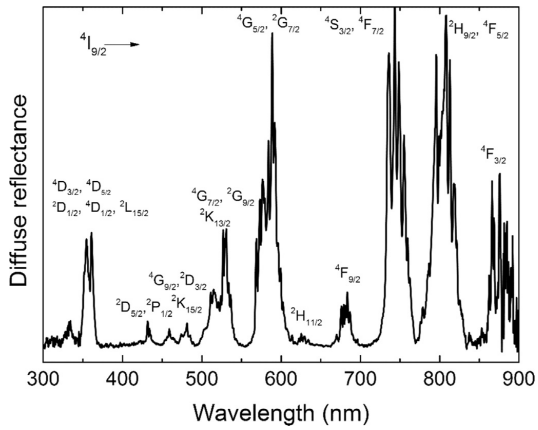

Fig. 2. Diffuse reflectance spectrum of the YAP: Nd^{3+}2.5% thermal treated at 1550 °C nano-perovskite powder in the UV–visible-NIR range at RT. All transitions start from the $^4I_{9/2}$ ground state to the indicated levels.

the different excited levels of the Nd^{3+} ion. All transitions were assumed to be electric-dipole in nature. The sharpness of the peak profiles of the diffuse reflectance spectrum confirms that the Nd^{3+} ions are incorporated in the nanocrystalline structure of the perovskite. The labels of the electronic transitions of the Nd^{3+} in the yttrium-aluminium nano-perovskites have been assigned according to the Dieke's diagram for this ion.

As it was confirmed by X ray-diffraction, depending on the ulterior thermal treatment at 1200 °C or 1550 °C, the weight of the contribution of different crystalline phases, perovskite and garnet, changes. Whereas in the first case, for 1200 °C heat treatment, there is a mixture between perovskite (YAP) and garnet (YAG) phases and, for the 1550 °C thermal treatment the YAP phase results to be the predominant one.

It is relevant to mention that changes in the optical properties of the YAP: Nd^{3+} samples are more related to the thermal treatments than the anisotropy nature of the YAP structure [22–24]. In the next section the emission spectra related with both cases are analyzed.

3.2.1. Heat treatment at 1200 °C

In order to distinguish the two possible different sites for the Nd^{3+} ions in the nanocrystal structure associated with YAP and YAG phases, site selection spectroscopy has been performed. It was possible to selectively excite luminescent impurity ions which exist in sites which are subtly different.

Fig. 3 shows the emission spectra of the YAP nano-perovskite sample doped with 1.0% mol of Nd^{3+} ions obtained at room temperature upon 529.5 and 531 nm excitation with a pulsed laser source. The emission peaks associated with the $^4F_{3/2} \rightarrow {}^4I_{9/2}$ (~880 nm) transition and their corresponding Stark levels were obtained.

Here, it can be observed that exciting with one or another wavelength, the site-selection of Nd^{3+} in the samples was possible, confirming the existence of two different environments for the Nd^{3+} ions. These two environments are associated with YAP (Site I) and YAG (Site II) phases, previously detected in the analysis of the X-ray diffraction patterns. As is observed in Fig. 3, the emission spectrum obtained at 529.5 nm consists in a mixture of these phases, being the Site I predominant compared with Site II. The former spectrum is very similar to that obtained for YAP: Nd^{3+} bulk samples [26]. On the other hand, exciting at 531 nm, Site II appears notably compared with Site I. This last spectrum resembles to the YAG: Nd^{3+} in nano-powders [28].

3.2.2. Heat treatment at 1550 °C

As regard the emission spectra of the YAP: Nd^{3+} samples treated at

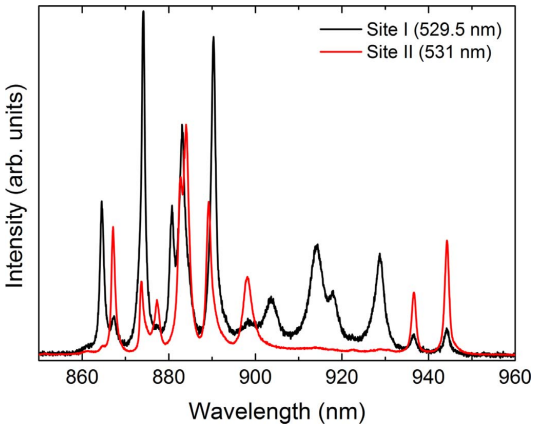

Fig. 3. Emission spectra of YAP nano-perovskite doped with 1.0 mol% of Nd^{3+} ions associated to the $^4F_{3/2} \rightarrow {}^4I_{9/2}$ transition obtained at room temperature upon 529.5 (black line) and 531 nm (red line) excitation with a pulsed laser source.

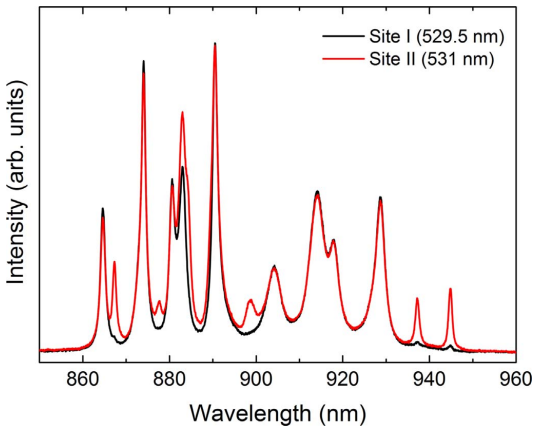

Fig. 4. Emission spectra of YAP nano-perovskite doped with 1.0 mol% of Nd^{3+} ions treated at 1550 °C associated to the $^4F_{3/2} \rightarrow {}^4I_{9/2}$ transition obtained at room temperature upon 529.5 (black line) and 531 nm (red line) excitation with a pulsed laser source.

1550 °C obtained with the same conditions that the sample treated at 1200 °C, the results were accurate according to the predictions of the XRD study for the samples treated at 1550 °C. In this case, the site selection spectroscopy resulted to be more difficult, because regardless of the excitation wavelength, the emission peaks associated with YAP phase appears strongly in all samples. This means that the YAP phase is predominant against YAG one (see Fig. 4). This result is in good agreement with the predictions of the XRD studies.

The emission decay curves for the $^4F_{3/2}$ level of Nd^{3+} ion of these samples were obtained by exciting at 529.5 nm and registering the $^4F_{3/2} \rightarrow {}^4I_{9/2}$ transition at around 914 nm (see Fig. 5). The decay curves for the samples presented non-exponential characters for short times due to the presence of multipolar interactions between Nd^{3+} ions, which are related with the quasi-resonant energy transfer cross-relaxation ($^4F_{3/2}$, $^4I_{9/2}$) → ($^4I_{15/2}$, $^4I_{15/2}$) channel. No rise time was observed in the decay curves exciting at Site I and detecting at Site II, confirming the inexistence of energy transfer between sites. Therefore, the assumption that the excitation wavelength excites both sites at the same time neglecting the possibility of energy transfer between Site I and Site II

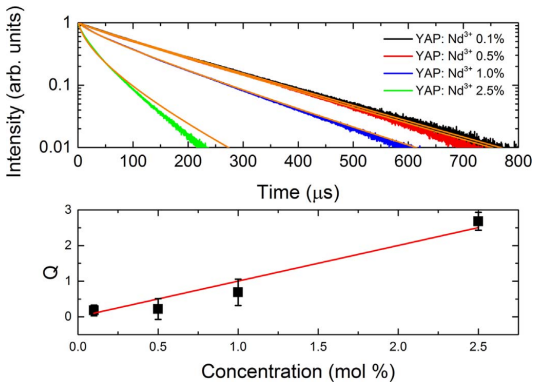

Fig. 5. (a) Emission decay curves of the $^4F_{3/2}$ level monitoring the $^4F_{3/2} \rightarrow {}^4I_{9/2}$ emission at 914 nm after exciting resonantly the $^4G_{7/2}$ level at 529.5 nm with a pulse laser source and the fitting curves to the Inokuti-Hirayama model with $S = 6$ (in red colour). (b) Transfer parameter Q values as functions of the Nd^{3+} concentration and the linear fitting according to Eq. (3) (red line). (For interpretation of the references to color in this figure legend, the reader is referred to the web version of this article.)

can be considered.

The multipolar interactions can be explained in the framework of the Inokuti-Hirayama model [29]. This model shows that the luminescence decay intensity *I(t)* after laser pulse excitation is given by the following equation:

$$I(t) = I(0)e^{\frac{-t}{\tau}-Q(\frac{t}{\tau})^{3/S}} \quad (2)$$

where *I(0)* is the intensity at time $t=0$ (in arbitrary units); τ is the intrinsic lifetime of the engaged donor level; S is related to the type of interaction between ions ($S=6$ for dipole-dipole interaction); and, in the case of a unique type of acceptor ion, the dimensionless energy transfer parameter, Q, is given by the following expression:

$$Q = \frac{4\pi}{3}\Gamma\left(1-\frac{3}{S}\right)C(C_{DA}\tau)^{3/S} \quad (3)$$

where Γ is the gamma function, C is the concentration of doping ions, and C_{DA} is the donor-acceptor energy transfer parameter [29].

In the mark of the Inokuti-Hirayama model, the decay curves of the YAP: Nd^{3+} samples treated at 1550 °C have been well-fitted taking S = 6, confirming the dipole-dipole interaction mechanism between the Nd^{3+} ions as main contribution to the energy transfer processes.

The lifetime τ and energy transfer parameters Q were calculated from the previous fitting process. The τ value was found to be 180 μs (with an uncertainty of ± 1.0 μs) which is very close to the one obtained in bulk matrix (175 μs) [26]. Moreover, the Q parameters obtained in the previous fittings show linear dependence (see Fig. 5) with doping concentration of Nd^{3+} ions according to the Eq. (3) ($Q = 1.0C$). It is important to mention, that the most concentrated sample did not fit very well in the frame of Inokuti-Hirayama model. This could be explained considering the diffusion processes among Nd^{3+} ions. Thus, for this case, it is necessary to employ a general model that considers the diffusion processes between donors, for instance, Yokota-Tanimoto model [30].

4. Conclusions

Yttrium aluminium nano-perovskite doped with Nd^{3+} were successfully synthesized by the Pechini sol-gel method with two different thermal treatments at 1200 °C and 1550 °C. XRD patterns analysis confirmed the monoclinic structure space group *P2/m* with a double contribution of the YAP and YAG phases in samples treated at 1200 °C and YAP orthorhombic structure space group *Pnma* with a minor presence of YAG phase in samples treated at 1550 °C. According to the XRD results about the existence of two possible environments for Nd^{3+} in YAP, site selection spectroscopy was carried out, exciting at 529.5 and 531 nm, confirming indeed the presence of the mentioned sites for Nd^{3+} in the samples treated at 1200 and 1550 °C. However, the site selection spectroscopy in YAP: Nd^{3+} nano-perovskites treated at 1550 °C resulted to be more difficult due to the predominance of the YAP phase compared with the YAG one. The study of the luminescence dynamics of the YAP: Nd^{3+} nano-perovskites treated at 1550 °C for all concentration of Nd^{3+} confirmed the existence of the energy transfer between these ions. Time resolved spectroscopy measurements allowed to confirm that the thermal treatment at 1550 °C was the proper one in order to obtain nano-perovskites.

Acknowledgements

This research was partially supported MINECO (MAT2013-46649-C4-4-P, MAT2015-71070-REDC, and MAT2016-75586-C4-4-P), and by the EU-FEDER. M.A. Hernández-Rodríguez thanks to MINECO by FPI grant (BES-2014–068666).

References

[1] E. Roduner, Size matters: why nanomaterials are different, Chem. Soc. Rev. 35 (2006) 583–592, http://dx.doi.org/10.1039/b502142c.
[2] E.C.C. De Souza, R. Muccillo, Properties and applications of perovskite proton conductors, Mater. Res. 13 (2010) 385–394, http://dx.doi.org/10.1590/S1516-14392010000300018.
[3] A. Boudali, A. Abada, M. Driss Khodja, B. Amrani, K. Amara, F. Driss Khodja, A. Elias, Calculation of structural, elastic, electronic, and thermal properties of orthorhombic $CaTiO_3$, Phys. B Condens. Matter 405 (2010) 3879–3884, http://dx.doi.org/10.1016/j.physb.2010.06.020.
[4] A. Vecht, D.W. Smith, S.S. Chadha, C.S. Gibbons, J. Koh, D. Morton, New electron excited light emitting materials*, J. Vac. Sci. Technol. B. 12 (1994).
[5] K. Lemański, P.J. Dereń, Spectroscopic properties of Dy^{3+} ions in $CaTiO_3$ nano-perovskites, J. Lumin. 145 (2014) 661–664, http://dx.doi.org/10.1016/j.jlumin.2013.08.048.
[6] K. Lemański, A. Gagor, M. Kurnatowska, R. Pzik, P.J. Dereń, Spectroscopic properties of Nd^{3+} ions in nano-perovskite $CaTiO_3$, J. Solid State Chem. 184 (2011) 2713–2718, http://dx.doi.org/10.1016/j.jssc.2011.08.004.
[7] P.J. Dereń, K. Lemański, Cross relaxation in $CaTiO_3$ and $LaAlO_3$ perovskite nanocrystals doped with Ho3+ ions, J. Lumin. 154 (2014) 62–67, http://dx.doi.org/10.1016/j.jlumin.2014.04.008.
[8] M. Manso, M. Langlet, J. Martínez-Duart, Testing sol–gel $CaTiO_3$ coatings for biocompatible applications, Mater. Sci. Eng. C 23 (2003), pp. 447–450, http://dx.doi.org/10.1016/S0928-4931(02)00319-3.
[9] C. Sameera Devi, G.S. Kumar, G. Prasad, Spectroscopic and electrical studies on Nd^{3+}, Zr^{4+} ions doped nano-sized BaTiO3 ferroelectrics prepared by sol–gel method, Spectrochim. Acta Part A Mol. Biomol. Spectrosc. 136 (2015) 366–372, http://dx.doi.org/10.1016/j.saa.2014.09.042.
[10] J. L, Y. J.W, M. Kuwabara, Photoluminescence and its Enhancement of Pr^{3+}-Doped $BaTiO_3$ Phosphor, Jpn. J. Appl. Phys. 44 (2005) L708, 〈http://stacks.iop.org/1347-4065/44/i=5L/a=L708〉.
[11] Z. Yao, H. Liu, Y. Liu, Z. Wu, Z. Shen, Y. Liu, M. Cao, Structure and dielectric behavior of Nd-doped $BaTiO_3$ perovskites, Mater. Chem. Phys. 109 (2008) 475–481, http://dx.doi.org/10.1016/j.matchemphys.2007.12.019.
[12] K. Yasuda, S. Usuda, H. Gunji, Properties of a YAP powder scintillator as alpha-ray detector, Appl. Radiat. Isot. 52 (2000) 365–368, http://dx.doi.org/10.1016/S0969-8043(99)00179-7.
[13] T.B. De Queiroz, C.R. Ferrari, D. Ulbrich, R. Doyle, A.S.S. De Camargo, Luminescence characteristics of YAP:Ce scintillator powders and composites, Opt. Mater. 32 (2010) 1480–1484, http://dx.doi.org/10.1016/j.optmat.2010.06.004.
[14] M. Harada, A. Ue, M. Inoue, X. Guo, K. Sakurai, Synthesis of YAP:CE phosphor through a complex polymerizing reaction, Scr. Mater. 44 (2001) 2243–2246, http://dx.doi.org/10.1016/S1359-6462(01)00756-4.
[15] Y. Zhydachevskii, A. Durygin, A. Suchocki, A. Matkovskii, D. Sugak, P. Bilski, S. Warchol, Mn-doped $YAlO_3$ crystal: a new potential TLD phosphor, Nucl. Instrum. Methods Phys. Res. Sect. B Beam Interact. Mater. At. 227 (2005) 545–550, http://dx.doi.org/10.1016/j.nimb.2004.09.013.
[16] H.B. Premkumar, H. Nagabhushana, S.C. Sharma, S.C. Prashantha, H.P. Nagaswarupa, B.M. Nagabhushana, R.P.S. Chakradhar, Structural, photo and thermoluminescence studies of Eu^{3+} doped orthorhombic $YAlO_3$ nanophosphors, J. Alloys Compd. 601 (2014) 75–84, http://dx.doi.org/10.1016/j.jallcom.2014.02.066.
[17] H.B. Premkumar, D.V. Sunitha, H. Nagabhushana, S.C. Sharma, B. Daruka Prasad, B.M. Nagabhushana, C. Shivakumara, J.L. Rao, N.O. Gopal, K.R. Prabhakara, S.-C. Ke, R.P.S. Chakradhar, Synthesis, structural and thermoluminescence properties of $YAlO_3$:Dy^{3+} nanophosphors, J. Alloys Compd. 591 (2014) 337–345, http://dx.doi.org/10.1016/j.jallcom.2013.12.217.
[18] Y. Wei, G. Zhang, C.-H. Huang, H.-Y. Zhu, L.-X. Huang, X.-J. Ou-Yang, G.-F. Wang, A single wavelength 1339nm Nd:YAP Nd: yap pulsed laser, Opt. Commun 282 (2009) 4397–4400, http://dx.doi.org/10.1016/j.optcom.2009.07.055.
[19] M. Fibrich, T. Hambálek, M. Němec, J. Šulc, H. Jelínková, Multiline generation capabilities of diode-pumped Nd:YAP and Nd:YAG lasers, Laser Phys 24 (2014), p. 35803, http://dx.doi.org/10.1088/1054-660X/24/3/035803.
[20] R. Moncorgé, B. Chambon, J.Y. Rivoire, N. Garnier, E. Descroix, P. Laporte, H. Guillet, S. Roy, J. Mareschal, D. Pelenc, J. Doury, P. Farge, Nd doped crystals for medical laser applications, Opt. Mater. 8 (1997) 109–119, http://dx.doi.org/10.1016/S0925-3467(97)00022-0.
[21] M.J. Weber, M. Bass, K. Andringa, R.R. Monchamp, Comperch.E, Czochralski growth and properties of $YAlO_3$ laser crystals, Appl. Phys. Lett. 15 (1969) 342–345, http://dx.doi.org/10.1063/1.1652851.
[22] M. Bass, Nd,Cr:$YAlO_3$ Laser tailored for high-energy Q-switched operation, Appl. Phys. Lett. 17 (1970) 395, http://dx.doi.org/10.1063/1.1653451.
[23] G.A. Massey, J.M. Yarborough, High average power operation and nonlinear optical generation with theNd: $YAlO_3$ Laser 576 (1971), http://dx.doi.org/10.1063/1.1653547.
[24] J. Rodríguez-Carvajal, Recent advances in magnetic structure determination by neutron powder diffraction, Phys. B Condens. Matter 192 (1993) 55–69, http://dx.doi.org/10.1016/0921-4526(93)90108-I.
[25] M.J. Weber, T.E. Varitimos, Optical Spectra and Intensities of Nd^{3+} in $YAlO_3$, J. Appl. Phys. 42 (1971) 4996, http://dx.doi.org/10.1063/1.1659885.
[26] B.G. Wybourne, Spectroscopic properties of rare earths, Opt. Acta Int. J. Opt. (1965) 12, http://dx.doi.org/10.1080/715120855.
[27] E. Caponetti, D.C. Martino, M.L. Saladino, C. Fisica, I.U. Palermo, O. Ii, I. Palermo, C. Leonelli, I. Ambientale, Preparation of Nd:YAG nanopowder in a confined

environment, Society 2 (2007) 3947–3952.
[28] M. Inokuti, F. Hirayama, Influence of energy transfer by the exchange mechanism on donor luminescence, J. Chem. Phys. 43 (1965) 1978, http://dx.doi.org/10.1063/1.1697063.
[29] M. Yokota, O. Tanimoto, Effects of diffusion on energy transfer by resonance, J. Phys. Soc. Jpn. 22 (1967) 779–784, http://dx.doi.org/10.1143/JPSJ.22.779.
[30] M. Tardocchi, A. Pietropaolo, C. Andreani, G. Gorini, S. Imberti, E. Perelli-Cippo, R. Senesi, N. Rhodes, E.M. Schooneveld, Comparison of Cadmium–Zinc–Telluride semiconductor and Yttrium–Aluminum–Perovskite scintillator as photon detectors for epithermal neutron spectroscopy, Nucl. Instrum. Methods Phys. Res. Sect. A Accel. Spectrometers, Detect. Assoc. Equip. 567 (2006) 337–340, http://dx.doi.org/10.1016/j.nima.2006.05.151.

4.1.2. Structural, Vibrational, and Elastic Properties of Yttrium Orthoaluminate Nanoperovskite at High Pressures

Authors: **M.A. Hernández-Rodríguez**, V. Monteseguro, A.D. Lozano-Gorrín, F.J. Manjón, J. González-Platas, P. Rodríguez-Hernández, A. Muñoz, V. Lavín, I.R. Martín and U.R. Rodríguez-Mendoza

Published in: **Journal of Physical Chemistry C;** Volume: **121;** Pages: **15353−15367;** DOI: 10.1021/acs.jpcc.7b04245; Accepted **24 April 2017**

In the present article, undoped $YAlO_3$ nano-perovskite was synthesized by sol-gel method with the proper thermal treatment (as it mentioned in section 3.1.1) with an average crystallite size around 40 nm.

XRD measurement at ambient conditions confirmed the orthorhombic *Pnma* structure of $YAlO_3$ nano-perovkiste (see Fig. 1b of this paper). This means, that $YAlO_3$ nano-perovskite has the same perovskite-type structure as bulk material. Crystal structure parameters obtained from Rietveld refinement were compared to the *ab initio* calculation finding a good agreement between the experimental and theoretical data. On the other hand, the experimental lattice parameters and atomic positions of $YAlO_3$ nano-perovskite were similar to those of its bulk counterpart, clearly indicating that the structural properties of the bulk $YAlO_3$ are reproduced in the nanoscale.

Afterwards, the experimental structural properties of $YAlO_3$ nano-perovskite were studied at different pressures up to 7 GPa. These results were in agreement with those given in the literature by Ross et al. who analyzed the XRD of $YAlO_3$ single crystal up to 9 GPa. In addition, an *ab initio* study of the structural changes of $YAlO_3$ under pressure up to 95 GPa were performed and it was found that lattice parameters *a*, *b* and *c* decreased with pressure, being the decreasing rate of the second one the most noticeable. This means that the *b*-axes was more compressible than *a* and *c*-axes. This behaviour could be observed in the experimental data of the lattice parameters as well as it is shown in the Fig. 2a of this paper.

Regarding the dependence of the unit cell volume of $YAlO_3$ nano-perovskite, it is shown that experimental data were partially in good agreement with those of the literature as it is shown in the Fig. 2b in this article. On the other hand, bulk modulus B_0 calculated via

ab initio simulation (B_0 = 204.5 GPa) was in agreement with the one reported in the literature by Huang et al. (B_0 = 210. 2 GPa). The experimental data of the $YAlO_3$ nano-perovskite unit cell with pressure were well-fitted to a second-order Birch-Murnaghan, yielding a B_0 value of 166.4 GPa which was in good agreement with the $YAlO_3$ one obtained by Ross et al (B_0 = 192 GPa).

The theoretical pressure dependence of the YO_{12} dodecahedron and AlO_6 octahedron volumes up to 95 GPa, which are the polyhedra units that compose the $YAlO_3$ structure, was studied as it shown in the Fig. 2b of this paper. It was observed that AlO_6 octahedron volume decreased faster than YO_{12} dodecahedron one, being this result in agreement with the one reported in the literature by Ross et al. The ratio between dodecahedron and octahedron compressibilities, k_{dod} and k_{oct} respectively, yielded a value minor to the unity, which was decreasing with pressure. This means that the structure tended to be more symmetrical (orthorhombic to cubic symmetry) as the pressure increased. This result was in agreement with data reported in the literature, and also this behaviour seems to be a general trend in all orthorhombic perovskite structures, such as $GdAlO_3$, $GdFeO_3$ and $ScAlO_3$ perovskites among others.

Concerning the RS experiments, it is found and indexed 16 out of 24 first order Raman-active modes theoretically predicted, in the Raman spectrum of $YAlO_3$ nano-perovskite at ambient pressure as it shown in the Fig 5. The experimental data of Raman-active mode frequencies of $YAlO_3$ nano-perovskite were compared to others orthorhombic structure perovskite-type ones, in which the elements in site *A* and *B* were different (Y and Al in our case, respectively) was different. This comparison led to an interesting result, in which the Raman frequency modes were affected in different ways depending on the *A* and *B* cation masses, for instance, in the low-frequency region, which is related to the AO_{12} dodecahedra vibrations, $YAlO_3$ Raman frequencies were shifted to higher values compared to those of $GdAlO_3$ due to the larger mass of Gd compared to Y one, since in the harmonic approximation, the frequency in such region goes as the square root of *A* cation mass, $m_A^{-1/2}$ (see Table 3 of this paper). This consideration also was applied in the high-frequency region, which is related to the BO_6 octahedra vibrations, finding that the frequency modes were shifted to higher values for $YAlO_3$ compared to those found in $YCrO_3$, due to the largest mass of Cr compared to Al one (see Table 3 of this paper).

The contribution each atoms and polyhedra units, i.e. YO_{12} and AlO_6 to the different Raman modes were also analyzed with the help of the partial and total phonon density of

states of $YAlO_3$ as it shown in the Fig. 6 of this work. This data allowed to associated the polyhedral units to each vibrational mode as it shown in the final paragraph of page 15359 of the manuscript.

RS measurement at high pressures up to 30 GPa was performed. The observed Raman peaks changed as the pressure increases, others simply dissapeared. All phonon frequencies showed a homogeneous increase as the pressure increased, except the $B_{2g}{}^3$ mode centered at 280 cm^{-1}. Even though, that there was an appreciable broadening in the Raman peaks over 10 GPa due to the partial loss of the hydrostatic conditions of the pressure-transmitting medium, the overall profile of the Raman modes in the RS spectra did not change up to 30 GPa. This result confirmed that the orthorhombic *Pnma* phase up to 30 GPa is stable in $YAlO_3$ nano-perovskite.

The pressure dependence of the observed Raman mode frequencies up to 30 GPa was compared to the theoretical one with a good agreement, as it depicted in the Fig 7 of this articule. All the first-order pressure coefficient were positive, except the one associated to the $B_{2g}{}^3$ Raman mode. The presence of negative pressure coefficients, such as the $B_{2g}{}^3$ indicated the softening of several bonds as the pressure increase, however, in the present case, it could not related directly to any structural instabilities, because no phase transition was observed in RS experiments up to 30 GPa. This issue was also supported by the elastic properties theoretical studies which predicted the structural stability of $YAlO_3$ up to 92 GPa.

THE JOURNAL OF PHYSICAL CHEMISTRY C

Article

pubs.acs.org/JPCC

Structural, Vibrational, and Elastic Properties of Yttrium Orthoaluminate Nanoperovskite at High Pressures

M. A. Hernández-Rodríguez,*[,†] V. Monteseguro,[#] A. D. Lozano-Gorrín,[†] F. J. Manjón,[⊥] J. González-Platas,[▽] P. Rodríguez-Hernández,[†,‡,∥] A. Muñoz,[†,‡,∥] V. Lavín,[†,‡,§] I. R. Martín,[†,‡,∥] and U. R. Rodríguez-Mendoza[†,‡,∥]

[†]Departamento de Física, Universidad de La Laguna, Apdo. 456. E-38200 San Cristóbal de La Laguna, Santa Cruz de Tenerife, Spain

[‡]MALTA Consolider Team, Universidad de La Laguna, Apdo. 456. E-38200 San Cristóbal de La Laguna, Santa Cruz de Tenerife, Spain

[§]Instituto Universitario de Estudios Avanzados en Física Atómica, Molecular y Fotónica (IUdEA), Universidad de La Laguna, Apdo. 456. E-38200 San Cristóbal de La Laguna, Santa Cruz de Tenerife, Spain

[∥]Instituto Universitario de Materiales y Nanotecnología (IMN), Apdo. 456. Universidad de La Laguna, E-38200 San Cristóbal de La Laguna, Santa Cruz de Tenerife, Spain

[⊥]Instituto de Diseño para la Fabricación y Producción Automatizada, MALTA Consolider Team, Universitat Politécnica de València, Cno. de Vera s/n, 46022 Valencia, Spain

[#]Beamlines BM23 & ID24, European Synchrotron Radiation Facility, 38043 Grenoble, France

[▽]Servicio de Difracción de Rayos X (SIDIX), Departamento de Física, Universidad de La Laguna, Apdo. 456. E-38200 San Cristóbal de La Laguna, Santa Cruz de Tenerife, Spain

S *Supporting Information*

ABSTRACT: The structural and vibrational properties of nanocrystalline yttrium orthoaluminate perovskite ($YAlO_3$) under compression have been experimentally studied. Experimental results have been compared to *ab initio* simulations of bulk $YAlO_3$ in the framework of the density functional theory. Furthermore, they have been complemented with an *ab initio* study of its elastic properties at different pressures. Calculated total and partial phonon density of states have allowed us to understand the contribution of the different atoms and structural units, YO_{12} dodecahedra and AlO_6 octahedra, to the vibrational modes. The calculated infrared-active modes and their pressure dependence are also reported. Finally, the pressure dependences of the elastic constants and the mechanical stability of the perovskite structure have been analyzed in detail, showing that this phase is mechanically stable until 92 GPa. In fact, experimental results up to 30 GPa show no evidence of any phase transition. A previously proposed possible phase transition in $YAlO_3$ above 80 GPa is also discussed.

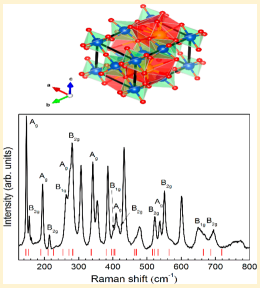

1. INTRODUCTION

Perovskites have been intensively researched due to their relevance from both the viewpoint of fundamental physics and device applications. In particular, ABO_3-type perovskite oxides, where *A* and *B* denote two different cations, have gained interest for their potential use in oxide-based electronics, due to their fascinating and multifunctional electronic properties beyond conventional semiconductors. Notably, most perovskite oxides are wide band gap semiconductors and show exceptional optical properties, which are employed for optoelectronic devices as nonlinear optical crystals,[1,2] scintillators,[3] photoluminescence and electroluminescence materials,[4,5] as well as solar cells.[6] In particular, perovskites can be found in several applications as optical sensors when they are doped with rare earth ions. For instance, optical temperature sensors are based on $Na_{0.5}Bi_{0.5}TiO_3$ doped with Er^{3+} or codoped with Er^{3+}/Yb^{3+},[7,8] and also on $BaTiO_3$ doped with Er^{3+}.[9] Among all perovskites, yttrium orthoaluminate perovskite ($YAlO_3$) has shown excellent physical and chemical properties, such as high hardness, good structural stability, and large mechanical strength, which make it an excellent candidate as a laser host material for lanthanide ions.[10−14]

Research in nanomaterials has attracted the interest of scientists from several fields due to their unique properties,[15] being one of their main advantages that they keep the bulk counterpart properties for sizes larger than 10−20 nm. The interest in rare-earth-doped nanoperovskites is based on the fact that the chemistry and optical spectroscopy of the analogous perovskite bulk crystals are well-known, opening the possibility to establish meaningful comparisons between the properties of the nanosized and bulk materials. In this regard, several works focused on studies of the properties of rare-earth-

Received: May 4, 2017
Revised: June 23, 2017
Published: June 24, 2017

DOI: 10.1021/acs.jpcc.7b04245
J. Phys. Chem. C 2017, 121, 15353−15367

doped nanoperovskites have been carried out.[16−20] Among interesting applications of nanoperovskites, we can cite their use as optical thermal sensors,[7−9,21] CO sensors,[22] and single photon emitters.[23]

Due to the numerous practical applications of perovskites, the study and understanding of their properties becomes an essential necessity. Especially, the knowledge of their elastic properties and mechanical stability at high pressure (HP) is a relevant subject that can also provide interesting information on their possible structural transformations through the stability criteria. On the other hand, since phonons play an important role in the electrical, thermal, and optical properties of materials, it is necessary to understand its lattice dynamics in order to go deeper into the physical properties of these compounds.

HP experiments in materials allow one to access interesting information just varying the interatomic distance and bonds. In this sense, the HP study of perovskites could provide a better understanding of possible changes occurring in their structural and vibrational properties and, hence, to understand possible changes of their luminescence properties when perovskites are doped, for instance, with rare earth ions. In particular, a number of experimental and theoretical HP studies have been performed in $AAlO_3$ (A = Sc, Y, Gd, Pr, Nd, La, ...) perovskites,[24−32] and in particular, joint HP studies of the structural and vibrational properties have been reported for $LaAlO_3$ and $PrAlO_3$.[33,34] In fact, a model to predict the structural behavior of perovskites at HP has been reported.[35] As regards $YAlO_3$, the pressure dependence of the fluorescence emission of Nd^{3+}, Cr^{3+}, and Mn^{4+} ions in $YAlO_3$ has already been studied.[36−38] However, the studies of the elastic properties of $YAlO_3$ and several perovskites ($SmAlO_3$, $GdAlO_3$, and $ScAlO_3$) have only been analyzed at ambient pressure,[39,40] with the elastic properties of $ScAlO_3$ perovskite being the only ones studied at HP to our knowledge.[41,42]

In this work, we report an extensive study of the structural, vibrational, and elastic properties of bulk and nanoscaled $YAlO_3$ perovskite at HP. Experimental X-ray diffraction (XRD) and Raman scattering (RS) measurements of the $YAlO_3$ nanoperovskite (with sizes around 40 nm) at HP have been compared to previously reported experimental and theoretical data of the bulk counterpart,[25,26,29] and with our *ab initio* calculations for bulk $YAlO_3$. Finally, the pressure dependence of the elastic constants and the HP mechanical stability of the $YAlO_3$ perovskite, including a possible phase transition above 80 GPa previously proposed,[29] is reported and discussed.

2. EXPERIMENTAL DETAILS

Nanocrystalline $YAlO_3$ was successfully synthesized by the Pechini citrate sol−gel method in air atmosphere.[43] Stoichiometric molar ratios of high-purity $Y(NO_3)_3{\cdot}4H_2O$ (Aldrich, 99.9%) and $Al(NO_3)_3{\cdot}9H_2O$ (Aldrich, 99.9%) materials were dissolved in 25 mL of 1 M HNO_3 under stirring at 80 °C (353 K) for 3 h. Then, citric acid, with a molar ratio of metal ions to citric acid of 1:2, was added to the solution, which was stirred and heated at 90 °C (363 K) until reaching the transparency of the solution. Then, 4 mg of polyethylene glycol was added to the solution. This last step created a gel that was fired at 400 °C (673 K) for 6 h in order to remove the residual nitrates and organic compounds. The subsequently obtained powder sample was burnt out at 1200 °C (1473 K) for 20 h, and finally, a second thermal treatment was performed at 1550 °C (1823 K) for 12 h that resulted in nanoperovskites with a homogeneous size distribution around 40 nm.

Powder XRD data were collected on a PANalytical X'Pert PRO diffractometer (Bragg−Brentano geometry) with an X'Celerator detector using the Cu $K\alpha_1$ radiation (λ = 1.5405 Å) in the angular range $5° < 2\theta < 80°$, by continuous scanning with a step size of 0.02°. For HP-XRD experiments, we have used a Rigaku SuperNOVA diffractometer equipped with an EOS detector and Mo radiation microsource (λ = 0.71073 Å). A Diacell Bragg-S Diamond anvil cell from Almax-Easylab, with an opening angle close to 90° and anvil culets of 600 μm, fitted with a stainless gasket containing a hole of 200 μm diameter and 60 μm depth was employed. A methanol−ethanol−water mixture (16:3:1) was used as a pressure-transmitting medium, which remains hydrostatic in the range of pressure used for this experiment.

RS measurements on $YAlO_3$ nanoperovskite powders at room temperature were performed in backscattering geometry, exciting with a laser source at 532 nm with an incident power of 50 mW and using a HORIBA Jobin Yvon LabRAM HR UV spectrometer in combination with a thermoelectrically cooled multichannel Synapse CCD detector with a resolution of 2 cm^{-1}. The beam was focused on the sample using a 50× objective with a beam diameter of approximately 2 μm at the sample. For HP-RS measurements up to 30 GPa, the sample was placed in a membrane-type DAC and a mixture of methanol−ethanol−water (16:3:1) was used as a pressure-transmitting medium. In spite of using a methanol−ethanol−water mixture above 10 GPa, where it behaves in a nonhydrostatic way, the influence of deviatoric stresses can be apparently neglected.[44] The pressure was estimated using the ruby fluorescence technique[45] with the pressure scale recalibrated by Syassen.[46] Experimental frequencies of the Raman modes were obtained by fitting peaks with a Voigt profile (Lorentzian convoluted with a Gaussian) after proper calibration and background subtraction of the experimental spectra. The Gaussian line width was fixed to the experimental setup resolution (2 cm^{-1}) in order to get the three variables of the Lorentzian profile for each peak.

3. *AB INITIO* SIMULATION DETAILS

Structural, vibrational, and elastic properties of bulk $YAlO_3$ perovskite at HP were theoretically obtained by means of *ab initio* total energy calculations. The study was carried out in the framework of density functional theory (DFT).[47] This method allows an accurate description of the physical properties of semiconductors at HP.[48] The simulations were conducted with the *Vienna Ab Initio Simulation Package* (VASP)[49] using the projector-augmented wave scheme (PAW)[50] to take into account the full nodal character of the all-electron charge density in the core region. In the simulation, 11 valence electrons ($4s^24p^65s^24d^1$) were used for yttrium, 3 valence electrons were considered for aluminum ($3s^23p^1$), and 6 valence electrons for oxygen ($2s^22p^4$). The presence of oxygen in $YAlO_3$ makes necessary the development of the set of plane waves up to a high energy cutoff of 520 eV. The exchange-correlation energy was described employing the generalized-gradient approximation (GGA) with the Perdew−Burke−Ernzenhof prescription for solids (PBEsol).[51] Integrations within the Brillouin zone (BZ) were performed with a dense mesh (6 × 4 × 6) of Monkhorst−Pack k-special points.[52] In this way, a high convergence of 1 meV per formula unit was accomplished. At a set of selected volumes, the lattice

DOI: 10.1021/acs.jpcc.7b04245
J. Phys. Chem. C 2017, 121, 15353−15367

parameters and atomic positions were fully optimized by calculating the forces on the atoms and the stress tensor. In the optimized resulting perovskite structures, the forces on the atoms were lower than 0.002 eV/Å and the deviation of the stress tensor components from the diagonal hydrostatic form less than 0.1 GPa. All of the calculations were performed at T = 0 K; temperature effects are not included in our study.

The elastic properties and mechanical stability of $YAlO_3$ were studied after computing the elastic constants that describe the mechanical properties of a material in the region of small deformations. These elastic constants were evaluated by computing the macroscopic stress for a small strain using the stress theorem.[53] According to their symmetry, the ground state and the fully optimized structures were strained in different directions.[54] The variation of the total energy was determined with a Taylor expansion of the total energy with respect to the employed strain.[55] The strain used in the calculations guarantees the harmonic behavior.

Lattice-dynamic calculations were carried out at the center of the Brillouin zone center (Γ point). The direct force-constant approach (or supercell method)[56] was employed, requiring highly converged results on forces. The diagonalization of the dynamical matrix determines the frequencies of Raman- and infrared-active modes as well as silent modes. From the calculations, the symmetries of the eigenvectors of the different vibrational modes are also identified at the Γ point.

The combination of experiments and DFT calculations is a powerful resource that leads to reliable results on the HP behavior of solids.[57−60] In addition to this, the combination of *ab initio* simulations with experimental studies also provides depth insight into the pressure behavior on the polyhedral compressibility, which is related to the macroscopic compression.[61]

4. RESULTS AND DISCUSSION

4.1. Structure under Pressure. Perovskites have the general formula ABO_3 and present four formula units per unit cell. The structure is formed by corner-linked octahedral BO_6 units, whereas A cations are located in the interstices of the structure, thus leading to dodecahedral AO_{12} units[62] (see Figure 1). Due to its high flexibility, the perovskite structure can crystallize in a huge number of space groups depending on the ratio of the cation sizes, which is responsible for tilts and twists of the octahedral units. In particular, $YAlO_3$ crystallizes in the orthorhombic *Pnma* structure, a.k.a. *Pbnm* when a different setting is used.[62]

The XRD pattern of $YAlO_3$ nanoparticles is shown in Figure 1, and it has been well indexed to a *Pnma* orthorhombic structure. This means that XRD measurements have confirmed that $YAlO_3$ nanoparticles have the same perovskite-type structure as the bulk material. No amorphous phase was detected in the sample. The average grain size D has been determined from the Scherrer formula[63]

$$D = \frac{0.89\lambda}{\beta \cos\theta} \quad (1)$$

where λ = 1.5406 Å, β is the full width at half-maximum of the peaks, and θ is the angle of diffraction. An average grain size value of around 40 nm has been found. Crystal structure parameters have been calculated after fitting the profiles of the nanoperovskites by the Rietveld method using the FULLPROF program (see Table 1). The reliability factors (χ^2, R_p, R_{exp}, and R_{Bragg}) obtained from this fitting were 4, 8.06, 16.8, and 0.02, respectively.

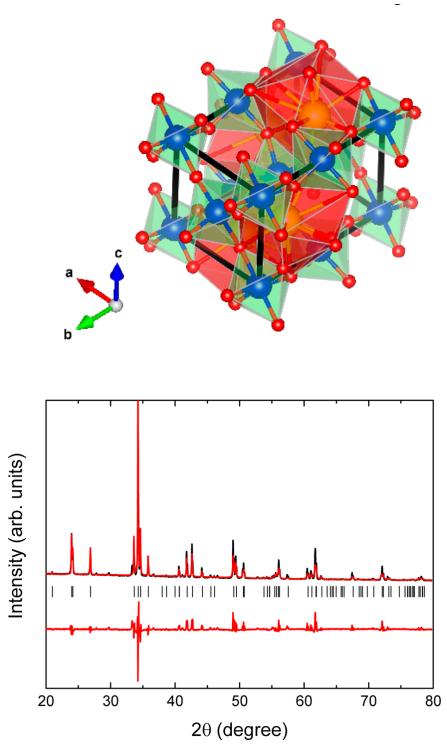

Figure 1. (a) Unit cell of the *Pnma* $YAlO_3$ perovskite structure. YO_{12} dodecahedra (red) and AlO_6 octahedra (green) are highlighted. Yellow spheres represent the Y atoms, blue ones correspond to the Al atoms, and the small red spheres to the O atoms. (b) XRD pattern of the $YAlO_3$ nanoperovskite. Rietveld refinements including the difference between calculated and observed patterns are also shown (red). The intensity of the peak at 34.25° has been divided by a factor of 4.

We have compared in Table 1 our *ab initio* calculated values of structural parameters of $YAlO_3$ under ambient conditions with previous calculations and experimental values. As observed, there is a nice agreement between our theoretical data and experimental values. These results give us confidence in the goodness of our calculations. Furthermore, we have found that the experimental lattice parameters and atomic positions of $YAlO_3$ nanoperovskite with 40 nm in size are similar to those of bulk $YAlO_3$, clearly indicating that the structural properties of the bulk perovskite are reproduced in the nanoscale.

The structural properties of $YAlO_3$ nanoperovskite have been experimentally studied at different pressures up to 7 GPa. The values of the lattice parameters and the volume of the unit cell have been obtained from the profile matching of the XRD data and are shown in Figure 2. Since XRD measurements have been performed with a conventional diffractometer and with a small quantity of sample in the DAC, XRD patterns exhibit low intensity and do not have good statistics; thus, only profile matching of the XRD patterns was carried out. However, if our

DOI: 10.1021/acs.jpcc.7b04245
J. Phys. Chem. C 2017, 121, 15353−15367

Table 1. Structural Parameters and Atomic Positions of $YAlO_3$ according to Setting 1 (*Pnma*) under Ambient Conditions, Volume (V_0), Bulk Modulus (B_0), and Its First Derivative (B_0')

	ab initio (this work)	*ab initio*[a,b]	*ab initio*[a,c] LDA	*ab initio*[a,c] GGA	experimental nano (this work)	experimental[a,d] bulk
a (Å)	5.332	5.27	5.27	5.41	5.327(2)	5.329
b (Å)	7.379	7.29	7.29	7.54	7.369(3)	7.370
c (Å)	5.177	5.13	5.12	5.31	5.175(3)	5.178
V_0 (Å^3)	203.76	197.08	196.70	216.60	202.40(23)	203.44
Y (4c)	0.55, 0.25, 0.51	0.55, 0.25, 0.51			0.552(1), 0.25, 0.521(1)	0.55, 0.25, 0.51
Al (4b)	0, 0, 0.5	0, 0, 0.5			0, 0, 0.5	0, 0, 0.5
O (8d)	0.29, 0.04, 0.71	0.29, 0.04, 0.71			0.297(1), 0.004(1), 0.739(1)	0.29, 0.04, 0.70
O (4c)	0.98, 0.25, 0.41	0.98, 0.25, 0.42			0.973(1), 0.25, 0.448(1)	0.98, 0.25, 0.42
B_0 (GPa)	204.5		210.2	210.8	166(3)	192
B_0'	3.99		4.56	4.85	4	7.3

[a]Transformed into setting 1 (*Pnma*) for better comparison with our results. [b]Reference 64. [c]Reference 40. [d]Reference 25. Our *ab initio* structural data are compared to other calculated data (refs 40 and 64) and experimental data for bulk (from ref 25) and nanocrystalline (our sample) perovskites.

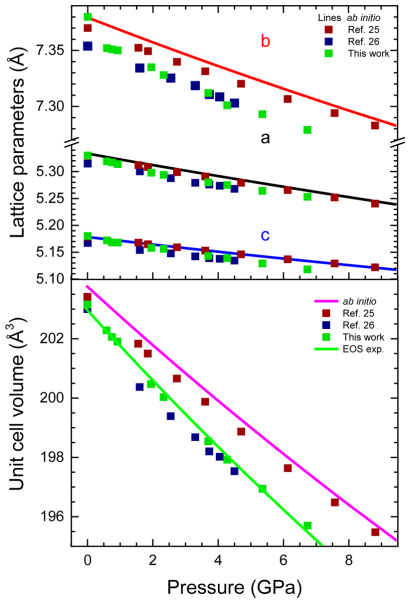

Figure 2. (a) Evolution with pressure of the lattice parameters and (b) the unit cell. Lattice parameters of refs 25 and 26 have been transformed into setting 1 (*Pnma*) for better comparison with our results. Error bars are not shown in these figures because they are smaller than data symbols.

results are compared with those given by Ross et al.[25,26] (see Figure 2), who analyzed the XRD of $YAlO_3$ single crystals as a function of pressure up to 9 GPa, it can be concluded that our study yields quite similar results to those of Ross et al. In fact, our lattice parameters and unit cell volume are slightly smaller than those presented in ref 25 and quite close to those of ref 26. Notice that data given by Ross et al. have been transformed into setting 1 (*Pnma*) to get better comparison with our results.

In order to illustrate the structural changes of $YAlO_3$ under pressure up to 95 GPa, we have performed *ab initio* calculations. Lattice parameters and the unit cell volume as well as the volumes of the dodecahedral (YO_{12}) and octahedral (AlO_6) units and the interatomic distances are shown in Figures 2, 3, and 4. First of all, the evolution of the lattice parameters as a function of pressure is shown in Figures 2 and

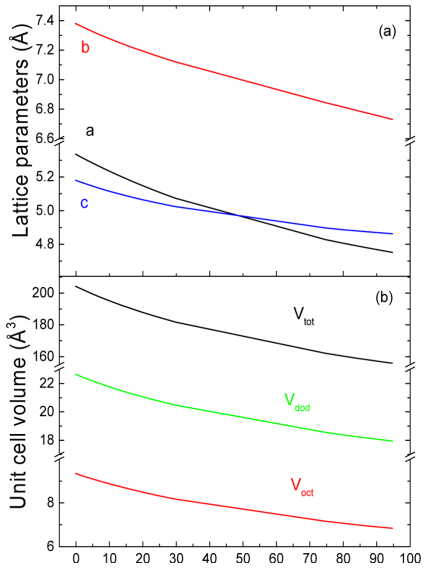

Figure 3. Theoretical pressure evolution of (a) the lattice parameters and (b) the unit cell, dodecahedral, and octahedral volumes of bulk $YAlO_3$ up to 95 GPa.

3. It can be observed that *a*, *b*, and *c* lattice parameters decrease with pressure at different rates that agree with those obtained from XRD measurements. Taking into account the definition of the relative compressibility, κ, of a certain physical magnitude

$$\kappa_X = -\frac{1}{x_0}\frac{\partial x}{\partial P} \quad (2)$$

where x_0 is the value of the magnitude at zero pressure, the calculated compressibilities of the *a*, *b*, and *c* lattice parameters are 2.02, 1.54, and 1.41 ($\times 10^{-3}$ GPa^{-1}), respectively, with the *a*-axis being more compressible than the *b*- and *c*-axes. These values are in good agreement with those already reported for $YAlO_3$ described with the *Pbnm* structure[25] where the *b*-axis,

DOI: 10.1021/acs.jpcc.7b04245
J. Phys. Chem. C 2017, 121, 15353−15367

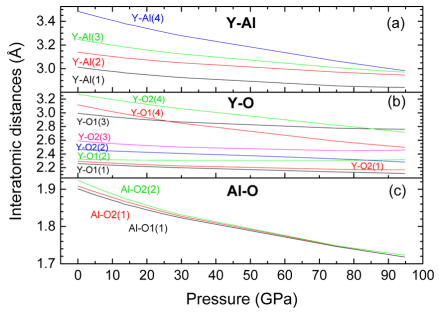

Figure 4. Pressure dependence of the theoretical interatomic distances in bulk $YAlO_3$: (a) Y−Al distances; (b) Y−O distances; (c) Al−O distances.

which corresponds to the *a*-axis in our setting, is also more compressible than the others, although slightly larger than those experimentally measured for single-crystalline and nanocrystalline $YAlO_3$ perovskites (see Figure 2).

The pressure dependence of the unit cell volume of $YAlO_3$ nanoperovskite is plotted in Figure 2, together with experimental data of refs 25 and 26 and *ab initio* calculation results. The pressure dependence of the unit cell volume of nanoperovskite $YAlO_3$ fits better with data from ref 26. Our theoretical bulk modulus (B_0), whose value is 204.5 GPa, is in agreement with the theoretical ones obtained by Huang et al.[40] (see Table 1). Our experimental unit cell volume as a function of pressure is well fitted to a second-order Birch−Murnaghan (BM2) equation of state (EOS),[65] yielding B_0 = 166.4 GPa (B_0' fixed to 4).

The experimental B_0 value in $YAlO_3$ nanocrystals is ∼14% lower than the experimental value for bulk $YAlO_3$ (192 GPa), as obtained by Ross et al.[25] by using a third-order Birch−Murnaghan (BM3) EOS (see Table 1). The fit of our data to a BM3 EOS yields B_0 = 133 GPa with B_0' = 18 (see the Supporting Information, section S3), which differs notably from the one obtained by Ross et al. (B_0 = 192 GPa) and gives an unreliable B_0'.[25]

The pressure dependence of the YO_{12} dodecahedron (V_{dod}), AlO_6 octahedron (V_{oct}), and unit cell volume (V_{tot}) are plotted in Figure 3. Overall, all of these volumes decrease with pressure, with the octahedron volume showing a higher compressibility (5.6×10^{-3} GPa^{-1}) than the dodecahedron one (4.35×10^{-3} GPa^{-1}). These results are in good agreement with those of Ross et al.[25,26] Zhao et al.[35] reported that the ratio between AO_{12} dodecahedron and BO_6 octahedron compressibilities ($\kappa_{dod}/\kappa_{oct}$) allows one to know the distortion degree of the structure with pressure toward more distorted or more symmetrical structures. When $\kappa_{dod}/\kappa_{oct} > 1$, BO_6 octahedra are more distorted with pressure compared with AO_{12} dodecahedra, thus suggesting that the structure becomes less symmetrical with pressure. Conversely, AO_{12} dodecahedra are more distorted than BO_6 octahedra on increasing pressure when $\kappa_{dod}/\kappa_{oct} < 1$, thus suggesting that the structure becomes more symmetrical with pressure and a tendency to undergo a phase transition to a cubic perovskite structure. Finally, both polyhedral units evolve in a similar way with pressure when $\kappa_{dod}/\kappa_{oct} \cong 1$, so in this case, pressure does not cause any distortion in the structure. According to our results, AlO_6 octahedral units present a higher compressibility than YO_{12} dodecahedral units. In particular, $\kappa_{dod}/\kappa_{oct} \cong 0.78$ at ambient pressure and it is always below 1 in the whole pressure range up to 95 GPa; therefore, our calculations indicate that $YAlO_3$ evolves toward a more symmetrical structure with increasing pressure, in good agreement with data reported in the literature.[25,26,29] It is also relevant to mention that this evolution toward more symmetrical structures occurs in other perovskites too, for instance, in orthorhombic $GdAlO_3$, $GdFeO_3$, and $ScAlO_3$ perovskites,[26,31,35] suggesting that the evolution toward a more symmetrical structure seems to be a general behavior in orthorhombic perovskites. In this respect, we have evaluated the departure of the orthorhombic structure of $YAlO_3$ from the cubic archetype one by calculating the cell distortion factor, *d*, introduced by Sasaki et al.[66] The normalized cell distortion factor with pressure, $d_{norm}(P)$, decreases as pressure increases in $YAlO_3$ nanoperovskites in good agreement with bulk $YAlO_3$ (see section S4 in the Supporting Information).[67]

The evolution of the interatomic distances with pressure up to 95 GPa is shown in Figure 4. Concerning the Y−O interatomic distances (see Table 2), it can be observed that some of them have similar decreasing rates with pressure: −2.72, −3.07, and −2.4 ($\times 10^{-3}$ Å·GPa^{-1}) for Y−O1(1), Y−O2(1), and Y−O2(2), respectively. On the other hand, the Y−O2(3), Y−O1(3), and Y−O2(4) interatomic distances present decreasing rates of −4.41, −5.94, and −8.33 ($\times 10^{-3}$ Å·GPa^{-1}). The Y−O1(4) distance shows the highest decreasing rate (-10.06×10^{-3} Å·GPa^{-1}), whereas Y−O1(2) shows the smallest one (-1.2×10^{-3} Å·GPa^{-1}). The Al−O interatomic distances decrease with pressure with similar rates (around -4.07×10^{-3} Å·GPa^{-1}), whereas all of the Y−Al interatomic distances decrease with pressure as well, with the Y−Al(4) with a decrease rate of -8.18×10^{-3} Å·GPa^{-1} being more significant. The large compressibility of Y−O1(4), Y−O2(4), and Y−O1(3) distances shown in Figure 4 clearly indicates that the coordination of Y in $YAlO_3$ at ambient pressure is indeed smaller than 12 (in fact, it is around 8 + 4, since there are four distances above 3 Å at ambient pressure) and that it tends to 9 + 3 on increasing pressure.

Table 2. Nearest-Neighbor Cation−Anion Distances in Bulk $YAlO_3$ at Selected Pressures[a]

	cation−anion distances (Å)		
	0 GPa	30 GPa	75 GPa
Y−O1 (1)	2.25307(1)	2.19074(1)	2.13078(1)
Y−O1 (2)	2.31767(1)	2.2991(1)	2.29936(1)
Y−O1 (3)	2.98824(1)	2.8434(1)	2.57966(1)
Y−O1 (4)	3.11212(1)	2.86012(1)	2.77046(1)
Y−O2 (1)	2.28602(1) (x2)	2.21788(1) (x2)	2.1677(1) (x2)
Y−O2 (2)	2.45827(1) (x2)	2.40035(1) (x2)	2.3209(1) (x2)
Y−O2 (3)	2.58368(1) (x2)	2.49305(1) (x2)	2.44245(1) (x2)
Y−O2 (4)	3.26932(1) (x2)	3.05455(1) (x2)	2.81457(1) (x2)
Al−O1 (1)	1.89981(1) (x2)	1.82132(1) (x2)	1.74460(1) (x2)
Al−O2 (1)	1.90706(1) (x2)	1.82561(1) (x2)	1.74636(1) (x2)
Al−O2 (2)	1.92292(1) (x2)	1.82949(1) (x2)	1.74677(1) (x2)

[a]O1 and O2 refer to the oxygens in the 4c and 8d Wyckoff positions, respectively. Numbers (1), (2), (3), and (4) refer to different Y−O and Al−O distances in the dodecahedron (YO_{12}) and octahedron (AlO_6), respectively.

4.2. Raman Spectroscopy. According to theoretical considerations, the *Pnma* structure of $YAlO_3$ with four formula units per primitive cell has 60 vibrational modes distributed in

DOI: 10.1021/acs.jpcc.7b04245
J. Phys. Chem. C 2017, 121, 15353−15367

24 Raman-active modes (Γ_R), 25 infrared-active modes (Γ_{IR}), 8 optically inactive (silent) modes (Γ_S), and 3 acoustic (Γ_{AC}) modes:

$$\Gamma_R = 7A_g + 5B_{1g} + 7B_{2g} + 5B_{3g}$$

$$\Gamma_{IR} = 9B_{1u} + 7B_{2u} + 9B_{3u}$$

$$\Gamma_S = 8A_u$$

$$\Gamma_{AC} = B_{1u} + B_{2u} + B_{3u} \quad (3)$$

In the following, we will analyze the lattice dynamics of $YAlO_3$ at ambient as well as at high pressures. A superindex has been added to the vibrational modes in order of increasing frequency.

4.2.1. Ambient Pressure. The Raman scattering (RS) spectrum of $YAlO_3$ nanoperovskite at ambient conditions is shown in Figure 5. Around 23 lines have been observed, but

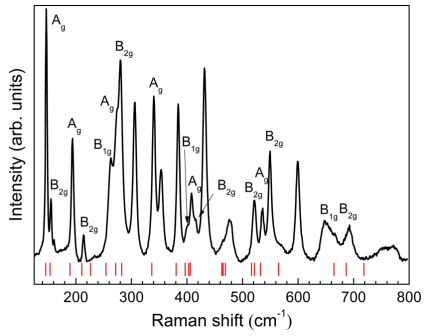

Figure 5. RS spectrum of $YAlO_3$ nanoperovskite obtained ambient conditions. Vertical lines indicate the *ab initio* frequencies of first-order Raman-active modes.

not all of them correspond to first-order Raman-active modes. Only 16 out of 24 first-order Raman-active modes theoretically predicted have been observed, while the rest have been attributed to second-order vibrational modes. The absence of the rest of the Raman-active modes could be due to accidental degeneracy of several modes or due to their weakness. For comparison, vertical marks at the bottom of the figure, which represent the theoretical Raman-active mode frequencies predicted under ambient conditions for bulk $YAlO_3$, were also included in Figure 5. The symmetries of the observed modes are assigned with the help of our theoretical calculations (based on both Raman-active frequencies and pressure coefficients). Experimental and theoretical frequencies of the Raman-active modes for $YAlO_3$ at ambient pressure are exposed in Table 3.

The comparison of the experimental RS spectrum of $YAlO_3$ nanoperovskite with other RS spectra of perovskite crystals, but containing different elements other than Y in site *A* and Al in site *B*, found in the literature hints that changing elements that occupy crystal sites *A* or *B* should selectively affect different vibrational modes: changing the element in site *A* should mainly affect modes involving rare earth ions, such as Y or Gd, in AO_{12} units without significant variations on the vibrational modes related to BO_6 octahedra. For instance, Chopelas et al.[68] compared the Raman frequencies of $YAlO_3$ and $GdAlO_3$ perovskites, and as expected, the low energy modes of $GdAlO_3$ were lower than those in $YAlO_3$ due to the larger mass of Gd compared to Y. This result was corroborated by Andreasson et al.[69]

Traditionally, changes in the RS spectrum of ABO_3 perovskites, with *A* being a rare earth, are attributed either to the effects of the unit cell dimension or the *A* cation mass. In the region of low frequencies, the main effect is given by *A* cation mass that, considering the harmonic approximation, goes as the square root of its mass, $m_A^{-1/2}$, since the ratio of the strength of the chemical bonding and the cation mass is mainly dominated by the latter. In the region of high frequencies, the principal effect is the different size of the unit cell that mainly depends on the strength of the *B*−O bonds.[68]

Taking into account the above considerations and comparing with vibrational frequencies of other perovskites (Table 3), it is reasonable that the low-frequency Raman modes in $YAlO_3$ nanoperovskite are practically the same (see the lowest frequency Raman A_g^1 mode in Table 3) as in $YCrO_3$, whereas the high-frequency Raman modes of $YAlO_3$ nanoperovskite are shifted to high energies compared to those of $YCrO_3$.[70] Similarly, it can be observed that the low-frequency Raman modes of $YAlO_3$ nanoperovskite (for example, the lowest frequency Raman A_g^1 mode in Table 3) are shifted to higher frequencies with respect to $GdAlO_3$, whereas the high-frequency Raman modes are similar for both compounds.[68] Finally, we want to mention that we have found that the experimental data of the Raman mode frequencies of $YAlO_3$ nanoperovskite are similar to those found in the literature for $YAlO_3$ bulk (see Table 3), thus suggesting that nano-$YAlO_3$ behaves as its bulk counterpart but in the nanoscale. This is in good agreement with the structural results discussed in the previous section.

It is worth noting that our measurements in $YAlO_3$ nanoperovskite and the help of lattice dynamics calculations have allowed the nature of the high-frequency modes to be clarified. Raman modes with frequencies around 663 and 694 cm^{-1} correspond to the theoretically proposed modes B_{1g}^5 and B_{2g}^7, respectively. Such modes were not reported as the highest Raman mode frequencies in previous studies of bulk $YAlO_3$, but they were assumed to be those at 550 (A_g^7), 552 (A_g^7), and 555 cm^{-1} (B_{1g}^4), respectively.[68,70,71]

For comparison with other perovskites, it is better to divide the Raman spectrum of nano-$YAlO_3$ into two regions:[72] the low-frequency region up to ∼280 cm^{-1}, which corresponds to the vibrations of Y−O (frequencies in this region are more or less unchanged with the *B* atom; see $YAlO_3$ and $YCrO_3$ in Table 3), and the high-frequency region from 280 cm^{-1} onward, which is related to the vibrational modes of the oxygens and in terms of the molecular structure to the AlO_6 octahedra. The symmetries of the observed modes are indexed on the basis of our theoretical calculations and on the comparison with previous studies of lattice dynamics in orthorhombic perovskites.[70,72−74] The nonindexed peaks likely correspond to second-order Raman modes. Overall, there is a good agreement between the experimental results in $YAlO_3$ nanoperovskite and the theoretical ones at ambient conditions (see Table 3). Note that there are some differences between the experimental and theoretical Raman-mode frequencies, which can be attributed to the GGA approximation that tends to underestimate vibrational frequencies.

The RS spectrum of perovskites can be interpreted assuming that the different Raman modes could be associated with the vibrational modes of dodecahedron (YO_{12}) and octahedral

DOI: 10.1021/acs.jpcc.7b04245
J. Phys. Chem. C 2017, 121, 15353−15367

Table 3. Theoretical and Experimental Raman Frequencies of Several Orthorhombic ABO_3 Perovskites[a]

$YAlO_3$, this work				$YAlO_3$, ref 64	$YAlO_3$, ref 71	$YAlO_3$, ref 68	$YAlO_3$, ref 70	$YCrO_3$, ref 70	$GdAlO_3$, ref 68
mode	theo. (cm^{-1})	Exp. (cm^{-1})	AlO_6 motion	theo. (cm^{-1})	exp. (cm^{-1})	exp. (cm^{-1})	exp. (cm^{-1})	exp. (cm^{-1})	exp. (cm^{-1})
A_g^1	146(2)	147(2)		147.3	152	148	150	156	95
B_{2g}^1	154(2)	156(2)		157.9		157	157		111
B_{3g}^1	189(2)			198	152	194	197	176	146
A_g^2	189(2)	195(2)		196.4	197	195	197	188	146
B_{2g}^2	211(2)	215(2)		216.1		216	219	223	160
B_{1g}^1	226(2)		$B_{1g}(3)$	233.8	160				174
B_{1g}^2	254(2)	264(2)		259.7	218	216	270	272	217
A_g^3	272(2)	274(2)		277.4	280	275	278	282	232
B_{2g}^3	282(2)	281(2)		283.6	267	284			222
A_g^4	337(2)	341(2)	$A_g(2)$	342.1	350	343	345	346	313
B_{3g}^2	381(2)		$B_{3g}(4)$	394.4					
B_{1g}^3	397(2)	403(2)	$B_{1g}(4)$	406.4	287	265	403	413	323
A_g^5	403(2)	416(2)	$A_g(1)$	409	415	411	412	429	368
B_{2g}^4	406(2)	409(2)	$B_{2g}(4)$	418	407		283	318	
B_{1g}^4	463(2)		$B_{1g}(2)$	464.2	422	403	555		400
A_g^6	465(2)		$A_g(3)$	469.2		438		492	
B_{3g}^3	469(2)		$B_{3g}(2)$	470.8			470	487	398
B_{3g}^4	516(2)		$B_{3g}(3)$	531			540	569	475
B_{2g}^5	521(2)	523(2)	$B_{2g}(3)$	536.1		418		502	414
A_g^7	532(2)	537(2)	$A_g(4)$	547.4	550	552	553	566	536
B_{2g}^6	564(2)	551(2)	$B_{2g}(2)$	581.3		543	552		512
B_{1g}^5	664(2)	663(2)	$B_{1g}(1)$	675.9					551
B_{2g}^7	686(2)	694(2)	$B_{2g}(1)$	697.7					
B_{3g}^5	718(2)		$B_{3g}(1)$	731.5	545	527			523

[a]Our values are compared to other theoretical and experimental values of Raman frequencies for bulk $YAlO_3$ and also to others ABO_3 compounds with *Pnma* structure. The AlO_6 motion assignment is also given according to ref 73.

(AlO_6) units. Nevertheless, this assignation is not straightforward, since these vibrational modes are coupled to each other. Therefore, and in order to understand the contribution of each polyhedral unit to every Raman mode, a calculation of the phonon density of states is required (see Figure 6). According to these results, Y atoms with dodecahedral coordination (YO_{12}) mainly contribute in the low-frequency region up to ~300 cm^{-1}, showing a maximum centered around 150 cm^{-1}. A minor contribution of this unit can be observed in the region between 300 and 500 cm^{-1}. On the other hand, Al atoms with octahedral coordination (AlO_6) present a high contribution in the region between ~300 and 750 cm^{-1}. The major contribution of this unit is around 420 cm^{-1}. It is relevant to notice that Al and O atoms contribute in both the low- and high-frequency regions, and that there is a small region between 220 and 300 cm^{-1} where Y and Al atoms have similar contributions.

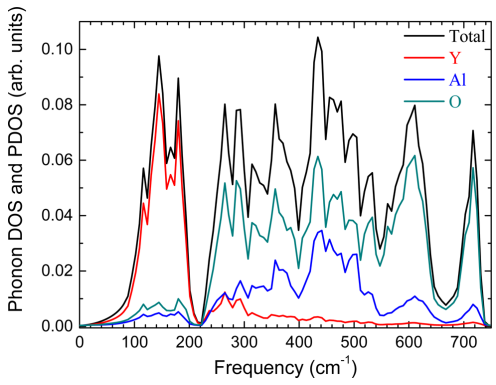

Figure 6. Partial and total phonon density of states of $YAlO_3$. The total phonon density is represented by the black curve.

Once the contributions of the individual atoms are known, it is possible to discuss the contributions of the polyhedra to each vibrational mode. The phonon modes of a perovskite with the general formula ABO_3 can be described as a combination of the molecular modes of the BO_6 units. This feature was used to describe the phonon modes of other similar perovskites.[72,73]

Concerning the contribution of the polyhedral units to each vibrational mode, the A_g^1 (146 cm^{-1}), B_{2g}^1 (154 cm^{-1}), B_{3g}^1 (189 cm^{-1}), A_g^2 (189 cm^{-1}), and B_{2g}^2 (210 cm^{-1}) modes of the low-frequency region are all associated with translational motions of the YO_{12} units without any contribution of AlO_6 units. The B_{1g}^2 (254 cm^{-1}), A_g^3 (271 cm^{-1}), and B_{2g}^3 (282 cm^{-1}) modes correspond to rotational movements of YO_{12} dodecahedra where there is an almost equal contribution of AlO_6 units. Regarding the high-frequency region, which is mainly due to AlO_6 octahedral motions (see Table 3), the A_g^4 (336 cm^{-1}), B_{3g}^2 (380 cm^{-1}), B_{2g}^4 (406 cm^{-1}), and A_g^7 (532 cm^{-1}) modes are related to rotations of AlO_6 units. On the other hand, the A_g^6 (465 cm^{-1}), B_{3g}^4 (516 cm^{-1}), B_{2g}^5 (521 cm^{-1}), and B_{2g}^6 (564 cm^{-1}) modes are mainly related to bending motions of AlO_6 units. Finally, the A_g^5 (403 cm^{-1}), B_{1g}^4 (463 cm^{-1}), B_{3g}^3 (469 cm^{-1}), B_{1g}^5 (664 cm^{-1}), B_{2g}^7 (686 cm^{-1}), and B_{3g}^5 (718 cm^{-1}) modes mainly correspond to stretching movements of AlO_6 units.

4.2.2. High Pressure. Selected RS spectra of $YAlO_3$ nanoperovskite at different pressures up to 30 GPa are depicted

DOI: 10.1021/acs.jpcc.7b04245
J. Phys. Chem. C 2017, 121, 15353−15367

in Figure 7. Although only 16 out of 24 Raman-active first-order modes were observed at ambient pressure, the number of

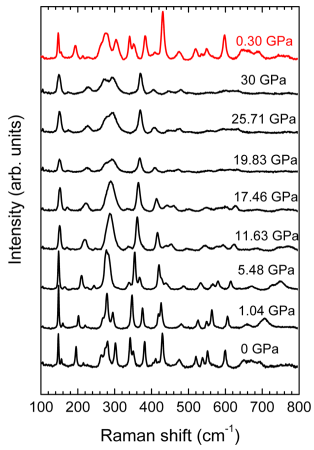

Figure 7. Selected experimental RS spectra of $YAlO_3$ nanoperovskite at different pressures up to 30 GPa. The Raman scattering spectrum at the top (red curve) is taken at 0.3 GPa after releasing pressure.

the observed Raman peaks changes as the pressure increases. In fact, the intensity of some peaks decreases with increasing pressure while others simply disappear. As a general rule, all phonon frequencies show a monotonous increase with pressure up to 30 GPa, except the B_{2g}^3 mode near 280 cm^{-1} which exhibits a slight shift to lower frequencies. At 4.36 GPa, we observed the appearance of the B_{1g}^1 mode near 239.5 cm^{-1}. Appreciable broadening was observed in the Raman peaks from ~10 GPa due to the partial loss of the hydrostatic conditions of the pressure-transmitting medium. However, the profiles of the Raman modes in the RS spectra do not change up to 30 GPa, so it can be concluded that the sample is stable in the *Pnma* phase up to this pressure. Furthermore, the RS spectrum obtained at 0.30 GPa after releasing pressure (see the RS spectrum at the top of Figure 7) is similar to the one obtained at ambient pressure before applying pressure (RS spectrum at the bottom of Figure 7), thus indicating a reversibility of the changes induced by pressure.

The pressure dependence of the experimental and theoretical Raman-active mode frequencies up to 30 GPa is depicted in Figure 8.

It can be observed that first-order pressure coefficients at ambient pressure are positive except for the B_{2g}^3 mode at 282 cm^{-1} (−0.23 cm^{-1} GPa^{-1}). In addition, the lowest-frequency Raman phonon mode A_g^1 has a very small pressure coefficient (0.11 cm^{-1} GPa^{-1}), which means that this mode shows a negligible dependence with volume and only depends on the mass of the *A* cation, as already commented. Table 4 summarizes the theoretical and experimental frequencies and pressure coefficients of the different Raman-active modes in $YAlO_3$ after fit to equation

$$\omega = \omega_0\left(\frac{\partial\omega}{\partial P}\right)P + \frac{1}{2}\left(\frac{\partial^2\omega}{\partial P^2}\right)P^2 \quad (4)$$

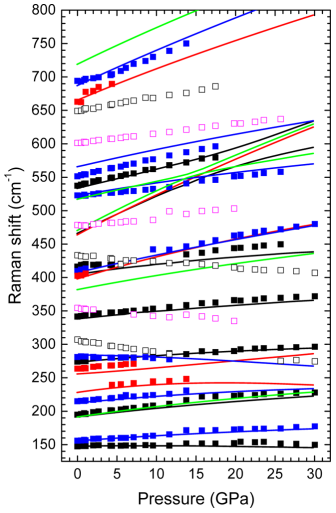

Figure 8. Pressure dependence of all peaks observed in RS spectra of $YAlO_3$ nanoperovskite (symbols) compared to theoretical data for bulk $YAlO_3$ (lines). Raman-active modes with different symmetry show different colors: A_g (black), B_{1g} (red), B_{2g} (blue), and B_{3g} (green). Open symbols correspond to other modes which likely correspond to second-order Raman modes despite the presence of photoluminescence lines cannot be fully discarded. Error bars are not included in this figure because they are shorter than data symbols.

The experimental and theoretical Grüneisen parameters, $\gamma = -(B_0/\omega_0)(\partial\omega/\partial P)$, for the Raman modes are also given in Table 4. The former parameters have been calculated by employing the theoretical bulk modulus, B_0 = 204.5 GPa, estimated from the third-order Birch−Murnaghan EOS.[75] It can be observed that theoretical and experimental Grüneisen parameters show a notable variation in both low- and high-frequency regions, with the last one being more noticeable, indicating that the restoring forces on the atoms of AlO_6 polyhedra are larger than YO_{12} ones. The A_g^1 mode, the lowest in frequency, corresponds to the translational motion of the YO_{12} unit and shows a very small pressure coefficient and Grüneisen parameter at ambient pressure.

Four peaks observed in the RS spectrum, around 355, 479, 601, and 649 cm^{-1}, do not correspond to first-order Raman active modes, as can be observed by comparison with our theoretical calculations. These modes are likely related to second-order Raman modes and not to photoluminescence lines, because chemical analysis corroborates the purity of our sample and the lack of doping with optically active ions. In any case, the presence of photoluminescence lines cannot be fully discarded, since these lines could appear for ions with a concentration below our detection limit. It is relevant to notice that the larger contraction of distances related to yttrium (Y−O) is reflected in the larger pressure coefficients for the modes related to Y atoms, between 146 and ~280 cm^{-1}, than those corresponding to AlO_6 units, which are usually located in the high-frequency region.

The presence of negative slopes with pressure in Raman modes, such as the B_{2g}^3 Raman mode at 282 cm^{-1}, indicates the softening of several bonds with increasing pressure. Nonetheless, the negative pressure coefficients of these modes cannot be

DOI: 10.1021/acs.jpcc.7b04245
J. Phys. Chem. C 2017, 121, 15353−15367

Table 4. Theoretical (Bulk) and Experimental (Nano-Perovskite) First-Order Raman-Active Mode Frequencies, Pressure Coefficients, and Grüneisen Parameters in $YAlO_3$ up to 30 GPa[a]

	theory				experiment			
mode	ω_0 (cm^{-1})	$\partial\omega/\partial P$ (cm^{-1} GPa^{-1})	$\partial^2\omega/\partial P^2$ (cm^{-1} GPa^{-2} × 10^3)	γ	ω_0 (cm^{-1})	$\partial\omega/\partial P$ (cm^{-1} GPa^{-1})	$\partial^2\omega/\partial P^2$ (cm^{-1} GPa^{-2} × 10^3)	γ
A_g^1	146(2)	0.11(2)	−13(2)	0.15	147(2)	0.40(2)	−16(2)	0.56
B_{2g}^1	154(2)	0.81(2)	−14(3)	1.08	156(2)	1.09(1)	−24(3)	1.45
B_{3g}^1	189(2)	1.67(1)	−20(1)	1.81			0	
A_g^2	189(2)	1.40(2)	−24(2)	1.51	195(2)	1.96(2)	−54(2)	2.12
B_{2g}^2	211(2)	1.09(2)	−26(1)	1.06	215(2)	1.04(3)	3.0(1)	1.01
B_{1g}^1	226(2)	1.47(2)	−80(3)	1.33		0.77(1)	132(1)	
B_{1g}^2	254(2)	0.90(2)	8.0(1)	0.72	264(2)[b]	1.43(2)[b]	−106(2)[b]	1.15
A_g^3	272(2)	1.08(3)	−26(2)	0.81	274(2)	0.99(4)	−20(3)	0.74
B_{2g}^3	282(2)	−0.23(1)	−23(3)	−0.17	281(2)	−0.1(1)	−28(3)	−0.07
A_g^4	337(2)	1.21(3)	−19(1)	0.73	341(2)	1.42(2)	−26(2)	0.86
B_{3g}^2	380(2)	2.23(3)	−29(2)	1.20				
B_{1g}^3	397(2)	3.51(1)	−54(1)	1.81	403(2)	3.24(2)	−62(2)	1.64
A_g^5	403(2)	1.65(2)	−36(1)	0.84	416(2)	1.10(3)	20(2)	0.54
B_{2g}^4	406(2)	2.72(2)	−24(1)	1.37	409(2)	3.15(2)	−54(3)	1.57
B_{1g}^4	463(2)	6.06(2)	−46(3)					
A_g^6	465(2)	6.44(2)	−140(2)	2.83				
B_{3g}^3	469(2)	7.04(1)	−216(2)	3.07				
B_{3g}^4	516(2)	1.93(1)	−123(2)	0.76				
B_{2g}^5	521(2)	2.03(1)	−30(2)	0.80	523(2)	1.12(2)	28(2)	0.44
A_g^7	532(2)	2.38(2)	−62(2)	0.91	537(2)	2.76(2)	−36(3)	1.06
B_{2g}^6	565(2)	2.69(4)	−27(2)	0.97	551(2)	2.79(3)	−26(2)	1.10
B_{1g}^5	665(2)	4.86(3)	29(1)	1.49	663(2)[b]	12.54(2)[b]	−3 × 10^3 [b]	3.86
B_{2g}^7	686(2)	5.42(3)	−37(3)	1.62	694(2)	4.50(4)	28(1)	1.34
B_{3g}^5	719(2)	5.65(2)	−46(3)	1.61				

[a]The second-order polynomial fit was used in order to obtain the pressure dependence of both theoretical and experimental frequencies. [b]The slope of this experimental value differs significantly from the theoretical value likely because of the lack of experimental data in a wider pressure range.

directly related to structural instabilities, because no phase transition was observed either in our experiments up to 30 GPa or in our calculations: no mechanical instability up to 92 GPa, as it will be discussed in the last section of this work; and no dynamical instability (zero frequency mode) up to 100 GPa. It is relevant to mention that we did not find any imaginary phonon at any pressure, neither in Raman, infrared, or silent modes up to 100 GPa. The smaller silent mode at 100 GPa is one A_u mode with a frequency of 167.6 cm^{-1}.

Additionally, Figure 9a shows the pressure dependence of the theoretical frequencies of infrared-active (IR) modes (B_{1u}, B_{2u}, and B_{3u}) for bulk $YAlO_3$. IR frequencies, pressure coefficients, and Grüneisen parameters after fits to eq 4 are given in Table 5. As observed, theoretical Grüneisen parameters of IR-active modes vary between 0.76 and 2.4 in a similar fashion as Raman-active modes. Finally, the pressure dependence of the frequencies of the silent (A_u) vibrational modes, which are active in hyper-Raman scattering, are plotted in Figure 9b.

In summary, our lattice dynamics calculations are in good agreement with experimental measurements on $YAlO_3$ nano-perovskite, thus confirming the large similitude between the bulk properties and those found in the 40 nm size nanoparticles, as was also previously found in nanogarnets with similar sizes.[76,77] Furthermore, they show the dynamical stability of the perovskite *Pnma* structure in $YAlO_3$ at least up to 30 GPa, thus suggesting that the related compound $GdAlO_3$ should not undergo a phase transition above 12 GPa, as previously suggested by Ross et al. from extrapolation of low-pressure data.[78]

4.3. Elastic Properties. The study of the elastic constants of materials is useful in order to understand their mechanical and thermodynamical properties as well as their structural stability. Orthorhombic $YAlO_3$ crystals are characterized by an elastic constant tensor with nine independent elastic constants: C_{11}, C_{22}, C_{33}, C_{44}, C_{55}, C_{66}, C_{12}, C_{13}, and C_{23}. The values of these constants at 0 GPa calculated with the GGA-PBEsol approximation are depicted in Table 6 and compared to those already reported by Huang et al.,[40] but translated from the *Pbnm* to the *Pnma* setting for the sake of comparison. In addition to this, a comparison of our calculation with the one obtained by Fang Gu et al. in $BaHfO_3$ cubic perovskite,[79] whose elastic constant tensor has only three independent elastic constants, C_{11}, C_{12}, and C_{44}, was carried out (see Table 6).

As observed, our calculated values with the GGA-PBEsol approximation are quite similar to those calculated with the LDA approximation but not so comparable to those calculated with the GGA approximation. In any case, we have to note that the agreement between experimental and theoretical lattice parameters is rather good in our calculations (see Table 1).

The elastic constants C_{11}, C_{22}, and C_{33} are associated with the deformation behavior and atomic bonding characteristics. It can be observed from Table 6 that $C_{33} > C_{22} > C_{11}$ for $YAlO_3$, both in our calculations and in previous ones.[40] This result indicates that the atomic bonds between nearest neighbors along the (001) direction of the *Pnma* structure are stronger than those along the (010) and (100) directions. This agrees with the fact that the lattice constant *c* is less sensitive to pressure than the other two lattice constants (see section 4.1). The C_{11}, C_{22}, and C_{33} elastic constants, which are related to the unidirectional

DOI: 10.1021/acs.jpcc.7b04245
J. Phys. Chem. C 2017, 121, 15353−15367

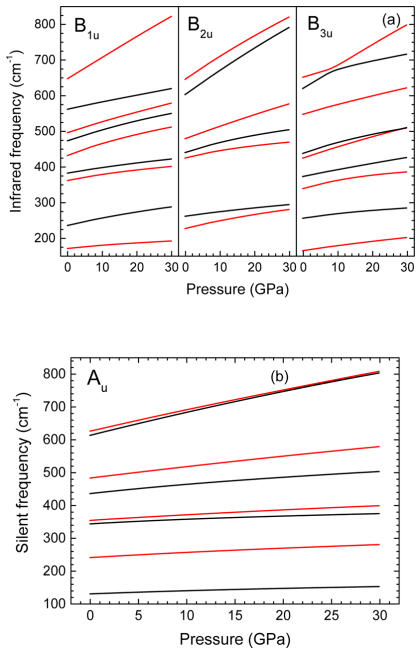

Figure 9. Theoretical pressure dependence of the B_{1u}, B_{2u}, and B_{3u} infrared (a) and Au silent (b) modes of bulk $YAlO_3$ up to 30 GPa. Colors are given just as a guide for the eyes.

compression along the principal crystallographic directions, are larger than the C_{44}, C_{55}, and C_{66}, constants, which represent the resistance to shear deformation. This result indicates the larger resistance of $YAlO_3$ to unidirectional compression than to shear deformation. The same behavior can be observed in $BaHfO_3$, since $C_{11} > C_{44}$ (see Table 6).

When a nonzero stress is applied to the crystal, the elastic constant (C_{ijkl}) cannot be used. Because of this, the elastic stiffness coefficients (B_{ijkl}) must be employed instead.

In the case of hydrostatic pressure applied to an orthorhombic system, the elastic stiffness coefficients convert to B_{ii} and B_{ij} which can be calculated according to refs 80 and 81.

The elastic stiffness constants allow us to obtain the elastic properties such as the bulk modulus B and the shear modulus G of a material at any hydrostatic pressure. We calculated the shear modulus, the bulk modulus, the Young's modulus E, and the Poisson's coefficient ν employing the Hill approximation,[82] which is defined as the arithmetic average of the Voigt and Reuss models.[83]

Another magnitude that can be estimated is the Vickers hardness (H_V) in the Hill approximation, which is used to predict the hardness of the material.[84]

The theoretical values of these moduli for $YAlO_3$ at 0 GPa are given in Table 7, in which they are also compared to those previously obtained by Huang et al.[40] Theoretical values of some of these elastic moduli of $BaHfO_3$ cubic perovskite are also shown in Table 7 for comparison.

The bulk modulus is a relevant parameter related to the resistance of the material to a uniform or hydrostatic

Table 5. Theoretical Frequencies, Pressure Coefficientsm and Grüneisen Parameters of IR-Active Modes for Bulk $YAlO_3$ up to 30 GPa[a]

	theoretical			
modes	ω_0 (cm^{-1})	$\partial\omega/\partial P$ (cm^{-1} GPa^{-1})	$\partial\omega/\partial P^2$ (cm^{-1} GPa^{-2} × 10^3)	γ
B_{3u}	163(2)	1.48(1)	−18(1)	1.86
B_{1u}	169(2)	0.96(2)	−19(2)	1.16
B_{2u}	225(2)	2.35(1)	−40(2)	2.13
B_{1u}	234(2)	2.22(4)	−34(3)	1.94
B_{3u}	254(2)	1.37(1)	−30(3)	1.10
B_{2u}	259(2)	1.36(2)	−20(2)	1.07
B_{3u}	337(2)	2.59(3)	−72(2)	1.57
B_{1u}	360(2)	1.84(4)	−36(2)	1.04
B_{3u}	371(2)	1.95(2)	−14(2)	1.07
B_{1u}	381(2)	1.65(1)	−24(1)	0.88
B_{3u}	423(2)	3.30(2)	−34(3)	1.59
B_{2u}	423(2)	2.26(2)	−56(3)	1.09
B_{1u}	430(2)	3.60(3)	−68(2)	1.71
B_{3u}	436(2)	3.26(2)	−62(3)	1.53
B_{2u}	439(2)	3.05(2)	−66(2)	1.42
B_{1u}	472(2)	3.29(1)	−56(2)	1.42
B_{2u}	478(2)	3.59(1)	−26(3)	1.54
B_{1u}	494(2)	3.17(1)	−30(2)	1.31
B_{3u}	546(2)	2.84(2)	−28(1)	1.06
B_{1u}	560(2)	2.09(4)	−14(2)	0.76
B_{2u}	602(2)	7.02(3)	−56(2)	2.38
B_{3u}	619(2)	5.68(3)	−181(2)	1.88
B_{2u}	644(2)	6.71(3)	−66(2)	2.13
B_{1u}	646(2)	6.11(3)	−22(2)	1.93
B_{3u}	650(2)	3.33(2)	112(3)	1.05

[a]A second-order polynomial fit was used in order to obtain the pressure dependence of the theoretical frequencies.

Table 6. Generalized Elastic Constants, C_{ij} (in GPa), of Bulk $YAlO_3$ at Ambient Pressure[a]

ij	C_{ij}, this work	C_{ij},[b] LDA	C_{ij},[b] GGA	C_{ij}[c]
11	304.0(2)	299.4	192.7	340
22	346.4(2)	330.0	285.5	
33	369.9(2)	397.0	337.0	
44	137.8(2)	158.4	140.3	72
55	102.9(2)	119.1	80.8	
66	160.4(2)	162.7	147.7	
12	134.0(2)	124.2	99.3	12
13	132.9(2)	121.7	90.4	
23	142.8(2)	140.3	136.0	

[a]Values of elastic constants of cubic perovskite $BaHfO_3$ (last column) of ref 78 are also shown for comparison. [b]Reference 40. [c]Reference 79. Our values calculated with the GGA-PBEsol approximation are compared to those of ref 40, translated into the *Pnma* setting, which used the LDA and GGA approximation.

compression. It is important to mention that the bulk modulus in the Voigt approximation, B_V (204.4(3) GPa), at 0 GPa is in good agreement with the one obtained from EOS (see Table 1). This coincidence of both results suggests the consistency of our calculations.

Another parameter that is convenient to analyze is the ratio of bulk to shear modulus B/G considering that the bulk modulus B is related to the resistance to compression, while the shear modulus G represents the resistance to plastic deformation. If $B/G > 1.75$, the material behaves in a ductile

DOI: 10.1021/acs.jpcc.7b04245
J. Phys. Chem. C 2017, 121, 15353−15367

Table 7. Values of Elastic Moduli at 0 GPa in Bulk $YAlO_3$ Using Voigt, Reuss, and Hill Approximations

	B_V	B_R	B_H	G_V	G_R	G_H	B/G	H_V	E	ν	A_U
this work	204.4(3)	119.3(3)	161.9(3)	120.9(3)	120.7(3)	120.8(3)	1.34(3)	19.66(3)	287(3)	0.19(1)	0.72(2)
LDA[a]	199.80	196.70	198.30	130.70	125.10	127.90	1.55	17.33	315.80	0.23	0.25
GGA[a]	163.0	150.4	156.7	106.4	95.4	100.9	1.55	14.63	249.2	0.23	0.66
GGA[b]			157			93	1.68		234	0.25	

[a]Reference 40. [b]Reference 79. The isotropic bulk modulus (B in GPa), shear modulus (G in GPa), and the universal anisotropy index (A_U). Young's modulus (E in GPa), Poisson's ratio (ν), Vickers hardness (H_V in GPa), and ratio of bulk to shear modulus of the polycrystalline phase (B/G) are estimated from values of Hill's approximation at 0 GPa. Our values are compared to those of ref 40 and using the LDA and GGA approximation. Comparison with the GGA approximation in $BaHfO_3$ cubic perovskite is also given (ref 79).

way and, otherwise, in a brittle manner.[85] The theoretical B/G ratio for $YAlO_3$ at 0 GPa is 1.34 (1.68 for $BaHfO_3$) (see Table 7). Hence, this material is brittle at ambient pressure in agreement with previous calculations.[40]

Concerning the Poisson coefficient ν, it is known that it is related to the volume change during elastic deformation.[83] In other words, it measures the stability of a crystal against shear. If ν = 0.5, it means that there is no volume change during elastic deformation. In addition to this, this parameter provides more information about characteristics of the bonding forces than any other elastic modulus.[83] A value of ν = 0.25 supposes the lower limit for central-force solids and 0.5 corresponds to infinite elastic anisotropy.[83] For $YAlO_3$, the value ν = 0.19 suggests that the interatomic forces in this material are noncentral, whereas $BaHfO_3$ interatomic forces are central.[79]

One of the most important elastic properties of crystal for both engineering and physics fields is the elastic anisotropy, because it is related to the possibility of inducing microcracks in the materials.[86] This property can be quantified with the universal elastic anisotropy index A_U.[87]

If A_U = 0, there is not anisotropy. The more this magnitude differs from 0, the more elastically anisotropic the crystalline structure. In our case, A_U = 0.72 at 0 GPa; thus, $YAlO_3$ is slightly anisotropic at ambient pressure, also in good agreement with previous calculations.[40]

The evolution of the B_{ij} elastic stiffness coefficients as a function of pressure (up to 95 GPa) is shown in Figure 10. It can be observed that B_{11}, B_{33}, B_{12}, B_{13}, and B_{23} increase with the pressure in the whole pressure range. On the other hand, B_{22} increases notably with pressure up to 75 GPa and then increases slowly, tending to saturation from 80 GPa upward. Concerning the stiffness coefficients B_{44}, B_{55}, and B_{66}, all of them increase up to a certain value of pressure and then decrease dramatically, increasing the first and the second one up to 34 GPa, while the last one only up to 14 GPa, and then decreasing all of them up to 95 GPa.

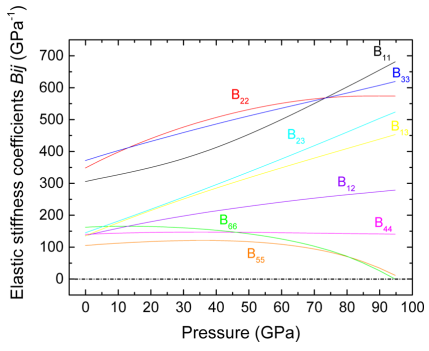

Figure 10. Evolution of the elastic stiffness constants B_{ij} as a function of pressure up to 95 GPa.

It is interesting to analyze the evolution of the elastic moduli with pressure in the whole range from 0 up to 95 GPa (see Figure 11). The Hill B_H bulk modulus increases until 80 GPa, above which it decreases. On the other hand, the Hill G_H shear modulus increases until 20 GPa, and begins to decrease above this pressure, with the decrease being more noticeable in the pressure range in which the material becomes unstable (~92 GPa), as will be commented later.

Concerning the Young's modulus E, which is related to the stiffness of the material, it increases until 34 GPa and then decreases, being more noticeable at ~90 GPa. This suggests that the pressure increases the hardness of the $YAlO_3$ but also becomes less stiff with it, due to the decrease of the Young's modulus with pressure.

The Poisson coefficient ν increases in the whole pressure range, taking a value of 0.35 before the material becomes unstable.

In the case of $BaHfO_3$ cubic perovskite, these elastic moduli increase in the whole range of pressure up to 80 GPa, suggesting that the pressure improves the hardness and the stiffness of the material.[79]

Regarding the ratio of bulk to shear modulus B/G, it increases with pressure, being more noticeable near the instability pressure region, indicating that the material becomes more ductile with increasing pressure. In fact, $YAlO_3$ presents a brittle behavior until 24 GPa and behaves as a ductile material above this pressure. Finally, the universal anisotropy index A_U increases with pressure, suggesting that the mechanical properties of this material become more anisotropic as pressure increases.

To conclude, we will analyze the mechanical stability of the orthorhombic *Pnma* structure of $YAlO_3$. It is well-known that the Born stability criteria are fulfilled when a crystal lattice is mechanically stable.[80,88]

Our calculated elastic constants of $YAlO_3$ at 0 GPa satisfy these criteria, thus confirming the mechanical stability of the orthorhombic structure of the $YAlO_3$ crystal at ambient pressure.

When a nonzero stress is applied to the crystal, the former stability criteria must be modified using the elastic stiffness coefficients instead of the elastic constants. The new condition criteria, known as the "*generalized Born stability criteria*", have to be considered.[89]

Thus, orthorhombic $YAlO_3$ crystal is mechanically stable under hydrostatic pressure when the generalized Born stability criteria are fulfilled at once.

DOI: 10.1021/acs.jpcc.7b04245
J. Phys. Chem. C 2017, 121, 15353−15367

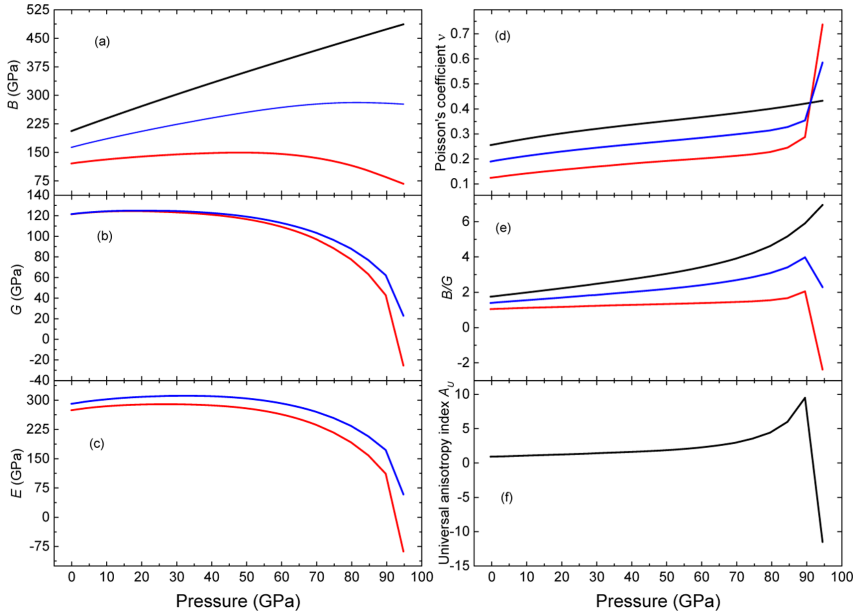

Figure 11. Pressure evolution up to 95 GPa of (a) B, (b) G, (c) E, (d) ν, (e) B/G, and (f) A_U in $YAlO_3$. Black, red, and blue curves refer to the Voigt, Reuss, and Hill approximations, respectively.

The evolution of the generalized Born stability criteria M_i (i = 1−6) as a function of pressure up to 95 GPa is depicted in Figure 12. It can be observed that the $M_4 > 0$ stability criterion

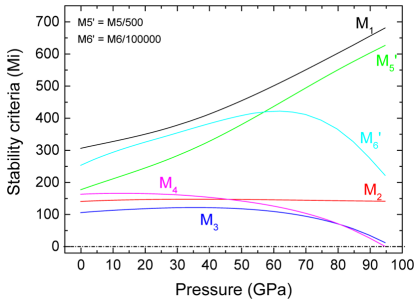

Figure 12. Pressure evolution of the generalized Born stability criteria up to 95 GPa.

is violated at 92 GPa and the $M_3 > 0$ criterion is also violated at a higher pressure. These results suggest that $YAlO_3$ becomes mechanically unstable above 92 GPa. Above this pressure, an amorphization or a phase transition could occur in $YAlO_3$. In the case of $BaHfO_3$ cubic perovskite, the mechanical stability criteria are not fulfilled since 82 GPa, where the instability occurs.[79]

It is relevant to notice that a phase transition in $YAlO_3$ from the orthorhombic *Pbnm* (or *Pnma*) phase to the tetragonal *I*4/*mcm* phase has been predicted at 80 GPa.[29] Our calculations of enthalpy at 0 K for these two phases predict this phase transition above 100 GPa. This discrepancy between the two *ab initio* calculations could be related to the use of different exchange-correlation functionals. In any case, we have shown that the low-pressure orthorhombic phase is not stable above 92 GPa, so a phase transition to the *I*4/*mcm* phase could be observed already near 92 GPa. In this respect, we have checked that the cubic perovskite *Pm-3m* phase, the postperovskite *Cmcm* phase,[90] the postperovskite *Pnma* phase of Sb_2S_3 as observed in $NaFeF_3$,[91] and the other possible phase of $YAlO_3$ reported in the ICDS database ($P6_3/mmc$)[90] are not competitive with the tetragonal *I*4/*mcm* phase in the pressure range above 80 GPa, so the pressure-induced phase transition to the *I*4/*mcm* phase is the most probable one we have found. We want to also note that in this tetragonal phase the coordination of Al atoms is 6 with Al−O bond distances near 1.7 Å, whereas the coordination of Y atoms is already 12 with four Y−O distances near 2.17 Å, four near 2.36 Å, and other four near 2.65 Å around 100 GPa. Moreover, this HP transition is consistent with the tendency of the orthorhombic structure of $YAlO_3$ toward a more symmetric structure on increasing pressure. Experiments of $YAlO_3$ up to the Mbar region are needed in order to verify this phase transition.

CONCLUSION

XRD and RS measurements of $YAlO_3$ nanoperovskite (with size around 40 nm) performed up to 7 and 30 GPa, respectively, have allowed us to study the experimental structural and vibrational properties of this material at HP and compare them to previously reported experimental and theoretical data of bulk $YAlO_3$.[25,26,29] Besides, our experimental results have been nicely compared to our own *ab initio* calculations, noticing that both structural parameters and vibrational modes of $YAlO_3$ nanoperovskite are similar to

DOI: 10.1021/acs.jpcc.7b04245
J. Phys. Chem. C 2017, 121, 15353−15367

those of bulk material. This result suggests that 40 nm size $YAlO_3$ nanocrystals behave as bulk material. The contribution of each atom and each polyhedral unit to the different vibrational modes has been discussed. Finally, the theoretical elastic properties of this perovskite have been discussed both at ambient and at high pressure. It has been found that generalized stability conditions are violated at 92 GPa, thus suggesting that $YAlO_3$ perovskite is mechanically stable up to 92 GPa. Consistent with theoretical calculations, no phase transition has been observed experimentally in our RS measurements up to 30 GPa. Therefore, a similar behavior is expected for $GdAlO_3$ at high pressures. Finally, it must be mentioned that our calculations support a possible phase transition from the *Pnma* phase to the tetragonal *I*4/*mcm* phase in $YAlO_3$ at pressures above 92 GPa.

■ ASSOCIATED CONTENT

Supporting Information

The Supporting Information is available free of charge on the ACS Publications website at DOI: 10.1021/acs.jpcc.7b04245.

Typical TEM image of the $YAlO_3$ nanoperovskite (section S1), table with the experimental lattice parameters, volume cell and refinement parameters obtained from profile matching at different pressures (section S2), table with the EOS equation state parameters for $YAlO_3$ (section S3), description and figure with the normalized cell distortion factor with pressure $d_{norm}(P)$ as a function of pressure of $YAlO_3$ nanoperovskite (section S4), figure with the theoretical and experimental pressure dependence of the A_g, B_{1g}, B_{2g}, and B_{3g} first-order Raman-active modes in bulk and nanoperovskite $YAlO_3$, respectively (section S5), description of elastic property equations (section S6), and references (PDF)

■ AUTHOR INFORMATION

Corresponding Author

*E-mail: miguelandreshr@gmail.com, mhernanr@ull.edu.es.

ORCID

M. A. Hernández-Rodríguez: 0000-0003-4434-2371

J. González-Platas: 0000-0003-3339-2998

Notes

The authors declare no competing financial interest.

■ ACKNOWLEDGMENTS

This research was partially supported by MINECO (MAT2013-46649-C4-2/3/4-P, MAT2015-71070-REDC, and MAT2016-75586-C4-2/3/4-P) and by EU-FEDER funds. M.A.H.-R. thanks MINECO for an FPI grant (BES-2014-068666).

■ REFERENCES

(1) Kaminow, I. P.; Johnston, W. D. Quantitative Determination of Sources of the Electro-Optic Effect in $LiNbO_3$ and $LiTaO_3$. *Phys. Rev.* **1967**, *160*, 519−522.
(2) Zhu, S. Quasi-Phase-Matched Third-Harmonic Generation in a Quasi-Periodic Optical Superlattice. *Science* **1997**, *278*, 843−846.
(3) Wojtowicz, A. J.; Drozdowski, W.; Wisniewski, D.; Lefaucheur, J. L.; Galazka, Z.; Gou, Z.; Lukasiewicz, T.; Kisielewski, J. Scintillation Properties of Selected Oxide Monocrystals Activated with Ce and Pr. *Opt. Mater.* **2006**, *28*, 85−93.
(4) Kan, D.; Terashima, T.; Kanda, R.; Masuno, A.; Tanaka, K.; Chu, S.; Kan, H.; Ishizumi, A.; Kanemitsu, Y.; Shimakawa, Y.; et al. Blue-Light Emission at Room Temperature from Ar+-Irradiated $SrTiO_3$. *Nat. Mater.* **2005**, *4*, 816−819.
(5) Takashima, H.; Shimada, K.; Miura, N.; Katsumata, T.; Inaguma, Y.; Ueda, K.; Itoh, M. Low-Driving-Voltage Electroluminescence in Perovskite Films. *Adv. Mater.* **2009**, *21*, 3699−3702.
(6) Yang, S. Y.; Seidel, J.; Byrnes, S. J.; Shafer, P.; Yang, C.-H.; Rossell, M. D.; Yu, P.; Chu, Y.-H.; Scott, J. F.; Ager, J. W.; et al. Above-Bandgap Voltages from Ferroelectric Photovoltaic Devices. *Nat. Nanotechnol.* **2010**, *5*, 143−147.
(7) Wang, S.; Zhou, H.; Wang, X.; Pan, A. Up-Conversion Luminescence and Optical Temperature-Sensing Properties of Er^{3+}-Doped Perovskite $Na_{0.5}Bi_{0.5}TiO_3$ Nanocrystals. *J. Phys. Chem. Solids* **2016**, *98*, 28−31.
(8) Du, P.; Luo, L.; Li, W.; Yue, Q. Upconversion Emission in Er-Doped and Er/Yb-Codoped Ferroelectric $Na_{0.5}Bi_{0.5}TiO_3$ and Its Temperature Sensing Application. *J. Appl. Phys.* **2014**, *116*, 014102−014106.
(9) Alencar, M. A. R. C.; Maciel, G. S.; De Araújo, C. B.; Patra, A. Er^{3+}-Doped $BaTiO_3$ Nanocrystals for Thermometry: Influence of Nanoenvironment on the Sensitivity of a Fluorescence Based Temperature Sensor. *Appl. Phys. Lett.* **2004**, *84*, 4753−4755.
(10) Weber, M. J.; Bass, M.; Andringa, K.; Monchamp, R. R.; Comperch, E. Czochralski Growth and Properties of $YAlO_3$ Laser Crystals. *Appl. Phys. Lett.* **1969**, *15*, 342−345.
(11) Neuroth, G.; Wallrafen, F. Czochralski Growth and Characterisation of Pure and Doped $YAlO_3$ Single Crystals. *J. Cryst. Growth* **1999**, *198*−*199*, 435−439.
(12) Rabinovich, W. S.; Bowman, S. R.; Feldman, B. J.; Winings, M. J. Tunable Laser Pumped 3 μm Ho: $YAlO_3$ Laser. *IEEE J. Quantum Electron.* **1991**, *27*, 895−897.
(13) Romero, J. J.; Montoya, E.; Bausá, L. E.; Agulló-Rueda, F.; Andreeta, M. R. B.; Hernandes, A. C. Multiwavelength Laser Action of Nd^{3+}: $YAlO_3$ Single Crystals Grown by the Laser Heated Pedestal Growth Method. *Opt. Mater.* **2004**, *24*, 643−650.
(14) Fibrich, M.; Hambálek, T.; Němec, M.; Šulc, J.; Jelínková, H. Multiline Generation Capabilities of Diode-Pumped Nd: YAP and Nd: YAG Lasers. *Laser Phys.* **2014**, *24*, 035803.
(15) Roduner, E. Size Matters: Why Nanomaterials Are Different. *Chem. Soc. Rev.* **2006**, *35*, 583−592.
(16) Lemański, K.; Gagor, A.; Kurnatowska, M.; Pzik, R.; Dereń, P. J. Spectroscopic Properties of Nd^{3+} Ions in Nano-Perovskite $CaTiO_3$. *J. Solid State Chem.* **2011**, *184*, 2713−2718.
(17) Lemański, K.; Dereń, P. J. Spectroscopic Properties of Dy^{3+} Ions in $CaTiO_3$ Nano-Perovskites. *J. Lumin.* **2014**, *145*, 661−664.
(18) Dereń, P. J.; Mahiou, R.; Pązik, R.; Lemanski, K.; Stręk, W.; Boutinaud, P. Upconversion Emission in $CaTiO_3$: Er^{3+} Nanocrystals. *J. Lumin.* **2008**, *128*, 797−799.
(19) Dereń, P. J.; Lemazski, K.; Gągor, A.; Watras, A.; Małecka, M.; Zawadzki, M. Symmetry of $LaAlO_3$ Nanocrystals as a Function of Crystallite Size. *J. Solid State Chem.* **2010**, *183*, 2095−2100.
(20) Lemański, K.; Dereń, P. J. Luminescent Properties of dysprosium(III) Ions in $LaAlO_3$ Nanocrystallites. *J. Rare Earths* **2011**, *29*, 1195−1197.
(21) Pereira, A. F.; Kumar, K. U.; Silva, W. F.; Santos, W. Q.; Jaque, D.; Jacinto, C. Yb^{3+}/Tm^{3+} Co-Doped $NaNbO_3$ Nanocrystals as Three-Photon-Excited Luminescent Nanothermometers. *Sens. Actuators, B* **2015**, *213*, 65−71.
(22) Shi, C.; Qin, H.; Zhao, M.; Wang, X.; Li, L.; Hu, J. Investigation on Electrical Transport, CO Sensing Characteristics and Mechanism for Nanocrystalline $La_{1-x}Ca_xFeO_3$ Sensors. *Sens. Actuators, B* **2014**, *190*, 25−31.
(23) Hu, F.; Zhang, H.; Sun, C.; Yin, C.; Lv, B.; Zhang, C.; Yu, W. W.; Wang, X.; Zhang, Y.; Xiao, M. Superior Optical Properties of Perovskite Nanocrystals as Single Photon Emitters. *ACS Nano* **2015**, *9*, 12410−12416.
(24) Zhao, J.; Ross, N. L.; Angel, R. J.; Carpenter, M. a; Howard, C. J.; Pawlak, D. A.; Lukasiewicz, T. High-Pressure Crystallography of

DOI: 10.1021/acs.jpcc.7b04245
J. Phys. Chem. C 2017, 121, 15353−15367

Rhombohedral $PrAlO_3$ Perovskite. *J. Phys.: Condens. Matter* **2009**, *21*, 235403−235411.
(25) Ross, N. L.; Zhao, J.; Angel, R. J. High-Pressure Single-Crystal X-Ray Diffraction Study of $YAlO_3$ Perovskite. *J. Solid State Chem.* **2004**, *177*, 1276−1284.
(26) Ross, N. L. Distortion of $GdFeO_3$ -Type Perovskites with Pressure: A Study of $YAlO_3$ to 5 GPa. *Phase Transitions* **1996**, *58*, 27−41.
(27) Guennou, M.; Bouvier, P.; Garbarino, G.; Kreisel, J. Structural Investigation of $LaAlO_3$ up to 63 GPa. *J. Phys.: Condens. Matter* **2011**, *23*, 395401−395405.
(28) Ross, N. L.; Zhao, J.; Angel, R. J. High-Pressure Structural Behavior of $GdAlO_3$ and $GdFeO_3$ Perovskites. *J. Solid State Chem.* **2004**, *177*, 3768−3775.
(29) Wu, X.; Qin, S.; Wu, Z. Generalized Gradient Approximation Calculations of the Pressure-Induced Phase Transition of $YAlO_3$ Perovskite. *J. Phys.: Condens. Matter* **2006**, *18*, 3907−3916.
(30) Verma, A. K.; Modak, P. Ab-Initio Investigations of R3c to Pm3m Transition in $RAlO_3$ (La, Pr and Nd) Perovskites under Pressure. *AIP Conf. Proc.* **2012**, *1512*, 86−87.
(31) Ross, N. L. High Pressure Study of $ScAlO_3$ Perovskite. *Phys. Chem. Miner.* **1998**, *25*, 597−602.
(32) Magyari-Köpe, B. High-Pressure Structure of $ScAlO_3$ Perovskite. *J. Geophys. Res.* **2002**, *107*, ECV 1-1−ECV 1-6.
(33) Bouvier, P.; Kreisel, J. Pressure-Induced Phase Transition in $LaAlO_3$. *J. Phys.: Condens. Matter* **2002**, *14*, 3981−3991.
(34) Kennedy, B. J.; Vogt, T.; Martin, C. D.; Parise, J. B.; Hriljac, J. A. Pressure-Induced Phase Transition in $PrAlO_3$. *Chem. Mater.* **2002**, *14*, 2644.
(35) Zhao, J.; Ross, N. L.; Angel, R. J. New View of the High-Pressure Behaviour of $GdFeO_3$-Type Perovskites. *Acta Crystallogr., Sect. B: Struct. Sci.* **2004**, *60*, 263−271.
(36) Hua, H.; Vohra, Y. K. Pressure-Induced Blueshift of Nd^{3+} Fluorescence Emission in $YAlO_3$: Near Infrared Pressure Sensor. *Appl. Phys. Lett.* **1997**, *71*, 2602.
(37) Barnett, J. D. An Optical Fluorescence System for Quantitative Pressure Measurement in the Diamond-Anvil Cell. *Rev. Sci. Instrum.* **1973**, *44*, 1.
(38) Zhydachevskii, Y.; Galanciak, D.; Kobyakov, S.; Berkowski, M.; Kamińska, A.; Suchocki, A.; Zakharko, Y.; Durygin, A. Photoluminescence Studies of Mn^{4+} Ions in $YAlO_3$ Crystals at Ambient and High Pressure. *J. Phys.: Condens. Matter* **2006**, *18*, 11385−11396.
(39) Bass, J. D. Elasticity of Single-Crystal $SmAlO_3$, $GdAlO_3$ and $ScAlO_3$ Perovskites. *Phys. Earth Planet. Inter.* **1984**, *36*, 145−156.
(40) Huang, Z.; Feng, J.; Pan, W. First-Principles Calculations of Mechanical and Thermodynamic Properties of $YAlO_3$. *Comput. Mater. Sci.* **2011**, *50* (10), 3056−3062.
(41) Kung, J.; Rigden, S.; Gwanmesia, G. Elasticity of $ScAlO_3$ at High Pressure. *Phys. Earth Planet. Inter.* **2000**, *118*, 65−75.
(42) Abdollahi, A.; Gholzan, S. M. Pressure-Temperature Dependence of Thermodynamic Properties of $ScAlO_3$ Perovskite from First Principles. *Int. J. Thermophys.* **2015**, *36*, 2273−2282.
(43) Galceran, M.; Pujol, M. C.; Aguiló, M.; Díaz, F. Sol-Gel Modified Pechini Method for Obtaining Nanocrystalline $KRE(WO_4)_2$ (RE = Gd and Yb). *J. Sol-Gel Sci. Technol.* **2007**, *42*, 79−88.
(44) Errandonea, D.; Muñoz, A.; González-Platas, J. Comment on "High-Pressure X-Ray Diffraction Study of YBO_3/Eu^{3+}, $GdBO_3$, and $EuBO_3$: Pressure-Induced Amorphization in $GdBO_3$". *J. Appl. Phys.* **2014**, *115*, 216101−216104.
(45) Mao, H. K.; Bell, P. M.; Shaner, J. W.; Steinberg, D. J. Specific Volume Measurements of Cu, Mo, Pd, and Ag and Calibration of the Ruby R1 Fluorescence Pressure Gauge from 0.06 to 1 Mbar. *J. Appl. Phys.* **1978**, *49*, 3276−3283.
(46) Syassen, K. High Pressure Research: An Ruby Under Pressure. *High Pressure Res.* **2008**, *28*, 75−126.
(47) Hohenberg, P.; Kohn, W. Inhomogeneous Electron Gas. *Phys. Rev.* **1964**, *136*, B864−B871.
(48) Mujica, A.; Rubio, A.; Muñoz, A.; Needs, R. J. High-Pressure Phases of Group-IV, III-V, and II-VI Compounds. *Rev. Mod. Phys.* **2003**, *75*, 863−912.
(49) Kresse, G.; Furthmüller, J. Efficient Iterative Schemes for Ab Initio Total-Energy Calculations Using a Plane-Wave Basis Set. *Phys. Rev. B: Condens. Matter Mater. Phys.* **1996**, *54*, 11169−11186.
(50) Blöchl, P. E. Projector Augmented-Wave Method. *Phys. Rev. B: Condens. Matter Mater. Phys.* **1994**, *50*, 17953−17979.
(51) Perdew, J.; Ruzsinszky, A.; Csonka, G.; Vydrov, O.; Scuseria, G.; Constantin, L.; Zhou, X.; Burke, K. Restoring the Density-Gradient Expansion for Exchange in Solids and Surfaces. *Phys. Rev. Lett.* **2008**, *100*, 136406−136410.
(52) Monkhorst, H. J.; Pack, J. D. Special Points for Brillouin-Zone Integrations. *Phys. Rev. B* **1976**, *13*, 5188−5192.
(53) Nielsen, O. H.; Martin, R. M. Quantum-Mechanical Theory of Stress and Force. *Phys. Rev. B: Condens. Matter Mater. Phys.* **1985**, *32*, 3780−3791.
(54) Le Page, Y.; Saxe, P. Symmetry-General Least-Squares Extraction of Elastic Data for Strained Materials from Ab Initio Calculations of Stress. *Phys. Rev. B: Condens. Matter Mater. Phys.* **2002**, *65*, 1−14.
(55) Beckstein, O.; Klepeis, J. E.; Hart, G. L. W.; Pankratov, O. First-Principles Elastic Constants and Electronic Structure of α-Pt_2Si and PtSi. *Phys. Rev. B: Condens. Matter Mater. Phys.* **2001**, *63*, 134112−134123.
(56) Parliuski, K. Department of Materials Research by Computers Institute of Nuclear Physics, Polish Academy of Sciences. Computer Code Phonon. http://wolf.ifj.edu.pl/phonon/.
(57) Garg, A. B.; Errandonea, D.; Rodríguez-Hernández, P.; López-Moreno, S.; Muñoz, A.; Popescu, C. High-Pressure Structural Behaviour of HoVO4: Combined XRD Experiments and Calculations Ab Initio. *J. Phys.: Condens. Matter* **2014**, *26*, 265402−265411.
(58) Sans, J. A.; Manjón, F. J.; Popescu, C.; Cuencia-Gotor, V. P.; Gomis, O.; Muñoz, A.; Rodríguez-Hernández, P.; Contreras-García, J.; Pellicer-Porres, J.; Pereira, A. L. J.; Santamaría-Pérez, D.; et al. Ordered Helium Trapping and Bonding in Compressed Arseolite: Synthesis of As_4O_6•2He. *Phys. Rev. B: Condens. Matter Mater. Phys.* **2016**, *93*, 054102−054106.
(59) Ibáñez, J.; Sans, J. A.; Popescu, C.; López-Vidrier, J.; Elvira-Betanzos, J. J.; Cuenca-Gotor, V. P.; Gomis, O.; Manjón, F. J.; Rodríguez-Hernández, P.; Muñoz, A. Structural, Vibrational, and Electronic Study of Sb_2S_3 at High Pressure. *J. Phys. Chem. C* **2016**, *120*, 10547−10558.
(60) Gomis, O.; Ortiz, H. M.; Sans, J. A.; Manjón, F. J.; Santamaría-Pérez, D.; Rodríguez-Hernández, P.; Muñoz, A. $InBO_3$ and $ScBO_3$ at High Pressures: An Ab Initio Study of Elastic and Thermodynamic Properties. *J. Phys. Chem. Solids* **2016**, *98*, 198−208.
(61) Errandonea, D.; Mun, A.; Rodr, P.; Gomis, O.; Achary, S. N.; Popescu, C.; Patwe, S. J.; Tyagi, A. K. High-Pressure Crystal Structure, Lattice Vibrations, and Band Structure of $BiSbO_4$. *Inorg. Chem.* **2016**, *55*, 4958−4969.
(62) Diehl, R.; Brandt, G. Crystal Structure Refinement of $YAlO_3$, a Promising Laser Material. *Mater. Res. Bull.* **1975**, *10*, 85−90.
(63) Matsushita, N.; Tsuchiya, N.; Nakatsuka, K. Precipitation and Calcination Processes for Yttrium Aluminum Garnet Precursors Synthesized by the Urea Method. *J. Am. Ceram. Soc.* **1999**, *82* (8), 1977−1984.
(64) Vali, R. Vibrational, Dielectric and Scintillation Properties of $YAlO_3$. *J. Lumin.* **2007**, *127*, 727−730.
(65) Gonzalez-Platas, J.; Alvaro, M.; Nestola, F.; Angel, R. EosFit7-GUI: A New Graphical User Interface for Equation of State Calculations, Analyses and Teaching. *J. Appl. Crystallogr.* **2016**, *49*, 1377−1382.
(66) Sasaki, S.; Prewitt, C. T.; Liebermann, R. C. The Crystal Structure of $CaGeO_3$ Perovskite and the Crystal Chemistry of the $GdFeO_3$-Type Perovskites. *Am. Mineral.* **1983**, *68*, 1189−1198.
(67) Ardit, M.; Dondi, M.; Cruciani, G. *Phys. Rev. B: Condens. Matter Mater. Phys.* **2017**, *95*, 24110−24117.

DOI: 10.1021/acs.jpcc.7b04245
J. Phys. Chem. C 2017, 121, 15353−15367

(68) Chopelas, A. Single-Crystal Raman Spectra of $YAlO_3$ and $GdAlO_3$: Comparison to Several Orthorhombic ABO_3 Perovskites. *Phys. Chem. Miner.* **2011**, *38*, 709−726.
(69) Andreasson, J.; Holmlund, J.; Rauer, R.; Käll, M.; Börjesson, L.; Knee, C. S.; Eriksson, A. K.; Eriksson, S. G.; Rübhausen, M.; Chaudhury, R. P. Electron-Phonon Interactions in Perovskites Containing Fe and Cr Studied by Raman Scattering Using Oxygen-Isotope and Cation Substitution. *Phys. Rev. B: Condens. Matter Mater. Phys.* **2008**, *78*, 1−13.
(70) Udagawa, M.; Kohn, K.; Koshizuka, N.; Tsushima, T.; Tsushima, K. Influence of Magnetic Ordering on the Phonon Raman Spectra in $YCrO_3$ and $GdCrO_3$. *Solid State Commun.* **1975**, *16*, 779−783.
(71) Suda, J.; Kamishima, O.; Hamaoka, K.; Matsubara, I.; Hattori, T.; Sato, T. The First-Order Raman Spectra and Lattice Dynamics for $YAlO_3$ Crystal. *J. Phys. Soc. Jpn.* **2003**, *72*, 1418−1422.
(72) Casu, A.; Ricci, P. C.; Anedda, A. Structural Characterization of $Lu_{0.7}Y_{0.3}AlO_3$ Single Crystal by Raman Spectroscopy. *J. Raman Spectrosc.* **2009**, *40*, 1224−1228.
(73) Iliev, M. N.; Lee, H.-G.; Popov, V. N.; Sun, Y. Y.; Thomsen, C.; Meng, R. L.; Chu, C. W. Raman Spectroscopy of Orthorhombic Perovskitelike $YMnO_3$ and $LaMnO_3$. *Phys. Rev. B: Condens. Matter Mater. Phys.* **1998**, *57*, 2872−2877.
(74) Koshizuka, N.; Ushioda, S. Inelastic-Light-Scattering Study of Magnon Softening in $ErFeO_3$. *Phys. Rev. B: Condens. Matter Mater. Phys.* **1980**, *22*, 5394−5399.
(75) Birch, F. Finite Elastic Strain of Cubic Crystals. *Phys. Rev.* **1947**, *71*, 809−824.
(76) Monteseguro, V.; Rodríguez-Hernández, P.; Vilaplana, R.; Manjón, F. J.; Venkatramu, V.; Errandonea, D.; Lavín, V.; Muñoz, A. Lattice Dynamics Study of Nanocrystalline Yttrium Gallium Garnet at High Pressure. *J. Phys. Chem. C* **2014**, *118*, 13177−13185.
(77) Monteseguro, V.; Rodríguez-Hernández, P.; Ortiz, H. M.; Venkatramu, V.; Manjón, F. J.; Jayasankar, C. K.; Lavín, V.; Muñoz, A. Structural, Elastic and Vibrational Properties of Nanocrystalline Lutetium Gallium Garnet under High Pressure. *Phys. Chem. Chem. Phys.* **2015**, *17*, 9454−9464.
(78) Ross, N. L.; Zhao, J.; Burt, J. B.; Chaplin, T. D. Equations of State of $GdFeO_3$ and $GdAlO_3$ Perovskites. *J. Phys.: Condens. Matter* **2004**, *16*, 5721−5730.
(79) Gu, F.; Chen, Y.; Zhang, X.; Zhang, J. First-Principles Calculations for the Structural, Elastic and Thermodynamic Properties of Cubic Perovskite $BaHfO_3$ under Pressure. *Phys. Scr.* **2014**, *89*, 105703−105714.
(80) Wallace, D. C. *Thermodynamics of Crystals*; Wiley: New York, 1972.
(81) Sin'ko, G. V.; Smirnov, N. A. Ab Initio Calculations of Elastic Constants and Thermodynamic Properties of Bcc, Fcc, and Hcp Al Crystals under Pressure. *J. Phys.: Condens. Matter* **2002**, *14*, 6989−7005.
(82) Hill, R. The Elastic Behaviour of a Crystalline Aggregate. *Proc. Phys. Soc., London, Sect. A* **1952**, *65*, 349−354.
(83) Ravindran, P.; Fast, L.; Korzhavyi, P. A.; Johansson, B.; Wills, J.; Eriksson, O. Density Functional Theory for Calculation of Elastic Properties of Orthorhombic Crystals: Application to TiSi. *J. Appl. Phys.* **1998**, *84*, 4891−4904.
(84) Tian, Y.; Xu, B.; Zhao, Z. Microscopic Theory of Hardness and Design of Novel Superhard Crystals. *Int. J. Refract. Hard Met.* **2012**, *33*, 93−106.
(85) Pugh, S. F. XCII. Relations between the Elastic Moduli and the Plastic Properties of Polycrystalline Pure Metals. *London, Edinburgh, Dublin Philos. Mag. J. Sci.* **1954**, *45*, 823−843.
(86) Tvergaard, V.; Hutchinson, J. W. Microcracking in Ceramics Induced by Thermal Expansion or Elastic Anisotropy. *J. Am. Ceram. Soc.* **1988**, *71*, 157−166.
(87) Ranganathan, S. I.; Ostoja-Starzewski, M. Universal Elastic Anisotropy Index. *Phys. Rev. Lett.* **2008**, *101*, 55504−55507.
(88) Born, M.; Huang, K. *Dynamical Theory of Crystal Lattices*; Oxford University Press: Oxford, U.K., 1954.
(89) Wang, J.; Yip, S.; Phillpot, S. R.; Wolf, D. Crystal Instabilities at Finite Strain. *Phys. Rev. Lett.* **1993**, *71*, 4182−4185.
(90) Bertaut, E. F.; Mareschal, J. Un Nouveau Type de Structure Hexagonale: $ATiO_3$ (T = Y, Eu, Gd, Tb, Dy, Ho, Er). *C. R. Acad. Sci.* **1963**, *257*, 867−870.
(91) Crichton, W. A.; Bernal, F. L.; Guignard, J.; Hanfland, M.; Margadonna, S. Observation of $Sb2S_3$-Type Post-Post Perovskite in $NaFe_3$. Implications for ABX_3 and A_2X_3 Systems at Ultrahigh Pressure. *Mineral. Mag.* **2016**, *80*, 659−674.

DOI: 10.1021/acs.jpcc.7b04245
J. Phys. Chem. C 2017, 121, 15353−15367

SUPPORTING INFORMATION

Structural, Vibrational, and Elastic Properties of Yttrium Orthoaluminate Nano-perovskite at High Pressures

M.A. Hernández-Rodríguez,[a,*] V. Monteseguro,[f] A.D. Lozano-Gorrín,[a] F.J. Manjón,[e] J. González-Platas,[g] P. Rodríguez-Hernández,[a,b,d] A. Muñoz,[a,b,d] V. Lavín,[a,b,c] I.R. Martín [a,b,d] and U.R. Rodríguez-Mendoza[a,b,d]

[a] Departamento de Física, Universidad de La Laguna. E-38200 San Cristóbal de La Laguna, Santa Cruz de Tenerife, Spain.

[b] MALTA Consolider Team, Universidad de La Laguna. E-38200 San Cristóbal de La Laguna, Santa Cruz de Tenerife, Spain

[c] Instituto Universitario de Estudios avanzados en Atómica, Molecular y Fotónica, Universidad de La Laguna. E-38200 San Cristóbal de La Laguna, Santa Cruz de Tenerife, Spain.

[d] Instituto Universitario de Materiales y Nanotecnología, Universidad de La Laguna, E-38200 San Cristóbal de La Laguna, Santa Cruz de Tenerife, Spain.

[e] Instituto de Diseño para la Fabricación y Producción Automatizada, MALTA Consolider Team, Universitat Politécnica de València, Cno. de Vera s/n, 46022 Valencia, Spain.

[f] Beamlines BM23 & ID24, European Synchrotron Radiation Facility, 38043 Grenoble, France

[g] Servicio de Difracción de Rayos X (SIDIX). Departamento de Física, Universidad de La Laguna. E-38200 San Cristóbal de La Laguna, Santa Cruz de Tenerife, Spain.

Content:

SECTION S1

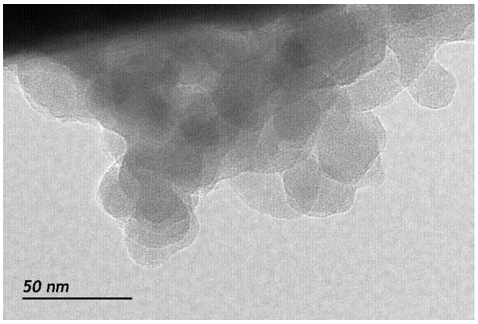

Figure S1. TEM image of the $YAlO_3$ nano-perovskite used in this study

SECTION S2

Table S2. Lattice Parameters, Volume Cell and Refinement Parameters Obtained from Profile Matching at Different Pressure

Pressure (GPa)	*a* (Å)	*b* (Å)	*c* (Å)	V (Å^3)	χ^2	R_p	R_{exp}	R_{Bragg}
0	5.327(2)	7.369(3)	5.175(2)	203.15(23)	8.06	16.8	8.71	0.02
0.59	5.319(2)	7.352(3)	5.172(2)	202.28(23)	6.91	19.2	13.3	16.0
0.75	5.317(2)	7.351(3)	5.168(2)	202.06(23)	6.56	19.0	13.5	15.8
0.92	5.314(2)	7.350(3)	5.168(2)	201.90(23)	5.12	17.4	15.3	16.1
1.95	5.298(2)	7.335(3)	5.158(2)	200.47(23)	6.67	19.4	13.2	14.6
2.33	5.294(2)	7.328(3)	5.156(2)	200.03(23)	6.98	21.5	16.9	17.7
3.7	5.280(2)	7.312(3)	5.143(2)	198.54(23)	5.77	18.1	14.2	14.9
4.28	5.275(2)	7.301(3)	5.139(2)	197.92(23)	5.28	17.8	13.0	14.1
5.36	5.264(2)	7.293(3)	5.129(2)	196.94(23)	7.10	22.4	18.1	20.1
6.74	5.253(2)	7.279(3)	5.118(2)	195.70(23)	6.25	18.8	14.6	16.7

SECTION S3

Table S3. Birch-Murnaghan Second (BM2) and Third Order (BM3) EOS Parameters of $YAlO_3$ Nano-perovskite (this work) and $YAlO_3$ Bulk (Ref.[1])

	This work	Ref.[1]	This work	Ref.[1]
	BM2		BM3	
V_0 (Å^3)	202.95(8)	203.29(4)	203.15(11)	203.401(19)
B_0 (GPa)	166(3)	207(2)	132(12)	192(2)

B_0'	4	4	18(6)	7.3(5)
a_0 (Å)	5.3250(15)	5.3289(3)	5.32668	5.3291(4)
M_0 (GPa)	435(18)	476(2)	322(28)	471(8)
M_0'	12	12	67(21)	13(2)
b_0 (Å)	7.3633(16)	7.3685(5)	7.36536	7.3700(2)
M_0 (GPa)	512(17)	697(7)	397(37)	637(7)
M_0'	12	12	63(24)	26(2)
c_0 (Å)	5.1762(10)	5.1775(5)	5.1762(13)	5.17874(4)
M_0 (GPa)	567(20)	755(10)	568(75)	660(22)
M_0'	12	12	12(24)	35(6)

SECTION S4

Normalized cell distortion factor with pressure d_{norm} (P) as a function of pressure:

A parameter which usefulness lies in the evaluation of the departure of an orthorhombic structure from the cubic archetype one is the cell distortion factor, d, introduced by Sasaki et al. [1] This parameter can be determinated by comparing the unit-cell axes through the relation $a \approx c \approx 2a_p$ and $b \approx (2a_p)^{1/2}$ (in the *Pnma* setting, $b>a>c$). This factor is defined by the next expression:

$$d = \frac{\left(a/\sqrt{2} - a_p\right)^2 + \left(b/\sqrt{2} - a_p\right)^2 + \left(c/2 - a_p\right)^2}{3a_p{}^2 \times 10^4} \qquad \text{(S4.1)}$$

where a_p is the pseudocubic subcell parameter which is defined by:

$$a_p = \frac{\left(a/\sqrt{2} + c/\sqrt{2} + b/2\right)}{3} \qquad \text{(S4.2)}$$

However a proper version of the parameter d of eq. (S2.1) is used instead, which is the normalized cell distortion factor, $d_{norm}(P)$.[2] This parameter describes the rate of change of the cell distortion pressure normalized with the value at ambient conditions (d_0)

$$d_{norm}(P) = \frac{1}{d_0}\left(\frac{\partial d}{\partial P}\right)_T \qquad \text{(S4.3)}$$

In our specific case, $YAlO_3$ nano-perovskite, d_{norm} (P) decreases with pressure (see. Fig S2), suggesting that $YAlO_3$ nano-perovskite evolves toward a cubic structure with pressure. [2]

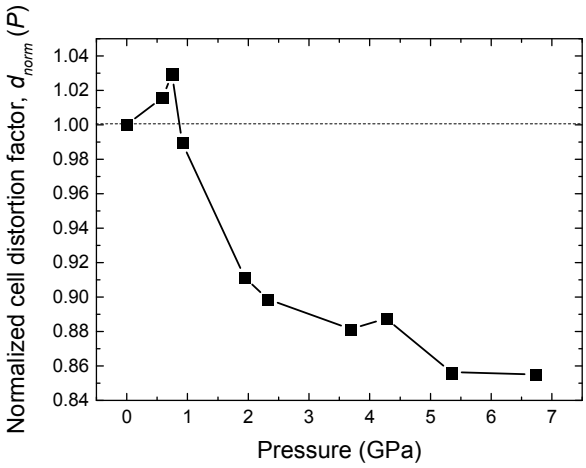

Figure S3. Normalized cell distortion factor with pressure d_{norm} (P) as a function of pressure of $YAlO_3$ nano-perovskite

SECTION S5

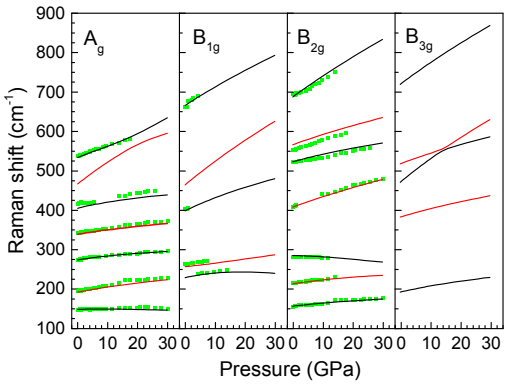

Figure S4. Theoretical (lines) and experimental (symbols) pressure dependence of the A_g, B_{1g}, B_{2g} and B_{3g} first-order Raman-active modes in bulk and $YAlO_3$ nano-perovskite, respectively.

SECTION S6

Elastic properties equations description:

When a non-zero stress is applied to the crystal, the elastic stiffness coefficients must be used instead of the elastic constants. The elastic stiffness coefficients are defined as:

$$B_{ijkl} = C_{ijkl} + \frac{1}{2}\left[\delta_{ik}\sigma_{jl} + \delta_{jk}\sigma_{il} + \delta_{il}\sigma_{jk} + \delta_{jl}\sigma_{ik} - 2\delta_{kl}\sigma_{ij}\right] \quad \text{(S6.1)}$$

where C_{ijkl} are the elastic constants evaluated at the current stressed state, σ_{ij} are the external stresses, and δ_{jl} is the Kronecker delta. In the case of hydrostatic pressure applied to an orthorhombic system, the elastic stiffness coefficients are [3,4]

$$\begin{aligned} B_{ii} &= C_{ii} - P\left(i = 1,4,5,6\right) \\ B_{ij} &= C_{ij} + P\left(i < j, j = 1-3\right) \end{aligned} \quad \text{(S6.2)}$$

The elastic stiffness constants allow us to obtain the elastic properties such as the bulk modulus *B* and the shear modulus *G* of a material at any hydrostatic pressure.
For the orthorhombic crystal system, the Voigt B_V and Reuss B_R bulk moduli are defined as:

$$\begin{aligned} B_V &= \frac{B_{11} + B_{22} + B_{33} + 2\left(B_{12} + B_{13} + B_{23}\right)}{9} \\ B_R &= \frac{1}{s_{11} + s_{22} + s_{33} + 2\left(s_{12} + s_{13} + s_{23}\right)} \end{aligned} \quad \text{(S6.3)}$$

whereas the Voigt G_V and Reuss G_R shear moduli are expressed by the following equations:

$$\begin{aligned} G_V &= \frac{B_{11} + B_{22} + B_{33} + 3\left(B_{44} + B_{55} + B_{66}\right) - \left(B_{12} + B_{13} + B_{23}\right)}{15} \\ G_R &= \frac{15}{4\left(s_{11} + s_{22} + s_{33}\right) - 4\left(s_{12} + s_{13} + s_{23}\right) + 3\left(s_{44} + s_{55} + s_{66}\right)} \end{aligned} \quad \text{(S6.4)}$$

where s_{ij} are the elastic compliance constants which are the matrix elements of the inverse of the elastic constants matrix. [5]

Therefore, bulk and shear moduli in the Hill approximation are expressed as:

$$\begin{aligned} B_H &= \frac{B_V + B_R}{2} \\ G_H &= \frac{G_V + G_R}{2} \end{aligned} \quad \text{(S6.5)}$$

In addition, the Young's modulus *E* and the Poisson's coefficient *v* are defined as:

$$E_H = \frac{9B_H \cdot G_H}{3B_H + G_H}$$
$$v_H = \frac{3B_H - 2G_H}{2(3B_H + G_H)} \quad \text{(S6.6)}$$

Another magnitude that can be estimated is the Vickers hardness (H_V) in the Hill approximation, which it is used to predict the hardness of the material[6] and it is defined by the equation:

$$H_V = 0.92\left(\frac{G_H}{B_H}\right)^{1.137} \cdot G_H{}^{0.708} \quad \text{(S6.7)}$$

where G_H and B_H are the shear and bulk moduli in Hill approximation.

The universal elastic anisotropy index A_U,[7] is defined as:

$$A_U = 5\left(\frac{G_V}{G_R}\right) + \left(\frac{B_V}{B_R}\right) - 6 \quad \text{(S6.8)}$$

where B_V, G_V, B_R and G_R are the bulk and shear moduli in Voigt and Reuss approximations, respectively. It is relevant to point out that A_U takes in consideration all the elastic stiffness coefficients B_{ij}.[7] If $A_U = 0$ there is not anisotropy. The more this magnitude differs from 0 the more elastically anisotropic is the crystalline structure.

It is well known that the Born stability criteria are fulfilled when a crystal lattice is mechanically stable.[3,8] In the case of an orthorhombic system, these criteria are:

$$C_{ij} > 0$$
$$C_{11} \cdot C_{22} - C_{12}^2 > 0 \quad \text{(S6.9)}$$
$$C_{11} \cdot C_{22} \cdot C_{33} + 2C_{12} \cdot C_{23} \cdot C_{13} - C_{22} \cdot C_{13}^2 - C_{11} \cdot C_{23}^2 - C_{33} \cdot C_{12}^2 > 0$$

When a non-zero stress is applied to the crystal, the former stability criteria must be modified using the elastic stiffness coefficients instead of the elastic constants. The new condition criteria, known as the "*generalized Born stability criteria*", are obtained just replacing in Eqs. (S4.9) the elastic constants C_{ij} by the B_{ij} coefficients.[9]

Thus, an orthorhombic system is mechanically stable under hydrostatic pressure when the generalized Born stability criteria:

$$M_1 = B_{11} > 0; M_2 = B_{44} > 0; M_3 = B_{55} > 0; M_4 = B_{66} > 0$$
$$M_5 = B_{11} \cdot B_{22} - B_{12}^2 > 0 \quad \text{(S6.10)}$$
$$M_6 = B_{11} \cdot B_{22} \cdot B_{33} + 2B_{12} \cdot B_{23} \cdot B_{13} - B_{22} \cdot B_{13}^2 - B_{11} \cdot B_{23}^2 - B_{33} \cdot B_{12}^2 > 0$$

are fulfilled at once.

SECTION S7

References

(1) Sasaki, S.; Prewitt, C. T.; Liebermann, R. C. The Crystal Structure of $CaGeO_3$ Perovskite and the Crystal Chemistry of the $GdFeO_3$-Type Perovskites. *Am. Mineral.* **1983**, *68*, 1189–1198.

(2) Ardit, M.; Dondi, M.; Cruciani, G. Locked Octahedral Tilting in Orthorhombic Perovskites : At the Boundary of the General Rule. **2017**, 95, *24110*-24117.

(3) Wallace, D. *Thermodynamics of Crystals*; New York; 1972.

(4) Sin'ko, G. V.; Smirnov, N. A. Ab Initio Calculations of Elastic Constants and Thermodynamic Properties of Bcc, Fcc, and Hcp Al Crystals under Pressure. *J. Phys. Condens. Matter* **2002**, *14*, 6989-7005.

(5) Nye, J. *Physical Properties of Crystals: Their Representation by Tensors and Matrices*; Oxford; 1985

(6) Tian, Y.; Xu, B.; Zhao, Z. Microscopic Theory of Hardness and Design of Novel Superhard Crystals. *Int. J. Refract. Met. Hard Mater.* **2012**, *33*, 93–106.

(7) Ranganathan, S. I.; Ostoja-Starzewski, M. Universal Elastic Anisotropy Index. *Phys. Rev. Lett.* **2008**, *101*, 55504.

(8) Born, M.; Huang, K. *Dynamical Theory of Crystal Lattices*. Oxford 1954.

(9) Wang, J.; Yip, S.; Phillpot, S. R.; Wolf, D. Crystal Instabilities at Finite Strain. *Phys. Rev. Lett.* **1993**, *71*, 4182–4185.

4.2. Optical sensor calibration with temperature

In this section, the third and fourth papers are included and suppose one of the main part of this thesis regarding the analysis of the viability of nano-perovskites doped with Ln^{3+} ions, i.e. Nd^{3+}-doped $YAlO_3$ and Tm^{3+}-doped $YAlO_3$ nano-perovskites as optical temperature sensors working in the NIR.

The third paper focused on the temperature evolution of the infrared luminescence Nd^{3+}-doped $YAlO_3$ nano-perovskite, in order to evaluate its viability as optical temperature sensor in NIR region, especifically in the well-known "near infrared biological windows". In addition, a first approximation of this optical temperature sensor in the bioimaing field was also analyzed.

The fourth paper studies the viability of the temperature evolution of the luminescence of Tm^{3+} ions in $YAlO_3$ nano-perovskite as optical temperature sensor working in NIR.

4.2.1. Comparison of the sensitivity as optical temperature sensor of nano-perovskite doped with Nd^{3+} ions in the first and second biological windows

Authors: **M.A. Hernández-Rodríguez**, A.D. Lozano-Gorrín, I.R. Martín, U.R. Rodríguez-Mendoza and V. Lavín

Published in: **Sensors and Actuators B;** Volume: **255;** Pages: **970-976;** DOI: 10.1016/j.snb.2017.08.140; Accepted **17 August 2017**

In the present article, the temperature dependency of the infrared luminescence of yttrium orthoaluminate nano-perovskite doped with 1 mol % of Nd^{3+} ions (YAP: Nd^{3+} 1.0%) was studied and analyzed its potential application as optical temperature sensor working in NIR.

The first part of this work consisted in the temperature calibration of YAP: Nd^{3+} 1.0% nano-perovskite from room temperature (RT) up to 610 K (337 ºC) by using the fluorescence intensity ratio technique (FIR) in the NIR. For this porpuse, the sample was placed in a tubular furnace and excited at 532 nm comercial laser, monitoring the emission bands centered at 820 and 890 nm associated to the $(^2H_{9/2}, {}^4F_{5/2}) \rightarrow {}^4I_{9/2}$ and $^4F_{3/2} \rightarrow {}^4I_{9/2}$ transitions respectively, as it is shown in the Fig. 2 of this paper. The experimental ratio,

R, obtained from the integrated areas of the former emissions was analyzed as a function of the temperature and fitted to a Boltzmann-type curve (see Fig. 3 of this article). The relative thermal sensitivity, S_{REL}, achieved in this experiment at 293 K (20º C) was around 0.0018 K^{-1} (with a temperature uncertainty δT around 0.9 K) and was compared with the S_{REL} values of other optical temperature sensors doped with Nd^{3+} ions at the same temperature (see Table 1 of the article), showing a notable performance that allows the potential application of YAP: Nd^{3+} 1.0% nano-perovskite as optical temperature sensor based on the FIR technique, working in the I-*BW*.

In the second part of this article, a second temperature calibration, but in the II-*BW*, was performed, taking advantage of the YAP: Nd^{3+} 1.0% nano-perovskite emission band centered around 1340 nm associated to the $^4F_{3/2} \rightarrow {}^4I_{13/2}$ transition. This time, the sample was excited by the same excitation laser at 532 nm and heated up, increasing the pump power of the former laser. In this case, the Full Width at Half Maximum (*FHWM*) of the Stark peak at 1348 nm was analyzed as a function of the temperature from RT up to 370 K (97 ºC), as it is shown in the Fig. 4 of this article. *FHWM* experimental points were well-fitted to a second order polynomial function (see Fig. 5). From the calibration procedure, the S_{REL} value achieved at 293 K was around 0.033 K^{-1} (with a temperature uncertainty δT around 0.37 K). This value was almost twice higher than the one achieved in the I-*BW* at the same temperature. In addition, by comparison with other optical temperature sensors working in the II-*BW*, YAP: Nd^{3+} 1.0% nano-perovskite showed a great performance, which allows its consideration as optical temperature sensor working in the II-*BW*.

In the last part of this paper, a straightforward experiment to test the possible application of YAP: Nd^{3+} 1.0% nano-perovskite in the bioimaging field, was carried out by a sub-tissue penetration study, via a vertical setup as is detailed in the manuscript (see Fig 6-left). This experiment allowed to measure the emission about 1350 nm associated with the Nd^{3+}: $^4F_{3/2} \rightarrow {}^4I_{13/2}$ transition as a function of the tissue thickness by simply filling a cuvette with a specific volume of the phantom tissue, reaching a sub-tissue penetration depth of 5.5 mm (see Fig 6-right). This result shows also the potential of YAP: Nd^{3+} 1.0% nano-perovskite for its application in sub-tissue luminescence imaging.

Sensors and Actuators B 255 (2018) 970–976

Contents lists available at ScienceDirect

Sensors and Actuators B: Chemical

journal homepage: www.elsevier.com/locate/snb

Research Paper

Comparison of the sensitivity as optical temperature sensor of nano-perovskite doped with Nd^{3+} ions in the first and second biological windows

M.A. Hernández-Rodríguez[a,*], A.D. Lozano-Gorrín[a], I.R. Martín[a,b,d], Ulises R. Rodríguez-Mendoza[a,b,d], V. Lavín[a,b,c]

[a] Departamento de Física, Universidad de La Laguna, E-38200, San Cristóbal de La Laguna, Santa Cruz de Tenerife, Spain
[b] MALTA Consolider Team, Universidad de La Laguna, E-38200, San Cristóbal de La Laguna, Santa Cruz de Tenerife, Spain
[c] Instituto Universitario de Estudios avanzados en Atómica, Molecular y Fotónica (IUdEA), Universidad de La Laguna, E-38200, San Cristóbal de La Laguna, Santa Cruz de Tenerife, Spain
[d] Instituto Universitario de Materiales y Nanotecnología (IMN), Universidad de La Laguna, E-38200, San Cristóbal de La Laguna, Santa Cruz de Tenerife, Spain

ARTICLE INFO

Article history:
Received 2 March 2017
Received in revised form 16 August 2017
Accepted 17 August 2017
Available online 23 August 2017

Keywords:
Nd^{3+}-doped nanocrystalline perovskites
Optical sensor
Biological windows
Biomedical applications
YAP

ABSTRACT

The temperature evolution of the infrared luminescence of yttrium orthoaluminate nano-perovskite, doped with 1.0 mol% of Nd^{3+} ions, was analyzed in order to check its viability as optical thermal sensor in the well-known "near infrared biological windows" of the human tissue. For this purpose, the dependences of the emission bands of the ($^2H_{9/2}$, $^4F_{5/2}$), $^4F_{3/2} \rightarrow {}^4I_{9/2}$ transitions from RT up to 610 K and the emission band of the $^4F_{3/2} \rightarrow {}^4I_{13/2}$ transition from RT up to 370 K for the first and second biological windows respectively, were measured and calibrated as functions of the temperature. From the calibration procedure of the optical sensor in the first biological window, the maximum value of the relative sensitivity was obtained and compared with others Nd-based optical sensors of the literature, showing a notable sensitivity. In addition, the relative sensitivity in the second biological window at RT was almost twice higher than the obtained one in the first biological window at the same temperature, showing a high sensitivity of the nano-perovskite in the biophysical temperature range (30–45 °C). Moreover, it has been studied among the emission sub-tissue penetration depth through a phantom tissue, taking advantage of the emission of Nd^{3+} in the second biological window. These results show the potential use of the yttrium orthoaluminate nano-perovskite doped with 1.0 mol% of Nd^{+3} for both sub-tissue luminescence imaging and luminescence-based thermal sensing

1. Introduction

The properties of a material, such as optical ones, for instance absorption and luminescence, depend notably on the environment conditions, such as temperature, pressure or pH among others [1,2]. Thus, when one of these parameters changes, the optical response of the material changes as well. According to this behavior, a new generation of devices, known as optical sensors, has been currently developed for applications probes to monitor physical or chemical fluctuations due to the changes in the environment conditions respect to their initial states. The optical sensor is mainly composed of two elements: an optically active material which acts as a probe and it can be placed at the point of interest, and a measurement system, normally compose of a low pump power laser for the excitation and an optical detector (spectrometer). In these kind of devices, the fluctuation of a physical or chemical parameter is recorded as a variation of the optical response of the material. The main advantage of these systems against other similar devices, such as thermocouples or pH-meters is that do not require physical connections because the propagation of the electromagnetic radiation does not need any guiding system. The development of efficient detectors and low cost lasers that can be employed in these optical sensors implies in finding novel materials with extraordinary luminescence responses [3]. At this point, the use of materials doped with trivalent rare earth (RE^{3+}) results to be a good choice to obtain optically active materials because the RE^{3+} ions present thermally coupled emitting levels. This feature implies that the relative

* Corresponding author.
E-mail addresses: miguelandreshr@gmail.com, mhernanr@ull.edu.es (M.A. Hernández-Rodríguez).

http://dx.doi.org/10.1016/j.snb.2017.08.140
0925-4005/

ion population of these levels, and, of course, their emission, depend on the temperature of the active material [4]. In order to study the RE^{3+} emission response as a function of the temperature, several optical parameters can be calibrated, being the relative intensities between two thermalize emission bands, commonly known as the fluorescence intensity ratio (FIR) technique, the most widely employed procedure to calibrate an optical sensor [5,6]. From the point of view of practical applications, not all the RE^{3+} can be used to calibrate the optical response employing the FIR technique.

The general requirements that the RE^{3+} need to accomplish in order to use it for optical calibration are: i) the energy gap between the thermalized levels must be large enough in order to avoid overlapping of the two emission bands and simultaneously, short enough to allow the minimum population of optically active ions of the upper level in the temperature range of interest; ii) the radiative probabilities of the thermalized levels must be enough in order to show large emission intensities. Erbium trivalent ion is the most used for this task, although, other RE^{3+} ions can also accomplish the mentioned requirements with similar results, for instance, Pr^{3+}, Ho^{3+}, Nd^{3+}, Eu^{3+}, Tb^{3+} and Sm^{3+}, among others [3,7–13]. Concerning the Nd^{3+} based optical temperature sensors, the interest of this ion has grown exponentially due to its capabilities to absorb and emit in the in the well-known "near infrared biological windows" (*NIR-BW*) of human tissue, where the scattering of the light due to water and hemoglobin is almost negligible [14]. This feature leads to several applications in biological systems as cellular temperature probe, fluorescence bioimaging or anticancer therapies [5,15–22]. In the framework of optical sensor, the research on nanomaterials field has become relevant, mainly due to their ability of keeping the properties of their bulk counterpart [23]. Among all nanomaterials hosts, yttrium orthoaluminate nano-perovskite (YAP) can be good candidates due to its mechanical and thermal properties, as well as chemical stability [24]. Doping these nano-perovskites with Nd^{3+} ions is very interesting due to the sharpness nature of the emission peaks in the near infrared range, allowing to check with high resolution any changes of these peaks with the temperature (wavelength shifts, full width at half maximum,.). In this work, YAP doped with 1.0 mol% of Nd^{3+} (YAP: Nd^{3+} 1.0%) was studied in order to check its viability as temperature probe in the first and second biological window as well its application in the bioimaging field.

2. Experimental details

YAP nano-perovskite of composition $Y_{(1-x)}Nd_xAlO_3$, with x = 0.01 (in mol%) was successfully synthesized by the sol–gel method in an air atmosphere. Stoichiometric molar ratios of high-purity $Y(NO_3)_3$&903;$4H_2O$ (ALDRICH, 99.9%), $Al(NO_3)_3$&903;$9H_2O$ (ALDRICH, 99.9%) and $Nd(NO_3)_3$&903;H_2O (ALDRICH, 99.9%) materials were dissolved in 25 mL of 1 M HNO_3 under stirring at 353 K for 3 h. Afterwards citric acid, with a molar ratio of metal ions to citric acid of 1:2, was added to the solution, which was stirred and heated at 363 K until reaching the transparency of the solution. Then, 4 mg of polyethylene glycol was added to the solution. The former step created a gel that was fired at 400 °C for 6 h in order to remove the residual nitrates and organic compounds and the subsequently obtained powder sample was finally burnt out at 1200 °C for 20 h. The second thermal treatment was performed at 1550 °C for 12 h. The luminescence measurements from RT to 610 K were carried out in a tubular electric furnace where the samples were placed at the center of it and heated at a rate of 1.77 K/min. The temperature of the sample was controlled with a K-type thermocouple in contact with it and connected to a voltmeter (Fluke Calibrator 714). The 532 nm commercial laser excited the sample from one side of the furnace, while the emission was collimated by a lens located on the other exit side, and then focalized with another lens into an optical fiber coupled to a 0.3 m single grating spectrometer (Andor SR-500i-B2-R). Finally, the detection was carried on with a cooled CCD detector (Newton DU490A-1.7) with a resolution of 0.7 nm (~25 cm^{-1}) and an integration time of 1 s.

Powder X-ray diffraction data were collected on a PANalytical X'Pert PRO diffractometer (Bragg-Brentano geometry) with an X'Celerator detector employing the Cu $K\alpha_1$ radiation (λ = 1.5405 Å) in the angular range 5° < 2θ < 80°, by continuous scanning with a step size of 0.02° (see section S1 of Supplementary information). TEM measurements were performed in a JEOL JEM 2100 equipment operanting at 200 kV (see section S2 of Supplementary information). Dynamic light scattering (DLS) measurements were carried out on a Mastersizer 2000/E (see section S3 of Supplementary information).

For the temperature calibration procedure in the "second biological window" (II-*BW*) of the human tissue, the YAP: Nd^{3+} 1.0% nano-perovskite was heated by the same excitation laser at 532 nm increasing the pump power. Therefore, it was possible to change the temperature from RT up to 370 K. The emission associated with the $^4F_{3/2} \rightarrow {}^4I_{13/2}$ transition was collimated by a lens located on the other exit side, and then focalized with another lens into an optical fiber coupled to the same spectrometer (Andor SR-500i-B2-R) and the detection was carried on the same CCD detector (Newton DU490A-1.7) with the same resolution of 0.7 nm.

For the depth penetration studies, YAP: Nd^{3+} 1.0% nano-perovskite was excited at 895 nm, using the laser line of a Ti: sapphire laser (3900S Spectra Physics) pumped by Millenia Prime laser (Millenia 15sJSPG).

The emission associated with the $^4F_{3/2} \rightarrow {}^4I_{13/2}$ transition, was detected through a solution of Intralipid®, which is an intravenous nutrient consisting of an emulsion of phospholipid miceless and water [25], as phantom tissue. The phantom tissue consists in an absorbing and scattering medium that has been extensively employed in the past to mimic the optical properties of human skin in the I-*BW* and II-*BW* [26–29], as a function of the depth penetration was recorded by using the same grating spectrometer with a NIR extended photomultiplier (HAMATSU H10330B-75). The concentration of Intralipid® used in this experiment was the equivalent to 0.025 mol of it in a volume of solution of 24.85 mL.

3. Theoretical background

The main feature of the development of RE^{3+} doped matrix temperature is that these materials have many pairs of energy levels with very small separation gap, of the order of the thermal energy. The fluorescence intensity ratio (FIR) technique was employed in the first part of this work to calibrate the temperature sensor [30–32] in the well-known "first biological window" (I-*BW*) of the human tissue which covers the range between 750 and 950 nm. In the present technique, the fluorescence intensity of two nearby levels are recorded as a function of the temperature to be studied in a simple three-level scheme system (see Fig. 1). The small energy gap between these two thermalized levels allows the population of the upper level from the lower level by thermal excitation. The main point here is that the temperature dependent ratio of these intensities does not depend of the source power intensity because the emitted intensities only depend on the proportionality of the population of each level involved. This relative population between these levels, R, obeys the Boltzmann's law:

$$R = \frac{I_{31}}{I_{21}} = \frac{\omega_{31}^R g_3 h\nu_3}{\omega_{21}^R g_2 h\nu_2} \cdot e^{-\frac{E_{32}}{K_B T}} = Ce^{-\frac{E_{32}}{K_B T}} \quad (1)$$

where K_B is the Boltzmann constant, E_{32} is the energy gap between these two excited thermalized levels, g_3, g_2 are the degeneracies

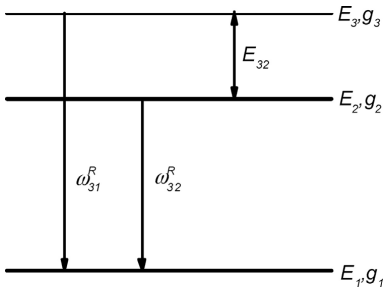

Fig. 1. Simplified diagram for three level system. E_{32} is the energy gap between the two excited levels, g_i is the degeneracy of the i-th level and ω_{ij}^R is the spontaneous emission rate between the *i*-th and *j*-*th* levels.

(2J + 1) of the levels, ω_{31}^R and ω_{21}^R are the spontaneous emission rates of the E_3 and E_2 levels to the E_1 level, respectively.

On the other hand, the sensor sensitivity S can be defined as the rate which the ratio R changes with the temperature:

$$S = \left|\frac{dR}{dT}\right| = R\left(\frac{E_{32}}{K_B T^2}\right) \quad (2)$$

However, it is necessary to introduce another parameter, the relative sensor sensitivity S_{REL} which is defined with the next relation:

$$S_{REL} = \frac{1}{R}\left|\frac{dR}{dT}\right| = \left(\frac{E_{32}}{K_B T^2}\right) \quad (3)$$

The advantage of this parameter is the independency with the emission intensity, it only depends on the temperature and the energy gap. This parameter allows the comparison with other optical sensors.

From the last equation, it is clear that if the energy gap between two thermalized levels is large, then the sensitivity too. Nevertheless, as the energy gap between these levels increases, the population and the intensity from the upper thermalized level decreases.

It is worth to mention that the use of the FIR technique for temperature sensing avoids accuracy problems resulting from fluctuations in the excitation, or absolute emission intensities due to the noise in the detection system.

The temperature uncertainty, δT, is the smallest temperature change that can be achieved in a given measurement and can be estimated by the equation [33]:

$$\delta T = \frac{1}{S_{REL}}\frac{\delta R}{R} \quad (4)$$

where S_{REL} is the relative sensitivity and the $\delta R/R$ is the relative uncertainty on R.

4. Results and discussion

4.1. Optical sensor calibration

The YAP: Nd^{3+} 1.0% nano-perovskite emission spectra as functions of the temperature are depicted in Fig. 2. It can be observed that at RT only two emission bands and their corresponding Stark levels associated to the $(^2H_{9/2}, {}^4F_{5/2}) \rightarrow {}^4I_{9/2}$ and $^4F_{3/2} \rightarrow {}^4I_{9/2}$ transitions are observed up to approximately 610 K. It can also be observed that the emission associated with the $(^2H_{9/2}, {}^4F_{5/2}) \rightarrow {}^4I_{9/2}$ transition increases as the temperature does. On the other hand, above 450 K, a third emission band related to the

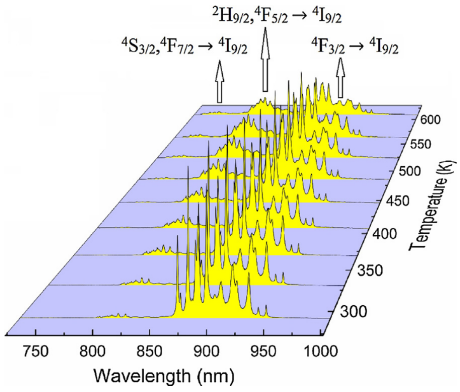

Fig. 2. Temperature evolution of the NIR emissions of the YAP: Nd^{3+} 1.0% nano-perovskite.

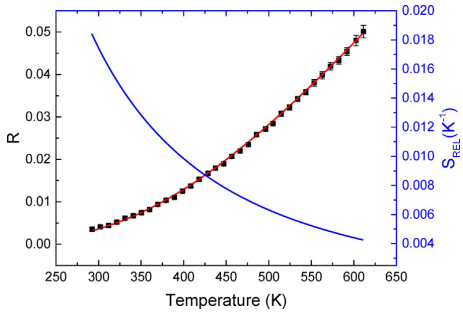

Fig. 3. Experimental intensity ratio (R) and relative sensitivity (S_{REL}) of the YAP: Nd^{3+} 1.0% nano-perovskite obtained from the emission bands associated to the $(^2H_{9/2}, {}^4F_{5/2}) \rightarrow {}^4I_{9/2}$ and $^4F_{3/2} \rightarrow {}^4I_{9/2}$ transitions. The experimental values were fitted to Eq. (1) (red line). (For interpretation of the references to colour in this figure legend, the reader is referred to the web version of this article.)

$(^4S_{3/2}, {}^4F_{7/2}) \rightarrow {}^4I_{9/2}$ transition slightly appears as a consequence of the thermally induced population of the upper $(^4S_{3/2}, {}^4F_{7/2})$ levels.

In Fig. 3 the experimental ratio obtained from the emission bands are shown. An analysis based on a simple three-level system formed by the $^2H_{9/2}$,$^4F_{5/2}$ (level 3), $^4F_{3/2}$ (level 2) and $^4I_{9/2}$ (level 1) was performed. The ratio between the intensities of the areas at 820 nm $(^2H_{9/2}, {}^4F_{5/2} \rightarrow {}^4I_{9/2})$ and 890 nm $(^4F_{3/2} \rightarrow {}^4I_{9/2})$ can be related to the temperature T according to Eq. (1). From the fitting process, the values of $C = 0.65$ and the experimental energy gap $E_{32} = 1101\ cm^{-1}$ have been determined. With this value of energy gap, the relative sensor sensitivity S_{REL} can be estimated according to Eq. (3).

The relative sensor sensitivity S_{REL} as a function of the temperature T, defined by Eq. (3) is also shown in Fig. 3.

In Table 1 the obtained sensitivity at 293 K is compared with others Nd-based temperature optical sensors working in the I-*BW*. As can be observed, YAP: Nd^{3+} 1.0% nano-perovskite under study shows a sensitivity of one order of magnitude higher than those optical thermal sensors where the ratio parameter is based on the intensity ratio between emission bands associated to $^4F_{3/2(1)} \rightarrow {}^4I_{9/2}$ and $^4F_{3/2(2)} \rightarrow {}^4I_{9/2}$ transitions (where $^4F_{3/2(1)}$ and $^4F_{3/2(2)}$ are the Stark components of the $^4F_{3/2}$ multiplet) and thus, due to the small energy gap between these levels, leading to

Table 1
Thermal relative sensitivity at 293 K of different host materials doped with Nd^{3+}. FIR fit equations and relative sensibilities as well as the temperature ranges.

Host material	FIR equation	Transition	Temperature range (K)	S_{REL} ($\times 10^{-3}$ K^{-1}) at 293 K	Ref.
Fluoroindogallate glass: Nd^{3+}	$267{\cdot}\exp(-1808/K_BT)-0.018$	$^4F_{7/2}$, $^4F_{3/2} \rightarrow {}^4I_{9/2}$	288–323	30	[34]
YAP: Nd^{3+} nanocrystal	$0.65{\cdot}\exp(-1101/K_BT)$	$^2H_{9/2}$,$^4F_{5/2}$; $^4F_{3/2} \rightarrow {}^4I_{9/2}$	293–611	18.3	This work
$(Gd_{0.991}Nd_{0.009})_2O_3$	$4.36{\cdot}\exp(-1092/K_BT)$[a]	$^2H_{9/2}$,$^4F_{5/2}$; $^4F_{3/2} \rightarrow {}^4I_{9/2}$	288–328	18.2	[36]
YVO_4: Nd^{3+} crystal	$3.46{\cdot}\exp(-967/K_BT)+1.30\times10^{-3}$	$^2H_{9/2}$,$^4F_{5/2}$; $^4F_{3/2} \rightarrow {}^4I_{9/2}$	299–523	16.1	[37]
Telluride glass: Nd^{3+}	$3.82{\cdot}\exp(-963.60/K_BT)$	$^2H_{9/2}$,$^4F_{5/2}$; $^4F_{3/2} \rightarrow {}^4I_{9/2}$	293–673	16	[31]
PKBAN: Nd^{3+}	$2.50{\cdot}\exp(-953.10/K_BT)$	$^2H_{9/2}$,$^4F_{5/2}$; $^4F_{3/2} \rightarrow {}^4I_{9/2}$	300–850	15.8	[38]
Fluoroindogallate glass: Nd^{3+}	$125{\cdot}\exp(-933/K_BT)-0.42$	$^2H_{9/2}$,$^4F_{5/2}$; $^4F_{3/2} \rightarrow {}^4I_{9/2}$	288–323	15.5	[34]
Fluorotellurite glass: Nd^{3+}	$2.67{\cdot}\exp(-906/K_BT)$	$^2H_{9/2}$,$^4F_{5/2}$; $^4F_{3/2} \rightarrow {}^4I_{9/2}$	300–650	15.1	[39]
ZBLANP: Nd^{3+}	$0.036{\cdot}\exp(689.30/K_BT)$	$^4F_{3/2(1)}$; $^4F_{3/2(2)} \rightarrow {}^4I_{9/2}$	296–473	11.5	[37]
$LiNdP_4O_{12}$ nanocrystal	$4.6{\cdot}\exp(-151/K_BT)$[a]	$^4F_{3/2(1)}$; $^4F_{3/2(2)} \rightarrow {}^4I_{9/2}$	250–500	2.5	[22]
$NaYF_4$: Nd^{3+} nanocrystal	$1.32{\cdot}\exp(-88.9/K_BT)$	$^4F_{3/2(1)}$; $^4F_{3/2(2)} \rightarrow {}^4I_{9/2}$	273–423	1.15	[32]
YAG: Nd^{3+} nanocrystal	$1.16{\cdot}\exp(-77.4/K_BT)$[a]	$^4F_{3/2(1)}$; $^4F_{3/2(2)} \rightarrow {}^4I_{9/2}$	283–343	1.3	[40]
LaF_3: Nd^{3+} nanoparticle	$0.71{\cdot}\exp(-64/K_BT)$[a]	$^4F_{3/2(1)}$; $^4F_{3/2(2)} \rightarrow {}^4I_{9/2}$	283–333	1.06	[16]

[a] FIR equations have been calculated by using the experimental results.

very low relative sensitivity values (see Eq. (3)). On the other hand, among the Nd-based optical sensors which use the intensity ratio between the emission bands related to $^2H_{9/2}$,$^4F_{5/2} \rightarrow {}^4I_{9/2}$ and $^4F_{3/2} \rightarrow {}^4I_{9/2}$ transitions, it is expected a sensitivity in the same order of magnitude, because the energy gap between the $^2H_{9/2}$,$^4F_{5/2}$ and $^4F_{3/2}$ levels are comparable. However, YAP: Nd^{3+} 1.0% shows the highest relative sensitivity value at 293 K.

Nonetheless, fluoroindogallate glass doped with Nd^{3+} reported by Nunes et al. [34] results to be notably higher because the intensity ratio was calculated, considering the $^4F_{7/2}$ and $^4F_{3/2}$ levels, which show a larger energy gap. Apart from the data included in Table 1, Marciniak et al. [35] reported the highest sensitivity so far in Cr^{3+}/Nd^{3+}-codoped YAG nanocrystals working in the I-*BW*, around of 0.035 K^{-1} in the biophysical range.

In spite of this, the YAP: Nd^{3+} 1.0% nano-perovskite under study shows a comparable sensitivity value with a minimum temperature uncertainty δT around of 0.9 K (see Fig. S4a of the Supplementary information for more details), can be considered potentially suitable to become a NIR luminescence material for optical temperature sensor based on the FIR technique, working in the I-*BW* of the human tissue.

The YAP: Nd^{3+} 1.0% nano-perovskite also exhibits an emission band and its corresponding Stark levels about 1350 nm associated with the $^4F_{3/2} \rightarrow {}^4I_{13/2}$ transition, which falls in the "second biological window" (II-*BW*) ranging from 980 nm up to 1500 nm. It is known that in the II-*BW* the optical scattering due to the absorption of water and other compounds present in tissues (such as hemoglobin) is further decreased when is compared to the I-*BW*, due to the use of longer wavelengths. At this point, the YAP: Nd^{3+} 1.0% nano-perovskite can be employed and calibrated with the temperature as an optical thermal sensor in this range as well.

The emission spectrum obtained exciting at 532 nm of the YAP: Nd^{3+} 1.0% nano-perovskite associated with the $^4F_{3/2} \rightarrow {}^4I_{13/2}$ transition at RT is shown in Fig. 4. The sharpness of the transition between Stark levels of the emission band, due to the nano-crystalline nature of the sample, allows to check with high resolution any change of these peaks with the temperature. In this sense, the Full Width at Half Maximum (*FHWM*) of the Stark peak at 1348 nm has been analyzed. Therefore, the temperature evolution of the Stark peak centered at 1348 nm from RT up to 370 K is also shown in the inset of Fig. 4.

Consequently, it is possible to use the *FHWM* as a parameter for the temperature calibration of the YAP: Nd^{3+} 1.0% nano-perovskite as an optical thermal sensor within the II-*BW* range.

The experimental data of the *FHWM* of the emission peak centered at 1348 nm as a function of the temperature starting at RT up to 370 K for its employment for the calibration procedure in the II-*BW* range is depicted in Fig. 5. In this case, the experimental data of the *FHWM* were well-fitted with a second order polynomial

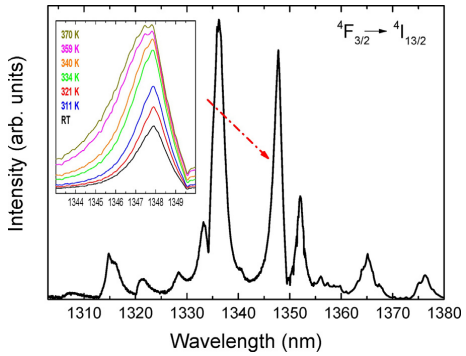

Fig. 4. YAP: Nd^{3+} 1.0% nano-perovskite emission spectrum associated with the $Nd^{3+4}F_{3/2} \rightarrow {}^4I_{13/2}$ transition at RT exciting at 532 nm. The temperature evolution of the Stark peak centered at 1348 nm starting at RT up to 370 K is also shown in an inset of the same figure.

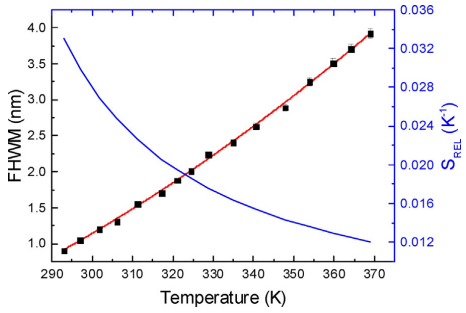

Fig. 5. Experimental data of the *FHWM* and relative sensitivity S_{REL} of the emission peak centered at 1348 nm of the YAP: Nd^{3+} 1.0% for the $^4F_{3/2} \rightarrow {}^4I_{13/2}$ transition. The experimental values were fitted. to a second order polynomial function given in Eq. (5) (red line). (For interpretation of the references to colour in this figure legend, the reader is referred to the web version of this article.)

function:

$$FHWM(T) = a + bT + cT^2 \quad (5)$$

where a, b and c are constants. From the fitting process, the values of $a = 0.73$ nm, $b = -0.03$ nm K^{-1} and $c = 1.05{*}10^{-4}$ nm K^{-2} have been obtained. The relative sensitivity S_{REL} of YAP: Nd^{3+} 1.0% sample was

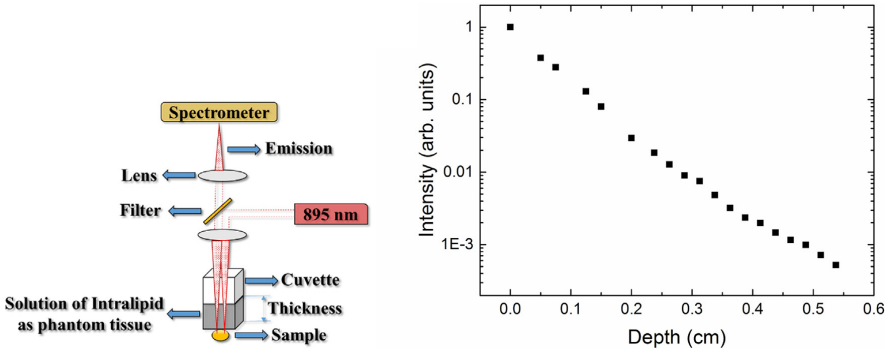

Fig. 6. Schematic diagram showing the experimental procedure to determine the penetration depth of YAP: Nd^{3+} 1.0% nano-perovskite (left). Sub-tissue luminescence intensity as a function of the phantom tissue thickness as obtained for the emission of Nd^{3+} associated with $^4F_{3/2} \rightarrow {}^4I_{13/2}$ of YAP: Nd^{3+} 1.0% nano-perovskite in semilogarithm scale (right).

determined by using the expression:

$$S_{REL} = \frac{1}{FHWM} \left| \frac{dFHWM}{dT} \right| \quad (6)$$

At the temperature of RT, the relative sensitivity of YAP: Nd^{3+} 1.0% nano-perovskite reached a value of 0.033 K^{-1}, which is almost twice larger than the obtained one within I-*BW*. The minimum temperature uncertainty δT achieved was around of 0.37 K (see Fig. S4b of the Supplementary information for more details).

In comparison with other Nd-based optical temperature sensors working in the II-*BW*, YAP: Nd^{3+} 1.0% shows a very high sensitivity, which is higher than the those ones reported in the literature, for instance, $NaGdF_4$: Nd^{3+}+PbS/CdS/ZnS@PLGA complex nanothermometer, which contains two different luminescence centers (RE^{3+} quantum dot) with a thermal sensitivity around of 0.016 K^{-1} at 293 K [18] or YVO_4: Nd^{3+} nanoparticle with a thermal sensitivity of 0.0025 K^{-1} in the biophysical range [19].

4.2. Sub-tissue penetration depth study

In order to check the viability of YAP: Nd^{3+} 1.0% nano-perovskite in biological experiments, a vertical setup has been made in order to excite the sample in similar way that experiments found in the literature [15,16]. The experiment was carried out, by using a liquid known as Intralipid dissolved at 10% as a phantom tissue. The experimental setup for the determination of the tissue penetration depth of the YAP: Nd^{3+} 1.0% is shown in Fig. 6 (left). Briefly, the YAP: Nd^{3+} 1.0% was placed into a holder which was located under a 1 mm size cuvette filled with a solution of Intralipid 10% (phantom tissue). The sample was optically excited with a continuous laser source at around 895 nm. Part of this laser was reflected to the sample by a filter and then was focused on the sample. After that, the emission about 1350 nm of the sample passed through the former filter and then was focused on the spectrometer by a second lens. The phantom tissue thickness was varying just filling a specific volume of the cuvette with a solution of Intralipid. This setup allowed to measure the emission about 1350 nm associated with the Nd^{3+}: $^4F_{3/2} \rightarrow {}^4I_{13/2}$ transition as a function of the tissue thickness by simply filling the cuvette with a specific volume of the phantom tissue.

From data included in Fig. 6 (right), it can be observed a monotonous decrease of the emission signal with the tissue thickness, indicating that the emission is attenuated within the phantom tissue either by absorption and/or scattering processes. Nevertheless, from the penetration depths results, it is evident that the use of YAP: Nd^{3+} 1.0% nano-perovskite allows for penetration depths into in vitro human skin tissues close to 5.5 mm in the II-*BW*. The penetration depth reported here is in the same order of magnitude as that reached by using LaF_3 nanoparticles doped with Nd^{3+} within the II-*BW* [15,16].

These previous results, together with its high relative sensitivity in the II-*BW*, show the potential use of the YAP: Nd^{3+} 1.0% nano-perovskite for both subtissue luminescence imaging and luminescence-based thermal sensing in the second biological window.

5. Conclusions

The temperature dependency of the infrared luminescence of YAP: Nd^{+3} 1.0% nano-perovskite, was studied in order to check its viability as optical thermal sensor in the well-known "near infrared biological windows" (*NIR-BW*) of the human tissue. For this purpose, the analysis of the ($^2H_{9/2}$, $^4F_{5/2}$), $^4F_{3/2} \rightarrow {}^4I_{9/2}$ transitions from RT up to 610 K exciting at 532 nm and the emission intensity of the $^4F_{3/2} \rightarrow {}^4I_{13/2}$ transition from RT to 370 K for the I-*BW* and II-*BW* respectively, were measured and calibrated with the temperature. The optical sensor calibration procedure for the I-*BW* was done by employing the FIR technique, while the analysis of the *FWHM* of the Stark level centered at 1348 nm of the emission associated with the $^4F_{3/2} \rightarrow {}^4I_{13/2}$ transition was used for the calibration procedure in the II-*BW*. The maximum value of the relative sensitivity for the calibration procedure for the I-*BW* (0.018 K^{-1} at 293 K) was compared with others Nd-based optical sensors of the literature, showing a notable thermal sensitivity. It is worth mentioning that the relative sensitivity obtained in the II-*BW* at RT was almost twice as big as the obtained in the I-*BW* at the same temperature and also, resulted to be very high compared with others Nd-based optical thermal sensors working in the II-*BW*. Thus, both results suggest that YAP: Nd^{3+} 1.0% nano-perovskite could be a great candidate as optical thermal sensor in the biological windows in the biological temperature range (30–45 °C). Taking advantage of the emission of YAP: Nd^{3+} 1.0% nano-perovskite related to the $^4F_{3/2} \rightarrow {}^4I_{13/2}$ transition, which lies in the II-*BW*, sub-tissue penetration depth study through a phantom tissue was carried out, reaching a sub-tissue penetration depth of 5.5 mm. This result shows also the potential of the YAP: Nd^{3+} 1.0% nano-perovskite for its application in sub-tissue luminescence imaging.

Acknowledgements

This research was partially supported MINECO (MAT2013-46649-C4-4-P, MAT2015-71070-REDC, and MAT2016-75586-C4-4-P), and by the EU-FEDER. M.A. Hernández-Rodríguez thanks to MINECO for FPI grant (BES-2014-068666).

Appendix A. Supplementary data

Supplementary data associated with this article can be found, in the online version, at http://dx.doi.org/10.1016/j.snb.2017.08.140.

References

[1] L. Ferrari, L. Rovati, P. Fabbri, F. Pilati, Disposable fluorescence optical pH sensor for near neutral solutions, Sensors 13 (2013) 484–499, http://dx.doi.org/10.3390/s130100484.
[2] U.R. Rodrííguez-Mendoza, S.F. Leoín-Luis, J.E. Mun˜oz-Santiuste, D. Jaque, V. Laviín, Nd^{3+}-doped $Ca_3Ga_2Ge_3O_{12}$ garnet: a new optical pressure sensor, J. Appl. Phys. 113 (2013) 213517–213524, http://dx.doi.org/10.1063/1.4809217.
[3] V.K. Rai, Temperature sensors and optical sensors, Appl. Phys. B: Lasers Opt. 88 (2007) 297–303, http://dx.doi.org/10.1007/s00340-007-2717-4.
[4] V.K. Rai, S.B. Rai, Temperature sensing behaviour of the stark sublevels, Spectrochim. Acta Part A: Mol. Biomol. Spectrosc. 68 (2007) 1406–1409, http://dx.doi.org/10.1016/j.saa.2007.02.017.
[5] D. Jaque, F. Vetrone, Luminescence nanothermometry, Nanoscale 4 (2012) 4301–4326, http://dx.doi.org/10.1039/c2nr30764b.
[6] V.K. Rai, S.B. Rai, A comparative study of FIR and FL based temperature sensing schemes: an example of Pr^{3+}, Appl. Phys. B: Lasers Opt. 87 (2007) 323–325, http://dx.doi.org/10.1007/s00340-007-2592-z.
[7] V.K. Rai, D.K. Rai, S.B. Rai, Pr^{3+} doped lithium tellurite glass as a temperature sensor, Sens. Actuators A: Phys. 128 (2006) 14–17, http://dx.doi.org/10.1016/j.sna.2005.12.030.
[8] R. Dey, A. Kumari, A.K. Soni, V.K. Rai, $CaMoO_4$:Ho^{3+}-Yb^{3+}-Mg^{2+} upconverting phosphor for application in lighting devices and optical temperature sensing, Sens. Actuators B: Chem. 210 (2015) 581–588, http://dx.doi.org/10.1016/j.snb.2015.01.007.
[9] V.K. Rai, Sm^{3+} as a fluorescence lifetime temperature sensing, IEEE Sens. J. 7 (2007) 1110–1111, http://dx.doi.org/10.1109/JSEN.2007.897939.
[10] S.F. Leo, S. Gonza, I.R. Martı, Analysis of Er^{3+} and Ho^{3+} codoped fluoroindate glasses as wide range temperature sensor, Mater. Res. Bull. 46 (2011) 1051–1054, http://dx.doi.org/10.1016/j.materresbull.2011.03.010.
[11] S.F. León-Luis, U.R. Rodríguez-Mendoza, I.R. Martín, E. Lalla, V. Lavín, Effects of Er^{3+} concentration on thermal sensitivity in optical temperature fluorotellurite glass sensors, Sens. Actuators B: Chem. 176 (2013) 1167–1175, http://dx.doi.org/10.1016/j.snb.2012.09.067.
[12] X. Wang, X. Kong, Y. Yu, Y. Sun, H. Zhang, Effect of annealing on upconversion luminescence of ZnO:Er^{3+} nanocrystals and high thermal sensitivity, J. Phys. Chem. C 111 (2007) 15119–15124, http://dx.doi.org/10.1021/jp0686689.
[13] J. Rocha, C.D.S. Brites, L.D. Carlos, Lanthanide organic framework luminescent thermometers, Chem. A: Eur. J. 22 (2016) 14782–14795, http://dx.doi.org/10.1002/chem.201600860.
[14] A.M. Smith, M.C. Mancini, S. Nie, Bioimaging: second window for in vivo imaging, Nat. Nanotechnol. 4 (2009) 710–711, http://dx.doi.org/10.1038/nnano.2009.326.
[15] U. Rocha, K.U. Kumar, C. Jacinto, I. Villa, F. Sanz-Rodríguez, M. Del Carmen Iglesias De La Cruz, A. Juarranz, E. Carrasco, F.C.J.M. Van Veggel, E. Bovero, J.G. Solé, D. Jaque, Neodymium-doped LaF_3 nanoparticles for fluorescence bioimaging in the second biological window, Small 10 (2014) 1141–1154, http://dx.doi.org/10.1002/smll.201301716.
[16] U. Rocha, C. Jacinto Da Silva, W. Ferreira Silva, I. Guedes, A. Benayas, L. Martínez Maestro, M. Acosta Elias, E. Bovero, F.C.J.M. Van Veggel, J.A. García Solé, D. Jaque, Subtissue thermal sensing based on neodymium-doped LaF_3 nanoparticles, ACS Nano 7 (2013) 1188–1199, http://dx.doi.org/10.1021/nn304373q.
[17] U. Rocha, C. Jacinto, K.U. Kumar, F.J. López, D. Bravo, J.G. Solé, D. Jaque, Real-time deep-tissue thermal sensing with sub-degree resolution by thermally improved Nd^{3+}:LaF_3 multifunctional nanoparticles, J. Lumin. 175 (2016) 149–157, http://dx.doi.org/10.1016/j.jlumin.2016.02.034.
[18] E.N. Cerón, D.H. Ortgies, B. Del Rosal, F. Ren, A. Benayas, F. Vetrone, D. Ma, F. Sanz-Rodríguez, J.G. Solé, D. Jaque, E.M. Rodríguez, Hybrid nanostructures for high-Sensitivity luminescence nanothermometry in the second biological window, Adv. Mater. 27 (2015) 4781–4787, http://dx.doi.org/10.1002/adma.201501014.
[19] I.E. Kolesnikov, E.V. Golyeva, A.A. Kalinichev, M.A. Kurochkin, E. Lähderanta, Nd^{3+} single doped YVO_4 nanoparticles for sub-tissue heating and thermal sensing in the second biological window, Sens. Actuators B: Chem. 243 (2017) 338–345, http://dx.doi.org/10.1016/j.snb.2016.12.005.
[20] C. Wu, K. Mino, H. Akimoto, M. Kawabata, K. Nakamura, M. Ozaki, Y. Ohmiya, In vivo far-red luminescence imaging of a biomarker based on BRET from Cypridina bioluminescence to an organic dye, Proc. Natl. Acad. Sci. U. S. A. 106 (2009) 15599–15603, http://dx.doi.org/10.1073/pnas.0908594106.
[21] E.C. Ximendes, U. Rocha, B. del Rosal, A. Vaquero, F. Sanz-Rodríguez, L. Monge, F. Ren, F. Vetrone, D. Ma, J. García-Solé, C. Jacinto, D. Jaque, N. Fernández, In vivo ischemia detection by luminescent nanothermometers, Adv. Healthcare Mater. 6 (2017) 1–8, http://dx.doi.org/10.1002/adhm.201601195.
[22] L. Marciniak, K. Prorok, A. Bednarkiewicz, A. Kowalczyk, D. Hreniak, W. Strek, Water dispersible $LiNdP_4O_{12}$ nanocrystals: new multifunctional NIR–NIR luminescent materials for bio-applications, J. Lumin. 176 (2016) 144–148, http://dx.doi.org/10.1016/j.jlumin.2016.03.034.
[23] E. Roduner, Size matters: why nanomaterials are different, Chem. Soc. Rev. 35 (2006) 583–592, http://dx.doi.org/10.1039/b502142c.
[24] R. Moncorgé, B. Chambon, J.Y. Rivoire, N. Garnier, E. Descroix, P. Laporte, H. Guillet, S. Roy, J. Mareschal, D. Pelenc, J. Doury, P. Farge, Nd doped crystals for medical laser applications, Opt. Mater. 8 (1997) 109–119, http://dx.doi.org/10.1016/S0925-3467(97)00022-0.
[25] S. Flock, S.L. Jacques, S.T. Flock, S.L. Jacques, B.C. Wilson, Optical properties of Intralipid: a phantom medium for light propagation studies, Lasers Surg. Med. 12 (1992) 510–519, http://dx.doi.org/10.1002/lsm.1900120510.
[26] H.J. van Staveren, C.J. Moes, J. van Marie, S. a Prahl, M.J. van Gemert, Light scattering in Intralipid-10% in the wavelength range of 400–1100 nm, App. Opt. 30 (1991) 4507–4514, http://dx.doi.org/10.1364/AO.30.004507.
[27] S. Nagarajan, Y. Zhang, Upconversion fluorescent nanoparticles as a potential tool for in-depth imaging, Nanotechnology 22 (2011) 395101–395107, http://dx.doi.org/10.1088/0957-4484/22/39/395101.
[28] K. Welsher, S.P. Sherlock, H. Dai, Deep-tissue anatomical imaging of mice using carbon nanotube fluorophores in the second near-infrared window, Proc. Natl. Acad. Sci. U. S. A. 108 (2011) 8943–8948, http://dx.doi.org/10.1073/pnas.1014501108.
[29] V.M. Kodach, J. Kalkman, D.J. Faber, T.G. van Leeuwen, Quantitative comparison of the OCT imaging depthat 1300 nm and 1600 nm, Biomed. Opt. Express 1 (2010) 176–185, http://dx.doi.org/10.1364/BOE.1.000176.
[30] P. Haro-González, I.R. Martín, L.L. Martín, S.F. León-Luis, C. Pérez-Rodríguez, V. Lavín, Characterization of Er^{3+} and Nd^{3+} doped Strontium Barium Niobate glass ceramic as temperature sensors, Opt. Mater. 33 (2011) 742–745, http://dx.doi.org/10.1016/j.optmat.2010.11.026.
[31] M. Sobczyk, Temperature-dependent luminescence and temperature-stimulated NIR-to-VIS up-conversion in Nd^{3+}-doped La_2O_3-Na_2O-ZnO-TeO_2 glasses, J. Quant. Spectrosc. Radiat. Transf. 119 (2013) 128–136, http://dx.doi.org/10.1016/j.jqsrt.2012.12.025.
[32] D. Wawrzynczyk, A. Bednarkiewicz, M. Nyk, W. Strek, M. Samoc, Neodymium(iii) doped fluoride nanoparticles as non-contact optical temperature sensors, Nanoscale 4 (2012) 6959–6961, http://dx.doi.org/10.1039/c2nr32203j.
[33] C.D.S. Brites, A. Milla, Lanthanides in luminescent thermometry, Handb. Phys. Chem. Rare Earth 49 (2016) 339–427, http://dx.doi.org/10.1016/bs.hpcre.2016.03.005.
[34] L.A.O. Nunes, A.S. Souza, L.D. Carlos, O.L. Malta, Neodymium doped fluoroindogallate glasses as highly-sensitive luminescent non-contact thermometers, Opt. Mater. 63 (2017) 42–45, http://dx.doi.org/10.1016/j.optmat.2016.08.038.
[35] L. Marciniak, A. Bednarkiewicz, J. Drabik, K. Trejgis, W. Strek, Optimization of highly sensitive YAG:Cr^{3+}, Nd^{3+} nanocrystal-based luminescent thermometer operating in an optical window of biological tissues, Phys. Chem. Chem. Phys. 19 (2017) 7343–7351, http://dx.doi.org/10.1039/C6CP07213E.
[36] S. Balabhadra, M.L. Debasu, C.D.S. Brites, L.A.O. Nunes, O.L. Malta, J. Rocha, M. Bettinelli, L.D. Carlos, Boosting the sensitivity of Nd^{3+}—based luminescent nanothermometers, Nanoscale 7 (2015) 17261–17267, http://dx.doi.org/10.1039/C5NR05631D.
[37] S.A. Wade, S.F. Collins, G.W. Baxter, Fluorescence intensity ratio technique for optical fiber point temperature sensing, J. Appl. Phys. 94 (2003) 4743–4756, http://dx.doi.org/10.1063/1.1606526.
[38] C. Pérez-Rodríguez, L.L. Martín, S.F. León-Luis, I.R. Martín, K.K. Kumar, C.K. Jayasankar, Relevance of radiative transfer processes on Nd^{3+} doped phosphate glasses for temperature sensing by means of the fluorescence intensity ratio technique, Sens. Actuators B: Chem. 195 (2014) 324–331, http://dx.doi.org/10.1016/j.snb.2014.01.037.
[39] E.A. Lalla, S.F. León-Luis, V. Monteseguro, C. Pérez-Rodríguez, J.M. Cáceres, V. Lavín, U.R. Rodríguez-Mendoza, Optical temperature sensor based on the Nd^{3+} infrared thermalized emissions in a fluorotellurite glass, J. Lumin. 166 (2015) 209–214, http://dx.doi.org/10.1016/j.jlumin.2015.05.029.
[40] A. Benayas, B. Del Rosal, A. Pérez-Delgado, K. Santacruz-Gómez, D. Jaque, G.A. Hirata, F. Vetrone, Nd:YAG near-infrared luminescent nanothermometers, Adv. Opt. Mater. 3 (2015) 687–694, http://dx.doi.org/10.1002/adom.201400484.

Biographies

Miguel A. Hernández-Rodríguez received the M.Sc. degree in 2012 at the La Laguna University (Spain). Currently, he is a Ph.D at La Laguna University. He joined the Laser Spectroscopy and High Pressure group in 2015 and has worked on optical materials. He also belongs to The MALTA Project (www.malta-consolider.com) that includes more than 70 scientists from 12 Spanish research groups dedicated to the study of diverse high pressure phenomena under a variety of different perspectives. His research interests cover the optical spectroscopy of nanomaterials doped with lanthanide ions at ambient and extreme conditions of pressure and temperature.

Antonio D. Lozano-Gorrín has been a researcher at University of La Laguna and other important institutions for the last two decades. He received his PhD in Chemistry from University of La Laguna in 2003. Since 2014 he collaborates in the *Laser Spectroscopy and High Pressure Group*. A. D. Lozano-Gorrín is an expert in the synthesis and characterization of nanomaterials by X-ray and neutron diffraction. Furthermore, he is co-author of several publications in peer reviewed journals and has contributed to several international conferences. Besides, he is member of different scientific societies and institutions.

Inocencio R. Martín is Associate Professor at the Department of Physics at the University of La Laguna, Spain. He received a Ph.D. in 1996 from the University of La Laguna. He is a member of the Laser Spectroscopy and High Pressure group and the MALTA Project and his research interests cover the optical characterization of glasses, crystals and nanocrystalline glass-ceramics doped with optically active ions. He has over 150 publications in peer reviewed journals. Currently, he is involved in optical characterization of microspheres doped with rare-earth ions and their applications in sensors.

U. R. Rodriguez-Mendoza is a professor in the Department of Fundamental and Experimental Physics at University of La Laguna, Spain. He has received a PhD in 2000 from University of La Laguna. He is a component of the Laser Spectroscopy and High Pressure group which belongs to this University and his research interests cover optical characterization of glasses and crystals optically active in ambient and extreme conditions of pressure and temperature, which includes optical spectroscopy, X ray diffraction and Raman spectroscopy. He has the author of over 80 publications in refereed journals and conference proceedings.

Lavín is a professor in the Department of Fundamental and Experimental Physics at University of La Laguna, Spain. He has received a PhD in 2000 from University of La Laguna. He is a component of the Laser Spectroscopy and High Pressure group which belongs to this University and his research interests cover optical characterization of glasses and crystals optically active in ambient and extreme conditions of pressure and temperature, which includes optical spectroscopy, X ray diffraction and Raman spectroscopy. He has the author of over 100 publications in refereed journals and conference proceedings.

Supplementary information

COMPARISON OF THE SENSITIVITY AS OPTICAL TEMPERATURE SENSOR OF NANO-PEROVSKITE DOPED WITH Nd^{3+} IONS IN THE FIRST AND SECOND BIOLOGICAL WINDOWS

M.A. Hernández-Rodríguez,[a] A.D. Lozano-Gorrín,[a] I.R. Martín,[a,b,d] Ulises R. Rodríguez-Mendoza [a,b,d] and V. Lavín [a,b,c]

[a] Departamento de Física, Universidad de La Laguna, E-38200 San Cristóbal de La Laguna, Santa Cruz de Tenerife, Spain.

[b] MALTA Consolider Team, Universidad de La Laguna, E-38200 San Cristóbal de La Laguna, Santa Cruz de Tenerife, Spain

[c] Instituto Universitario de Estudios avanzados en Atómica, Molecular y Fotónica (IUdEA), Universidad de La Laguna, E-38200 San Cristóbal de La Laguna, Santa Cruz de Tenerife, Spain.

[d] Instituto Universitario de Materiales y Nanotecnología (IMN), Universidad de La Laguna, E-38200 San Cristóbal de La Laguna, Santa Cruz de Tenerife, Spain.

Content:

SECTION S1

X-ray diffraction (XRD) patterns were measured on a diffractometer (PANalytical X′Pert Pro) using CuKα1 radiation. The diffraction pattern of the powder sample shows a predominant phase that has been well indexed to an orthorhombic space group Pnma perovskite-type structure as shown in Figure 1. We have recently published an article that gives all details concerning the mentioned structure fitting [1].

SECTION S2

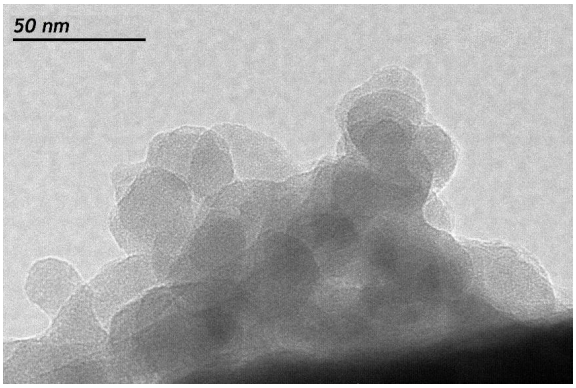

Figure S2. TEM picture of the YAP: Nd^{3+} 1.0% nano-perovskite

SECTION S3

Dynamic light scattering (DLS) experiments were performed on a Mastersizer 2000/E in order to obtain the conglomerated particle size distribution of the sample, as can be seen in Figure S3. After a couple of minutes under sonication, we were able to decrease the size of the conglomerates significantly (see inset in Figure S3)

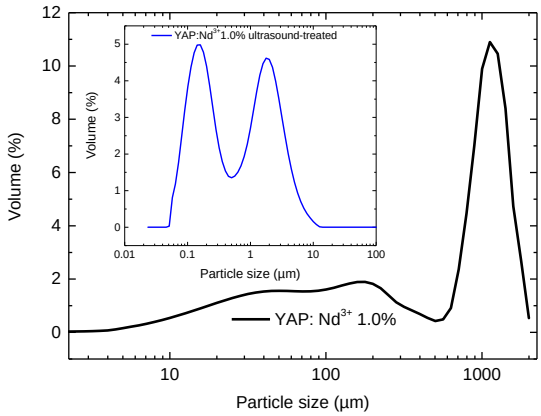

Figure S3. YAP: Nd^{3+} 1.0% DLS scattering spectra performed before and after (inset) sonication.

SECTION S4

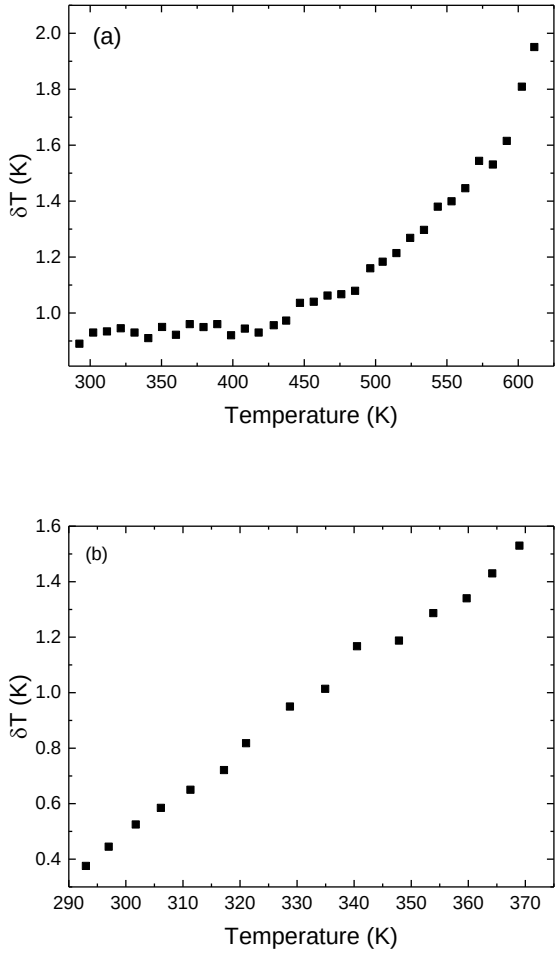

Figure S4. Temperature uncertainty δT as a function of the temperature obtained in (a) I-*BW* and (b) II-*BW* temperature calibration procedures of YAP: Nd^{3+} 1.0% respectively.

SECTION S5

References

[1] M.A. Hernández-Rodríguez, A.D. Lozano-Gorrín, I.R. Martín, U.R. Rodríguez-Mendoza, V. Lavín, Spectroscopic properties of Nd^{3+} ions in YAP nano-perovskites, J. Lumin. 188 (2017) 204–208. doi:10.1016/j.jlumin.2017.04.031.

4.2.2. Yttrium orthoaluminate nanoperovskite doped with Tm^{3+} ions as upconversion optical temperature sensor in the near-infrared region

Authors: **M.A. Hernández-Rodríguez**, A.D. Lozano-Gorrín, V. Lavín, U.R. Rodríguez-Mendoza and I.R. Martín

Published in: **Optics Express;** Volume: **25;** Pages: **27845-27856;** DOI: 10.1364/OE.25.027845; Accepted **18 July 2017**

In the present article, the thermal sensing properties of a $YAlO_3$ nano-perovskite doped with 2.5 mol % of Tm^{3+} ions (YAP: Tm^{3+}) were studied.

The first part of this work consisted in a briefly structural characterization of YAP: Tm^{3+} nano-perovskite with its corresponding XRD study, confirming the perovskite-type structure with an orthorhombic space group, *Pnma* (see Fig. 2 of this article). In addition, TEM image of YAP: Tm^{3+} was taken, showing a homogeneous and reduced size of the crystallites at a 20 nm scale, as is shown in the Fig. 3 of the manuscript. In order to complete the structural characterization, dynamic light scattering (DLS) measurements were also performed (see Fig. 4).

The second part of this work was focused on the temperature calibration of YAP: Tm^{3+} nano-perovskite from room temperature (RT) up to 425 K (152 ºC) by using the fluorescence intensity ratio technique (FIR) in the NIR. For this porpuse, the sample was placed in a tubular furnace and excited at 1210 nm OPO laser, monitoring the upconverted emission bands around 700 and 800 nm associated to the $^3F_{2,3}\rightarrow{}^3H_6$ and $^3H_4\rightarrow{}^3H_6$ transitions respectively, as it is shown in the Fig. 5 of this article. Just the emission band, around 800 nm associated to the $^3H_4\rightarrow{}^3H_6$ transition at RT was observed. As the temperature increased, the emission band at 700 nm related to the $^3F_{2,3}\rightarrow{}^3H_6$ transition started to show up due to thermally-induced population of the $^3F_{2,3}$ multiplets from the $^3H_4$ lower emitting level. The emission associated to the $^3H_4\rightarrow{}^3H_6$ transition also increased with temperature due to cross-relaxation processes between Tm^{3+} ions, which favored the population of the $^3F_{2,3}$ and $^3H_4$ states, suggesting that the upconversion process was enhanced with the increase of temperature (see Fig. 5). The experimental ratio, *R*, obtained directly from the integrated areas of the former upconverted emission bands, was analyzed as a function of the temperature from 324 to 425 K, and fitted to a Boltzmann-type curve, as it is shown in the Fig. 6 of the manuscript. The relative thermal

sensitivity, S_{REL}, obtained in this calibration procedure at 324 K (51 ºC) was around 0.0026 K^{-1} and was compared with the S_{REL} values of other optical temperature sensors doped with Ln^{3+} ions at the same temperature (see Table 2 of the article), showing the thermal sensing capabilities of YAP: Tm^{3+} nano-perovskite as optical temperature sensor based on the FIR technique, working in the I-*BW* and excited whitin II-*BW* with a high sensitivity.

Since the former calibration procedure was ineffective in the physiological range (293-333 K), i.e. ratio was close to zero, another calibration process of YAP: Tm^{3+} nano-perovskite was used, this time, considering the ratio of the maximum intensity of the Stark levels at 776.42 and 821.5 nm of the emission related to the $^3H_4 \rightarrow {}^3H_6$ transition from RT up to 325 K, as it is shown in the Fig. 8 of this work. The relative thermal sensitivity, S_{REL}, achieved in this calibration procedure at 294 K (21 ºC) was around 0.0013 K^{-1} and was compared with the S_{REL} values of other optical temperature sensors doped with Ln^{3+} ions at the same temperature (see Table 3 of the article), showing a great performance. It is worth mentioning that the former ratio in the physiological range showed a change around of 43% which is notably higher compared other Ln^{3+}-based optical sensors that have been tested as thermal probes for biological applications, whose ratios only changes around 4%. Futhermore, with these results and features, the viability of the YAP: Tm^{3+} nanoperovskite as optical temperature sensor working in the NIR and in the physiological ranges is evidenced and its application in biological systems could be considered.

Research Article | Vol. 25, No. 22 | 30 Oct 2017 | OPTICS EXPRESS 27845

Optics EXPRESS

Yttrium orthoaluminate nanoperovskite doped with Tm^{3+} ions as upconversion optical temperature sensor in the near-infrared region

M. A. Hernández-Rodriguez,* A. D. Lozano-Gorrín, V. Lavín, U. R. Rodríguez-Mendoza, and I. R. Martín

Departamento de Fisica, MALTA Consolider Team, IUdEA and IMN, Universidad de La Laguna, Apdo. 456, E-38200 San Cristóbal de La Laguna, Santa Cruz de Tenerife, Spain
**miguelandreshr@gmail.com*

Abstract: The thermal sensing capability of the Tm^{3+}-doped yttrium orthoaluminate nanoperovskite in the infrared range, synthetized by a sol-gel method, was studied. The temperature dependence of the infrared upconverted emission bands located at around 705 nm ($^3F_{2,3}\rightarrow{}^3H_6$) and 800 nm ($^3H_4\rightarrow{}^3H_6$) of YAP: Tm^{3+} nanoperovskite under excitation at 1210 nm was analyzed from RT up to 425 K. Calibration of the optical sensor has been made using the fluorescence intensity ratio technique, showing a high sensitivity in the near-infrared compared to other trivalent rare-earth based optical sensors working in the same range. In addition, a second calibration procedure of the YAP: Tm^{3+} optical sensor was performed by using the FIR technique on the emission band associated to the $^3H_4\rightarrow{}^3H_6$ transition in the physiological temperature range (293-333 K), showing a very high relative sensitivity compared with other rare-earth based optical temperature sensors working in the physiological range. Moreover, the main advantage compared with other optical sensors is that the excitation source and the upconverted emissions do not overlap, since they lie in different biological windows, thus allowing its potential use as an optical temperature probe in the near-infrared range for biological applications.

OCIS codes: (280.4788) Optical sensing and sensors; (190.0190) Nonlinear optics; (160.4236) Nanomaterials; (160.5690) Rare-earth-doped materials; (160.6840) Thermo-optical materials; (160.4670) Optical materials.

References and links

1. L. Ferrari, L. Rovati, P. Fabbri, and F. Pilati, "Disposable fluorescence optical pH sensor for near neutral solutions," Sensors (Basel) **13**(1), 484–499 (2012).
2. U. R. Rodríguez-Mendoza, S. F. León-Luis, J. E. Muñoz-Santiuste, D. Jaque, and V. Lavín, "Nd^{3+}-doped $Ca_3Ga_2Ge_3O_{12}$ garnet: A new optical pressure sensor," J. Appl. Phys. **113**(21), 213517 (2013).
3. V. K. Rai, "Temperature sensors and optical sensors," Appl. Phys. B Lasers Opt. **88**(2), 297–303 (2007).
4. V. K. Rai and S. B. Rai, "Temperature sensing behaviour of the stark sublevels," Spectrochim. Acta - Part A Mol. Biomol. Spectrosc. **68**(5), 1406–1409 (2007).
5. D. Jaque and F. Vetrone, "Luminescence nanothermometry," Nanoscale **4**(15), 4301–4326 (2012).
6. V. K. Rai and S. B. Rai, "A comparative study of FIR and FL based temperature sensing schemes: An example of Pr^{3+}," Appl. Phys. B Lasers Opt. **87**(2), 323–325 (2007).
7. E. Roduner, "Size matters: why nanomaterials are different," Chem. Soc. Rev. **35**(7), 583–592 (2006).
8. A. F. Pereira, K. U. Kumar, W. F. Silva, W. Q. Santos, D. Jaque, and C. Jacinto, "Yb^{3+}/Tm^{3+} co-doped $NaNbO_3$ nanocrystals as three-photon-excited luminescent nanothermometers," Sens. Actuators B Chem. **213**, 65–71 (2015).
9. V. Lojpur, M. Nikolic, L. Mancic, O. Milosevic, and M. D. Dramicanin, "Y_2O_3: Yb,Tm and Y_2O_3:Yb,Ho powders for low-temperature thermometry based on up-conversion fluorescence," Ceram. Int. **39**(2), 1129–1134 (2013).
10. S. Nagarajan and Y. Zhang, "Upconversion fluorescent nanoparticles as a potential tool for in-depth imaging," Nanotechnology **22**(39), 395101 (2011).
11. U. Rocha, K. U. Kumar, C. Jacinto, I. Villa, F. Sanz-Rodríguez, M. del Carmen Iglesias de la Cruz, A. Juarranz, E. Carrasco, F. C. J. M. van Veggel, E. Bovero, J. G. Solé, and D. Jaque, "Neodymium-doped LaF_3 nanoparticles for fluorescence bioimaging in the second biological window," Small **10**(6), 1141–1154 (2014).
12. U. Rocha, C. Jacinto da Silva, W. Ferreira Silva, I. Guedes, A. Benayas, L. Martínez Maestro, M. Acosta Elias, E. Bovero, F. C. J. M. van Veggel, J. A. García Solé, and D. Jaque, "Subtissue thermal sensing based on

#294691 https://doi.org/10.1364/OE.25.027845
Journal © 2017 Received 27 Apr 2017; revised 5 Jul 2017; accepted 18 Jul 2017; published 27 Oct 2017

neodymium-doped LaF_3 nanoparticles," ACS Nano **7**(2), 1188–1199 (2013).
13. A. Benayas, B. Del Rosal, A. Pérez-Delgado, K. Santacruz-Gómez, D. Jaque, G. A. Hirata, and F. Vetrone, "Nd:YAG Near-Infrared Luminescent Nanothermometers," Adv. Opt. Mater. **3**(5), 687–694 (2015).
14. R. Moncorgé, B. Chambon, J. Y. Rivoire, N. Garnier, E. Descroix, P. Laporte, H. Guillet, S. Roy, J. Mareschal, D. Pelenc, J. Doury, and P. Farge, "Nd doped crystals for medical laser applications," Opt. Mater. **8**(1-2), 109–119 (1997).
15. J. Rodríguez-Carvajal, ""Recent advances in magnetic structure determination by neutron powder diffraction," Phys. B Condens," Matter. **192**, 55–69 (1993).
16. A. M. Smith, M. C. Mancini, and S. Nie, "Bioimaging: second window for in vivo imaging," Nat. Nanotechnol. **4**(11), 710–711 (2009).
17. W. Xu, J. Chen, P. Wang, Z. Zhang, and W. Cao, "Intense red upconversion luminescence from Tm^{3+}/Yb^{3+} codoped transparent glass ceramic," Opt. Lett. **37**(2), 205–207 (2012).
18. L. Xing, Y. Xu, R. Wang, W. Xu, and Z. Zhang, "Highly sensitive optical thermometry based on upconversion emissions in Tm^{3+}/Yb^{3+} codoped $LiNbO_3$ single crystal," Opt. Lett. **39**(3), 454–457 (2014).
19. W. Xu, X. Gao, L. Zheng, Z. Zhang, and W. Cao, "An optical temperature sensor based on the upconversion luminescence from Tm^{3+}/Yb^{3+} codoped oxyfluoride glass ceramic," Sens. Actuators B Chem. **173**, 250–253 (2012).
20. X. Wang, J. Zheng, Y. Xuan, and X. Yan, "Optical temperature sensing of $NaYbF_4$: $Tm^{3+}@SiO_2$ core-shell micro-particles induced by infrared excitation," Opt. Express **21**(18), 21596–21606 (2013).
21. C. Pérez-Rodríguez, L. L. Martín, S. F. León-Luis, K. K. Martín, K. K. Kumar, and C. K. Jayasankar, "Relevance of radiative transfer processes on Nd3+ doped phosphate glasses for temperature sensing by means of the fluorescence intensity ratio technique," Sens. Actuators B Chem. **195**, 324–331 (2014).
22. M. Sobczyk, "Temperature-dependent luminescence and temperature-stimulated NIR-to-VIS up-conversion in Nd^{3+}-doped La_2O_3-Na_2O-ZnO-TeO_2 glasses," J. Quant. Spectrosc. Radiat. Transf. **119**, 128–136 (2013).
23. S. A. Wade, S. F. Collins, and G. W. Baxter, "Fluorescence intensity ratio technique for optical fiber point temperature sensing," J. Appl. Phys. **94**(8), 4743–4756 (2003).
24. N. Rakov and G. S. Maciel, "Nd^{3+}-Yb^{3+} doped powder for near-infrared optical temperature sensing," Opt. Lett. **39**(13), 3767–3769 (2014).
25. D. Wawrzynczyk, A. Bednarkiewicz, M. Nyk, W. Strek, and M. Samoc, "Neodymium(III) doped fluoride nanoparticles as non-contact optical temperature sensors," Nanoscale **4**(22), 6959–6961 (2012).
26. A. F. Pereira, J. F. Silva, A. S. Gouveia-Neto, and C. Jacinto, "1.319um excited thulium doped nanoparticles for subtissue thermal sensing with deep penetration and high contrast imaging," Sens. Actuators B Chem. **238**, 525–531 (2017).
27. N. N. Dong, M. Pedroni, F. Piccinelli, G. Conti, A. Sbarbati, J. E. Ramírez-Hernández, L. M. Maestro, M. C. Iglesias-de la Cruz, F. Sanz-Rodriguez, A. Juarranz, F. Chen, F. Vetrone, J. A. Capobianco, J. G. Solé, M. Bettinelli, D. Jaque, and A. Speghini, "NIR-to-NIR two-photon excited CaF_2:Tm^{3+},Yb^{3+} nanoparticles: multifunctional nanoprobes for highly penetrating fluorescence bio-imaging," ACS Nano **5**(11), 8665–8671 (2011).

1. Introduction

It is known that the optical properties of materials depend strongly on the environment conditions, e.g., temperature, pressure, etc [1,2]. Therefore, any changes in these parameters will lead to changes in the optical response of materials. Taking advantage of this behavior, a new researching issue is the development of optical sensors and thus, the searching for novel materials with extraordinary luminescence responses [3] that could be applied as probes that could monitor physical or chemical fluctuations of the environment with respect to their initial conditions.

The main idea of an optical sensor is to record any physical or chemical fluctuation of the environment as a variation of its optical properties. Among the materials that can be employed in the development of optical temperature sensors, those doped with trivalent rare-earth (RE^{3+}) ions turns out to be great candidates to obtain optically active materials, due to the extraordinary optical properties of RE^{3+}, having thermally coupled emitting levels (TCL). The relative population of these TCL depends on the environment temperature, and, therefore, so does their emission [4]. The study of the temperature evolution of the RE^{3+} emission response implies the use of several optical parameters as calibration tools, e.g., bandwidth, lifetime, band shift, etc. However, the relative intensities between the TCL, known as the fluorescence intensity ratio technique (FIR), is the most used procedure to calibrate an optical temperature sensor [5,6].

From the point of view of the optical sensors, the research on nanomaterials field has become a relevant issue, because these nano-materials present the ability of keeping the

properties of their bulk counterpart [7]. On the other hand, these materials, especially RE^{3+}-doped nano-materials, present enormous advantages compared to other materials such as organic dyes and quantum dots. First of all, the RE^{3+}-doped nano-materials can be synthetized through cheap methods that cannot be used in quantum-dots syntheses. Secondly, these materials present extraordinary chemical and photostability properties as well as good biocompatibility, and most importantly, low toxicity, which are very important for biological applications. It is possible to find several works focused on RE^{3+}-doped nano-materials as optical temperature sensors in the literature, for instance, Yb^{3+}/Tm^{3+}-based optical sensor, such as $NaNbO_3$:Yb^{3+}/Tm^{3+} nanocrystals [8] or Y_2O_3:Yb^{3+}/Tm^{3+} and Y_2O_3:Yb^{3+}/Ho^{3+} nanopowders [9]. In addition, Tm^{3+}/Yb^{3+} and Nd^{3+}-based optical sensors has been successfully used due to their potential employment in medical applications such as fluorescence bioimaging, cellular temperature probe or anticancer and photodynamic therapies, for example, $NaYF_4$:Tm^{3+}/Yb^{3+} [10], LaF_3:Nd^{3+} nanoparticles [11,12] or yttrium aluminum nano-garnets doped with Nd^{3+} ions (YAG:Nd^{3+}) [13].

Among the RE^{3+}-doped nano-materials, the yttrium orthoaluminate nanoperovskite (YAP) appear to be good candidates due to their mechanical and thermal properties, as well as chemical stability, such as their bulk counterpart [14]. Furthermore, combining the quantum-chemical properties of the YAP nanoperovskite with the optical properties of Tm^{3+} ions, which show absorption and emission bands that lie in the near-infrared (NIR), the viability of the orthoaluminate nanoperovskite doped with 2.5 mol% of Tm^{3+} ions as an optical temperature sensor in the NIR was analyzed.

2. Experimental details

Nano-crystalline YAP perovskite of composition $Y_{0.975}Tm_{0.025}AlO_3$ (YAP: Tm^{3+}) was successfully prepared by the Pechini citrate sol–gel method in an air atmosphere. Stoichiometric molar ratios of high-purity precursor salts of $Y(NO_3)_3{\cdot}4H_2O$ (ALDRICH, 99.9%), $Al(NO_3)_3{\cdot}9H_2O$ (ALDRICH, 99.9%) and $Tm(NO_3)_3{\cdot}5H_2O$ (ALDRICH, 99.9%) materials were mixed and dissolved in 25 ml of 1 M HNO_3 under stirring at 353 K for 3 h. Then citric acid, with a molar ratio of metal ions to citric acid of 1:2, was added to the solution, which was stirred and heated at 363 K until reaching the transparency of the solution. Afterwards, 4 mg of polyethylene glycol was added to the solution. This last step created a gel that was fired at 673 K for 6 h in order to remove the residual nitrates and organic compounds and the subsequently obtained powder sample was finally annealed out at 1473 K for 20 h. The second thermal treatment was performed at 1823 K for 12 h. The sample obtained by this synthesis method is chemically stable.

Powder X-ray diffraction data were collected on a PANalytical X'Pert PRO diffractometer (Bragg-Brentano geometry) with an X'Celerator detector employing the Cu $K\alpha_1$ radiation (λ=1.5405 Å) in the angular range $5° < 2\theta < 80°$, by continuous scanning with a step size of 0.02°. TEM measurements were performed in a JEOL JEM 2100 equipment operanting at 200 kV. Dynamic light scattering (DLS) measurements were carried out on a Mastersizer 2000/E.

Luminescence measurements from 294 K to 425 K were carried out in a tubular electric furnace (Gero RES-E 230/3) where the sample was placed at its center. Temperature of the sample was controlled with a type *K* thermocouple in contact with it and connected to a voltmeter (Fluke Calibrator 714). Upconverted emissions of YAP: Tm^{3+} nanoperovskite were measured by exciting at 1210 nm with a 10 ns pulsed optical parametric oscillator OPO (EKSPLA/NT342/3/UVE). Emissions were focused on the entrance slit of a spectrograph (Andor SR-303i-A) equipped with a cooled CCD (Andor Newton). All spectra were corrected from the spectral response of the equipment.

3. Fluorescence intensity ratio technique (FIR)

FIR seeks the determination of the temperature analyzing the changes in the band shape of RE^{3+} emissions. This technique studies the relative emission intensities of two nearby energy levels, close enough in energy to allow the thermal redistribution of the population from the lower level (E_2) to the upper one (E_3) (see Fig. 1). Therefore, the intensity ratio of these levels depends on the temperature T, but at the same time, this ratio is independent of the source power excitation, because the population of each level is proportional to the pump power used. Under low pump power excitation, the intensity ratio between the emitting E_2 and E_3 levels, R, is described by Boltzmann's law, given by:

$$R = \frac{I_{31}}{I_{21}} = \frac{\omega_{31}^R g_3 h\nu_3}{\omega_{21}^R g_2 h\nu_2} e^{\frac{-\Delta E}{k_B T}} = Ce^{\frac{-\Delta E}{k_B T}} \quad (1)$$

where k_B is the Boltzmann constant, $\Delta E = E_3 - E_2$ is the energy gap between E_3 and E_2 excited thermalized levels, g_3 and g_2 are the degeneracies $(2J+1)$ of the levels, and ω_{31}^R and ω_{21}^R are the spontaneous emission rates of the E_3 and E_2 levels to the ground level (E_1), respectively.

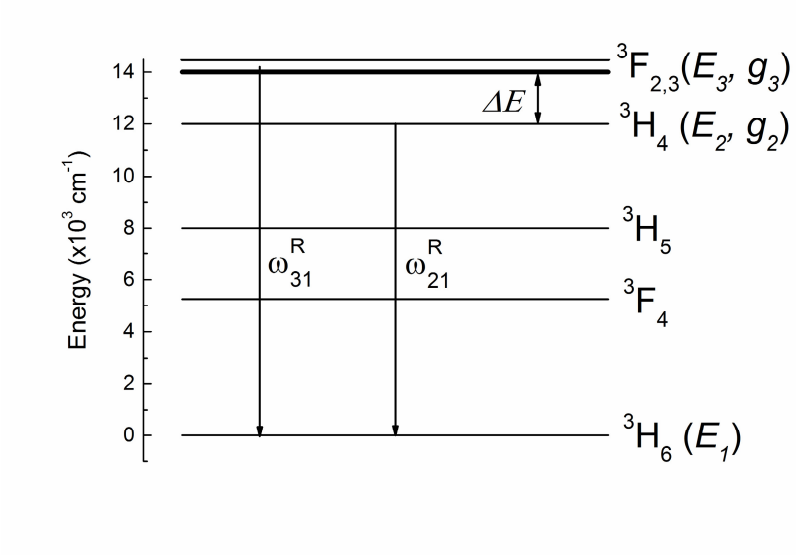

Fig. 1. Simplified diagram for three levels particularized to Tm^{3+} ion. ΔE is the energy gap between the two excited levels (E_2 and E_3), g_i is the degeneracy of the *i-th*-level and ω_{ij}^R is the spontaneous emission rate between the *i-th* and *j-th* levels.

The sensor sensitivity S can be defined as the rate at which R changes with temperature:

$$S = \left|\frac{dR}{dT}\right| = R\left(\frac{\Delta E}{k_B T^2}\right) \quad (2)$$

However, it is necessary to introduce another parameter, the relative sensor sensitivity S_{REL}, which is defined as follows:

$$S_{REL} = \frac{1}{R}\left|\frac{dR}{dT}\right| = \left(\frac{\Delta E}{k_B T^2}\right) \quad (3)$$

that only depends on the temperature. Hence, it allows the comparison with other optical temperature sensors.

From the last equation, it is clear that the larger the energy gap between two thermalized levels the larger the sensitivity. Nevertheless, as the energy gap between these levels increases, the population and the intensity from the upper thermalized level decreases.

4. Results and discussion

4.1 Structural characterization

The X-ray diffraction (XRD) pattern of YAP: Tm^{3+} is depicted in Fig. 2. It was indexed to an orthorhombic structure space group, *Pnma*. Hence, XRD confirms the perovskite-type structure of YAP: Tm^{3+}. The unit cell of the nanoperovskite is also shown in Fig. 2. The crystal structure parameters have been obtained from the fitting of the profile of the nanoperovskite by the Rietveld method using FULLPROF program [15] (see Table 1).

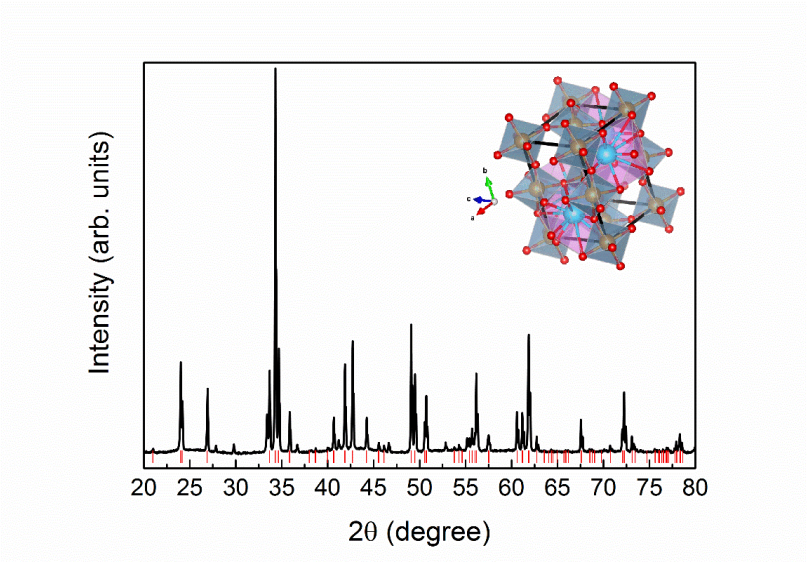

Fig. 2. XRD pattern of the YAP: Tm^{3+} nanoperovskite. The unit cell and the Bragg positions (red ticks) allowed for the space group *Pnma* are also depicted.

Table 1. Cell Parameters and Reliability Factors Obtained From Fitting of XRD Pattern for YAP: Tm^{3+}

a (Å)	*b* (Å)	*c* (Å)	V (Å^3)	χ^2	R_p	R_{wp}	R_{exp}
5.327(1)	7.368(1)	5.177(1)	203.2(1)	5.44	21.2	26.5	14.8

The average grains size, *D*, was determined from Scherrer formula:

$$D = \frac{0.89\lambda}{\beta \mathrm{Cos}\,\theta} \quad (4)$$

where λ= 1.5406 Å, β is the full width at half maximum of the peaks and θ is the angle of diffraction. The average grains size value was around 35 nm. No amorphous phase was detected in the nanoperovskite sample.

TEM image shows the homogenous and reduced size of the crystallites. Fig. 3 shows the size of such crystallites at a 20 nm scale.

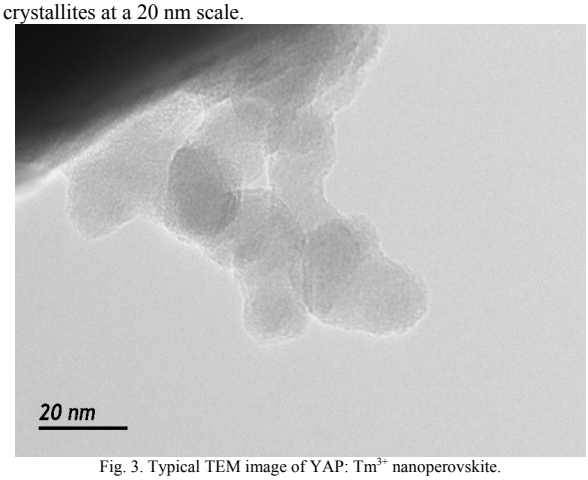

Fig. 3. Typical TEM image of YAP: Tm^{3+} nanoperovskite.

DLS measurements on the sample were carried out on a MASTERSIZER 2000E instrument and the conglomeration of most of the particles around 1 micrometer was observed (see Fig. 4). The sonication of it allowed the reduction of the conglomeration down to 0.1 micrometer.

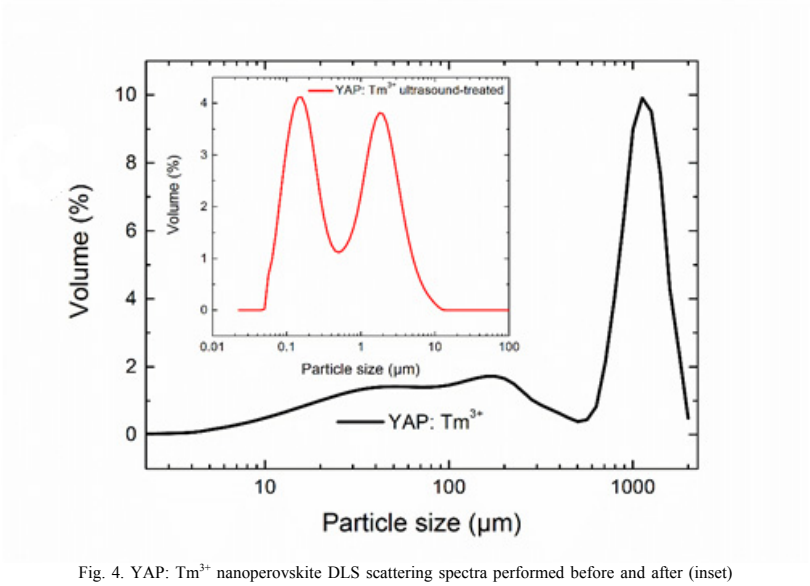

Fig. 4. YAP: Tm^{3+} nanoperovskite DLS scattering spectra performed before and after (inset) sonication.

4.2 Optical sensor calibration

Trivalent Thulium (Tm^{3+}) ion shows absorption and emission bands lying in the well-known "near-infrared biological windows" (*NIR-BW*). These biological windows are those infrared spectral regions in which the transmission of the light through the human skin is more effective, because in these regions the optical scattering due to the absorption of water and other compounds present in tissues (such as hemoglobin) is lower compared to other spectral regions, such as the visible one [16]. Commonly, *NIR-BW* is divided in two main regions, the first biological window (*I-BW*), which ranges between 650 and 950 nm, and the second window (*II-BW*) between 1000 and 1300 nm [16]. Thus, YAP: Tm^{3+} nanoparticles are analyzed in order to study their viability as optical temperature probes in the *I-BW* by exciting in the *II-BW*.

The upconverted emission spectra of the YAP: Tm^{3+} at room temperature (RT) up to 425 K exciting resonantly the $^3H_6 \rightarrow {}^3H_5$ transition at 1210 nm are shown in Fig. 5. Just one emission band and their corresponding Stark levels associated to the $^3H_4 \rightarrow {}^3H_6$ transition at RT are observed. When the temperature increases, the emission associated with the $^3F_{2,3} \rightarrow {}^3H_6$ transition starts to show up due to thermally-induced population of the $^3F_{2,3}$ multiplets from the $^3H_4$ lower emitting level. The emission associated to the $^3H_4 \rightarrow {}^3H_6$ transition also increases with temperature, suggesting that the upconversion process is favored with the increase of temperature. In addition, cross-relaxation processes between Tm^{3+} ions favor the population of the $^3F_{2,3}$ and $^3H_4$ states [17].

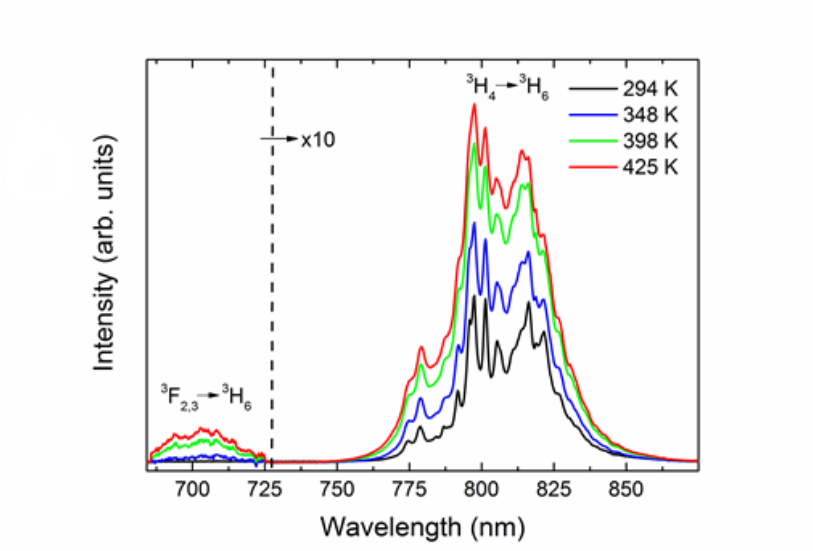

Fig. 5. Temperature evolution of upconversion emission spectra of YAP: Tm^{3+} nanoperovskite from 294 up to 425 K exciting at 1210 nm. Transitions are also indicated. Emission band associated to $^3F_{2,3} \rightarrow {}^3H_6$ has been magnified ten times for a better observation.

From the upconverted emission spectra, the experimental intensities were calculated by the integration of the emission bands associated with the $^3F_{2,3} \rightarrow {}^3H_6$ and $^3H_4 \rightarrow {}^3H_6$ transitions for the calibration procedure. The ratio of these areas, measured from 324 K up to 425 K, can be described by using Eq. (1). From the fitting procedure, the values of C=4.61 and the

energy gap ΔE=1926 cm^{-1} were obtained. The relative sensor sensitivity S_{REL} as a function of temperature T, defined by the Eq. (3), is also shown in Fig. 6. The relative sensitivity of this sensor reaches its maximum value of 0.026 K^{-1} at 324 K. According to this result, the calibration procedure of the YAP: Tm^{3+} optical sensor could be suitable for its employment in the *I-BW* exciting within the *II-BW* with a notable sensitivity.

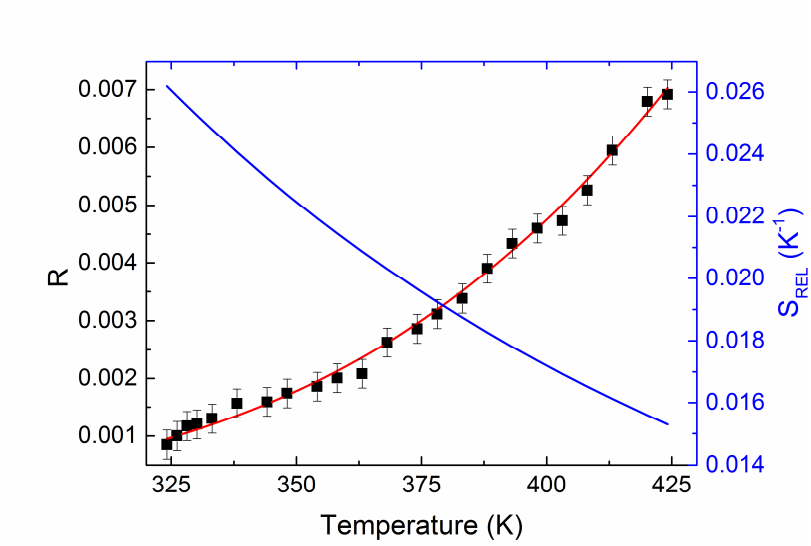

Fig. 6. Experimental intensity area ratio and relative sensitivity of the YAP: Tm^{3+} of $^3F_{2,3}\rightarrow{}^3H_6$ and $^3H_4\rightarrow{}^3H_6$ transitions obtained exciting at 1210 nm. The experimental values were fitted to a single exponential function. The fit curve (red line) of the experimental intensity ratio is also shown.

As can be observed (see Table 2), YAP: Tm^{3+} nanoperovskite shows a notably sensitivity value, which allows its consideration to become a NIR luminescence material for optical temperature sensor based on the FIR technique. Moreover, in YAP this result has been obtained exciting and detecting in different biological windows taking advantage of the non-linear upconversion processes of the Tm^{3+} ions, which means that the overlapping between excitation and emission is neglected.

Table 2. Thermal Relative Sensitivity Values of Different RE^{3+}-based Temperature Optical Sensors.

Optical sensor	FIR equation	λ range (nm)		Temperature range (K)	λ_{Exc} (nm)	S_{REL} (x10^{-3} K^{-1}) at 324 K	Ref.
		Upper energy level	Lower energy level				
$LiNbO_3$:Tm/Yb	2.42*exp(-2192/k_BT) + 4.5*10^{-3}	670-730	750-850	323-773	980	29	[18]
Oxyflouride glass ceramic:Tm/Yb	2.78*exp(-1980.65/k_BT) + 14*10^{-3}	660-730	750-850	293-703	980	27	[19]
YAP:Tm	4.61*exp(-1926/ k_BT)	680-725	750-875	324-424	1210	26.1	This work
$NaYbF_4$:Tm@SiO_2	6.01*exp(-1874.17/k_BT) + 25*10^{-3}	670-730	750-875	100-700	980	25	[20]
PKBAN:Nd	5.36*exp(-908/ k_BT)	780-845	845-925	300-850	532	13.1	[21]
Telluride glass:Nd	3.82*exp(-963.60/k_BT)	778-848	846-938	293-673	586	13	[22]
YAG:Nd	3.46*exp(-967/ k_BT) + 1.3*10^{-3}	820-850	890-900	299-523	748	12	[23]
Yttrium silicate powder:Nd/Yb	3.46*exp(-497.61/k_BT)	905-930	960-990	298-673	808	6.8	[24]
$NaYF_4$:Nd	1.22*exp(-60/ k_BT)	860-864	865-880	273-423	830	0.8	[25]

Another possibility that can be considered is the calibration of YAP: Tm^{3+} nanoperovskite in the physiological range. Nonetheless, the first calibration procedure for this range turned out to be ineffective, because the obtained sensitivity was very low, i.e, the ratio of the intensity of the thermally coupled emitting levels was close to zero. Therefore, another optical sensor calibration procedure was considered in the temperature range between 294 K and 325 K. This time, the intensity ratio between the Stark levels at 776.42 nm and 821.50 nm of the emission band associated with $^3H_4 \rightarrow {}^3H_6$ transition were employed for the optical calibration procedure by using the FIR technique (see Fig. 7).

The experimental maximum intensities of these Stark peaks were considered in order to calculate the ratio between them as shown in Fig. 8. The ratio between these intensities follows the Boltzmann distribution law, according to the Eq. (1). This equation was evaluated by recording the emission spectra with the temperature, starting at RT up to 325 K. From the fitting procedure, the values of C=0.15 and the energy gap ΔE=784.10 cm^{-1} were obtained. The relative sensor sensitivity S_{REL} as a function of temperature, defined by the Eq. (3) is also shown in Fig. 8. The relative sensitivity of this sensor reaches its maximum value of 0.013 K^{-1} at 294 K. The sensitivity of this optical sensor is very high if it is compared with others RE^{3+}-based optical sensors working in the physiological range (see Table 3). Thus, YAP: Tm^{3+} nanoperovskite can be considered as a potential candidate as temperature sensor based on the FIR technique in the physiological range with a high sensitivity and, furthermore, for biological applications.

It is relevant to point out that most of relative sensitivity data presented in Table 2 and Table 3 have been obtained in different conditions (materials dispersed in fluids) compared to YAP: Tm^{3+}. Even though it is true that the overall emission efficiency can vary notably between having or not having the sample dispersed in fluids, the intensity ratio between two emission bands should not change significantly and thus, the sensitivity neither.

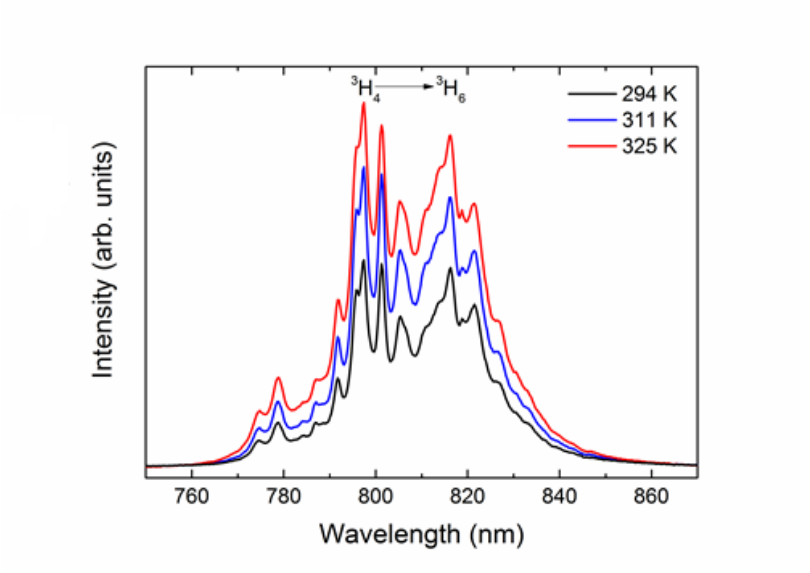

Fig. 7. Temperature upconversion emission spectra of YAP: Tm^{3+} nanoperovskite from 294 up to 325 K exciting at 1210 nm.

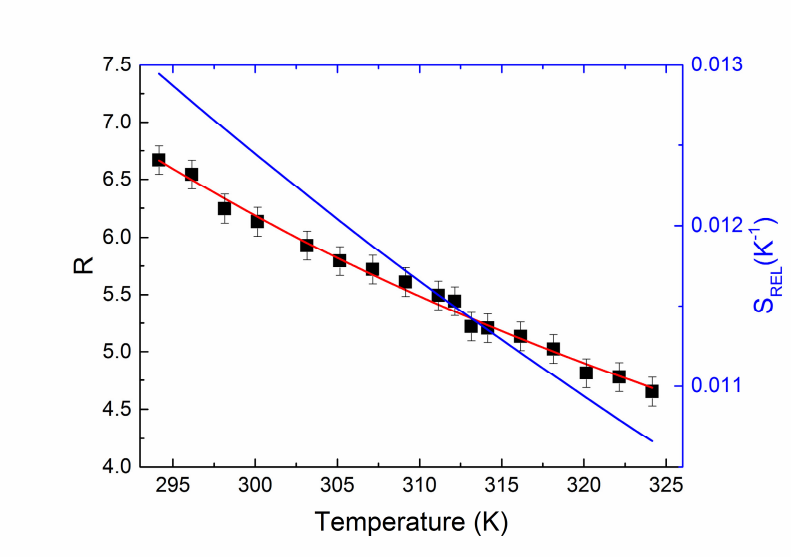

Fig. 8. Experimental intensity area ratio and relative sensitivity of the YAP: Tm^{3+} Stark levels centered at 776.42 and 821.50 nm associated to the $^3H_4 \rightarrow {}^3H_6$ transition. The experimental values were fitted to a single exponential function. The fit curve (red line) of the experimental intensity ratio is also shown.

Table 3. Thermal Relative Sensitivity Values of Different RE^{3+}-based Temperature Optical Sensors Working in the NIR and Physiological Range[a]

Optical sensor	FIR equation	λ range (nm)		Temperature range (K)	λ_{Exc} (nm)	S_{REL} (x10^{-3} K^{-1}) at 299 K	Ref.
		Upper energy level	Lower energy level				
YAP:Tm	0.15*exp(784.10/k_B T)	792-800	800-803	294-324	1210	12.5	This work
$NaNbO_3$:Tm	1.18+6.6 x 10^{-3}T	797	807	303-333	1319	8.3	[26]
CaF_2:Tm/Yb	2.05*exp(−155.56/k_B T)	785-795	795-805	299-323	920	2.5	[27]
YAG:Nd	1.25*exp(−95/k_BT)	935-941	943-950	283-343	808	1.5	[13]
$NaYF_4$:Nd	1.22*exp(−60/ k_BT)	860-864	865-880	273-423	830	1.0	[25]
LaF_3:Nd	0.68*exp(−56.12/k_B T)	862-878	880-895	283-343	808	0.9	[12]

[a] FIR equations, wavelength ranges used to calculate the fluorescence intensities originating from the thermalized levels of interest for the RE^{3+} based optical sensors, the excitation wavelength (λ_{Exc}) and the temperature ranges are also included.

It is worth mentioning that the intensity ratio of the YAP:Tm^{3+} nanoperovskite in the temperature range between 294 and 325 K changes around 43% (twice higher than the one found in $NaNbO_3$: Tm^{3+} nanoparticles [26]), which is notably higher compared with others RE^{3+}-based optical sensors that have been tested as thermal probes for biological applications. For instance, LaF_3 doped with Nd^{3+} ions, which has been successfully used for subtissue thermal sensing and photothermal treatments [11,12], shows a change of around 4%.

Another advantage of the YAP: Tm^{3+} nanoperovskite optical sensor compared with those showed in Table 2 and Table 3 (except Ref [26]. that has lower sensitivity), is that the used excitation source lies in the *II-BW,* in which the optical scattering due to the absorption of water and other compounds present in tissues (such as hemoglobin) is further decreased when is compared to the *I-BW*, due to the use of longer wavelengths. Thus, with these results and features, the viability of the YAP: Tm^{3+} nanoperovskite as optical temperature sensor working in the NIR and in the physiological ranges is evidenced and its application in biological systems could be considered.

5. Conclusion

The thermal sensing capability of the YAP: Tm^{3+} nanoperovskite in the infrared range NIR, synthetized by sol-gel method was studied. The temperature dependence of the infrared upconverted emission bands located around 705 nm ($^3F_{2,3}\rightarrow{}^3H_6$) and 800 nm ($^3H_4\rightarrow{}^3H_6$) respectively of YAP: Tm^{3+} nanoperovskite under excitation at 1210 nm was analyzed from RT up to 425 K, allowing the calibration of the optical sensor by using the FIR technique. The YAP: Tm^{3+} nanoperovskite shows a high sensitivity in the NIR compared to other RE^{3+}-based optical sensors working in the same range. In addition, a second calibration procedure of the YAP: Tm^{3+} optical sensor was carried out by using the FIR technique on the upconverted emission band associated to the $^3H_4\rightarrow{}^3H_6$ transition in the physiological range, showing a very relative sensitivity compared with others RE^{3+}-based optical sensors. The intensity ratio shows large changes that turned out to be very high compared with other optical sensors. These features allow the potential utility of YAP: Tm^{3+} nanoperovskite as optical thermal probe in the NIR and physical range for biological applications with the advantage that the excitation (at 1210 nm) lies in the *II-BW* while the emission does it in the *I-BW*, avoiding by this way, the overlap between the excitation and the emission.

Funding

MINECO (MAT2013-46649-C4-4-P, MAT2015-71070-REDC, and MAT2016-75586-C4-4-P), EU-FEDER funds, and FPI grant (BES-2014-068666).

4.3. Optical sensor calibration with pressure

In this section, the fifth and sixth paper are included and suppose the last part of the experimental results of this thesis, focusing in the analysis of the viability of nano-perovskites doped with Nd^{3+} ions, i.e. $YAlO_3$ nano-perovskite doped with 1 mol % Nd^{3+} ions (Nd^{3+}: $YAlO_3$) as optical pressure sensors working in the NIR.

The fifth paper was focused on pressure evolution of the infrared luminescence Nd^{3+}-doped $YAlO_3$ nano-perovskite associated to the $^4F_{3/2}\rightarrow{}^4I_{9/2}$ and $^4F_{3/2}\rightarrow{}^4I_{11/2}$ transitions from ambient conditions up to 29 GPa. In addition, a detailed theoretical study of the crystal field of the former sample was performed in order to support the experimental data obtained in the luminescence at high-pressures experimeriment. Finally, the viability of the Nd^{3+}: $YAlO_3$ nano-perovskite up to 29 GPa within NIR was analyzed.

The sixth paper studies the pressure evolution of the anti-Stokes emissions of Nd^{3+}: $YAlO_3$ nano-perovskite associated to the $^4F_{7/2}+{}^4S_{3/2}\rightarrow{}^4I_{9/2}$ and $^4F_{9/2}\rightarrow{}^4I_{9/2}$ transitions up to 10 GPa.

4.3.1. High pressure luminescence of Nd^{3+} in $YAlO_3$ nano-perovskites. A crystal-field analysis

Authors: **Miguel A. Hernández-Rodríguez**, Juan E. Muñoz-Santiuste, Víctor Lavín, Antonio D. Lozano-Gorrín, Plácida Rodríguez-Hernández, Alfonso Muñoz, Vemula Venkatramu, Inocencio R. Martín and Ulises R. Rodríguez-Mendoza

Published in: **Journal of Chemical Physics;** Volume: **In press;** Pages: **In press;** DOI: **In press;** Accepted **9 January 2018**

The first part of this work consisted in the study pressure evolution of the near-infrared emission lines associated to the $^4F_{3/2}\rightarrow{}^4I_{9/2}$ and $^4F_{3/2}\rightarrow{}^4I_{11/2}$ transitions of Nd^{3+} ions in $YAlO_3$ nano-crystalline perovskites (YAP: Nd^{3+}) from ambient conditions up to 29 GPa exciting at 785 nm. Due to the low point symmetry of the Nd^{3+} sites in the $YAlO_3$ structure, probably even lower due to the distortion expected for an ion with larger ionic radius, there is a complete breakdown of the (2J+1)/2 degeneracies of the $^{2S+1}L_J$ multiplets. Thus, the C_S (C_{1h}) crystal-field interaction will give rise to the R_1 and R_2 Stark, or crystal-field, levels of the $^4F_{3/2}$ multiplet, the Y_j (j=1-6) Stark levels of the $^4I_{11/2}$ first

excited level and the Z_j (j=1-5) levels of the $^4I_{9/2}$ ground state; the ones that are relevant in this work. Transitions between these Stark levels will show the largest luminescence intensities, as it is showed in the Fig. 1 of this paper. Two different behaviours were observed in the dependence of the emission lines with pressure, especially the ones associated to the $^4F_{3/2} \rightarrow {}^4I_{9/2}$ transition. On one side, emission lines associated to the $^4F_{3/2}(R_{1,2}) \rightarrow {}^4I_{9/2}(Z_{1,2,3})$ transitions showed wavelength blue-shifts as the pressure increased that have been also observed in YAP bulk crystal. On the other side, emission lines associated to the $^4F_{3/2}(R_{1,2}) \rightarrow {}^4I_{9/2}(Z_{4,5})$ transitions showed a significant wavelength red-shifts, which have been also observed in garnet crystal, as it is shown in Fig. 3 of the manuscript

Concerning the emission lines associated to the $^4F_{3/2}(R_{1,2}) \rightarrow {}^4I_{11/2}(Y_{1\text{-}6})$ Stark transitions, $R_{1,2} \rightarrow Y_{2\text{-}6}$ emission lines show clearly wavelength red-shifts, whereas only the $R_2 \rightarrow Y_1$ line shows a slight blue-shift, as it is shown in Fig. 3 of the manuscript.

In general, the evolution of these emission lines showed a linear behaviour with pressure in the pressure range between 1 atm up to 30 GPa, as it shown in Fig, 3 of the manuscript. The pressure coefficients achieved in this experiment were, in general, negative, being the $R_{1,2} \rightarrow Z_5$ emission lines the most sensitive to pressure with coefficients of -4.70 and -4.58 cm^{-1}/ GPa, while the $R_1 \rightarrow Y_{4,5,6}$ lines showed pressure coefficients around -3.10, -3.18 and -3.69 cm^{-1}/GPa, respectively, and the $R_2 \rightarrow Y_5$ one with -3.15 cm^{-1}/GPa (see Table 2 of this article). These values are good enough to consider the use of YAP: Nd^{3+} nano-perovskite as optical pressure sensor working in NIR.

The second part of this work consisted in an extensive analysis of the crystal field. The energy shifts have been related to pressure-induced changes in the interactions between the Nd^{3+} ions, located at the yttrium site, and their twelve oxygen ligands. Potentiality of the Simple Overlap Model, combined with *ab initio* structural calculations, in the description of the effects of these interactions on the energy levels and luminescence properties of the optically active Nd^{3+} ion has been successfully tested. Simulations show how the energies of the $4f^3$ ground configuration and the barycenters of the multiplets increase with pressure, whereas the Coulomb interaction between *f*-electrons decreases and the crystal-field strength increases. The combination of these effects explains the wavelength blue-shift of some near–infrared emission lines of Nd^{3+} ions.

This manuscript was accepted by J. Chem. Phys. Click here to see the version of record.

High pressure luminescence of Nd^{3+} in $YAlO_3$ perovskite nanocrystals. A crystal-field analysis

Miguel A. Hernández-Rodríguez,[a] Juan E. Muñoz-Santiuste,[b] Víctor Lavín,[a] Antonio D. Lozano-Gorrín,[a] Plácida Rodríguez-Hernández,[a] Alfonso Muñoz,[a] Vemula Venkatramu,[c] Inocencio R. Martín,[a] and Ulises R. Rodríguez-Mendoza [a,*]

[a] *Departamento de Física, IMN, IUdEA, and MALTA Consolider Team, Universidad de La Laguna. Apdo. 456, E-38200 San Cristóbal de La Laguna, Santa Cruz de Tenerife, Spain.*
[b] *Departamento de Física and MALTA Consolider Team, Escuela Politécnica Superior, Universidad Carlos III de Madrid. Avenida de la Universidad 30, E-28913 Leganés, Madrid, Spain.*
[c] *Department of Physics, Yogi Vemana University, Kadapa 516 003, India.*

**Corresponding autor: Dr. U.R. Rodríguez-Mendoza (urguez@ull.edu.es)*

Keywords: Nd^{3+}; perovskite nano-particles; luminescence; high pressure; optical pressure sensor

Abstract: Pressure-induced energy blue- and red-shifts of the $^4F_{3/2} \rightarrow {}^4I_{9/2,11/2}$ near-infrared emission lines of Nd^{3+} ions in $YAlO_3$ perovskite nano-particles have been measured from ambient conditions up to 29 GPa. Different positive and negative linear pressure coefficients have been calibrated for the emission lines and related to pressure-induced changes in the interactions between those Nd^{3+} ions and their twelve oxygen ligands at the yttrium site. Potentiality of the Simple Overlap Model, combined with *ab initio* structural calculations, in the description of the effects of these interactions on the energy levels and luminescence properties of the optically active Nd^{3+} ion is emphasized. Simulations show how the energies of the $4f^3$ ground configuration and the barycenters of the multiplets increase with pressure, whereas the Coulomb interaction between *f*-electrons decreases and the crystal-field strength increases. All these effects combined explain the wavelength blue-shifts of some near–infrared emission lines of Nd^{3+} ions. Large pressure rates of various emission lines suggest that $YAlO_3$ perovskite nano-crystal can be a potential candidate for near-infrared optical pressure sensor.

This manuscript was accepted by J. Chem. Phys. Click here to see the version of record.

1. Introduction

High pressure research involves different science fields, such as physics, chemistry, geology, biology, and food technology.[1] Applying pressure to an organic or inorganic material allows tuning, in a controllable way, the volume of the sample, changing their interatomic distances and structural distribution. Therefore, this process modifies, in a reversible or irreversible way, its structural, vibrational, electric, magnetic and optical properties. Among several applications of this technique, such as reproducing and studying the phenomena that occur in the inner cores of planetary objects, it is really interesting to highlight its application in the study of structural and optical properties of inorganic compounds, since it presents several advantages over ambient pressure condition techniques.[2,3] On one hand, it provides a continuous change of the network structure and the local coordination environments, allowing a singular view of the electronic structure and optical properties of materials doped with lanthanide ions and, hence, of all their physical properties. On the other hand, reduction of the sample´s volume allows a wide range of structures and bindings of a specific chemical composition to be achieved.[2,3]

Since its development in the 1960s, diamond anvil cell (DAC) has been the usual way to reach ultrahigh pressures.[1] Its use requires calibrated standards for the determination of pressure inside the hydrostatic chamber. The most widely used sensors are the optical pressure ones (P-sensor), taking advantage of variations of luminescence properties of optically active ions under pressure. An optical P-sensor needs to accomplish some general requirements, such as, show a single emission line or well separated lines with no broadening or weakening, large shifts with pressure, and small temperature-dependent line shifts and linewidths.[4] The α-Al_2O_3:Cr^{3+} ruby crystal [1-3,5] is the most commonly used optical P-sensor due to the intense $^2E \rightarrow {}^4A_2$ (R-lines) luminescence of Cr^{3+} ions, their large line shifts with pressure and easy excitation with commercial lasers (Argon or diodes). However, its main drawbacks are the broadening and loss of intensity at high temperatures, as well as a low pressure sensitivity below 1 GPa, the pressure range of interest for life-related high-pressure

research.[2,5] Therefore, the development of new optical P-sensors is required in order to overcome these disadvantages, while keeping the advantages of ruby. For this purpose, the lanthanide-based sensors have drawn special attention. [2,3] Due to the shielding of *4f* electrons, absorption and emission lines of lanthanides in crystals in the UV-VIS-NIR optical range are quite sharp and, consequently, pressure measurements result to be more accurate. In addition, these lines are less sensitive to the environment and to temperature compared to those of *3d* electrons of Cr^{3+} ion in ruby.

Several oxide-based active materials have been extensively studied as optical P-sensors.[2,3] Among them, Neodymium(III)-doped garnets and perovskites have received special attention due to their optical properties, since the main near-infrared (NIR) emission in the range of 850-1100 nm may avoid the luminescence of impurities present in natural diamonds.[6-14] Different Nd^{3+}-doped or Cr^{3+}-Nd^{3+} co-doped systems such as $Ca_3Ga_2Ge_3O_{12}$ (CGGG),[15] $Gd_3Ga_5O_{12}$ (GGG),[16] $Y_3Al_5O_{12}$ (YAG),[17] $La_3Lu_2Ga_3O_{12}$ (LLGG),[18] and $Gd_3Sc_2Ga_3O_{12}$ (GSGG),[19] garnets have been presented as potential P-sensors, focusing on the pressure-induced red-shifts of the $^4F_{3/2}(R_{1,2})\rightarrow{}^4I_{9/2}(Z_5)$ emission lines of the Nd^{3+} ion (see Fig. 1). In addition, Nd^{3+}-doped $YAlO_3$ (YAP) perovskite has been also studied because of its small temperature coefficient at high temperatures, seven times lower than ruby [4], and by the fact that its emission is located near 900 nm, just in the NIR, which does not overlap in the visible range with typical emissions from other optically active ions. Luminescence of Nd^{3+} ion in YAP bulk crystal have been previously tested up to 80 GPa measuring the pressure-induced blue-shifts of the $^4F_{3/2}(R_{1,2})\rightarrow{}^4I_{9/2}(Z_{1\text{-}3})$ lines (see Fig. 1),[6] but nothing was said about the $^4F_{3/2}(R_{1,2})\rightarrow{}^4I_{9/2}(Z_{4,5})$ lines that are the most sensitive to pressure, as well as the $^4F_{3/2}(R_{1,2})\rightarrow{}^4I_{11/2}(Y_{1\text{-}6})$ lines.

From the luminescence point of view, advantages of nanocrystals versus bulk counterparts are found, especially in the field of nano-bioimaging, nano-thermometry, and as alternative to quantum dots in photonic devices [20-23]. In our case, luminescence properties of nanocrystals of sizes around 30 nm, seems to have the same behavior of their bulk counterparts. In this work, and for the first time to

our knowledge, high-pressure luminescence properties of YAP:Nd^{3+} have been extended to nanocrystals, focusing the attention not only on the emission from the $^4F_{3/2}$ multiplet to the $^4I_{9/2}$ ground state, but also from the $^4I_{11/2}$ first excited multiplet, in the pressure range from 1 atm up to 29 GPa. High-pressure behavior indicates different wavelength blue and red-shifts of the $^4F_{3/2}(R_{1,2})\rightarrow{}^4I_{9/2}(Z_{1\text{-}5})$ and $^4F_{3/2}(R_{1,2})\rightarrow{}^4I_{11/2}(Y_{1\text{-}6})$ emission lines, showing pressure coefficients large enough to consider the use of this Nd^{3+}-doped nanocrystal as an optical P-sensor in the NIR range. These pressure-induced wavelength shifts are analyzed and simulated in the framework of the crystal-field theory, taking advantage of the combination of Simple Overlap Model (SOM) and *ab initio* structural calculations.

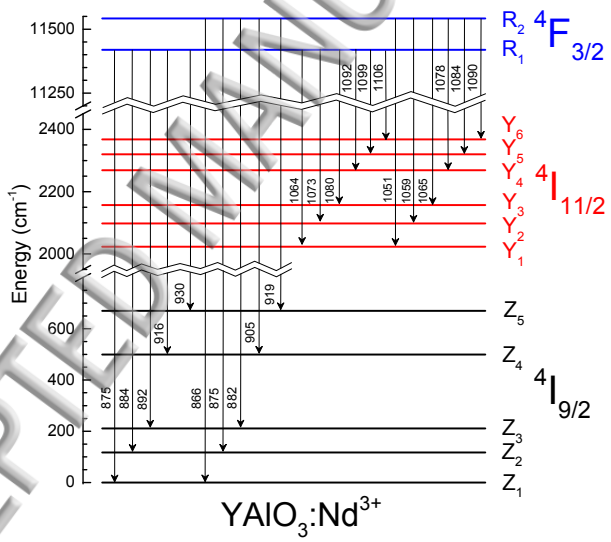

Figure 1. Partial energy level diagram and main emission lines of Nd^{3+} ion in $YAlO_3$ nano-perovskite. Numbers in arrows are given in nanometers.

2. Experimental

Crystalline YAP perovskite in the form of nano-powder with composition $Y_{0.99}Nd_{0.01}AlO_3$ were successfully synthesized by the Pechini citrate sol–gel method in air atmosphere. Details of the synthesis procedure are given elsewhere,[14] although it is worth noting that a high temperature of 1550 ºC (1823 K) was reached in the final calcination process in order to obtain a pure perovskite phase. High pressure was generated with a membrane-DAC from ambient pressure up to ~29 GPa at room temperature. A 200 µm tungsten carbide gasket was pre-indented to 50 µm and a centered hole was made using a spark eroder to make a hydrostatic chamber with a diameter of around 150 µm. Luminescence of ruby sphere chips of around 10 µm was used as pressure calibrant, and a 16:3:1 methanol-ethanol-water mixture served as pressure transmitting medium, providing hydrostatic conditions up to ~14 GPa.[3] High-pressure luminescence of Nd^{3+} ions was detected using a micro-Raman confocal microscope (Renishaw InVia), using a 785 nm laser and a cooled CCD.

Powder XRD data at ambient conditions were collected on a diffractometer (PANalytical X'Pert 123 PRO) in a Bragg−Brentano geometry with a detector (124 X'Celerator) using the Cu $K_{\alpha 1}$ radiation (λ=1.5405 Å) in the angular range $5°<2\theta<80°$, by continuous scanning 126 with a step size of 0.02°. A Rietveld refinement [24] of the pattern was carried out using the FullProf program,[25] in which a pseudo-Voigt function was used to describe the peak shape and a polynomial function with five refined coefficients for the background. Table T1 included in the supplementary material shows the cell parameters and agreement factors obtained from Rietveld fitting. Results are the same as those presented previously.[14,26] Structural properties of the local dodecahedral site occupied by the Yttium(III) and Neodymium(III) ions at ambient as well as at high pressures were theoretically calculated for bulk $YAlO_3$ perovskite by means of *ab initio* total energy calculations using the Density Functional Theory (DFT).[26] Crystal-field definitions and Simple Overlap Model (SOM) simulation details are described in supplementary material.

3. Results and discussion

3.1 Crystal structure

The diffraction pattern of the YAP:Nd^{3+} (1%) nano-powder sample has been well indexed to a major orthorhombic lattice with space group *Pnma*,[14] with an average grains size of around 35 nm, determined from the Scherrer formula. No amorphous phase was found in it, and the crystal structure parameters (a=5.33 Å, b=7.38 Å, c=5.18 Å) obtained for this nano-powder after fitting are almost identical to those found for the bulk counterpart (a=5.33 Å, b=7.37 Å, c=5.18 Å),[26] indicating that the structural properties of the bulk remain in the nanoscale.

Ab initio calculation of the bulk modulus for the $YAlO_3$ structure gives a large value of 204.5 GPa, explaining its hardness and mechanical stability up to 92 GPa, above which a possible phase transition from the *Pnma* phase to the tetragonal *I4/mcm* phase may occur.[26] Pressure dependence of the YO_{12} dodecahedron (V_{dod}), AlO_6 octahedron (V_{oct}), and unit cell (V_{tot}) volumes are given in Fig. 2 (bottom). As a general feature, all volumes decrease with pressure, although the octahedron volume shows a higher compressibility (5.6×10^{-3} GPa^{-1}) than the dodecahedron one (4.35×10^{-3} GPa^{-1}), indicating an overall pressure evolution of the $YAlO_3$ network towards a more symmetrical structure.[26] This can also be observed when following the evolutions of the interatomic distances between the Y^{3+}, or Nd^{3+}, ion and its oxygen ligands (see top of Fig. 2). At ambient pressure the coordination number of the Y^{3+}, or Nd^{3+}, ion in $YAlO_3$ is practically smaller than 12 (around 8 + 4), since there are 4 oxygens at distances above 3 Å. In addition, these 8 closer oxygens show small changes in their distances to the yttrium ion with pressure. However, the large compressibility of the distances of the other 4 outer oxygens at high pressures clearly indicates that they start to have more influence on the environment of the Nd^{3+} site. That is why SOM calculations have used all 12 oxygen ligands in all the calculations of the crystal-field parameters. On the other side, it should be emphasized that while the studied (doped or un-doped) YAP phase is orthorhombic, the stoichiometric $NdAlO_3$ (NdAP) compound is rhombohedral,[27] with different distances between the Y^{3+}, or Nd^{3+}, ions and the oxygens occupying the dodecahedral environments in both structures.

Thus, SOM calculations have been carried out assuming that Nd^{3+} ions occupy the yttrium lattice site without any distortion although, since Nd^{3+}ion (0.98 Å) is about 10% larger than Y^{3+} ion (0.90 Å), local distortions are expected. Unfortunately we cannot predict what kind of distortion can be introduced when the Nd^{3+} ion is located in the Y^{3+} site (it could be strong since the $NdAlO_3$ has a different structure than the $YAlO_3$). In other words, it is not clear how this deformation can be quantified and introduced in the calculation. In spite of this fact, it seems evident that the simulation carried out, properly reproduces the observed behavior with the pressure of the energy levels. Even, in some cases, the position of the emission lines with the pressure are properly reproduced, especially in the high energy side of each transition and particularly for the intense $^4F_{3/2}(R_{1,2})\rightarrow{}^4I_{9/2}(Z_{1,25})$ transitions that, taking place at 860- 900 nm, are easily measured using most of conventional fluorimeters.

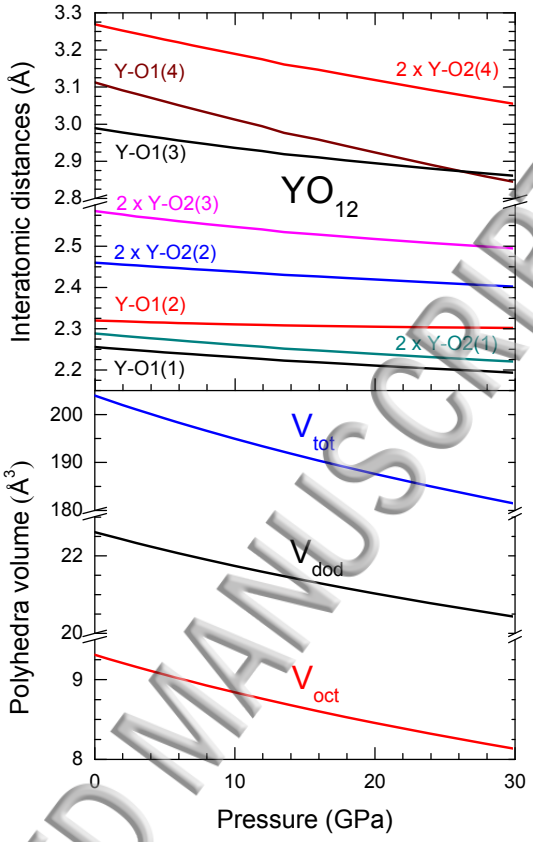

Figure 2. Pressure evolution up to 30 GPa of the *ab initio* calculated (Up) Yttrium-Oxygen interatomic distances in the YO_{12} dodecahedral site, and (Bottom) of the unit cell, dodecahedral, and octahedral volumes in bulk $YAlO_3$ structure.

3.2 Luminescence under pressure

Luminescence properties of Nd^{3+} ion, as the rest of optically active lanthanides, are ruled by the local point symmetry of the site, or local environment, of the lattice in which it is located. The point symmetry group at the yttrium dodecahedral YO_{12} site is *Cs* (*C1h*), which includes a reflection plane in addition to the identity operation. Due to the low point symmetry of the Nd^{3+} sites in the $YAlO_3$ structure, probably even slightly lower due to the distortion expected for an optically active ion with larger ionic radius compared to that of the Y^{3+} ion in the perovskite network, there is a complete

breakdown of the (2J+1)/2 degeneracies of the $^{2S+1}L_J$ multiplets. Thus the C_S (C_{1h}) crystal-field interaction will give rise to the R_1 and R_2 Stark, or crystal-field, levels of the $^4F_{3/2}$ multiplet, the Y_j (j=1-6) Stark levels of the $^4I_{11/2}$ first excited multiplet and the Z_i (i=1-5) levels of the $^4I_{9/2}$ ground state; the ones that are relevant in this work. Transitions between these Stark levels will show the largest luminescence intensities (see Figs. 1 and 3).[15,28]

The emission spectrum at ambient conditions has been measured resonantly exciting at 785 nm the $^4I_{9/2}\rightarrow{}^4F_{5/2}$ absorption transition of the Nd^{3+} ions in YAP nanocrystals, from which a fast multiphonon relaxation to the $^4F_{3/2}$ doublet occurs. Spontaneous emissions from the R_1 and R_2 thermalized Stark levels of the $^4F_{3/2}$ emitting level to those of the $^4I_{9/2}$, in the range from 860 to 940 nm, and to the $^4I_{11/2}$ Stark levels, from 1040 to 1110 nm, result in well-defined narrow peaks that can be assigned to nine $^4F_{3/2}(R_{1,2})\rightarrow{}^4I_{9/2}(Z_{1\text{-}5})$ transitions and twelve $^4F_{3/2}(R_{1,2})\rightarrow{}^4I_{11/2}(Y_{1\text{-}6})$ transitions, respectively (see Fig. 3). From these spectra, an identification of the energy level scheme of the Stark levels and the emission lines relevant for this work at ambient pressure are shown in Figs. 1, 3 and 4. The range of hydrostaticity inside the high pressure chamber was followed monitoring the widths of the ruby emission lines. In our case, measurements revealed that up to 16 GPa it is maintained; a fact also reflected in the emissions bands of the Nd^{3+} ions, which remain wide and sharp during this pressure range, with only small broadenings observed at pressures above 16 GPa in the wavelength range of 1080-1110 nm.

The main feature in these spectra is that two different behaviors can be observed in the evolution of the energies of the emission lines with pressure, particularly for transitions between Stark levels of the $^4F_{3/2}$ emitting level and the $^4I_{9/2}$ ground state: On one side, the $^4F_{3/2}(R_{1,2})\rightarrow{}^4I_{9/2}(Z_{1,2,3})$ emission lines show wavelength blue-shifts (to lower wavelengths - higher energies) as the volume of the nanocrystal decrease, in agreement with those obtained in its bulk counterpart,[6] especially the $R_2\rightarrow Z_1$ transition for which this shift is more evident; On the other side, the most sensitive transitions to pressure, the $^4F_{3/2}(R_{1,2})\rightarrow{}^4I_{9/2}(Z_{4,5})$ emission lines, show significant wavelength red-

shifts, as it has been also observed in garnet crystals.[15-19] Regarding the $^4F_{3/2}(R_{1,2})\rightarrow{}^4I_{11/2}(Y_{1\text{-}6})$ transitions, emission lines associated with the $R_{1,2}\rightarrow Y_{2\text{-}6}$ emission lines show clearly wavelength red-shifts, whereas only the $R_2\rightarrow Y_1$ line shows a slight blue-shift (see Fig. 3). As it will be shown later, these behaviors are related to different energy shift rates of the Stark levels with pressure, which unexpectedly make the emissions from the $R_{1,2}$ Stark levels to the $Z_{1\text{-}3}$ ones to shift to lower wavelengths (higher energies).

In the range from ambient pressure up to ~29 GPa, evolution of the emission lines and, hence, of the Stark energy levels, can be described by simple linear equations, although at higher pressures the fitting should include higher order polynomials.[6] Thus for high-pressure calibration purposes, in a first approximation, linear pressure evolutions of the $^4F_{3/2}(R_{1,2})\rightarrow{}^4I_{9/2}(Z_{1\text{-}5})$ and $^4F_{3/2}(R_{1,2})\rightarrow{}^4I_{11/2}(Y_{1\text{-}6})$ emission lines were considered in order to obtain a scale in the range of pressures achieved (see Fig. 3 and Table T2; the latter included in supplementary material). The $R_{1,2}\rightarrow Z_5$ emission lines resulted to be the most sensitives to pressure with coefficients of -4.70 and -4.58 cm^{-1}/GPa, respectively. Concerning the spectral range of the $^4F_{3/2}\rightarrow{}^4I_{11/2}$ transition, it is worth noting that the $R_1\rightarrow Y_{4,5,6}$ lines show pressure coefficients around -3.10, -3.18 and -3.69 cm^{-1}/GPa, respectively, and the $R_2\rightarrow Y_5$ one with -3.15 cm^{-1}/GPa. These rates are smaller than ruby emission lines (-7.35 cm^{-1}/GPa),[5] but they are good enough to consider the use of YAP:Nd^{3+} nano-perovskite as an optical P-sensor in the NIR range.

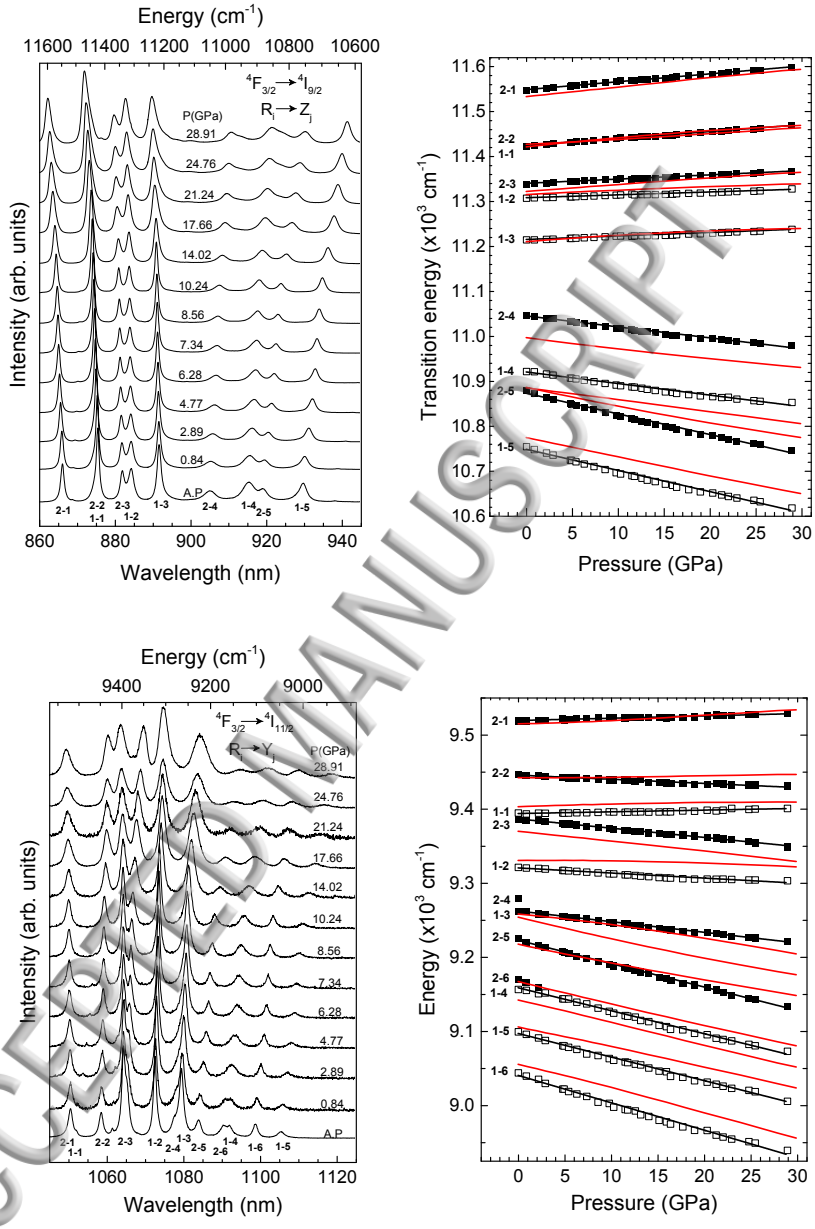

Figure 3. (Right) Room temperature Nd^{3+} emission spectra as a function of pressure associated with the $^4F_{3/2}(R_{1,2})\rightarrow{}^4I_{9/2}(Z_{1\text{-}5})$ and $^4F_{3/2}(R_{1,2})\rightarrow{}^4I_{11/2}(Y_{1\text{-}6})$ transitions exciting resonantly at 785 nm the $^4I_{9/2}\rightarrow{}^4F_{5/2}$ transition in $YAlO_3$ nano-perovskites. Identifications of the $R_i\rightarrow Z_j$ and $R_i\rightarrow Y_j$ transitions between Stark levels are also given. (Left) Experimental (open symbols) and linearly fitted (black lines) energies of emission lines as a function of pressure. Crystal-field simulations of the emission energies (red lines) using the Simple Overlap Model (SOM) are also shown.

Since $YAlO_3$ crystal has been one of the most successful lanthanide laser host materials, just behind the $Y_3Al_5O_{12}$ (YAG) garnet, its energy level diagram is well known up to the $^2P_{1/2}$ level at around 23160 cm^{-1} [7] and to the $^2P_{3/2}$ doublet located at 25981 and 26123 cm^{-1} [29] (see Table T3 in supplementary material), although recent works increases the number of Stark levels into the UV range.[30] In addition, from emission spectra it has been possible to extract the energy level scheme of those multiplets relevant for this work, i.e. the $^4I_{9/2}$ ground, $^4I_{11/2}$ first excited, and $^4F_{3/2}$ lowest emitting levels of the Nd^{3+} ions in $YAlO_3$ nano-perovskite at ambient conditions, which are compared to those of Duan *et al.* [30], as well as at high pressures (see Fig. 4).

A rough estimation of the maximum splitting increasing rates of these multiplets up to around ~29 GPa, and assuming linear variations, gives rise to $\Delta E(Z_5\text{-}Z_1)$= +6.2 cm^{-1}/GPa for the $^4I_{9/2}$ ground multiplet, $\Delta E(Y_6\text{-}Y_1)$= +3.85 cm^{-1}/GPa for the $^4I_{11/2}$ multiplet and $\Delta E(R_2\text{-}R_1)$= +0.22 cm^{-1}/GPa for the $^4F_{3/2}$ emitting multiplet. These results clearly point to a pressure-induced increase of the crystal-field strength felt by the Nd^{3+} ion when distances to its oxygen ligands decrease, as it is usually observed for many systems.[2,3] The extremely low rate of the splitting $\Delta E(R_2\text{-}R_1)$ of the $^4F_{3/2}$ level compared to those of the ground and first excited multiplets would play a relevant role in the explanation of the wavelength blue-shifts of many emission lines associated to transitions between Stark levels of these multiplets, i.e. the $^4F_{3/2}(R_{1,2})\rightarrow{}^4I_{9/2}(Z_{1\text{-}3})$ and $^4F_{3/2}(R_{1,2})\rightarrow{}^4I_{11/2}(Y_1)$ emission lines.

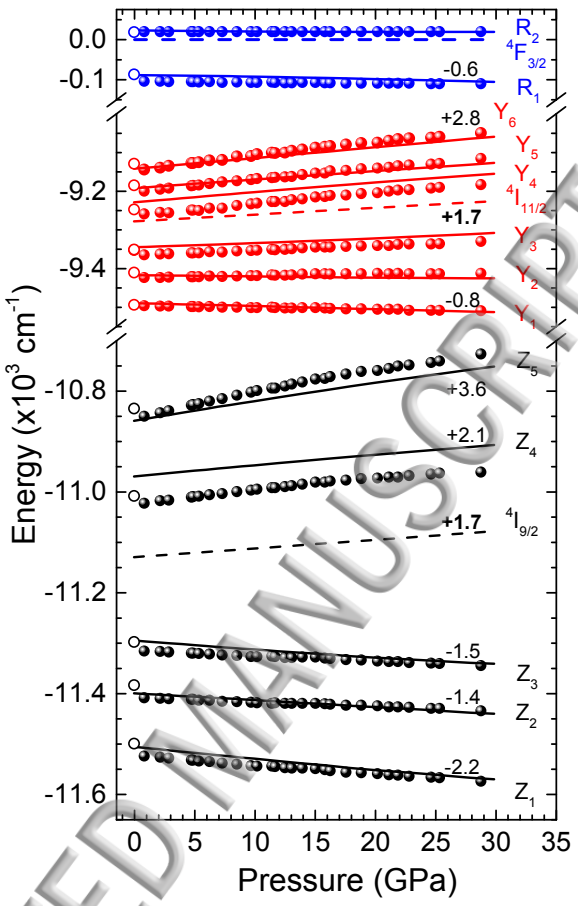

Figure 4. Nd^{3+} Stark energy levels under pressure in $YAlO_3$ nano-perovskite obtained from the emission lines (solid symbol) and from the simulations using the Simple Overlap Model (SOM) (solid lines). Experimental Stark levels by Duan *et al*. [30] at ambient conditions (open symbols) are also given. Barycenter of the $^4F_{3/2}$ emitting level (blue dashed line) has been taken as the zero of energy and some relative energy shift rates values of simulated Stark levels and barycenters (dashed lines) are highlighted.

A simple comparison with other crystalline matrices let us say that the rate of +6.2 cm^{-1}/GPa for the maximum splitting $\Delta E(Z_5\text{-}Z_1)$ of the $^4I_{9/2}$ ground multiplet is smaller than +10 cm^{-1}/GPa found in CGGG [15] or +8.1 cm^{-1}/GPa in GSGG garnets.[19] However, it is worth noting that a completely different behavior is observed for the rate of change of the maximum splitting $\Delta E(R_2\text{-}R_1)$ of the $^4F_{3/2}$ multiplet compared to what is found in garnets, in which decreases with negatives rates of -5.0 cm^{-1}/GPa in YAG, -2.6 cm^{-1}/GPa in GSGG, or -2.0 cm^{-1}/GPa in CGGG [15] due to structural atomic

redistribution with pressure, which effectively reduces the orthorhombic distortion making the site more "cubic", i.e. with a lower splitting. This splitting has been considered as a measured of the degree of local distortion of the local structure,[15] and since in garnets it is still larger in absolute magnitude than for the perovskite structure, it can be concluded that the local structure around the Nd^{3+} optically active ion does not suffer large distortions in the atomic arrangement with pressure up to ~29 GPa, confirming the *ab initio* calculations.

3.4 Crystal-field analysis

When a lanthanide ion enters in a solid structure, free-ion $^{2S+1}L_J$ multiplets are red-shifted while their degeneracies are partially or totally lifted by the crystal-field interaction. If pressure is applied to this solid, there is a continuous decrease of its volume, which can be directly understood as decreasing distances between the lanthanide ions and their ligands, together with changes in the relative spatial distributions of those atoms. As pointed out by Tröster,[2] in almost all cases absorption and luminescence lines of lanthanide ions shift to lower energies under pressure, an effect that can be understood as an overall contraction of the $4f^N$ ground configuration, which reduces the energy differences between ground and excited multiplets. This effect can be related to decreasing Coulomb and spin-orbit interactions through changes in the covalency of bonds, named the nephelauxetic effect. In addition, a generalization of the crystal-field interaction under pressure can also be given, in such a way that, superimposed on the reduction of the energy gaps between multiplets, there is an increase in their hyperfine Stark energy level splittings due to increasing lanthanide-ligands mutual interaction when distances decrease. However, in some cases also decreasing splittings have been reported, related to specific changes of the structural distribution of the atoms of the lanthanide´s local site that decreases the crystal-field strength felt by the optically active ion.[15-19,31] It is worth noting that $YAlO_3$ crystal has been claimed to be one of the scarce exceptions to these generalizations, since blue-shifts of some emission peaks have been observed under pressure.[4,6]

Up to now, a clear explanation of this anomalous behavior in Nd^{3+}-doped $YAlO_3$ has not been given. Some authors suggested as main factors the site symmetry and the shorter distance between the lanthanide and its ligands, showing a higher hybridation of the *4f* wavefunctions of the Nd^{3+} ion in this system. Another simple explanation would point to increasing Coulomb and spin-orbit coupling interactions, which should be connected with an increasing volume of the YO_{12} dodecahedral unit,[2] an effect that does not occur in YAP perovskite structure (see Fig. 2).

It is worth noting that the complete picture of the effects of pressure on this system has not been given. In previous works,[4,6] there were no measurements of the rest of $R_{1,2}\rightarrow Z_{4,5}$ emission lines above 900 nm (11,111 cm^{-1}), which show red-shifts with rates even larger than those of blue-shifted lines, as well as the $R_{1,2}\rightarrow Y_{1\text{-}6}$ emissions beyond 10,000 cm^{-1}, with similar results (see Fig. 3). In addition, no attempt to understand how the atomic and crystal-field interactions change with pressure and their influence on the energy levels and emission lines was done.

3.4.1 Simulation at ambient pressure

The first attempt to simulate the crystal-field interaction of Nd^{3+} ion in $YAlO_3$ perovskite was done by Karayianis *et al.*[32] by diagonalization of six low-*J* lying multiplets and using 27 experimental levels. A few more simulations were later published,[33,34] although no correlation exists among the different sets of calculated parameters, mainly due to differences in calculations as well as in the definition of the Hamiltonian used. As a general feature, there is a lack of sufficient experimental energy levels and ambiguities in the identification of high energy multiplets, due to overlapping, that have complicated these simulations. In addition, small errors in the computer files of reduced matrix elements used in these calculations, recently detected by several authors,[35-37] introduced additional uncertainty in the reliability of the early calculations. Thus the first reliable calculation was done in 2007 by Duan *et al.*,[30] when they revisited the study of the crystal-field interaction felt by Nd^{3+} and Er^{3+} ions in $YAlO_3$ perovskite.

For a proper parameterization of the crystal-field interaction, most of the energy levels in the ^4I_J and ^4F_J multiplets (<15000 cm^{-1}) are needed. Since in this work the energy level positions obtained from experimental data are clearly not enough for a complete description of the system, the starting point of our analysis using SOM model is based not only on previous spectroscopic data but also, and this is one of the key points of this work, on the use of crystallographic data of the yttrium site in the perovskite structure.

The first step in our simulation procedure is obtaining the barycenters and the Stark energy levels of all the $^{2S+1}L_J$ multiplets up to the $^2P_{1/2}$ singlet at ~23160 cm^{-1} (see Table T3 in supplementary material). In a second step, and keeping the same free-ion parameters obtained by Duan *et al.*,[30] SOM model has been used to obtain the crystal-field (CF) parameters (see Table 1 and Simulation II in Table T3 in supplementary material). These values give an overall CF strength at ambient conditions of 560.9 cm^{-1}. Simulation II gives an uncertainty of around 18 cm^{-1} when compared with the experimental Stark energy levels given by Kaminskii.[29] CF parameters in Simulations I and II (Table T3) are clearly different, although this is not surprising since a local distortion at the optically active ion site is expected when Nd^{3+} ion is placed at the Y^{3+} lattice position. Using the free-ion of Duan *et al.*[30] and the CF parameters of SOM as starting point, a new fit to the Kaminskii data, named Simulation III, is also reported in Table 1 and Table T3 (supplementary material), giving a *rms* uncertainty of around 12 cm^{-1}.

Table 1. Atomic and crystal-field parameters (in cm^{-1}) calculated for the Nd^{3+} ion in $YAlO_3$ nano-crystal.

Atomic and crystal-field parameters	Simulation I [23] (0 GPa)	Simulation II (0 GPa)	Simulation III (0 GPa)	This work (30 GPa)
E_{AV}	24114	24116	24116	24133
$F^{(2)}$	70925	70925	70925	70565
B_0^2	-154	-487	-160	-319
B_2^2	578	526	604	669

B_0^4	-541	-420	-410	-566
B_2^4	967	594	925	617
B'^4_2	24	349	164	607
B_4^4	-309	-484	-332	-732
B'^4_4	608	727	599	183
B_0^6	-671	-753	-738	-974
B_2^6	512	151	525	315
B'^6_2	-18	-214	2	-193
B_4^6	1611	1583	1586	1390
B'^6_4	0	480	188	1643
B_6^6	0	22	-51	-357
B'^6_6	132	326	141	350
S	565.4	560.9	562.8	676.4
$S^{(2)}$	214.8	229.5	224.4	257.9
$S^{(4)}$	338.5	313.3	326.0	330.9
$S^{(6)}$	398.7	404.7	400.1	530.6
$\%S^{(2)}$	14.4	16.7	15.9	14.5
$\%S^{(4)}$	35.8	31.2	33.6	23.9
$\%S^{(6)}$	49.7	52.1	50.5	61.5

Fixed atomic parameter (in cm^{-1}) from ref. [23]: $F^{(4)}$=50794; $F^{(6)}$=35424; ζ_{4f}=875; α=23; β=-691; γ=1690; T^2=458; T^3=38.4; T^4=75.8; T^6=-290; T^7=237; T^8=469; M^0=1.9; M^2=1.06; M^4=0.72; P^2=206; P^4=154.5; P^6=103.

3.4.2 Simulation at high pressures

To theoretically simulate the pressure evolution of the Nd^{3+} energy levels and, hence, their emission lines involved in these transitions, the total Hamiltonian within the $4f^3$ ground configuration must be solved. The starting point begins with considering the accessible experimental energy transitions between Stark levels obtained from emission spectra under pressure: in our case only 21 lines corresponding to the $^4F_{3/2}(R_{1,2})\rightarrow{}^4I_{9/2}(Z_{1\text{-}5})$ and $^4F_{3/2}(R_{1,2})\rightarrow{}^4I_{11/2}(Y_{1\text{-}6})$ transitions. These energies have been used to generate only 13 experimental Stark energy levels at different pressures (see Fig. 4). The insufficient experimental data does not allow us to follow any fitting procedure to obtain both atomic and CF parameters using the Hamiltonian given in Eq.(1) (see supplementary material). That is why we have chosen an approach similar to that used at ambient

conditions: simulate the Stark energy level diagrams using as CF parameters those obtained from SOM combined with the information of the local structure of Nd^{3+} first coordination shell at different pressures up to ~30 GPa given by *ab initio* calculations. Free-ion parameters obtained in former simulations at ambient pressure were also used but, and this is an important point, assuming slight changes in their magnitudes with pressure.

It is worth noting the importance of the free-ion Hamiltonian in this study, since it contributes to the observed shift in the energy level positions due to the pressure-induced displacements of the barycenters of all multiplets. To simulate these displacements, only $F^{(2)}$ Slater parameter was allowed to vary freely, together with the average energy E_{AVG} of the $4f^3$ configuration, (see supplementary material).

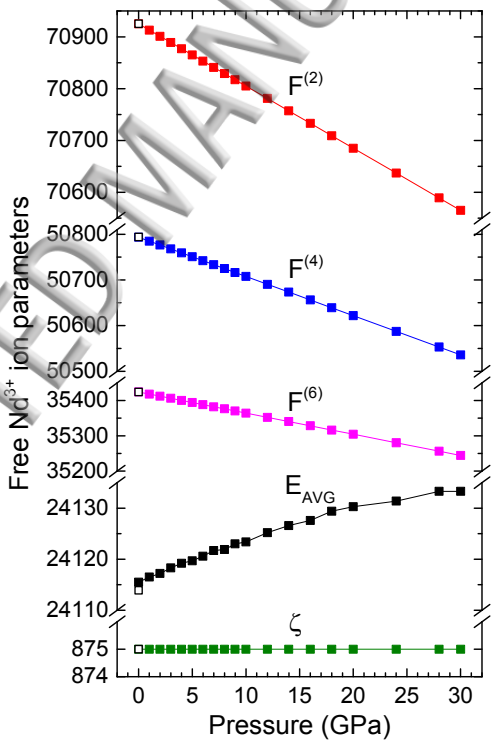

Figure 5. Nd^{3+} atomic parameters simulated by the Simple Overlap Model (SOM) in $YAlO_3$ nano-perovskite under pressure. Calculated values obtained by Duan *et al.*[23] at ambient conditions (open symbols) are also given.

Focusing our attention first on the atomic parameters corresponding to the Nd^{3+} free-ion Hamiltonian, depicted in Fig. 5, it can be observed that E_{AVG} parameter shows a continuous increasing with pressure. Up to ~20 GPa, an apparent linear behavior is obtained with a slope of +0.75 cm^{-1}/GPa, whereas at higher pressures this rate of growth is gradually reduced becoming less linear. E_{AVG} parameter corresponds to the totally spherically symmetric parts of the total (free-ion plus crystal-field) Hamiltonian, i.e. closed shells of Nd^{3+} ion and oxygen ligands plus their nuclei, giving rise to a repulsive central potential that increases in magnitude with pressure and shifts the whole $4f^3$ configuration to higher energies. On the other side, for the electrostatic repulsion radial integral $F^{(2)}$, a linear behavior is obtained with a slope of –12.0 cm^{-1}/GPa, following the expected tendency of the free-ion interaction under pressure. This decrease is due to the increase of covalency effects related to orbital overlapping, giving a relative reduction of $\Delta F^{(2)}/F^{(2)}_{AMB}$= –0.51%, in the pressure range from ambient up to 30 GPa, similar to those obtained in other systems.[2] In overall, the final effect, apart from the crystal-field effect, is a blue-shift of the whole $4f^3$ configuration together with a contraction of the ^{2S+1}L terms with pressure up to 30 GPa.

Calculated CF parameters show, as usual in low local symmetries, different variations with pressure (see Fig. 6). The axial parameters of *4*- and *6*-rank, B_0^4 and B_0^6, increase in magnitude while *2*-rank axial B_0^2 parameter decreases, reflecting that charge distribution over long distances becomes less axial as pressure brings the distant oxygen ions towards the position of the Nd^{3+} ion in the dodecahedral site (see Fig. 2). Consequently, the distorted environment of the Nd^{3+} ion, formed by 8 nearby oxygens and 4 more distant ones, becomes more symmetric, upholding the *ab initio* calculations.[26] As shown in Fig. 2, distances to the latter oxygens change very sharply with pressure. In addition, it is worth noting that the evolution of the interatomic distances, although important, is not the only source of variations in the CF parameters, which also show a high sensitivity to changes in relative angular positions (see supplementary material).

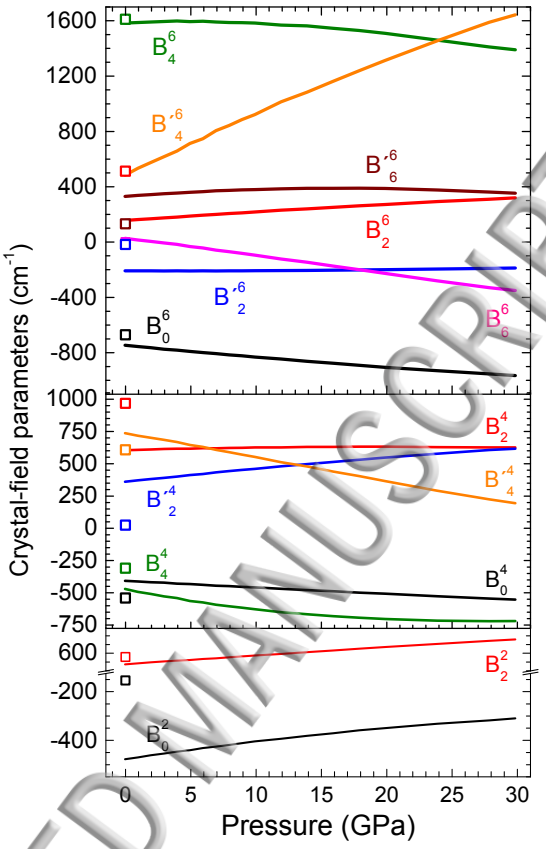

Figure 6. Nd^{3+} crystal-field parameters calculated by the Simple Overlap Model (SOM) (solid lines) in $YAlO_3$ nano-perovskite. Experimental Stark levels by Duan *et al.*[23] at ambient conditions (open symbols) are also given.

Simulations also confirm that the crystal-field interaction increases in magnitude as pressure (volume) increases (decreases) when the CF strength parameter *S* (see supplementary material) is calculated as a function of pressure. Fig. 7 shows an almost linear increase, from ~550 cm^{-1} to ~675 cm^{-1}, of the magnitude of the crystal-field interaction with pressure, as it is generally observed in many systems. Its relative change in $YAlO_3$ is similar to that found in $MgO:LiNbO_3$ oxide,[37] but can be considered small compared to other oxide systems such as YVO_4 [38] or $Ca_3Ga_2Ge_3O_{12}$ garnet.[15] Increase of the total CF strength felt by the Nd^{3+} ions can be easily related to the shortening of Nd-O

distances induced by pressure (see Fig. 2), which increases the Coulomb interaction between the *f*-electrons of the optically active ion and the valence electrons of oxygen ligands. This small change in the relative overall CF strength value has been previously related to high rigidity in the local (nearest) environment of the lanthanide, playing the role of an impurity.[37]

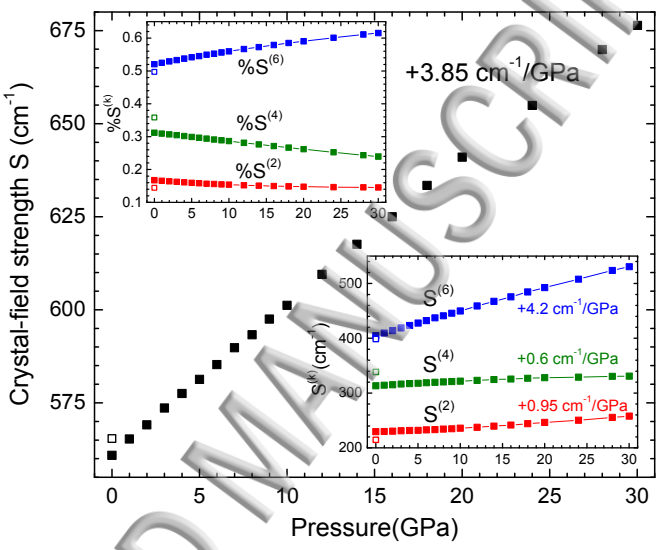

Figure 7. Crystal-field strength parameter *S* as a function of pressure. Insets show the *2*-, *4*- and *6*-rank CF strength parameters $S^{(k)}$ and the contribution in percentage values $\%S^{(k)}$ as a function of pressure. Linear rates with pressure are shown for the $S^{(k)}$ parameters.

However, for the discussion it is better to analyse the contribution to the strength parameter of those CF parameters of the same *k*-rank, $S^{(k)}$, and their percentage contribution, $\%S^{(k)}$, to the total CF strength. Bottom inset in Fig. 7 shows how all CF parameters increases in magnitude giving rise to increasing $S^{(k)}$ contribution, although *4*-rank CF parameters show the lowest rate, while the 6-rank ones show the highest rate due to the large variations of B_4^6 and B_6^6 CF parameters. In the same way, $S^{(2)}$ contribution increases, although it must be overestimated since only small changes are observed for the splitting of the $^4F_{3/2}$ emitting level, and its percentage contribution to the total strength is very small. Top inset in Fig. 7 show how $\%S^{(2)}$ contributes in only 15% to the total CF value and this

value remains almost unchanged up to ~30 GPa, whereas $\%S^{(4)}$ percentage is reduced from 32% to 24%. On the contrary, $\%S^{(6)}$ parameter shows the largest pressure variation and the largest contribution to *S* values. Thus, as pressure increases, the influence of *6*-rank parameters increases at expenses of those of *4*-rank indicating that, since the dependence of crystal field B_q^k parameters with the distance from the central Nd^{3+} ion goes as $\sim(1/R^{k+1})$, the interaction between the Nd^{3+} ion and its nearest ligands is more intense at distances closer to the central lanthanide optically active ion, and the immediate environment contribution to the *S* value dominates, the more the higher the pressure. This means that the local environment surrounding the optically active ions is rigid enough to consider that very small displacements are allowed for the 8 nearest oxygen ligands and larger displacements for those 4 distant ones. This behaviour would explain all the effects related to the free-ion and crystal-field interactions under pressure.

High pressure simulations show that all the barycenters of the $^{2S+1}L_J$ multiplets suffer wavelengths blue-shifts, but with different rates. Looking closely at Fig. 4 one could see how, when the barycenter of the $^4F_{3/2}$ emitting multiplet is been taken as the origin of energies, the relative positions of the barycenters corresponding to both the $^4I_{9/2}$ and $^4I_{11/2}$ multiplets becomes closer as the pressure increases. This fact is due to the differences in their respective slopes of +1.7 cm^{-1}/GPa, resulting in an effective approach between the emitting and low lying multiplets with pressure that can be related to the nephelauxetic effect. Conversely, the increasing of the crystal-field interaction with pressure enlarges the splitting of both $^4F_{3/2}$ and $^4I_{9/2}$ states with different magnitudes (see supplementary information section): while the splitting of emitting $^4F_{3/2}$ doublet shows no sensitivity with pressure, the maximum splitting of the $^4I_{9/2}$ ground state is around ~200 cm^{-1}, with negative relative slopes for the $Z_{1\text{-}3}$ Stark levels, and ~106 cm^{-1} for the $^4I_{11/2}$ first excited state, with a negative relative slope for the Y_1 Stark level (see Fig. 4).

The combination of both effects as pressure increases, effective approaching of multiplets and increasing hyperfine splitting, explains the behaviors of the Stark energy level scheme and the

emission lines observed in Figs. 3 and 4. Especially, they explain the overall blue-shifts (towards higher energies) of some emission lines associated with the $^4F_{3/2}(R_{1,2})\rightarrow{}^4I_{9/2}(Z_{1\text{-}3})$ and $^4F_{3/2}(R_2)\rightarrow{}^4I_{11/2}(Y_1)$ transitions. Good agreement between calculated and experimental energies are found, with only a relatively large difference of around 50 cm^{-1} for the Z_4 Stark level, and, although they are a slightly larger for the simulated emission line, it is worth noting how their tendencies with pressure are well described. Thus, typical behaviors, i.e. decreasing of atomic parameters and increasing of CF strength with pressure, are also observed for the Nd^{3+} optical properties in $YAlO_3$ nano-crystals.

3. Conclusions

Pressure-induced energy blue- and red-shifts of the $^4F_{3/2}\rightarrow{}^4I_J$ (J=9/2,11/2) near-infrared emission lines of Nd^{3+} ions in $YAlO_3$ nano-crystalline perovskites have been observed under pressure. Although their pressure coefficient rates are smaller than those of ruby, they are large enough to consider the $YAlO_3$:Nd^{3+} as a candidate for P-sensor in high pressure experiments. These energy shifts have been related to pressure-induced changes in the interactions between the Nd^{3+} ions, located at the yttrium site, and their twelve oxygen ligands. These shifts have been explained using a combination of SOM simulations and *ab initio* calculations, using only the lanthanide ion first coordination environment, have allowed us to successfully reproduce the trends observed in the experimental emission lines and the Stark energy level scheme at high pressures. Only a large difference, of around 50 cm^{-1}, between calculated and experimental energies has been found for the Z_4 Stark level, although these differences are slightly larger for the simulated emission lines, their tendencies with pressure are well described. In addition, it is worth noting how these simulations have also allowed analyzing the main affects responsible for the optical properties of Nd^{3+} ion in $YAlO_3$ under pressure: a general increase of CF magnitude and a blue-shift of the average energy of the $4f^3$ configuration.

Supplementary material

The supplemental material contains the theoretical background of the simulation, as well as the procedures followed for the fittings. Different tables related to Rietveld fittings, identification of the Nd^{3+} emission lines, and the experimental and calculated Nd^{3+} energy levels for different simulations were also included.

Acknowledgements

This work has been partially supported by MINECO (MAT2015-71070-REDC, MAT2016-75586-C4-3-P, and MAT2016-75586-C4-4-P), and by the EU-FEDER funds. M.A. Hernández-Rodríguez thanks MINECO for FPI grant (BES-2014-068666).

References

(1) Holzapfel W.B.; Isaacs N. S. High Pressure Techniques in Chemistry and Physics - A Practical Approach, Oxford University Press (1997).

(2) Tröster, Th. Optical Studies of Non-Metallic Compounds under Pressure. in: Handbook on the Physics and Chemistry of Rare Earths, edited by Gschneidner K.A., Jr, Bünzli J.-C.G., Pecharsky V.K., ch. 217, vol. 33, p. 515-589. North-Holland (2003).

(3) Bray, K.L. High Pressure Probes of Electronic Structure and Luminescence Properties of Transition Metal and Lanthanide Systems. In: Transition Metal and Rare Earth Compounds. Excited States, Transitions, Interaction I; Yersin, H., Ed.; Topics in Current Chemistry; Springer Berlin Heidelberg, 2001; Vol. 213, pp 1–94.

(4) Barnett, J. D. An Optical Fluorescence System for Quantitative Pressure Measurement in the Diamond-Anvil Cell. *Rev. Sci. Instrum.* **1973**, *44* (1), 1-9.

(5) Syassen, K. Ruby under Pressure. *High Press. Res.* **2008**, *28* (2), 75–126.

(6) Hua, H.; Vohra, Y. K. Pressure-Induced Blueshift of Nd^{3+} Fluorescence Emission in $YAlO_3$:

Near Infrared Pressure Sensor. *Appl. Phys. Lett.* **1997**, *71* (18), 2602-2604.

(7) Weber, M. J.; Varitimos, T. E. Optical Spectra and Intensities of Nd^{3+} in $YAlO_3$. *J. Appl. Phys.* **1971**, *42* (12), 4996-5005.

(8) Dereń, P. J.; Mahiou, R.; Pązik, R.; Lemanski, K.; Stręk, W.; Boutinaud, Ph. Upconversion Emission in $CaTiO_3:Er^{3+}$ Nanocrystals. *J. Lumin.* **2008**, *128* (5–6), 797–799.

(9) Yamada, Y.; Kanemitsu, Y. Photoluminescence Spectra of Perovskite Oxide Semiconductors. *J. Lumin.* **2013**, *133*, 30–34.

(10) Venkatramu, V.; León-Luis, S. F.; Rodríguez-Mendoza, U. R.; Monteseguro, V.; Manjón, F. J.; Lozano-Gorrín, A. D.; Valiente, R.; Navarro-Urrios, D.; Jayasankar, C. K.; Muñoz, A.; Lavín, V. Synthesis, Structure and Luminescence of Er^{3+}-Doped $Y_3Ga_5O_{12}$ Nano-Garnets. *J. Mater. Chem.* **2012**, *22* (27), 13788-13799.

(11) Lupei, V. RE^{3+} Emission in Garnets: Multisites, Energy Transfer and Quantum Efficiency. *Opt. Mater.* **2002**, *19* (1), 95–107.

(12) Papagelis, K.; Arvanitidis, J.; Kanellis, G.; Ves, S.; Kourouklis, G. A. High-Pressure Effects on the Raman Spectrum and the Force Constants of the Rare-Earth Aluminium Garnets ($RE_3Al_5O_{12}$). *J. Phys. Condens. Matter* **2002**, *14* (15), 3875-3890.

(13) Fibrich, M.; Hamálek, T.; Němec, M.; Šulc, J.; Jelínková, H. Multiline Generation Capabilities of Diode-Pumped Nd:YAP and Nd:YAG Lasers. *Laser Phys.* **2014**, *24* (3), 035803 (5pp).

(14) Hernández-Rodríguez, M. A.; Lozano-Gorrín, A. D.; Martín, I. R.; Rodríguez-Mendoza, U. R.; Lavín, V. Spectroscopic Properties of Nd^{3+} Ions in YAP Nano-Perovskites. *J. Lumin.* **2017**, *188*, 204–208.

(15) Rodríguez-Mendoza, U. R.; León-Luis, S. F.; Muñoz-Santiuste, J. E.; Jaque, D.; Lavín, V. Nd^{3+}-Doped $Ca_3Ga_2Ge_3O_{12}$ Garnet: A New Optical Pressure Sensor. *J. Appl. Phys.* **2013**, *113* (21), 213517 (8pp).

(16) Kamińska, A.; Buczko, R.; Paszkowicz, W.; Przybylińska, H.; Werner-Malento, E.; Suchocki, A.; Brik, M.; Durygin, A.; Drozd, V.; Saxena, S. Merging of the $^4F_{3/2}$ Level States of Nd^{3+} Ions in the Photoluminescence Spectra of Gadolinium-Gallium Garnets under High Pressure. *Phys. Rev. B* **2011**, *84* (7), 075483 (6pp).

(17) Kobyakov, S.; Kamińska, A.; Suchocki, A.; Galanciak, D.; Malinowski, M. Nd^{3+}-Doped Yttrium Aluminum Garnet Crystal as a near-Infrared Pressure Sensor for Diamond Anvil Cells. *Appl. Phys. Lett.* **2006**, *88* (23), 2004–2006.

(18) Kamińska, A.; Kaczor, P.; Durygin, A.; Suchocki, A.; Grinberg, M. Low-Temperature High-Pressure Spectroscopy of Lanthanum Lutetium Gallium Garnet Crystals Doped with Cr^{3+} and Nd^{3+}. *Phys. Rev. B* **2002**, *65* (10), 104106–104113.

(19) León-Luis, S. F.; Muñoz-Santiuste, J. E.; Lavín, V.; Rodríguez-Mendoza, U. R. Optical Pressure and Temperature Sensor Based on the Luminescence Properties of Nd^{3+} Ion in a Gadolinium Scandium Gallium Garnet Crystal. *Opt. Express* **2012**, *20* (9), 10393-10398.

(20) V. Venkatramu, M. Giarola, G. Mariotto, S. Enzo, S. Polizzi, C. K. Jayasankar, F. Piccinelli, M. Bettinelli, and A. Speghini. Nanocrystalline lanthanide-doped $Lu_3Ga_5O_{12}$ garnets: interesting materials for light-emitting devices. *Nanotechnology* **2010**, 21(17), 175703

(21) A. Speghini, F. Piccinelli, and M. Bettinelli. Synthesis, characterization and luminescence spectroscopy of oxide nanopowders activated with trivalent lanthanide ions: The garnet family". *Opt. Mater*. **2011** 33(3), 247–257.

(22) R. Krsmanović, V. A. Morozov, O. I. Lebedev, S. Polizzi, A. Speghini, M. Bettinelli, and G. Van Tendeloo. Structural and luminescence investigation on gadolinium gallium garnet nanocrystalline powders prepared by solution combustion synthesis. *Nanotechnology*. **2007**, 18(32), 325604.

(23) R. Naccache, F. Vetrone, A. Speghini, M. Bettinelli, and J. A. Capobianco, "Cross relaxation and upconversion processes in Pr^{3+} singly doped and Pr^{3+}/Yb^{3+} codoped nanocrystalline

Gd3Ga5O12: The sensitizer/activator relationship," *J. Phys. Chem. C.* **2008** 112(20), 7750–7756.

(24) Rietveld, H. M. A Profile Refinement Method for Nuclear and Magnetic Structures. *J. Appl. Phys.* **1969**, *2*, 65–71.

(25) Rodríguez-Carvajal, J. Recent Advances in Magnetic Structure Determination by Neutron Powder Diffraction. *Phys. B Condens. Matter* **1993**, *192* (1–2), 55–69.

(26) Hernández-Rodríguez, M. A.; Monteseguro, V.; Lozano-Gorrín, A. D.; Manjón, F. J.; González-Platas, J.; Rodríguez-Hernández, P.; Muñóz, A.; Lavín, V.; Rodríguez-Mendoza, U. R. Structural , Vibrational , and Elastic Properties of Yttrium Orthoaluminate Nanoperovskite at High Pressures. *J. Phys. Chem. C* **2017**, *121*, 15353–15367.

(27) Vasylechko L.; Senyshyn A.; Bismayer U. Perovskite-type Aluminates and Gallates, in: Handbook on the Physics and Chemistry of Rare Earths. Gschneidner K.A., Jr, Bünzli J.-C.G., Pecharsky V.K., editors,vol. 39, p. 113–295. North-Holland (The Netherlands, 2009).

(28) Monteseguro, V.; Rathaiah, M.; Linganna, K.; Lozano-Gorrín, A. D.; Hernández-Rodríguez, M. A.; Martín, I. R.; Babu, P.; Rodríguez-Mendoza, U. R.; Manjón, F. J.; Muñoz, A.; et al. Chemical Pressure Effects on the Spectroscopic Properties of Nd^{3+}-Doped Gallium Nano-Garnets. *Opt. Mater. Express* **2015**, *5* (8), 1661-1673.

(29) Kaminskii, A. A. *Laser Crystals*; Springer-Verlag: Berlin, 1981.

(30) Duan, C. K.; Tanner, P. A.; Makhov, V. N.; Kirm, M. Vacuum Ultraviolet Spectra and Crystal Field Analysis of $YAlO_3$ Doped with Nd^{3+} and Er^{3+}. *Phys. Rev. B* **2007**, *75* (19), 1–12.

(31) Bungenstock, C.; Tröster, T.; Holzapfel, W. B.; Bini, R.; Ulivi, L.; Cavalieri, S. Study of the Energy Level Scheme of Pr^{3+}:LaOCl under Pressure. *J. Phys. Condens. Matter* **1998**, *10*, 9329–9342.

(32) Karayianis, N.; Wortmann, D.E.; Morrison, C. A. *Solid State Commun.* 18 (1976) 1299- 1302

(33) Deb, K. K. Crystal Field Splittings and Luminescence Properties for Nd^{3+}, Er^{3+} and Dy^{3+} in

Yttrium Orthoaluminate ($YAlO_3$). *J. Phys. Chem. Solids* **1982**, *43* (9), 819–823.

(34) Faucher, M.; Garcia, D.; Moune, O. K. Crystal Field Effects in Rare Earth Compounds Influence of Second Nearest Neighbours. *J. Lumin.* **1992**, *51*, 341–350.

(35) Judd, B.R.; Lo, E. *J. Phys.: Condens. Matter* 6 (1994) L799.

(36) Chen, X.; Liu, G.; Margerie, J.; Reid, M. F. A Few Mistakes in Widely Used Data Files for f^N Configurations Calculations. *J. Lumin.* **2008**, *128*, 421–427.

(37) Muñoz Santiuste, J.E.; Lavín, V.; Rodríguez-Mendoza, U. R.; Tardio, M. M.; Ramírez-Jiménez, R. Pressure-Induced Effects on the Spectroscopic Properties of Nd^{3+} in MgO:$LiNbO_3$ Single Crystal. A Crystal Field Approach. *J. Lumin.* **2017**, *184*, 293-303.

(38) Manjón, F. J.; Jandl, S.; Riou, G.; Ferrand, B.; Syassen, K. Effect of Pressure on Crystal-Field Transitions of Nd-Doped YVO 4. *Phys. Rev. B* **2004**, *69*, 165121–165127.

SUPPLEMENTARY MATERIAL

Contents

Note: Table 1 and all figures cited here are included in the main paper.

S1. Simulation details

The energy level scheme of trivalent Nd^{3+} ion in $YAlO_3$ was reproduced by solving the total Hamiltonian acting within the $4f^3$ configuration. This Hamiltonian is divided into two main parts: the free-ion Hamiltonian $H_{FREE\text{-}ION}$, which includes as principal contributions the Coulomb repulsion and the spin-orbit coupling, mainly responsible for the shift of barycenters of the $^{2S+1}L_J$ multiplets, and the crystal-field Hamiltonian H_{CF}, which reflects the point group symmetry of the site occupied by the Nd^{3+} ion in the matrix and accounts for the hyperfine structure of Stark levels after the breakdown of the degeneracy of the multiplets in a solid.[1] The angular parts of the Hamiltonian are solved using the group theory, whereas the radial parts are parametrized and must be fitted with the experimental energy levels. Thus the total Hamiltonian can be expressed as, [1]

$$H = H_{FREE-ION} + H_{CF} = H_{FREE-ION} + \sum_{k=2,4,6}\sum_{q=-k}^{k} B_q^k \cdot C_q^k$$

$$= E_{AV} + \sum_{k=2,4,6} F^{(k)} \cdot \hat{f}_k + \zeta_{4f} \cdot \sum_{i=1}^{N} \widehat{s_i} \cdot \widehat{l_i} + \alpha \cdot \hat{\boldsymbol{L}}^2 + \beta \cdot \hat{G}(G_2) + \gamma \cdot \hat{G}(R_2)$$

$$+ \sum_{j=0,2,4} M^{(j)} \cdot \widehat{m_j} + \sum_{k=2,4,6} P^{(k)} \cdot \hat{p}_k + \sum_{r=2,3,4,6,7,8} T^{(r)} \cdot \hat{t}_r$$

$$+B_0^2 \cdot C_0^2 + B_2^2 \cdot (C_{-2}^2 + C_2^2)$$

$$+B_0^4 \cdot C_0^4 + B_2^4 \cdot (C_{-2}^4 + C_2^4) + i \cdot B'^4_2 \cdot (C_{-2}^4 + C_2^4) + B_4^4 \cdot (C_{-4}^4 + C_4^4) + i \cdot B'^4_4 \cdot (C_{-4}^4 + C_4^4)$$

$$+B_0^6 \cdot C_0^6 + B_2^6 \cdot (C_{-2}^6 + C_2^6) + i \cdot B'^6_2 \cdot (C_{-2}^6 + C_2^6) + B_4^6 \cdot (C_{-4}^6 + C_4^6) + i \cdot B'^6_4 \cdot (C_{-4}^6 + C_4^6)$$

$$+B_6^6 \cdot (C_{-6}^6 + C_6^6) + i \cdot B'^6_6 \cdot (C_{-6}^6 + C_6^6)$$

(1)

There are 20 adjustable parameters corresponding to the free-Nd^{3+} ion Hamiltonian, whereas for the crystal-field one the number of parameters depends on the point symmetry of the lanthanide ion in the host. In the case of YAP, Nd^{3+} ion substitutes the Y^{3+} one in the

dodecahedral site of C_S (C_{1h}) point symmetry (only one plane of symmetry), low enough to completely break the degeneracies of the $^{2S+1}L_J$ multiplets. Non-zero parameters are limited to even values of k and q, due to symmetry considerations. The adequate election of axes leads to a model Hamiltonian with only 14 independent real and imaginary CF parameters to describe this system, as shown in Eq. (1).[2]

Handing such a large number of CF parameters will lead to different sets of results, without any link between them, which may fit the experimental levels at ambient conditions; a situation that can be chaotic at high pressures. Thus, the strategy followed in the calculation of the CF parameters has been obtaining their values based on the crystallographic positions of the Nd^{3+} ion and its 12 oxygen ligands, obtained by *ab initio* calculations at high pressures. [3] From the YO_{12} crystallographic data, and assuming a small distortion of the site when occupied by a larger Nd^{3+} ion, it is possible to calculate the values of the CF parameters by using the Simple Overlap Model (SOM). [4] We have selected this model due of its simplicity, since it uses only the nearest coordination environment of the Nd^{3+} ion, which is usually well resolved. In this model the CF parameters are given by

$$B_q^k = e^2 \sum_{L=1}^{N} g_L \, \rho \left(\frac{2}{1 \pm \rho}\right)^{k+1} \frac{\langle r^k \rangle}{R_L^{k+1}} \sqrt{\frac{4\pi}{2k+1}} \, (-1)^q \, Y_k^{-q}(\theta_L, \varphi_L) \tag{2}$$

where ρ is the overlap between the rare-earth cation and the ligand orbitals; the ± sign characterizes the displacement of the charge barycenter from the average cation-ligands distance; $\langle r^k \rangle$ are the radial expectation values of the rare-earth ion (Freeman values) [5] and the sum is extended only to the first coordination sphere around the optically active ion.

In this expression, $q_L = g_L\rho$ represent the effective charge of the cation-ligand bond in electron charge units and the factor $[2/(1 \pm \rho)]^{k+1}$ plays the role of a shielding factor. [6,7] The effective charges, used in the SOM, are proportional to the overlap ρ and must be also proportional to the bond strengths s_L that we will assume follow an exponential dependence with the bond length, as in the usual bond valence model, [8] $s_L = \exp((A - R_L)/b)$, and must obey the valence sum rule, $\sum_L s_L = v$, i.e., the sum of the bond strengths for a given cation is equal to its valence *v*. [9] Thus to correlate the bond-distance and the bond-valence, and additionally fulfil the superposition model requirements, the overlap is taken as a constant (a value of ρ = 0.05 is used [4]) and the effective charge is described by an exponential law with the distance in the form:

$$q_L = g_L\rho = g_0\rho s_L = g_0\rho \cdot exp[(\mathrm{A} - R_L)/b] \tag{3}$$

in which g_0 is a charge factor accounting for the introduction of the overlap ρ in relating effective charge and valence; R_L is the observed bond length; *A* is a parameter that represent the smallest length of a bond; and *b* is a measure of the softness of the interaction between the two atoms which value is usually set to 0.37 Å.[8]

In addition, and in order to simplify the description of the crystal-field interaction, Auzel [10,11] and Chang *et al.*[12] have introduced the rotationally invariant crystal-field strength parameter *S*, which roughly speaking, provides the maximum splitting of each $^{2S+1}L_J$ multiplet

$$S = \left[\sum_{k=2,4,6} \left(S^{(k)}\right)^2\right]^{1/2} = \left[\frac{1}{3}\sum_{k=2,4,6} \frac{1}{2k+1}\left(\left(B_0^k\right)^2 + 2\sum_{\substack{q\le k \\ q>0}}\left(\left(B_q^k\right)^2 + \left(B'^k_q\right)^2\right)\right)\right]^{1/2} \tag{4}$$

From these values, it is possible to separate and estimate in percentage the *k*-rank contribution to the *S* parameter as [13]

$$\%S^{(k)} = 100\left(\frac{S^{(k)}}{S}\right)^2 \quad (5)$$

that characterizes the influence of the ligands´ charge at short (*k*=6), medium (*k*=4), and long (*k*=2) average metal-ligands distances.

S2. Simulation procedures

S2.1 Simulation at ambient pressure

We have used the free-ion and CF parameters obtained by Duan *et al*.,[2] who chose arbitrarily zero values for B'^6_4 and B^6_6 parameters (see Table 1 of the main paper), to fit the experimental energy levels collected by Kaminskii. [14] This simulation (I, in Table T3 and Table 1 of the main paper) gives a *rms* uncertainty of around 12 cm^{-1}, although some reported energy level positions are doubtful and have not been used in this estimation, e.g. the lowest $^4G_{5/2}$ Stark level at 16849 cm^{-1} given by Weber & Varitimos [15] corresponds to a transition from the first $^4I_{9/2}$ Stark level.[2] Keeping the same free-ion parameters obtained by Duan *et al*.,[2] SOM model has been used to obtain the CF parameters taking into account the available crystallographic data of yttrium dodecahedron site (see Simulation II in Table T3 and Table 1 of the main paper).[3] In this SOM simulation it has been assumed an effective charge for oxygen ions that follows the exponential dependence of Eq. (3) with A=1.997 Å, giving a relative valence of -3 for the 12 oxygen ligand ions, a value of $g_0 = 2.6$ as charge factor in Eq. (3), and the minus sign is used in Eq. (2) indicating a relatively

covalent Nd-O bonding. Obtained parameters are reported in Table 1 of the main paper and calculated energy levels in Table T3.

It is worth noting that no changes in free-ion parameters are observed (an E_{AVE} variation of only 2 cm^{-1} is the only noticeable change), but the set of calculated CF parameters are slightly different to those of Duan *et al*.[2] A more careful look at these parameters let us conclude that all of them have the same sign and only important differences are observed for B_2^4, B'^4_2 , B_2^6, and B'^6_2 , as well as for B'^4_4 and B_6^6 CF parameters that are no longer zero. It is worth noting that all the CF strength parameters calculated using these fittings can be considered equivalents with a value ranging from 561 to 566 cm^{-1}, indicating the goodness of the simulations (I, II, and III) made.

S2.2 Simulation at high pressures

To simulate these displacements, only $F^{(2)}$ Slater parameter was allowed to vary freely, together with the average energy of the $4f^3$ configuration, $E_{AVG.}$ The other Slater integrals were restricted to those $F^{(k)}/F^{(2)}$ ratios obtained in the ambient pressure fitting and the rest of the free-ion parameters were held fixed in the simulation procedure. Thus, only two free-ion, or atomic, parameters were used to describe the barycenters shifts. In addition, the spin-orbit parameter ζ_{4f} was kept constant to its ambient conditions value (see Fig. 5), since there are only two experimental multiplets that can be used to calculate it and compare its variation with pressure. Anyhow, appears evident that the small change with pressure, expected in this parameter, can be disregarded in this simulation. In addition, the parameter *A* in equation Eq. (3) has been changed to fulfil valence sum rule at each pressure obtaining a variation from *A*=1.997 Å, at ambient pressure, to *A*=1.925 Å, at 30 GPa.

Thus, relating the structural modifications with the variation of the CF parameters is not an easy task, particularly in low local symmetries. Typical variations of the magnitudes of CF parameters ranges from 100 to 250 cm^{-1} up to ~30 GPa, except for remarkable variations of the B_4^4, B_4^6 and B_6^6 real CF parameters and their imaginary parts, showing larger sensibilities to pressure with variations of ~400 cm^{-1} that increases up to 1100 cm^{-1} for the imaginary B'^6_4 sixth-rank CF parameter. This fact can be attributed to some angular displacement resulting from local rearrangement of ions at medium and short distances that, in addition, results in increases of the "*length*" $\sqrt{(B_q^k)^2 + (B'^k_q)^2}$ of these complex parameters.

The simulated maximum splitting rates of these multiplets up to ~30 GPa are, assuming linear variations, $\Delta E(Z_5\text{-}Z_1)$= +5.8 cm^{-1}/GPa for the $^4I_{9/2}$ ground state, $\Delta E(Y_6\text{-}Y_1)$=+3.56 cm^{-1}/GPa for the $^4I_{11/2}$ first excited multiplet, and $\Delta E(R_2\text{-}R_1)$= +0.44 cm^{-1}/GPa for the $^4F_{3/2}$ emitting multiplet. These simulated results are in reasonable agreement with the experimental ones, except for the splitting of the $^4F_{3/2}$ lowest emitting level that varies with a rate of +0.22 cm^{-1}/GPa and it is clearly overestimated compared to the experimental results that do not show appreciably changes with pressure (see Fig. 3). This feature indicates that B_q^2 parameters, the main responsible of the splitting of the $^4F_{3/2}$ emitting level, are overestimated using SOM.

S3. Tables

Table T1. Cell parameters and agreement factors obtained from the Rietveld fitting

Compound	*a* (Å)	*b* (Å)	*c* (Å)	χ^2	R_p	R_{wp}	R_{exp}
$YAlO_3$: Nd^{3+} 1.0%	5.33	7.38	5.18	3.66	7.21	10.8	1.78

Table T2. Identification of the Nd^{3+} emission lines associated with the $^4F_{3/2}(R_{1,2})\rightarrow{}^4I_{9/2}(Z_{1\text{-}5})$ and $^4F_{3/2}(R_{1,2})\rightarrow{}^4I_{11/2}(Y_{1\text{-}6})$ transitions between Stark levels and the slopes of the linear fits of their evolutions with pressure.

$^4F_{3/2}\rightarrow{}^4I_{9/2}$ Stark levels $R_i\rightarrow Z_j$	E_0 (cm^{-1}) at 1 atm	Linear fit slope (cm^{-1}/GPa)	$^4F_{3/2}\rightarrow{}^4I_{11/2}$ Stark levels $R_i\rightarrow Y_j$	E_0 (cm^{-1}) at 1 atm	Linear fit slope (cm^{-1}/GPa)
2-1	11546	+1.75	2-1	9519	+0.31
2-2; 1-1	11422	+1.53	2-2	9447	-0.56
2-3	11337	+0.94	1-1	9395	+0.23
1-2	11307	+0.64	2-3	9388	-1.25
1-3	11214	+0.77	1-2	9322	-0.69
2-4	11046	-2.43	2-4	9278	--
1-4	10922	-2.57	1-3	9262	-1.43
2-5	10879	-4.58	2-5	9224	-3.15
1-5	10755	-4.70	2-6	9170	--
			1-4	9156	-3.10
			1-5	9099	-3.18
			1-6	9043	-3.69

Table T3. Experimental and calculated Nd^{3+} Stark energy levels at ambient conditions in $YAlO_3$.

$^{2S+1}L_J$ multiplet (degeneracy) Barycenter (cm^{-1}) and shift under pressure (cm^{-1}/GPa)	**Experimental** Energy levels (cm^{-1}) Kaminskii [14] 77 K	**Experimental** Energy levels (cm^{-1}) Weber & Varitimos [15] RT	**Simulation I** Calculated Energy levels (cm^{-1}) Duan *et al.*[2] rms= 12 cm^{-1}	**Simulation II** Calculated Energy levels (cm^{-1}) rms=18 cm^{-1}	**Simulation III** Calculated Energy levels (cm^{-1}) rms=12 cm^{-1}
$^4I_{9/2}$(5)	0	0	5	0	4
	118	117	121	107	123
364 (+4.5)	212	211	207	212	213
	500	499	498	538	505
	671	670	671	649	669
$^4I_{11/2}$(6)	2023	2023	2013	2018	2017
	2097	2098	2096	2091	2099
2217 (+4.7)	2158	2157	2156	2164	2157
	2264	2269	2260	2280	2265
	2323	2320	2322	2316	2324
	2378	2368	2378	2367	2378
$^4I_{13/2}$(7)	3953	3953	3939	3941	3942
	4021	4017	4013	4046	4018
4185 (+4.8)	4092	4087	4086	4060	4084
	4200	4190	4184	4208	4189
	4291	4285	4280	4272	4286
	4328	4324	4326	4318	4325
	4446	4439	4437	4432	4437
$^4I_{15/2}$(8)	5757	5760	5747	5735	5749
	5893	5896	5892	5944	5899
6224 (+5.0)	6011	6011	6024	5992	6018
	6240	6199	6226	6238	6238
	6307	6242	6311	6327	6313
	6402	6311	6402	6398	6402
	6687	6404	6687	6675	6690
	6743	6748	6740	6750	6746
$^4F_{3/2}$(2)	11421	11419	11421	11421	11421
11496 (+2.7)	11550	11542	11527	11533	11532
$^4F_{5/2}$(3)	12411	12302	12389	12389	12392
	12447	12413	12446	12449	12452
12529 (+2.8)	12511	12450	12501	12510	12500

$^{2}H_{9/2}(5)$	12561	12513	12554	12549	12553
	12593	12561	12597	12587	12597
12695 (+3.9)	12713	12715	12712	12717	12717
	12742	12745	12772	12774	12774
	12883	12887	12864	12869	12868
$^{4}F_{7/2}(4)$	13323	13332	13317	13316	13317
	13452	13455	13453	13459	13455
13492 (+3.0)	13565	13566	13568	13564	13570
	13589	13590	13577	13583	13581
$^{4}S_{3/2}(2)$	13607	13608	13598	13604	13601
	13651	13652	13646	13649	13650
13577 (+2.9)					
$^{4}F_{9/2}(5)$	14665	14680	14673	14688	14673
	14723	14730	14724	14705	14726
14767 (+3.4)	14740	14746	14739	14736	14741
	14793	14795	14781	14790	14784
	14928	14925	14913	14920	14916
$^{2}H_{11/2}(6)$	15858	15865	15894	15890	15894
	15893		15898	15901	15900
16002	15903	15906	15915	15921	15918
	15995	15992	15969	15967	15971
	16095	16095	15979	15979	15983
			16053	16054	16056
$^{4}G_{5/2}(3)$	16963	16964	16961	16942	16959
	17023	17027	17011	17028	17027
17120	17116		17109	17122	17112
$^{2}G_{7/2}(4)$	17295	*17114	17271	17283	17275
	17313	17310	17324	17330	17321
17255	17364	17367	17347	17361	17353
	17456	17458	17452	17436	17454
$^{4}G_{7/2}(4)$	18846	18850	18834	18837	18839
	18893	18896	18888	18884	18886
19029	18975	18972	18977	19006	18988
	19077	19073	19094	19085	19103
$^{2}G_{9/2}(5)$	19245	19234	19245	19242	19250
	19309	19301	19304	19336	19311
19418	19350	19342	19363	19379	19365
	19425		19392	19401	19398
	19546	19547	19412	19436	19412

$^2K_{13/2}(7)$			19499	19481	19500
	19637		19518	19513	19524
19589	19652		19554	19533	19554
	19747		19662	19625	19653
	19806		19751	19752	19745
	19873		19882	19890	19887
	19924		19961	19983	19970
$^2K_{15/2}(8)$		*20774			
	20865	20832	20855	20857	20853
21059	20894	20887	20873	20862	20873
	20955	20946	20893	20903	20902
$^4G_{9/2}(5)$	21041	21034	20943	20941	20947
			20977	21002	20987
21116	21110	21103	21035	21061	21037
	21231	21232	21101	21125	21108
$^2D_{3/2}(2)$	21276	21288	21214	21221	21225
	21294		21267	21247	21269
21338	21367		21312	21306	21311
	21464		21373	21351	21377
$^4G_{11/2}(6)$	21536	21525	21469	21458	21463
	21580		21512	21509	21514
21569	21630		21574	21577	21577
	21654		21628	21620	21620
	21718		21641	21640	21645
	21748	21745	21704	21705	21703
	21834	21835	21748	21762	21742
	21906		21847	21854	21846
	21930	21924	21913	21894	21925
			21940	21963	21942
$^2P_{1/2}(1)$	23164	23151	23156	23155	23158
23161					

In ref. [15] the lowest $^4G_{5/2}$ Stark level at 16849 cm^{-1} corresponds to a transition from the first $^4I_{9/2}$ Stark level (see ref. [2]).

S4. References

(1) Wybourne B.G., Spectroscopic Properties of Rare Earths Wiley-Interscience (New York, 1965).

(2) Duan, C. K.; Tanner, P. A.; Makhov, V. N.; Kirm, M. Vacuum Ultraviolet Spectra and Crystal Field Analysis of $YAlO_3$ Doped with Nd^{3+} and Er^{3+}. *Phys. Rev. B* **2007**, *75* (19), 1–12.

(3) Hernández-Rodríguez, M. A.; Monteseguro, V.; Lozano-Gorrín, A. D.; Manjón, F. J.; González-Platas, J.; Rodríguez-Hernández, P.; Muñóz, A.; Lavín, V.; Rodríguez-Mendoza, U. R. Structural , Vibrational , and Elastic Properties of Yttrium Orthoaluminate Nanoperovskite at High Pressures. *J. Phys. Chem. C* **2017**, *121*, 15353–15367.

(4) Malta, O. L. Theoretical Crystal-Field Parameters For The YOCl: Eu^{3+} System. A Simple Overlap Model. *Chem. Phys. Lett.* **1982**, *88*, 353–356.

(5) Freeman, A.J.; Watson R.E., Theoretical Investigation of Some Magnetic and Spectroscopic Properties of Rare-Earth Ions, *Phys. Rev.* **1962**, *127 (6)*, 2058-2075.

(6) Malta, O.L.; Brito, H.F.; Menezes, J.F.S.; Gonçalves e Silva, F.R.; Alves Jr., S.; Farias Jr., F.S.; de Andrade, A.V.M. Spectroscopic properties of a new light-converting device Eu(thenoyltrifluoroacetonate)3 2(dibenzyl sulfoxide). A theoretical analysis based on structural data obtained from a sparkle model. *J. Lumin.* **1997**, *75*, 255-268.

(7) Freire, R.O.; Mesquita, M.E.; Couto dos Santos, M.A.; da Costa Jr., N.B. Sparkle model and photophysical studies of Europium $BiqO_2$-cryptate. *Chem. Phys. Lett.* **2007**, *442*, 488-491.

(8) Brown, I. D. Recent Developments in the Methods and Applications of the Bond

Valence Model. *Chem. Rev.* **2009**, *109*, 6858–6919.

(9) Albuquerque, R.Q.; Rocha, G.B.; Malta, O.L.; Porcher, P. On the charge factors of the simple overlap model for the ligand field in lanthanide coordination compounds. *Chem. Phys. Lett.* **2000**, *331*, 519-525.

(10) Auzel, F. L'Auto-Extinction de Nd^{3+}: Son Mecanisme Fondamental et Critere Predictif Simple Pour Les Materiaux Minilaser. *Mater. Res. Bull.* **1979**, *14*, 223–231.

(11) Auzel, F.; Malta, O. L. A Scalar Crystal Field Strength Parameter for Rare-Earth Ions : Meaning and Usefulness. *J. Phys.* **1983**, *44*, 201–206.

(12) Chang, N. C.; Gruber, J. B.; Leavitt, R. P.; Morrison, C. A.; Chang, N. C.; Gruber, J. B. Optical Spectra, Energy Levels, and Crystal-field Analysis of Tripositive Rare Earth Ions in Y_2O_3 . I . Kramers Ions in C_2 Sites. *J. Chem. Phys.* **1982**, *76*, 3877–3889.

(13) Muñoz-Santiuste, J. E.; Rodríguez-Mendoza, U. R.; González-platas, J.; Lavín, V. Structural Study of the Eu^{3+} Environments in Fluorozirconate Glasses : Role of the Temperature-Induced and the Pressure-Induced Phase Transition Processes in the Development of a Rare Earth's Local Structure Model. *J. Chem. Phys.* **2009**, 130, 154501–154518.

(14) Kaminskii, A. A. *Laser Crystals*; Springer-Verlag: Berlin, 1981.

(15) Weber, M. J.; Varitimos, T. E. Optical Spectra and Intensities of Nd^{3+} in $YAlO_3$. *J. Appl. Phys.* **1971**, *42* (12), 4996-5005.

4.3.2. High pressure sensitivity of anti-Stokes fluorescence in Nd^{3+} doped yttrium orthoaluminate nano-perovskites

Authors: **M.A. Hernández-Rodríguez**, U. R. Rodríguez-Mendoza, V. Lavín, J.E. Muñoz-Santiuste, I. R. Martín and A.D. Lozano-Gorrín

Published in: **Journal of Luminescence;** Volume: **196;** Pages: **20-24;** DOI: doi.org/10.1016/j.jlumin.2017.12.008; Accepted date: **4 December 2017**

In the first part of this article, a study of the Nd^{3+}:$YAlO_3$ nano-perovskite anti-Stokes emission under 785 nm laser excitation at ambient pressure condition was carried out. The spectrum showed several well resolved narrow bands in the 660-760 nm spectral range, which were assigned to transitions between multiplets of the excited state $^4F_{9/2}$ and $^4I_{9/2}$ the ground state ($K_i \rightarrow Z_j$), and those peaks in the 730-760 nm spectral range between multiplets of the $^4F_{7/2}$+$^4S_{3/2}$ excited states and the ground state ($Q_i \rightarrow Z_j$), as it shown in the Fig. 1 of the paper. The mechanism which is responsible of the population of these levels was related to local heating in the sample, as a consequence of high power density excitation due to the employed confocal setup, which condensed the laser beam energy in a micro-size spot.

A study of the dependence of the intensity of anti-Stokes luminescence with the pump power of the excitation of the laser, showed slopes less than 1 for each considered transition. The explanation that supported the former tendency was due to the confocal setup used in the experiment, which focused the laser beam in a surface less than 5 μm, with a maximum of the order of 12 mW, resulting in high power densities and therefore in saturation in the observed emission.

The last part of this work, a high pressure study of anti-Stokes fluorescence spectra of Nd^{3+}:$YAlO_3$ nano-perovskite has been performed from ambient conditions up to 10.32 GPa. As the pressure increased, some loss of structure was observed, mainly the emissions associated to $^4F_{7/2}$+$^4S_{3/2}(Q_{3,4,5,6}) \rightarrow {}^4I_{9/2}(Z_1)$ Stark transitions, which can be correlated with distortions induced by pressure in the surroundings of Nd^{3+} ions, resulting in inhomogeneous broadenings. On the other hand, blue and red induced pressure shift could be observed, which was supported by the comparison of the experimental pressure evolution data with the theoretical ones given by the crystal field analysis.

In general, most of observed bands presented linear pressure-induced shifts, and some of them showing high pressure coefficients (see Fig. 4 of the manuscript), which are comparable with those reported in Cr^{3+}, suggesting the possible application of Nd^{3+}: $YAlO_3$ nano-perovskite as a NIR optical pressure sensor, mostly in those lines with high intensities, which in this case correspond to those assigned to $^4F_{7/2} + {}^4S_{3/2} \rightarrow {}^4I_{9/2}$ transitions from ambient conditions up to 10 GPa.

Journal of Luminescence 196 (2018) 20–24

Contents lists available at ScienceDirect

Journal of Luminescence

journal homepage: www.elsevier.com/locate/jlumin

High pressure sensitivity of anti-Stokes fluorescence in Nd^{3+} doped yttrium orthoaluminate nano-perovskites

M.A. Hernández-Rodríguez[a], U.R. Rodríguez-Mendoza[a,c,*], V. Lavín[a,c], J.E. Muñoz-Santiuste[b,c], I.R. Martín[a,c], A.D. Lozano-Gorrín[a]

[a] Departamento de Física, IMN, and IUdEA, Universidad de La Laguna, Apdo. 456, E-38200 San Cristóbal de La Laguna, Santa Cruz de Tenerife, Spain
[b] Departamento de Física, Escuela Politécnica Superior, Universidad Carlos III de Madrid, Avenida de la Universidad 30, E-28913 Leganés, Madrid, Spain
[c] MALTA Consolider Team, Spain

ARTICLE INFO

Keywords:
Nd^{3+}:$YAlO_3$, Anti-Stokes
Optical pressure sensor
Nano-perovskite

ABSTRACT

Pressure-induced energy shifts of anti-Stokes emissions of Nd^{3+}:$YAlO_3$ nano-perovskite has been studied up to 10 GPa. Emission lines have been identified as thermally-induced transitions between $^4F_{7/2}$, $^4S_{3/2}$, and $^4F_{9/2}$ multiplets and the $^4I_{9/2}$ ground state, which emerge as a consequence of the heat produced in the sample by using a confocal set up, which condenses the energy of the laser beam in a micro-sized spot. Blue and red-shifts have been observed with linear pressure coefficients that range from $+3.15\ cm^{-1}$/GPa to $-7.21\ cm^{-1}$/GPa. These results suggest the use of Nd^{3+}:$YAlO_3$ nano-perovskite in high pressure experiments as an optical pressure sensor in the wavelength interval from 660 to 760 nm.

1. Introduction

Inorganic materials doped with trivalent neodymium (Nd^{3+}) ions have caught attention in several areas, from fundamental science research to industry applications. It is known that Nd^{3+} ions present a strong, broad absorption band around 806 nm and a strong emission near to 1064 nm, leading to a "four-level" laser scheme. Another feature of Nd^{3+} ions is that the $^4F_{3/2}$ lowest emitting level can be easily populated by low-cost commercial laser diodes [1–4]. In addition to this, this ion has several intense pumping levels and efficient up-converted emissions [2,5–9].

Concerning host materials, perovskite crystals have been studied due to their outstanding structural, chemical and physical properties that allow their use in several fields, for instance, laser applications. In particular, $YAlO_3$ has found use as laser crystals [1,4,10–12] (Cr^{3+}, Nd^{3+}, Yb^{3+} and Ho^{3+} doped), scintillator [13–16] (Tm^{3+}, Yb^{3+}, and Ce^{3+} doped), phosphors [17,18] (Mn^{2+} doped and Gd^{3+}-Pr^{3+} co-doped) and as detector material [19] (Mn^{2+} doped). $YAlO_3$ crystals doped with Nd^{3+} ions have been studied for its application as high pressure (HP) optical sensor in the near-infrared (NIR) as well [20]. However, it cannot be forgotten the strong rise of the nanomaterials research the last decade, which has been caught the sight of many scientists from many fields due to the splendid properties that these nano-sized materials present that can be taken advantage in several fields [21]. A special mention must be made to their capability to behave as their bulk counterparts, allowing useful comparisons between them. In this sense, many works have been focused in studies of properties of nanomaterials doped with lanthanide ions, especially in nano-perovskite in ambient conditions, including upconversion (UC) fluorescence studies [22–27].

As far as we know, anti-Stokes fluorescence of Nd^{3+} ions in $YAlO_3$ nano-perovskite at HP conditions has not been studied yet. For this reason, its pressure evolution in the range of 0 ~ 10 GPa is analyzed, focusing in bands corresponding to $^4F_{9/2} \rightarrow {}^4I_{9/2}$, $^2H_{11/2} \rightarrow {}^4I_{11/2}$ and $^4F_{7/2} + {}^4S_{3/2} \rightarrow {}^4I_{9/2}$ transitions, in order to check its viability as an optical pressure sensor working in the NIR.

2. Experimental details

Yttrium orthoaluminate nano-perovskites of composition $Y_{(1-x)}Nd_xAlO_3$, with $x = 1$ mol% was synthesized by sol–gel method in air atmosphere. Stoichiometric molar ratios of high-purity Y $(NO_3)_3{\cdot}4H_2O$ (Aldrich, 99.9%), $Al(NO_3)_3{\cdot}9H_2O$ (Aldrich, 99.9%) and Nd $(NO_3)_3{\cdot}H_2O$ (Aldrich, 99.9%) materials were dissolved in 25 ml of 1 M HNO_3 under stirring at 80 °C (353 K) for 3 h. Then citric acid, with a molar ratio of metal ions to citric acid of 1:2, was added to the solution, which was stirred and heated at 90 °C (363 K) until reaching the transparency of the solution. Then, 4 mg of polyethylene glycol was added to the solution. This last step created a gel that was fired at 400 °C (673 K) for 6 h in order to remove the residual nitrates and

* Corresponding author at: Departamento de Física, Universidad de La Laguna, Apdo. 456, E-38200 San Cristóbal de La Laguna, Santa Cruz de Tenerife, Spain.
E-mail address: urguez@ull.edu.es (U.R. Rodríguez-Mendoza).

https://doi.org/10.1016/j.jlumin.2017.12.008
Received 25 September 2017; Received in revised form 23 November 2017; Accepted 4 December 2017
Available online 05 December 2017

organic compounds, and the subsequently obtained powder sample went through two thermal treatments at 1200 °C (1473 K) and 1500 °C (1773 K) for 20 h and 12 h, respectively. The details of the characteristics of the nanocrystals obtained have not been discussed, since a deep study including XRD measurements was published by the authors elsewhere [28]. The average grains size of the nano-crystal was determined from Scherrer formula, applied on the main peaks of the XRD pattern, resulting in nano-crystals of around 30–40 nm. Besides, the obtained TEM images confirm the mentioned nanometric size (see supplementary information published in [29]). It is worth mentioning that from the point of view of absorption and luminescence properties, our nano-crystals behave like their bulk counterparts [30,31].

Confocal anti-Stokes luminescence images were acquired using a commercial scanning confocal Raman instrument (Renishaw InVia) exciting with a cw diode laser at 785 nm and detecting with a cooled CCD. A 20x SLWD objective was used to achieve a laser-spot diameter of less than 5 μm on the sample. High pressure was generated with a membrane-type diamond anvil cell designed at Université Pierre et Marie Curie (Paris VI). A 200 μm tungsten carbide gasket was pre-indented to 70 μm to make the hydrostatic chamber with typical diameter of 150 μm. For pressure calibrants, ruby chips less than 10 μm was used and 16:3:1 methanol- ethanol-water mixture served as pressure transmitting medium, providing hydrostatic pressures of up to ~16 GPa [32]. The HP luminescence measurements were carried out up to 10.3 GPa.

3. Results and discussion

3.1. Ambient pressure anti-Stokes fluorescence

The anti-Stokes spectrum was obtained under cw excitation at 785 nm, just in the band tail of the $^4I_{9/2} \rightarrow {}^4F_{5/2} + {}^2H_{9/2}$ of the Nd^{3+}:$YAlO_3$ nanocrystals, as can be observed from the diffuse reflectance spectrum [28]. The spectrum shows several well resolved narrow bands in the 660–760 nm spectral range, whereas it is important noting that no more bands were observed for shorter wavelengths (see Fig. 1).

Due to the complexity of the energy level diagram for Nd^{3+} ions, assignation of emission bands is not simple and has been tentatively ascribed according to the partial energy level diagram constructed from our experimental data [28] and those given by Morrison et al [31] for the Nd^{3+}:$YAlO_3$ bulk crystal. A partial energy level diagram is shown in Fig. 2. For the 660–715 nm spectral bulk range, bands observed were assigned to transitions between multiplets of the excited state $^4F_{9/2}$ and

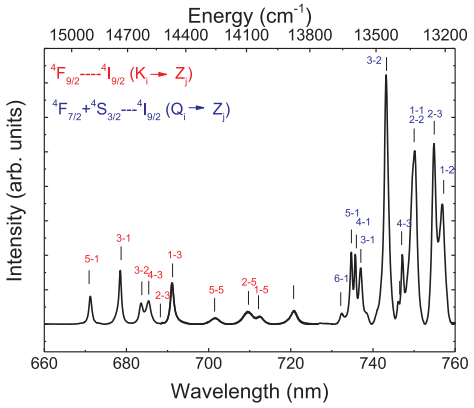

Fig. 1. Ambient pressure anti-Stokes emission spectrum under 785 nm excitation of Nd^{3+}: $YAlO_3$ nano-crystal monitoring the $^4F_{9/2} \rightarrow {}^4I_{9/2}$ and $^4F_{7/2} + {}^4S_{3/2} \rightarrow {}^4I_{9/2}$ transitions. The identification of the Stark levels is also shown.

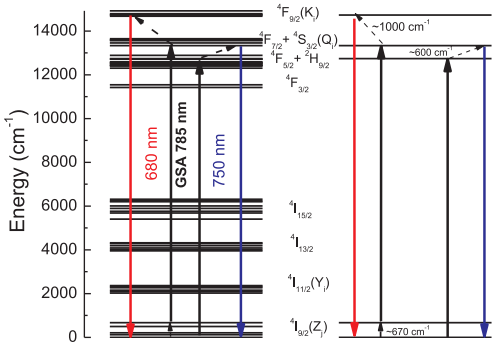

Fig. 2. Partial energy level diagram of Nd^{3+}: $YAlO_3$ nano-crystals. Possible mechanisms of anti-Stokes emission after excitation with 785 nm in $^4F_{5/2} + {}^2H_{9/2}$ states are also depicted.

$^4I_{9/2}$ ground state, and those peaks in the 730–760 nm spectral range between multiplets of the $^4F_{7/2} + {}^4S_{3/2}$ excited states and the ground state. According to Dieke's nomenclature for Stark levels of the Nd^{3+} multiplets, transitions can be written as $^4F_{9/2}(K_{1-5}) \rightarrow {}^4I_{9/2}(Z_{1-5})$ and $^4F_{7/2} + {}^4S_{3/2}(Q_{1-6}) \rightarrow {}^4I_{9/2}(Z_{1-5})$. One of the emission lines observed does not fit with the assignation proposed, in particular that around 720 nm, according to the energy level diagram should correspond to $^2H_{11/2} \rightarrow {}^4I_{11/2}(C_1\text{-}Y_4)$ and, since its intensity vanished with pressure, it has not been subsequent follow-up.

Fluorescence through hot band absorption processes seems to be responsible for the emission observed. Consequently, most likely mechanisms considered for the population of emission states are depicted in (Fig. 2) and can be described as follows: Since five Starks of the ground state $^4I_{9/2}$ shows a maximum energy gap, between the lowest Z_1 and the highest one Z_5, around 670 cm^{-1}, all upper Starks levels of the ground state are thermally populated at relatively low temperatures, favored by the heat transfer supplied from the excitation laser beam. According to Boltzmann factor, and considering this maximum energy gap, the population of Z_5 can be estimated in a 10% at 400 K, this would allow to the one photon pumping excitation at 785 nm to promote resonantly electrons either to $^4F_{5/2} + {}^2H_{9/2}$ or $^4F_{7/2} + {}^4S_{3/2}$ excited states, the latter namely a direct single-photon hot band absorption process (see Fig. 2). Once both states have been populated, emission from the $^4F_{7/2} + {}^4S_{3/2}$ state takes place either by direct excitation or followed by one or multiphonon-assisted transition, which is a non-resonant energy transfer process in which the mismatch in energy between two states involved is compensated by annihilation of one or more phonons, so from the $^4F_{5/2} + {}^2H_{9/2}$ state it can promote the excited ion to the upper $^4F_{7/2} + {}^4S_{3/2}$ state [6,8]. In the case of $^4F_{9/2}$ state it is more likely that took place by a direct excitation of $^4F_{7/2} + {}^4S_{3/2}$ state, followed by a multiphonon-assisted transition, favored by the local heating in the sample, as a consequence of high power density excitation, favoring the population of $^4F_{7/2} + {}^4S_{3/2}$ and $^4F_{9/2}$ thermally coupled states. In this case, the small energy gap between those levels and the excitation energy (~600 cm^{-1} between the excitation energy and $^4F_{7/2} + {}^4S_{3/2}$ states and 1000 cm^{-1} between $^4F_{7/2} + {}^4S_{3/2}$ and $^4F_{9/2}$ states), can be bridged by one or two phonons, respectively, since for this nanocrystal the highest phonon energy is around 650 cm^{-1} [33,34]. Similar results have been found in other Nd^{3+} doped systems like fluorindate glasses, tellurite glasses, $NaYF_4$ crystals and oxyfluoride glass ceramic [6,35–37]. A comparison between the relative intensities of emissions indicates that the most populated state is, as expected, the low-lying $^4F_{7/2} + {}^4S_{3/2}$, since this level can be directly excited with the pumping laser. This assignation will be confirmed in the next section, analyzing the pressure evolution of the energy of these transitions.

Except for the $^4H_{11/2} \rightarrow {}^4I_{11/2}$ $(C_1\text{-}Y_4)$ emission line, the main

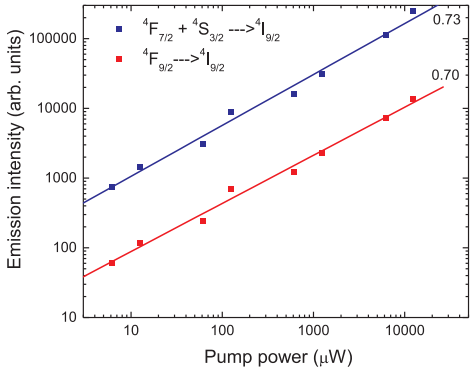

Fig. 3. Pump power dependence of the anti-Stokes emission intensities (peak area) of the Nd^{3+}:$YAlO_3$ nano-perovskites.

arguments of these assignments are, on the one hand, the linear dependence observed for the emission intensity I_{EM} with the excitation pump power P_{PUMP}. As it is known, at low power excitation densities P_{PUMP}, the intensity of the anti-Stokes luminescence I_{EM} is proportional to the n-th power of the IR pumped excitation intensity I_{PUMP}, i.e. $I_{EM} \propto C\ P_{PUMP}{}^n$, where C is a constant and n is the number of IR photons involved in the pumping process. In Fig. 3 the log-log representations of I_{EM} versus P_{PUMP} for emission bands are depicted with slopes close but less than one, indicating one photon mechanisms in the anti-Stokes processes. For I_{EM}, the integrated area of the peaks corresponding to each transition has been considered. On the other hand, the experimental pressure evolution of these bands has been compared to those theoretically calculated from simulation procedures made by the authors, solving the total Hamiltonian of Nd^{3+} in this nano-crystal [38] and will be treated in the next section.

The fact of slopes less than 1 for each transition considered could indicate some kind of saturation in the anti-Stokes emission as a consequence of the increase of temperature as the pump-power of excitation is raised [5,39]. The explanation of the results obtained lies on the setup used to measure the anti-Stokes luminescence [40], in which the confocal microscope focus the spot of the laser in a surface less than 5 μm, with a maximum of the order of 12 mW, resulting in high power densities and, therefore, in saturation in the emission observed [39].

3.2. High pressure anti-Stokes fluorescence

A high pressure study of anti-Stokes fluorescence spectra of Nd^{3+}:$YAlO_3$ nano-perovskite has been carried out from ambient conditions up to 10.3 GPa. Changes in relative intensities of $^4F_{9/2}\rightarrow{}^4I_{9/2}$ and $^4F_{7/2}+{}^4S_{3/2}\rightarrow{}^4I_{9/2}$ transitions occur during pressure increasing, observing a decrease in the intensity of the $^4F_{9/2}\rightarrow{}^4I_{9/2}$ sub-bands related to $^4F_{7/2}+{}^4S_{3/2}\rightarrow{}^4I_{9/2}$ ones, as it can be observed in Fig. 3, where normalized spectra at different pressures are presented. At ambient pressure only 18 emission lines associated with the $^4F_{9/2}\rightarrow{}^4I_{9/2}$, and $^4F_{7/2}+{}^4S_{3/2}\rightarrow{}^4I_{9/2}$ transitions were observed. Upon applying pressure some loss of structure is appreciable mainly in the $^4F_{7/2}+{}^4S_{3/2}(Q_{3,4,5,6})\rightarrow{}^4I_{9/2}(Z_1)$ Stark transitions, which can be correlated with distortions induced by pressure in the surroundings of Nd^{3+} ions, resulting in inhomogeneous broadenings.

In the crystallographic site of the Nd^{3+} ions, the point symmetry group is very low, i.e. C_S ($C_{1\,h}$), with the subsequent breakdown of the $(2J+1)/2$ degeneracies of the $^{2S+1}L_J$ multiplets [38] and the pressure evolution of emission lines of transitions is different depending on the energy positions of Stark levels within each multiplet: higher energy emission lines undergo blue-shifts, in contrast to lower ones which experiment red-shifts (see Fig. 4). This behavior can be explained in

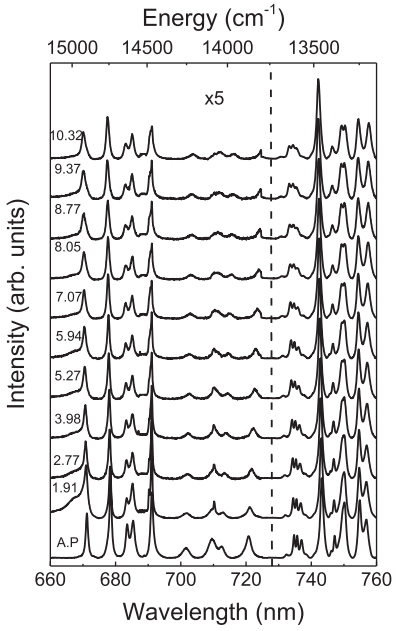

Fig. 4. Anti-Stokes normalized emission spectra under 785 nm excitation of Nd^{3+}: $YAlO_3$ nano-perovskite monitoring the $^4F_{7/2}$ + $^4S_{3/2}\rightarrow{}^4I_{9/2}$ and $^4F_{9/2}\rightarrow{}^4I_{9/2}$, $x^2H_{11/2}\rightarrow{}^4I_{11/2}$ transitions from AP up to 10.32 GPa.

terms of the pressure evolution of the Stark energy levels of Nd^{3+} ions that can be theoretically reproduced by solving the total Hamiltonian acting within the $4f^3$ configuration [41], given by

$$
\begin{aligned}
H &= H_{FREE-ION} + H_{CF} \\
&= H_{FREE-ION} + \sum_{k=2,4,6}\sum_{q=-k}^{k} B_q^k \cdot C_q^k \\
&= E_{AV} + \sum_{k=2,4,6} F^{(k)} \cdot \hat{f}_k + \zeta_{4f} \cdot \sum_{i=1}^{N} \hat{s}_i \cdot \hat{l}_i + \alpha \cdot \hat{L}^2 \\
&\quad + \beta \cdot \hat{G}(G_2) + \gamma \cdot \hat{G}(R_2) + \sum_{j=0,2,4} M^{(j)} \cdot \hat{m}_j \\
&\quad + \sum_{k=2,4,6} P^{(k)} \cdot \hat{p}_k + \sum_{r=2,3,4,6,7,8} T^{(r)} \cdot \hat{t}_r + B_0^2 \cdot C_0^2 \\
&\quad + B_2^2 \cdot (C_{-2}^2 + C_2^2) + i \cdot B_2' 2 \cdot (C_{-2}^2 + C_2^2) + B_0^4 \cdot C_0^4 + B_2^4 \cdot (C_{-2}^4 + C_2^4) \\
&\quad + i \cdot B_2' 4 \cdot (C_{-2}^4 + C_2^4) + B_4^4 \cdot (C_{-4}^4 + C_4^4) + i \cdot B_4' 4 \cdot (C_{-4}^4 + C_4^4) \\
&\quad + B_0^6 \cdot C_0^6 + B_2^6 \cdot (C_{-2}^6 + C_2^6) + i \cdot B_2' 6 \cdot (C_{-2}^6 + C_2^6) + B_4^6 \cdot (C_{-4}^6 + C_4^6) \\
&\quad + i \cdot B_4' 6 \cdot (C_{-4}^6 + C_4^6) + B_6^6 \cdot (C_{-6}^6 + C_6^6) + i \cdot B_6' 6 \cdot (C_{-6}^6 + C_6^6)
\end{aligned}
\tag{1}
$$

As it was already commented in the introduction, a detailed pressure study of the crystal field experimented by Nd^{3+} ions in this host been done by the authors [38]. Briefly speaking, the crystal-field (CF) analysis has been carried out by successfully combining the crystallographic positions of the Nd^{3+} ion and its 12 oxygen ligands at the YO_{12} dodecahedral site in $YAlO_3$ structure, obtained by theoretical ab initio calculations as a function of pressure [29], and the Simple Overlap Model [38]. As a general feature, as pressure increases the volume of the dodecahedral site decreases, giving rise to a smooth enhancement of the crystal-field interaction between the Nd^{3+} ions and its oxygen ligands. Our simulations also show that the energies of the $4f^3$ ground configuration and the barycenters of the multiplets increase.

Table 1
Results of atomic and crystal-field parameters derived from the fittings for Nd^{3+}:$YAlO_3$ at ambient pressure and 10 GPa. All parameters values are given in cm^{-1}.

Atomic parameters	0 GPa	10 GPa	Crystal-field parameters	0 GPa	10 GPa
E_{AV}	24,115	24,123	B_0^2	−487	−413
F^2	70,925	70,805	B_2^2	526	576
F^4	50,794	50,708	B_0^4	−420	−471
F^6	35,424	35,364	B_2^4	594	616
ζ_{4f}	875	875	$B_2'^4$	349	449
α	23	23	B_4^4	−484	−640
β	−691	−691	$B_4'^4$	727	543
γ	1690	1690	B_0^6	−753	−839
T^2	458	458	B_2^6	151	213
T^3	38.4	38.4	$B_2'^6$	−214	−213
T^4	75.8	75.8	B_4^6	1583	1583
T^6	−290	−290	$B_4'^6$	480	920
T^7	237	237	B_6^6	22	−99
T^8	469	469	$B_6'^6$	326	375
M^0	1.9	1.9			
M^2	1.06	1.06			
M^4	0.72	0.72			
P^2	206	206			
P^4	154.5	154.5			
P^6	103	103			

The combination of these effects accounts for the wavelength blue-shift of some Nd^{3+} emission levels (see Fig. 5) [38].

In Table 1, Nd^{3+} free-ion and CF parameters resulting from fittings to experimental data are given for ambient pressure and 10 GPa. Fig. 5(a,b) shows the experimental pressure evolution of the peaks of emission lines belonging to $^4F_{9/2}\rightarrow{}^4I_{9/2}$, and $^4F_{7/2}+{}^4S_{3/2}\rightarrow{}^4I_{9/2}$ transitions, which has been compared with those theoretically simulated from the Hamiltonian analysis. As can be observed, both, the shift trends and the energies, match reasonably well, confirming the assignation of these bands to those transitions previously commented.

In overall, most of observed bands present pressure-induced shifts that can be considered as linear (see Fig. 4a,b). In the case of $^4F_{7/2}+{}^4S_{3/2}\rightarrow{}^4I_{9/2}$ multiplets transitions slopes range from 3.15 cm^{-1}/GPa (Q_6-Z_1) to −1.25 cm^{-1}/GPa (Q_1-Z_2), whereas for $^4F_{9/2}\rightarrow{}^4I_{9/2}$ slopes vary from 2.31 cm^{-1}/GPa (K_5-Z_1) to −7.21 cm^{-1}/GPa (K_1-Z_5). Some of these pressure coefficients are comparable with those obtained for Cr^{3+} in ruby (−7.35 GPa) [42,43], suggesting the possible application of the Nd^{3+}: $YAlO_3$ nano-perovskite as a NIR optical pressure sensor, mostly in those lines with high intensities, which in this case correspond to those assigned to $^4F_{7/2}$ + $^4S_{3/2}\rightarrow{}^4I_{9/2}$ transitions (Fig. 5).

4. Conclusions

Anti-Stokes emission of the Nd^{3+}:$YAlO_3$ nano-perovskite, under 785 nm laser excitation, at ambient and high pressure conditions has been studied. Several narrow emission lines close to the excitation wavelength were observed and associated to transitions between Stark levels of $^4F_{9/2}$, and $^4F_{7/2}+{}^4S_{3/2}$ excited multiplets and the $^4I_{9/2}$ ground state. The identification of these excited states has been made on the basis of the slopes obtained from the log-log representation of I_{EM} versus P_{PUMP}, with values of less than one, indicating a single-photon hot band absorption process followed by multiphonon assisted transferences for the recorded emission. To corroborate this assumption, experimental data have been fitted to the theoretical ones obtained from the resolution of the total Hamiltonian as a function of pressure given by the authors elsewhere. In view of the obtained results it can be concluded the truth of this assumption. The pressure evolution of bands shows different behaviors, highlighting the $^4F_{7/2}$ + $^4S_{3/2}(Q_6)\rightarrow{}^4I_{9/2}(Z_1)$ and $^4F_{9/2}(K_1)\rightarrow{}^4I_{9/2}(Z_5)$ emission lines with linear pressure coefficients of +3.15 cm^{-1}/GPa and −7.21 cm^{-1}/GPa, respectively. These results suggest the possible application of the Nd^{3+}:$YAlO_3$ as a NIR optical pressure sensor in high pressure experiments from ambient conditions up to 10 GPa.

Acknowledgements

This work has been partially supported by MINECO (MAT2013-46649-C4-4-P, MAT2015-71070-REDC, and MAT2016-75586-C4-4-P), and by the EU-FEDER funds. M.A. Hernández-Rodríguez thanks MINECO for FPI grant (BES-2014-068666).

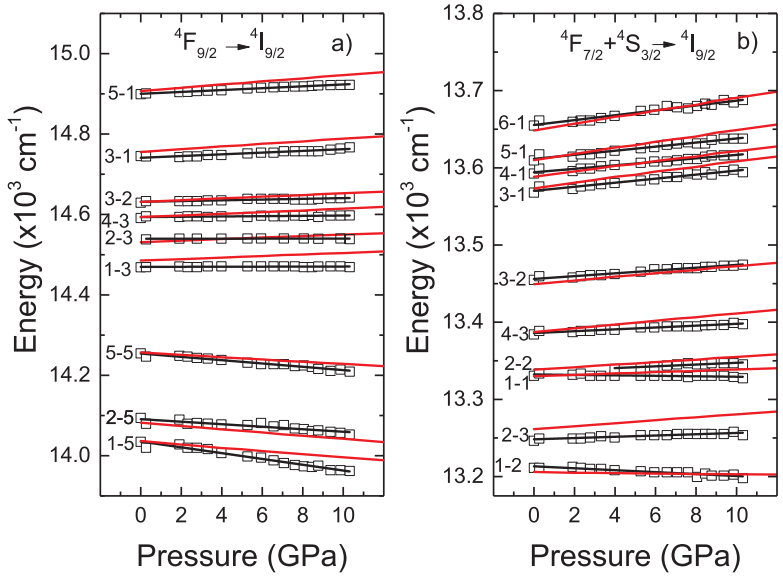

Fig. 5. RT Pressure evolution of emission lines corresponding to a) $^4F_{9/2}\rightarrow{}^4I_{9/2}$, $^2H_{11/2}\rightarrow{}^4I_{11/2}$ and b) $^4F_{7/2}$ + $^4S_{3/2}\rightarrow{}^4I_{9/2}$ transitions form AP up to 10.32 GPa. Experimental data (empty black squares), linear fits (solid black lines) and the theoretical simulation obtained solving the total Hamiltonian (red solid lines) are also included. (For interpretation of the references to color in this figure legend, the reader is referred to the web version of this article.)

References

[1] J.J. Romero, E. Montoya, L.E. Bausá, F. Agulló-Rueda, M.R.B. Andreeta, A.C. Hernandes, Multiwavelength laser action of Nd^{3+}:$YAlO_3$ single crystals grown by the laser heated pedestal growth method, Opt. Mater. 24 (2004) 643–650, http://dx.doi.org/10.1016/S0925-3467(03)00179-4.

[2] I. Iparraguirre, J. Azkargorta, J.M. Fernández-Navarro, M. Al-Saleh, J. Fernández, R. Balda, Laser action and upconversion of Nd^{3+} in tellurite bulk glass, J. Non Cryst. Solids 353 (2007) 990–992, http://dx.doi.org/10.1016/j.jnoncrysol.2006.12.103.

[3] Y. Wei, G. Zhang, C.-H. Huang, H.-Y. Zhu, L.-X. Huang, X.-J. Ou-Yang, G.-F. Wang, A single wavelength 1339 nm Nd: YAP pulsed laser, Opt. Commun. 282 (2009) 4397–4400, http://dx.doi.org/10.1016/j.optcom.2009.07.055.

[4] M. Fibrich, T. Hambálek, M. Němec, J. Šulc, H. Jelínková, Multiline generation capabilities of diode-pumped Nd: YAP and Nd: YAG lasers, Laser Phys. 24 (2014) 35803, http://dx.doi.org/10.1088/1054-660X/24/3/035803.

[5] M. Pollnau, D.R. Gamelin, S.R. Lüthi, H.U. Güdel, M.P. Hehlen, Power dependence of upconversion luminescence in lanthanide and transition-metal-ion systems, Phys. Rev. B. 61 (2000) 3337–3346, http://dx.doi.org/10.1103/PhysRevB.61.3337.

[6] L.D.S. Menezes, G.S. Maciel, C.B. De Araújo, Y. Messaddeq, Thermally enhanced frequency upconversion in Nd^{3+}-doped fluoroindate glass, J. Appl. Phys. 90 (2001) 4498–4501, http://dx.doi.org/10.1063/1.1410326.

[7] I. Iparraguirre, R. Balda, M. Voda, M. Al-saleh, J. Fernandez, Infrared-to-visible upconversion in $K_5Nd(MoO_4)_4$ stoichiometric laser crystal, J. Opt. Soc. Am. B. 19 (2002) 2911–2920, http://dx.doi.org/10.1364/JOSAB.19.002911.

[8] D.Y. Wang, Y. Min, S.D. Xia, V.N. Makhov, N.M. Khaidukov, J.C. Krupa, Upconversion fluorescence of Nd^{3+} ions in K_2YF_5 single crystal, J. Alloy. Compd. 361 (2003) 294–298, http://dx.doi.org/10.1016/S0925-8388(03)00442-0.

[9] R. Balda, J. Fernández, M.A. Arriandiaga, J.M. Fernández-Navarro, Spectroscopy and frequency upconversion in Nd^{3+} -doped TeO_2 –TiO_2 –Nb_2O_5 glass, J. Phys. Condens. Matter 19 (2007) 86223, http://dx.doi.org/10.1088/0953-8984/19/8/086223.

[10] W.S. Rabinovich, S.R. Bowman, B.J. Feldman, M.J. Winings, Tunable laser pumped 3 μm Ho: $YAlO_3$ laser, IEEE J. Quantum Electron. 27 (1991) 895–897.

[11] R. Diehl, G. Brandt, Crystal structure refinement of $YAlO_3$, a promising laser material, Mater. Res. Bull. 10 (1975) 85–90, http://dx.doi.org/10.1016/0025-5408(75)90125-7.

[12] H. Zhang, D. Sun, J. Luo, J. Chen, H. Yang, J. Xiao, Q. Zhang, S. Yin, Growth, thermal, and spectroscopic properties of a Cr,Yb,Ho,Eu: YAP laser crystal, Opt. Mater. 36 (2014) 1361–1365, http://dx.doi.org/10.1016/j.optmat.2014.03.029.

[13] K. Yasuda, S. Usuda, H. Gunji, Properties of a YAP powder scintillator as alpha-ray detector, Appl. Radiat. Isot. 52 (2000) 365–368, http://dx.doi.org/10.1016/S0969-8043(99)00179-7.

[14] T.B. De Queiroz, C.R. Ferrari, D. Ulbrich, R. Doyle, A.S.S. De Camargo, Luminescence characteristics of YAP:Ce scintillator powders and composites, Opt. Mater. 32 (2010) 1480–1484, http://dx.doi.org/10.1016/j.optmat.2010.06.004.

[15] D. Totsuka, T. Yanagida, M. Sugiyama, J. Pejchal, Y. Fujimoto, Y. Yokota, A. Yoshikawa, Investigations of optical and scintillation properties of Tm^{3+}-doped $YAlO_3$, Opt. Mater. 34 (2012) 627–631, http://dx.doi.org/10.1016/j.optmat.2011.09.008.

[16] T. Yasumune, M. Kurihara, K. Maehata, K. Ishibashi, A. Yoshikawa, Scintillation properties of Yb^{3+}-doped $YAlO_3$ in the temperature range from 4.2 to 175 K, Nucl. Instrum. Methods Phys. Res. A 726 (2013) 37–40, http://dx.doi.org/10.1016/j.nima.2013.05.128.

[17] Y. Zhydachevskii, A. Durygin, A. Suchocki, A. Matkovskii, D. Sugak, P. Bilski, S. Warchol, Mn-doped $YAlO_3$ crystal: a new potential TLD phosphor, Nucl. Instrum. Methods Phys. Res. Sect. B. 227 (2005) 545–550, http://dx.doi.org/10.1016/j.nimb.2004.09.013.

[18] Y. Shimizu, K. Ueda, F. Massuyeau, S. Jobic, Preparation of thin films of perovskite-type YAlO3:Gd^{3+}–Pr^{3+} UV phosphors, Thin Solid Films 571 (2014) 90–93, http://dx.doi.org/10.1016/j.tsf.2014.09.075.

[19] Y. Zhydachevskii, A. Suchocki, M. Berkowski, P. Bilski, S. Warchol, Characterization of $YAlO_3$:Mn^{2+} thermoluminescent detectors, Radiat. Meas. 45 (2010) 516–518, http://dx.doi.org/10.1016/j.radmeas.2009.12.035.

[20] H. Hua, Y.K. Vohra, Pressure-induced blueshift of Nd^{3+} fluorescence emission in $YAlO_3$: near infrared pressure sensor, Appl. Phys. Lett. 71 (1997) 2602, http://dx.doi.org/10.1063/1.119341.

[21] E. Roduner, Size matters: why nanomaterials are different, Chem. Soc. Rev. 35 (2006) 583–592, http://dx.doi.org/10.1039/b502142c.

[22] P.J. Dereń, R. Mahiou, R. Pązik, K. Lemanski, W. Stręk, P. Boutinaud, Upconversion emission in $CaTiO_3$:Er^{3+} nanocrystals, J. Lumin. 128 (2008) 797–799, http://dx.doi.org/10.1016/j.jlumin.2007.11.057.

[23] P.J. Dereń, K. Lemański, A. Gągor, A. Watras, M. Małecka, M. Zawadzki, Symmetry of $LaAlO_3$ nanocrystals as a function of crystallite size, J. Solid State Chem. 183 (2010) 2095–2100, http://dx.doi.org/10.1016/j.jssc.2010.07.015.

[24] K. Lemański, A. Gagor, M. Kurnatowska, R. Pzik, P.J. Dereń, Spectroscopic properties of Nd^{3+} ions in nano-perovskite $CaTiO_3$, J. Solid State Chem. 184 (2011) 2713–2718, http://dx.doi.org/10.1016/j.jssc.2011.08.004.

[25] K. Lemański, P.J. Dereń, Luminescent properties of dysprosium(III) ions in LaAlO3 nanocrystallites, J. Rare Earths. 29 (2011) 1195–1197, http://dx.doi.org/10.1016/S1002-0721(10)60625-4.

[26] K. Lemański, P.J. Dereń, Spectroscopic properties of Dy^{3+} ions in $CaTiO_3$ nano-perovskites, J. Lumin. 145 (2014) 661–664, http://dx.doi.org/10.1016/j.jlumin.2013.08.048.

[27] P.J. Dereń, K. Lemański, Cross relaxation in $CaTiO_3$ and $LaAlO_3$ perovskite nanocrystals doped with Ho^{3+} ions, J. Lumin. 154 (2014) 62–67, http://dx.doi.org/10.1016/j.jlumin.2014.04.008.

[28] M.A. Hernández-Rodríguez, A.D. Lozano-Gorrín, I.R. Martín, U.R. Rodríguez-Mendoza, V. Lavín, Spectroscopic properties of Nd^{3+} ions in YAP nano-perovskites, J. Lumin. 188 (2017) 204–208, http://dx.doi.org/10.1016/j.jlumin.2017.04.031.

[29] M.A. Hernández-Rodríguez, V. Monteseguro, A.D. Lozano-Gorrín, F.J. Manjón, J. González-Platas, P. Rodríguez-Hernández, A. Muñoz, V. Lavín, I.R. Martín, U.R. Rodríguez-Mendoza, Structural, vibrational, and elastic properties of yttrium orthoaluminate nanoperovskite at high pressures, J. Phys. Chem. C. 121 (2017) 15353–15367, http://dx.doi.org/10.1021/acs.jpcc.7b04245.

[30] M.J. Weber, T.E. Varitimos, Optical spectra and intensities of Nd^{3+} in $YAlO_3$, J. Appl. Phys. 42 (1971) 4996–5005, http://dx.doi.org/10.1063/1.1659885.

[31] C.A. Morrison, R.P. Leavitt, Handbook on the Physics and Chemistry of the Rare Earths 5 Noth-Holland Publishing Company, Amsterdam, 1982, p. 461.

[32] H.K. Mao, J. Xu, P.M. Bell, Calibration of the ruby pressure gauge to 800 kbar under quasi-hydrostatic conditions, J. Geophys. Res. 91 (1986) 4673, http://dx.doi.org/10.1029/JB091iB05p04673.

[33] A. Chopelas, Single-crystal Raman spectra of $YAlO_3$ and $GdAlO_3$: comparison to several orthorhombic ABO_3 perovskites, Phys. Chem. Miner. 38 (2011) 709–726, http://dx.doi.org/10.1007/s00269-011-0444-1.

[34] M.A. Hernández-Rodríguez, V. Monteseguro, A.D. Lozano-Gorrín, F.J. Manjón, J. González-Platas, P. Rodríguez-Hernández, A. Muñóz, V. Lavín, U.R. Rodríguez-Mendoza, Structural, vibrational, and elastic properties of yttrium orthoaluminate nanoperovskite at high pressures, J. Phys. Chem. C. 121 (2017) 15353–15367, http://dx.doi.org/10.1021/acs.jpcc.7b04245.

[35] M.S. Marques, L.D.S. Menezes, W. Lozano B, L.R.P. Kassab, C.B. De Araújo, Giant enhancement of phonon-assisted one-photon excited frequency upconversion in a Nd^{3+}-doped tellurite glass, J. Appl. Phys. 113 (2013) 053102–053105, http://dx.doi.org/10.1063/1.4789965.

[36] X. Tian, X. Wei, Y. Chen, C. Duan, M. Yin, Temperature sensor based on ladder-level assisted thermal coupling and thermal-enhanced luminescence in $NaYF_4$:Nd^{3+}, Opt. Express 22 (2014) 30333–30345, http://dx.doi.org/10.1364/OE.22.030333.

[37] W. Xu, H. Zhao, Z. Zhang, W. Cao, Highly sensitive optical thermometry through thermally enhanced near infrared emissions from Nd^{3+}/Yb^{3+} codoped oxyfluoride glass ceramic, Sens. Actuators B Chem. 178 (2013) 520–524, http://dx.doi.org/10.1016/j.snb.2012.12.050.

[38] M.A. Hernández-Rodríguez, J.E. Muñoz-Santiuste, V. Lavín, A.D. Lozano-Gorrín, P. Rodríguez-Hernández, A. Muñoz, V. Venkatramu, I.R. Martín, U.R. Rodríguez-Mendoza, High pressure luminescence of Nd^{3+} in $YAlO^3$ nano-perovskites: A crystal field analysis, (Submitted). (n.d.).

[39] J.F. Suyver, A. Aebischer, P. Gerner, H.U. Güdel, Anomalous power dependence of sensitized upconversion luminescence (2005) pp. 1–9. doi: ‹http://dx.doi.org/10.1103/PhysRevB.71.125123›.

[40] C. Lin, M.T. Berry, R. Anderson, S. Smith, P.S. May, Highly luminescent NIR-to-visible upconversion thin films and monoliths requiring no high-temperature treatment (2009) pp. 3406–3413. doi: ‹http://dx.doi.org/10.1021/cm901094m›.

[41] W.T. Carnall, G.L. Goodman, K. Rajnak, R.S. Rana, A systematic analysis of the spectra of the lanthanides doped into single, J. Chem. Phys. 90 (1989) 3443–3457, http://dx.doi.org/10.1063/1.455853.

[42] J.D. Barnett, S. Block, G.J. Piermarini, An optical fluorescence system for quantitative pressure measurement in the diamond-anvil cell, Rev. Sci. Instrum. 44 (1973) 1–9, http://dx.doi.org/10.1063/1.1685943.

[43] K. Syassen, Ruby under pressure, High. Press. Res. 28 (2008) 75–126, http://dx.doi.org/10.1080/08957950802235640.

5. CONCLUSIONS

In the last section of this thesis, the main goals achieved during this research are summarized as follows:

I. Synthesis, optical and structural characterization

- Site selection spectroscopy on $YAlO^3$ nano-perovskites doped with different concentration of Nd_{3+} ions, allowed to optimize the synthesis method of the nano-perovskites, fixing the proper thermal treatment in which the desired phase of the $YAlO_3$ structure is obtained and confirmed later by XRD measurements, i.e. the *Pnma* orthorhombic structure.

- XRD patterns of undoped and Ln^{3+}-nano-perovskites were well indexed to a *Pnma* orthorhombic structure, without the presence of amorphous phases on them. This meant that XRD measurements confirmed that these nano-perovskites show the same perovskite type as the $YAlO_3$ crystal bulk. The crystallites size achieved was around 40 nm.

- XRD experiment of undoped $YAlO_3$ nano-perovskite was performed from ambient condition of pressure up to 7 GPa. The results of this experiment showed a nice agreement with those found in $YAlO_3$ bulk crystal experimentally. The experimental results of the structural properties of $YAlO_3$ nano-perovskite were also well compared to those obtained with *ab-initio* calculations on $YAlO_3$ bulk crystal.

II. Vibrational and elastic properties

- Experimental Raman scattering spectrum of undoped $YAlO_3$ nano-perovskite showed 16 out of 24 first order Raman-active modes theoretically predicted by *ab-initio* calculation in $YAlO_3$ crystal bulk, at ambient conditions.

- Experimental RS spectrum of undoped $YAlO_3$ nano-perovskite was compared to theoretical one of $YAlO_3$ bulk crystal, observing that there are not relevant differences between the vibrational properties of $YAlO_3$ nano-perovskite and its bulk counterpart at ambient conditions.

- RS measurement at high pressure up to 30 GPa was performed. The overall profile of the Raman modes in the RS spectra did not change up to 30 GPa. This result confirmed that the orthorhombic *Pnma* phase up to 30 GPa is stable in $YAlO_3$ nano-perovskite.
- The pressure dependence of the observed Raman mode frequencies up to 30 GPa was compared to the theoretical one with a good agreement.
- The presence of negative pressure coefficients, such as the $B_{2g}{}^3$ Raman mode, indicated the softening of several bonds as the pressure increase, however, in the present case, it could not related directly to any structural instabilities, because no phase transition was observed in RS experiments up to 30 GPa. This issue was also supported by the elastic properties theoretical studies that predicted the structural stability of $YAlO_3$ up to 92 GPa.

III. Nd^{3+}-doped $YAlO_3$ nano-perovskite as optical temperature sensor

- The emission bands centered at 820 and 890 nm, associated to the Nd^{3+} ($^2H_{9/2}$, $^4F_{5/2}$) → $^4I_{9/2}$ and $^4F_{3/2}$ → $^4I_{9/2}$ transitions, was monitored from RT up to 610 K (337 ºC) under 532 nm excitation. The experimental ratio, *R*, obtained from the integrated areas of the former emissions was analyzed as a function of the temperature and fitted to a Boltzmann-type curve.
- The relative thermal sensitivity, S_{REL}, achieved at 293 K (20 ºC) was around 0.0018 K^{-1} (with a temperature uncertainty δT around 0.9 K) and was compared with the S_{REL} values of other optical temperature sensors doped with Nd^{3+} ions at the same temperature, showing a notable performance that allows the potential application of YAP: Nd^{3+} 1.0% nano-perovskite as optical temperature sensor based on the FIR technique, working in the I-*BW*.
- The temperature calibration in the II-*BW* was performed, analyzing the temperature dependence of the *FHWM* of the emission band centered around 1340 nm, associated to the $^4F_{3/2}$ → $^4I_{13/2}$ transition, from RT up to 370 K (97 ºC) under 532 nm excitation and heated up by increasing the pump power of the excitation source.

- The S_{REL} value achieved at 293 K was around 0.033 K^{-1} (with a temperature uncertainty δT around 0.37 K). By comparison with other optical temperature sensors working in the II-*BW*, Nd^{3+}-doped $YAlO_3$ nano-perovskite showed a great performance, which allows its consideration as optical temperature sensor working in the II-*BW*.

- The potential application of Nd^{3+}-doped $YAlO_3$ nano-perovskite in the biomaging field was also proven by a straightforward sub-tissue luminescence depth experiment, reaching a penetration depth about 5.5 mm.

IV. Tm^{3+}-doped $YAlO_3$ nano-perovskite as optical temperature sensor

- The upconverted emission bands around 700 and 800 nm associated to the Tm^{3+} $^3F_{2,3}\rightarrow{}^3H_6$ and $^3H_4\rightarrow{}^3H_6$ transitions was monitored from RT up to 425 K (152 ºC) under 1210 nm pulse excitation. The experimental ratio, *R*, obtained directly from the integrated areas of the former upconverted emission bands, was analyzed as a function of the temperature from 324 to 425 K, and fitted to a Boltzmann-type curve.

- The S_{REL} obtained in this calibration procedure at 324 K (51 ºC) was around 0.0026 K^{-1} and was compared with the S_{REL} values of other optical temperature sensors doped with Ln^{3+} ions at the same temperature showing the thermal sensing capabilities of Tm^{3+}-doped $YAlO_3$ nano-perovskite as optical temperature sensor based on the FIR technique, working in the I-*BW* and excited whitin II-*BW* with a high sensitivity.

- The potential application of Tm^{3+}-doped $YAlO_3$ nano-perovskite in biological system was also proven by a second temperature calibration procedure in the physiological range, considering the ratio of the maximum intensity of the Stark levels at 776.42 and 821.5 nm of the emission related to the $^3H_4\rightarrow{}^3H_6$ transition, from RT up to 325 K. The S_{REL} achieved in this calibration procedure at 294 K (21 ºC) was around 0.0013 K^{-1} and was compared with the S_{REL} values of other optical temperature sensors doped with Ln^{3+} ions at the same temperature.

V. Nd^{3+}-doped $YAlO_3$ nano-perovskite as optical pressure sensor

- The pressure evolution of the near-infrared emission lines associated to the $^4F_{3/2}\rightarrow{}^4I_{9/2}$ and $^4F_{3/2}\rightarrow{}^4I_{11/2}$ transitions of Nd^{3+} ions in $YAlO_3$ nano-crystalline perovskites from ambient conditions up to 29 GPa exciting at 785 nm, were performed.

- Two different behaviours were observed in the pressure dependence of the emission lines, especially the ones associated to the $^4F_{3/2}\rightarrow{}^4I_{9/2}$ transition. The emission lines associated to the $^4F_{3/2}(R_{1,2}) \rightarrow{}^4I_{9/2}(Z_{1,2,3})$ transitions showed wavelength blue-shifts as the pressure increased that have been also observed in YAP bulk crystal. On the other hand, emission lines associated to the $^4F_{3/2}(R_{1,2}) \rightarrow {}^4I_{9/2}(Z_{4,5})$ transitions showed a significant wavelength red-shifts, also observed in garnet crystals. Emission lines associated to the $^4F_{3/2}(R_{1,2}) \rightarrow {}^4I_{11/2}(Y_{1\text{-}6})$ Stark transitions, $R_{1,2}\rightarrow Y_{2\text{-}6}$ emission lines showed clearly wavelength red-shifts, whereas only the $R_2\rightarrow Y_1$ line showed a slight blue-shift.

- The pressure coefficients achieved in high-pressure were higher enough to consider the possible application of Nd^{3+}-doped $YAlO_3$ nano-perovskite as optical pressure sensor working in NIR, especially the ones associated with the $R_{1,2}\rightarrow Z_5$, $R_1\rightarrow Y_{4,5,6}$ and $R_2\rightarrow Y_5$ lines with -4.70, -4.58, -3.10, -3.18, -3.69 and -3.15 cm^{-1}/GPa respectively.

- Simulations performed by Potentiality of the Simple Overlap Model in combination of *ab-initio* calculations, showed how the energies of the $4f^3$ ground configuration and the barycenters of the multiplets increase with pressure, whereas the Coulomb interaction between *f*-electrons decreases and the crystal-field strength increases. The combination of these effects explains the wavelength blue-shift of some near–infrared emission lines of Nd^{3+} ions.

- The pressure evolution of the anti-Stokes fluorescence showed different behaviors, highlighting the $^4F_{7/2} + {}^4S_{3/2}(Q_6) \rightarrow {}^4I_{9/2}(Z_1)$ and $^4F_{9/2}(K_1) \rightarrow {}^4I_{9/2}(Z_5)$ emission lines with linear pressure coefficients of +3.15 and -7.21 cm^{-1}/GPa, respectively. These results suggest the possible application of the Nd^{3+}-doped $YAlO_3$ nano-perovskite as a NIR optical pressure sensor in high pressure experiments from ambient conditions up to 10 GPa, with a pressure sensitivity comparable with ruby.

6. ANNEXES

In this section, unpublished articles yet are presented. Other works published during the PhD period are also listed.

6.1. Analysis of the upconversion emission of yttrium orthoaluminate nano-perovskite co-doped with Er^{3+}/Yb^{3+} ions for thermal sensing applications

In this paper, which was already submitted, the upconversion emission properties of $YAlO_3$: Er^{3+}/Yb^{3+} nano-perovskite have been analyzed. Strong green and red upconversion emissions, were observed exciting the sample at 980 nm as it is shown in the Fig. 3 of this article. Upconversion mechanism responsible for the UC process in $YAlO_3$: Er^{3+}/Yb^{3+} nano-perovskite was also studied with the temporal evolution of the UC emissions and the pump power dependence of the upconverted band intensities (see Fig. 5)

Under 980 nm excitation, the green UC emissions at 530 nm ($^2H_{11/2} \rightarrow {}^4I_{15/2}$) and 550 nm ($^4S_{3/2} \rightarrow {}^4I_{15/2}$) as functions of temperature from RT to 600 K were studied. The obtained results show a high sensitivity in YAP: Er^{3+}/Yb^{3+} nano-perovskite (0.0123 K^{-1} with a temperature uncertainty around of 0.42 K), as it is shown in Fig. 8 of this paper, which is better than many other optical temperature sensors based on Er^{3+} and Er^{3+}/Yb^{3+}, suggesting its viability as optical temperature sensor based on the FIR technique working in the VIS range exciting in NIR. The temperature of the YAP: Er^{3+}/Yb^{3+} nano-perovskite can be controlled by heating with the pump power of the excitation laser, suggesting its potential viability in laser heating applications (see Fig. 9).

Analysis of the upconversion emission of yttrium orthoaluminate nano-perovskite co-doped with Er^{3+}/Yb^{3+} ions for thermal sensing applications

M.A. HERNÁNDEZ-RODRIGUEZ,*[,1] A.D. LOZANO-GORRÍN[1], V. LAVÍN[1], U.R. RODRÍGUEZ-MENDOZA[1], I.R. MARTÍN[1] AND F.J. MANJÓN[2]

[1]*Departamento de Física, MALTA Consolider Team, IUdEA and IMN, Universidad de La Laguna. Apdo. 456. E-38200 San Cristóbal de La Laguna, Santa Cruz de Tenerife, Spain.*
[2]*Instituto de Diseño para la Fabricación y Producción Automatizada, MALTA Consolider Team, Universitat Politécnica de València, Cno. de Vera s/n, 46022 Valencia, Spain*
**miguelandreshr@gmail.com*

Abstract: The upconversion emissions of yttrium orthoaluminate nano-perovskite co-doped with Er^{3+}/Yb^{3+} have been studied. Strong green and red upconversion emissions, which can be observed by naked eyes, were observed when exciting the sample at 980 nm. In particular, the green band was monitored as a function of temperature and the obtained results suggest that this nano-perovskite can be used as an optical temperature sensor by exciting in the infrared range. The viability of YAP: Er^{3+}/Yb^{3+} nano-perovskite in laser heating applications has been tested and discussed.

1. Introduction

Lanthanide doped materials have been extensively researched due to their applications in several fields, for instance, laser materials [1–5], bio-imaging [6–11], optoelectronic [12,13] and optical temperature sensors [14–22]. Special attention has been paid to the down- and up-conversion (UC) emission properties of the Erbium trivalent ion (Er^{3+}) [23]. Moreover, several studies revealed that Er^{3+}-based ferroelectrics present excellent electrical and luminescence properties [24]. Nonetheless, the low absorption of Er^{3+} around 980 nm yield a low emission efficiency that limits the practical application of this ion in commercial devices. Fortunately, Ytterbium trivalent ion (Yb^{3+}) presents a strong and broad absorption band ranging from 850 to 1050 nm [21] and a good energy transfer (ETU) from Yb^{3+} to Er^{3+} [25]. Therefore, host co-doping with Er^{3+}/Yb^{3+} is very interesting for practical applications because Yb^{3+} can be used as an excellent sensitizer in highly luminescent Er^{3+}-doped materials.

Another issue which has drawn much attention in the last years is the research on optical thermal sensors based on UC emissions of materials and nanomaterials doped with lanthanide ions. For instance, nano-phosphors [26,27] and $NaYF_4$: Er^{3+}/Yb^{3+} nanoparticles can be used a nano-thermometer with high temperature resolution [28], while $NaNbO_3$: Yb^{3+}/Tm^{3+} nanocrystals and Y_2O_3: Yb^{3+}/Ho^{3+} nanopowders can be used as optical thermal sensors [29,30].

In this sense, the research on nanomaterials has become an important issue to concern, due to the outstanding properties of these materials [31]. Among nanomaterials hosts, yttrium orthoaluminate nano-perovskite (YAP) can be a good candidate due to its excellent chemical stability and mechanical and thermal properties [32]. In order to explore the combination of the excellent mechanical-chemical properties of YAP nano-perovskite with the high UC emission efficiency of Er^{3+} ions, enhanced by Yb^{3+} ions as Er^{3+} sensitizers, we study in this work the viability of YAP nano-perovskite co-doped with 2.5 mol % of Yb^{3+}/Er^{3+} as an optical temperature sensor and its potential use in laser heating applications.

2. Experimental details

YAP nano-perovskite of composition $Y_{(1-x-y)}Er_xYb_yAlO_3$, with x = 0.025 and y = 0.025 (in mol %) (YAP: Er^{3+}/Yb^{3+} from now) was successfully synthesized by the sol–gel method in an air atmosphere. Stoichiometric molar ratios of high-purity $Y(NO_3)_3{\cdot}4H_2O$ (ALDRICH, 99.9%), $Al(NO_3)_3{\cdot}9H_2O$ (ALDRICH, 99.9%), $Er(NO_3)_3{\cdot}5H_2O$ (ALDRICH, 99.9%) and $Yb(NO_3)_3{\cdot}5H_2O$ (ALDRICH, 99.9%) materials were dissolved in 25 ml of 1 M HNO_3 under stirring at 353 K for 3 h. Then citric acid, with a molar ratio of metal ions to citric acid of 1:2, was added to the solution, which was stirred and heated at 363 K until the solution becomes transparent. Subsequently, 4 mg of polyethylene glycol was added to the solution to form a gel. This gel was fired at 400 ºC for 6 h to remove the residual nitrates and organic compounds and get the powder sample. This powder was initially burnt out at 1200ºC for 20 h in a first

thermal treatment and then at 1550ºC for 12 h in a second thermal treatment. The object of the thermal treatments is to achieve the orthorhombic structure of the $YAlO_3$ (more details about this in ref [33]). Powder X-ray diffraction data were collected on a PANalytical X'Pert PRO diffractometer (Bragg-Brentano geometry) with an X'Celerator detector employing the Cu $K\alpha_1$ radiation (λ=1.5405 Å) in the angular range $5º < 2\theta < 80º$, by continuous scanning with a step size of 0.02º. On the other hand, the luminescence measurements from RT to 600 K were carried out in a tubular electric furnace where the samples were placed at the center of it and heated at a rate of 1.25 K/min. The temperature of the sample was controlled with a type K thermocouple in contact with it and connected to a voltimeter (Fluke Calibrator 714). A 980 nm commercial laser with a maximum power of 343 mW excited the sample from one side of the furnace, while the emission was collimated by a lens located on the other exit side, and then focalized with a another lens into an optical fiber coupled to a 0.5 m single grating spectrometer (Andor SR-500i-B2-R). The laser spot size on the sample (defined as the $1/e^2$ radius of the intensity) was shown to be 5.6 µm of diameter. Detection of luminescence signal was carried out with a cooled CCD detector (Newton DU490A-1.7) with a resolution of 0.7 nm (~25 cm^{-1}) and an integration time of 1 s. The luminescence decay curves were measured by exciting the sample with a pulsed parametric oscillator OPO (EKSPLA/NT342/3/UVE) laser and using an analogic storage oscilloscope (LeCroy WS424) coupled to the detection system. All spectra were corrected for the spectral response of the equipment.

3. Fluorescence intensity ratio technique

The fluorescence intensity ratio (FIR) technique was used in the second part of this work in order to calibrate the YAP: Er^{3+}/Yb^{3+} nano-perovskite emission with the temperature. In this technique, the fluorescence intensity of two nearby levels, i.e. $^2H_{11/2}$ and $^4S_{3/2}$ levels of Er^{3+} levels, is registered as a function of temperature and interpreted in terms of a simple three-level scheme system (see Fig.1). Since the energy gap of this pair of thermalized levels is very small, the population of the upper level from the lower level is allowed by thermal excitation. The issue here is that the ratio of these intensities is independent of the laser source, because the emitted intensities only depend on the population proportionality of the involved levels. Thus, the relationship between the relative population of the thermalized levels, *R*, and the temperature can be described by the Boltzmann's distribution law by the equation:

$$R = \frac{I_{31}}{I_{21}} = \frac{\omega_{31}^R g_3 h\nu_3}{\omega_{21}^R g_2 h\nu_2} e^{-E_{32}/kT} = Ce^{-E_{32}/kT} \quad (1)$$

where *k* is the Boltzmann constant, E_{32} is the energy gap between the pair of thermalized levels, g_3, g_2 are the degeneracies *(2J+1)*, I_{31}, I_{21} are the integrated intensities of the thermalized levels, ω_{31}^R and ω_{21}^R are the spontaneous emission rates of the E_3 and E_2 levels to the E_1 level, respectively.

The sensor relative sensitivity S_{REL} is defined as follows:

$$S_{REL} = \frac{1}{R}\left|\frac{dR}{dT}\right| = \left(\frac{E_{32}}{kT^2}\right) \quad (2)$$

The sensor relative sensitivity S_{REL} permits the comparison of the sensitivity with other optical temperature sensor ones, because it only depends on the temperature. It is evident that a larger energy gap between the thermalized levels, leads to a higher sensitivity. However, larger energy gap also means lower population in the upper thermalized level and thus, lower intensity.

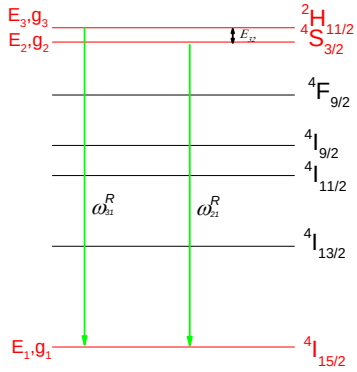

Fig. 1. Simplified diagram for three level system applied on the Er^{3+} ion energy level scheme. E_{32} is the energy gap between the two excited levels, g_i is the degeneracy of the i-th level and ω_{ij}^R is the spontaneous emission rate between the i-th and j-th levels.

The main of FIR technique for temperature sensing is that it neglects accuracy problems resulting from fluctuations of the excitation or from the lack of absolute emission intensities which could occur by noise in the detection system.

Concerning the temperature uncertainty, δT, it is known that this magnitude is the smallest temperature change (temperature resolution) that can be achieved in a given measurement and can be calculated by the equation [34]:

$$\delta T = \frac{1}{S_{REL}} \frac{\delta R}{R} \tag{3}$$

where S_{REL} is the relative sensitivity and the $\delta R/R$ is the relative uncertainty on R.

4. Results and discussion

4.1. Structural characterization

X-ray diffraction spectrum of YAP: Er^{3+}/Yb^{3+} is depicted in Fig.2. The XRD pattern of the YAP: Er^{3+}/Yb^{3+} nano-perovskite was indexed to an orthorhombic structure space group *Pnma* phase. Hence, XRD confirms the perovskite-type structure of YAP: Er^{3+}/Yb^{3+}. Unit cell of YAP: Er^{3+}/Yb^{3+} nano-perovskite is also given in Fig.2. Crystal structure parameters have been obtained from fitting process of the the profiles of the nano-perovskites by the Rietveld method using FULLPROF program [35] (see Table 1).

Table 1. Cell Parameters and Reliability Factors Obtained From Fitting of XRD Pattern for YAP: Er^{3+}/Yb^{3+}

***a* (Å)**	***b* (Å)**	***c* (Å)**	**V (Å^3)**	χ^2	R_p	R_{wp}	R_{exp}
5.323(1)	7.364(1)	5.174(1)	202.8(1)	4.95	24.3	29.5	17.1

The average grains size "*D*" was determined from Scherrer formula:

$$D = \frac{0.89\lambda}{\beta \operatorname{Cos}\theta} \tag{4}$$

where λ= 1.5406 Å, β is the full width at half maximum of the peaks and θ is the angle of diffraction. The average grains size value was around 35-40 nm. No amorphous phase was detected in the nano-perovskite sample.

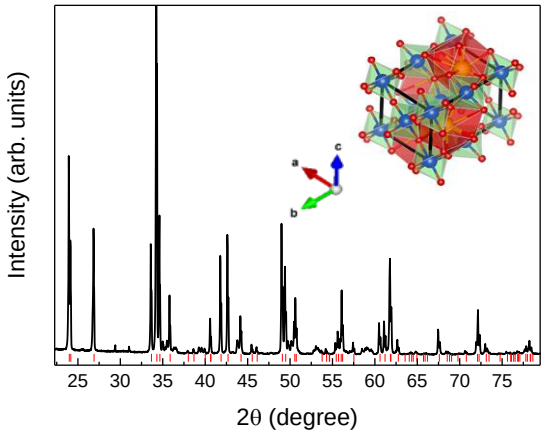

Fig 2. XRD patterns of the YAP: Er^{3+}/Yb^{3+} nano-perovskite and the corresponding *Pnma* symmetry Rietveld refinement at ambient conditions. The unit cell is also shown.

4.2. Upconversion mechanism

Under 980 nm excitation and ambient conditions, YAP: Er^{3+}/Yb^{3+} nano-perovskite shows a strong UC emission which can be observed by naked eye as well (see Fig. 3). The UC spectrum can be divided in two parts, the first one is attributed to the green emissions assigned to ($^2H_{11/2}$, $^4S_{3/2}$) → $^2I_{15/2}$ transitions and the second one is attributed to the red emission related to the $^4F_{9/2}$→ $^2I_{15/2}$ transition.

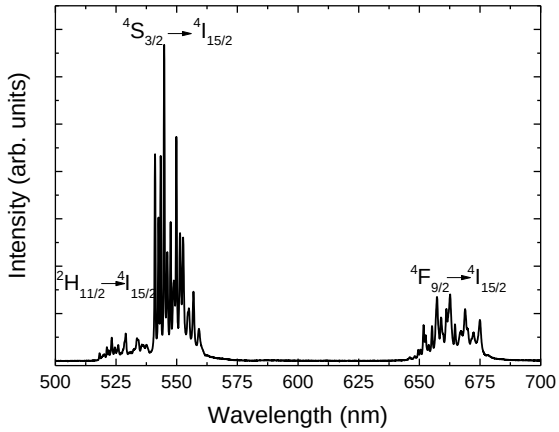

Fig 3. UC emission spectrum of YAP. Er^{3+}/Yb^{3+} nano-perovskite obtained at ambient conditions under 980 nm excitation.

To understand the physical mechanism responsible for the UC process in YAP: Er^{3+}/Yb^{3+} nano-perovskite, the dependence of the UC emissions with the pump power was analyzed. It is known that the

number of photons, *n*, which are needed to populate the upper emitting state can be estimated by the formula:

$$I_{UC} \propto I_{Pump}^{n} \tag{5}$$

where I_{UC} is the intensity of the UC band emission, I_{Pump} is the pump power of the excitation source. Increasing the pump power of the 980 nm laser source, it can be observed that the UC emission intensities increase with the pump power (see Fig. 4(a)). The *n* values of YAP: Er^{3+}/Yb^{3+} nano-perovskite for the green (550 nm) and red (660 nm) emission bands are 1.77 and 1.76 respectively, as shown in Fig. 4(b). This result suggests that a two-photon process is involved in both the population of $^4S_{3/2}$ and $^4F_{9/2}$ levels.

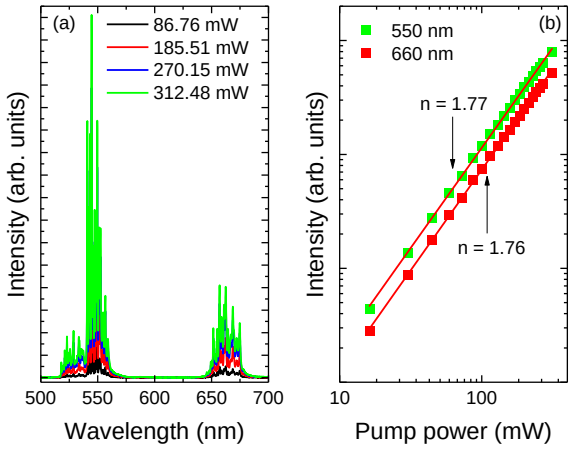

Fig. 4. (a) UC emission spectra of YAP: Er^{3+}/Yb^{3+} under different pump powers at ambient conditions and (b) UC intensities of YAP: Er^{3+}/Yb^{3+} nano-perovskite as functions of the pump power at 980 nm in a double-log scale. Linear fit dependences give slopes of 1.77 and 1.76 for the 550 nm and 660 nm bands, respectively.

The temporal evolution of the UC intensities at 550 nm and 660 nm are shown in Fig.5. The rise time that can be seen in both curves indicates that the UC mechanism is based on energy transfer processes (ETU) in which an excited ion transfers its energy to a neighbor excited ion, which is promoted to a higher excited state. Otherwise, when the rise time is negligible, then the UC processes are due to an excited state absorption mechanism (ESA) that involves the absorption of a photon by a unique ion that promotes to a higher excited state.

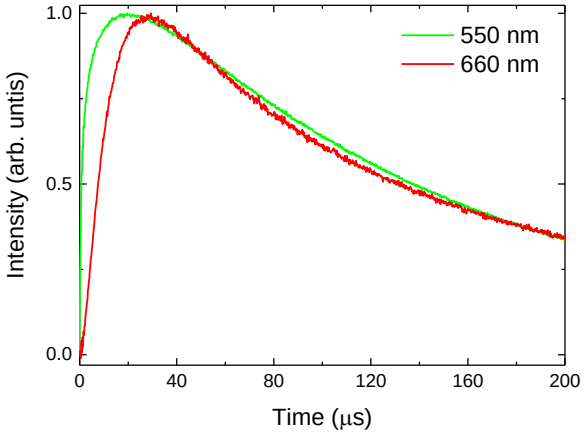

Fig. 5. Temporal evolutions of the UC emissions of YAP: Er^{3+}/Yb^{3+} nano-perovskite at 550 nm and 660 nm under excitation at 980 nm.

Based on the results shown in Figs. 4 and 5, it can be confirmed that the mechanism behind the UC emission is an ETU process with different steps. The simplified energy level diagram of YAP: Er^{3+}/Yb^{3+} nano-perovskite is depicted in Fig. 6. The UC mechanism for YAP: Er^{3+}/Yb^{3+} nano-perovskite is the energy transfer ETU from Yb^{3+} to Er^{3+} ions. Exciting at 980 nm, Yb^{3+} ions in the ground level promote to the $^2F_{5/2}$ level by ground state absorption (GSA) and then, the energy of these ions is transferred to Er^{3+} ions. Afterwards, electrons that are coming from Er^{3+} ions are excited to the $^4I_{11/2}$ level and partly decay to the $^4I_{13/2}$ level by multiphonon relaxation (MPR) processes. At this stage, a second energy photon can be absorbed by Yb^{3+} ions and transferred to Er^{3+} ions again, during the lifetime of the $^4I_{11/2}$ and $^4I_{13/2}$ levels. This leads to the population $^4F_{7/2}$ and $^4F_{9/2}$ levels from the excitation of the electrons that come from $^4I_{11/2}$ and $^4I_{13/2}$ levels, respectively. Then, these electrons decay to the $^2H_{11/2}$, $^4S_{3/2}$ and $^4F_{9/2}$ levels via MPR process. Finally, a radiative transition process occurs leading to the green and red emissions related to the ($^2H_{11/2}$, $^4S_{3/2}$) → $^2I_{15/2}$ and $^4F_{9/2}$→ $^2I_{15/2}$ transitions, respectively.

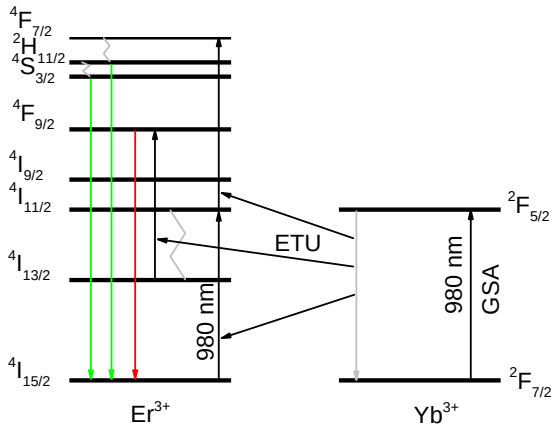

Fig. 6. Partial energy level diagram of YAP: Er^{3+}/Yb^{3+} nano-perovskite under 980 nm excitation and possible UC proccesses.

4.3. Optical sensor calibration

Since YAP: Er^{3+}/Yb^{3+} nano-perovskite shows strong UC emission intensities, its viability as optical thermal sensor was analyzed.

The temperature evolution of the YAP: Er^{3+}/Yb^{3+} nano-perovskite UC emission spectra from room temperature up to 600 K are shown in Fig.7. It can be observed that the emission band associated with the $^4S_{3/2} \rightarrow {}^4I_{15/2}$ (550 nm) transition was decreasing as the temperature increases, while the emission band associated with the $^2H_{11/2} \rightarrow {}^4I_{15/2}$ (530 nm) transition was increasing, because of the thermally induced population that comes from the $^4S_{3/2}$ level.

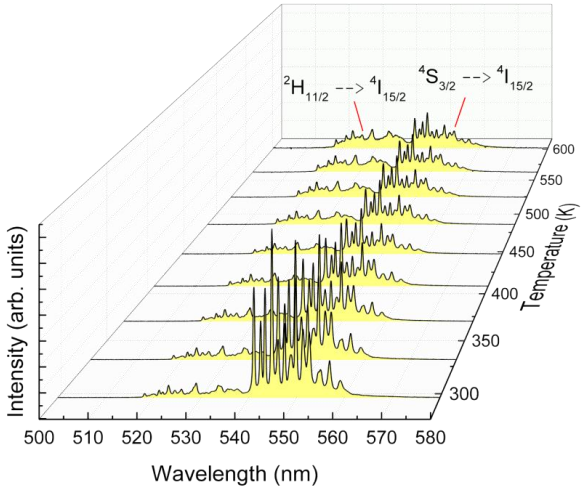

Fig. 7. Temperature evolution of the upconversion emission of the YAP: Er^{3+}/Yb^{3+} nano-perovskite.

An analysis based on a simple three-level system scheme formed by $^2H_{11/2}$ (level 3), $^4S_{3/2}$ (level 2) and $^4I_{15/2}$ (level 1) was performed. The ratio between the integrated intensities for $^2H_{11/2} \rightarrow {}^4I_{15/2}$ and $^4S_{3/2} \rightarrow {}^4I_{15/2}$ was increasing with the temperature, following a tendency that can be described by Eq. (1). From the fitting process, the values of $C = 5.77$ and the energy gap $E_{32} = 751.10$ cm^{-1} have been determinate. The relative sensor sensitivity S_{REL} as a function of the temperature T, defined by the Eq. (2) is also shown in Fig.8. The temperature uncertainty δT achieved in the optical calibration procedure is also shown in Fig.8.

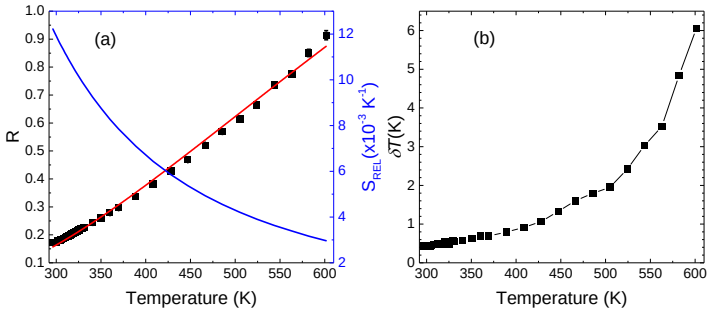

Fig. 8. (a) Experimental integrated intensity ratio (R) (black squares) and relative sensitivity (S_{REL}) (blue line) of the YAP: Er^{3+}/Yb^{3+}nano-perovskite obtained from the emission bands associated to the $^2H_{11/2} \rightarrow {}^4I_{15/2}$ and $^4S_{3/2} \rightarrow {}^4I_{15/2}$ transitions. The experimental values were fitted to Eq. (1) (red line). (b) Temperature uncertainty δT computed by Eq. (3).

The maximum relative sensitivity achieved for YAP: Er^{3+}/Yb^{3+} nano-perovskite was 0.0123 K^{-1} with a temperature uncertainty around of 0.42 K. The relative sensitivity of YAP: Er^{3+}/Yb^{3+} nano-perovskite was compared with others RE^{3+}- based temperature optical sensors (see Table 2). YAP: Er^{3+}/Yb^{3+} shows a very high sensitivity, and thus, it can be considered as potential candidate to become an optical temperature sensor based on the FIR technique working in the VIS range exciting in NIR.

Table 2. Thermal Relative Sensitivity at 296 K of Different RE^{3+}- Based Temperature Optical Sensors[a]

Er^{3+}/Yb^{3+} doped host material	FIR equation	Transition	Temperature range (K)	λ_{EXC} (nm)	S_{REL} (x10^{-3} K^{-1}) at 300K	Ref.
$NaBiTO_3$: Er^{3+}/Yb^{3+} ceramic	9.77•exp(-795/kT)	($^2H_{11/2}$, $^4S_{3/2}$) → $^4I_{15/2}$	200-443	980	12.6	[24]
YAP: Er^{3+}/Yb^{3+} nano-perovskite	5.77•exp(-751.10/kT)	($^2H_{11/2}$, $^4S_{3/2}$) → $^4I_{15/2}$	296-600	980	11.9	This work
$NaYF_4$: Er^{3+} nano-crystalline	10•exp(-741/kT)	($^2H_{11/2}$, $^4S_{3/2}$) → $^4I_{15/2}$	294-720	488	11.7	[19]
Lanthanum Oxysulfide powder:Er^{3+}	8.75•exp(-712.57/kT)	($^2H_{11/2}$, $^4S_{3/2}$) → $^4I_{15/2}$	240-300	806	11.3	[20]
Al_2O_3: Er^{3+}/Yb^{3+} nano-particles	9.63•exp(-674/kT)	($^2H_{11/2}$, $^4S_{3/2}$) → $^4I_{15/2}$	295-975	978	10.6	[23]
$Na_{0.5}Bi_{0.5}TiO_3$: Er^{3+}/Yb^{3+} ceramic	4.71•exp(-579.10/kT)	($^2H_{11/2}$, $^4S_{3/2}$) → $^4I_{15/2}$	93-613	980	9.2	[36]
Chalcogenide glass: Er^{3+}/Yb^{3+}	5.98•exp(-555/kT)	($^2H_{11/2}$, $^4S_{3/2}$) → $^4I_{15/2}$	293-493	1060	8.8	[37]
$Na_2Y_2B_2O_7$: Er^{3+}/Yb^{3+} nano-phosphor	27.6•exp(-536.40/kT)	($^2H_{11/2}$, $^4S_{3/2}$) → $^4I_{15/2}$	300-613	980	8.5	[26]
Silicate glass: Er^{3+}/Yb^{3+}	3.65•exp(-414.80/kT)	($^2H_{11/2}$, $^4S_{3/2}$) → $^4I_{15/2}$	296-723	978	6.6	[38]
$CaMoO_4$: Er^{3+}/Yb^{3+} nano-phosphor	5.10•exp(-379.40/kT)	($^2H_{11/2}$, $^4S_{3/2}$) → $^4I_{15/2}$	300-535	980	6	[27]

[a] FIR Equations, transitions of interest, relative sensibilities as well as the temperature ranges and excitation wavelengths are also included.

4.4. Laser heating application

Taking advantage of the temperature calibration of the YAP: Er^{3+}/ Yb^{3+} performed in the previous section of this work, it is possible to obtain the temperature heating of the 980 nm laser source. The increment of temperature and ratio as a function of the pump power of the laser source are shown in Fig. 9. As can be observed, it is possible to heat the nano-perovskite sample and control its temperature with the laser power. Therefore, with a pump power of 350 mW it is possible to increase its temperature 100 K with an uncertainty lower than 1 K in this temperature range (according to Fig. 8b).

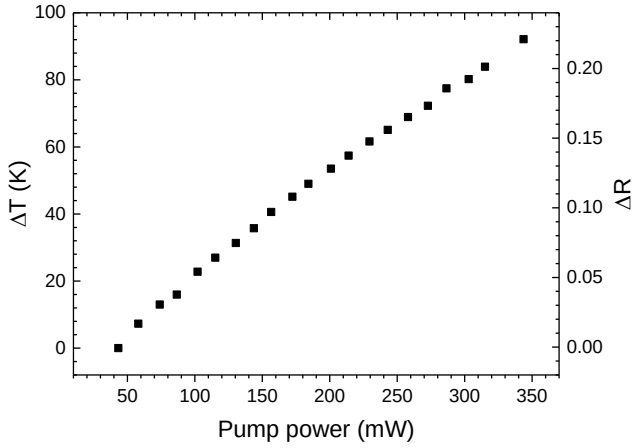

Fig. 9. Temperature and ratio increments as functions of the pump power of the laser source.

5. Conclusions

Upconversion properties of YAP: Er^{3+}/Yb^{3+} nano-perovskite exciting at 980 nm have been analyzed. Under 980 nm excitation, the green UC emissions at 530 nm ($^2H_{11/2} \rightarrow {}^4I_{15/2}$) and 550 nm ($^4S_{3/2} \rightarrow {}^4I_{15/2}$) as a function of temperature from RT to 600K were studied. The obtained results show a high sensitivity in YAP: Er^{3+}/Yb^{3+} nano-perovskite (0.0123 K^{-1} with a temperature uncertainty around of 0.42 K) which is better than many other optical temperature sensors based on Er^{3+} and Er^{3+}/Yb^{3+}, suggesting its viability as optical temperature sensor based on the FIR technique working in the VIS range exciting in NIR. The temperature of the YAP: Er^{3+}/Yb^{3+} nano-perovskite can be controlled by heating with the pump power of the excitation laser, suggesting its potential viability in laser heating applications.

References and links

1. J.J. Romero, E. Montoya, L.E. Bausá, F. Agulló-Rueda, M.R.B. Andreeta, A. C. Hernandes, "Multiwavelength laser action of Nd^{3+}:$YAlO_3$ single crystals grown by the laser heated pedestal growth method", Opt. Mater. **24** (2004) 643–650. doi:10.1016/S0925-3467(03)00179-4.
2. M. Bass, Nd,Cr : "YAlO3 LASER TAILORED FOR HIGH-ENERGY Q-SWITCHED OPERATION", Appl. Phys. Lett. **17** (1970) 395-398. doi:10.1063/1.1653451.
3. I. Iparraguirre, J. Azkargorta, J.M. Fernández-Navarro, M. Al-Saleh, J. Fernández, R. Balda, "Laser action and upconversion of Nd^{3+} in tellurite bulk glass", J. Non. Cryst. Solids. **353** (2007) 990–992. doi:10.1016/j.jnoncrysol.2006.12.103.
4. M.J. Weber, M. Bass, T.E. Varitimos, D.P. Bua, "Laser Action from Ho^{3+}, Er^{3+}, and Tm^{3+} in $YAlO_3$, IEEE J. Quantum Electron". **QE-9** (1973) 1079–1086. doi:10.1109/JQE.1973.1077426.
5. M.J. Weber, M. Bass, K. Andringa, R.R. Monchamp, Comperch.E, "Czochralski Growth and Properties of $YAlO_3$ Laser Crystals", Appl. Phys. Lett. **15** (1969) 342–345. doi:10.1063/1.1652851.
6. D. Jaque, F. Vetrone, "Luminescence nanothermometry", Nanoscale. 4 (2012) 4301–4326. doi:10.1039/c2nr30764b.
7. S. Xu, S. Huang, Q. He, L. Wang, "Upconversion nanophosphores for bioimaging", Trends Anal. Chem. **66** (2015) 72–79. doi:10.1016/j.trac.2014.11.014.
8. U. Rocha, K.U. Kumar, C. Jacinto, I. Villa, F. Sanz-Rodríguez, M. Del Carmen Iglesias De La Cruz, A. Juarranz, E. Carrasco, F.C.J.M. Van Veggel, E. Bovero, J.G. Solé, D. Jaque, "Neodymium-doped LaF_3 nanoparticles for fluorescence bioimaging in

the second biological window", Small. **10** (2014) 1141–1154. doi:10.1002/smll.201301716.
9. D. Wawrzynczyk, A. Bednarkiewicz, M. Nyk, W. Strek, M. Samoc, "Neodymium(iii) doped fluoride nanoparticles as non-contact optical temperature sensors", Nanoscale. **4** (2012) 6959. doi:10.1039/c2nr32203j.
10. H. Söderlund, S. Andersson-engels, "Increasing depth penetration in biological tissue imaging using 808-nm upconverting nanoparticles", J. Biomed. Opt. **20** (2015) 086008–0860014. doi:10.1117/1.JBO.20.8.086008.
11. U. Rocha, C. Jacinto Da Silva, W. Ferreira Silva, I. Guedes, A. Benayas, L. Martínez Maestro, M. Acosta Elias, E. Bovero, F.C.J.M. Van Veggel, J.A. García Solé, D. Jaque, "Subtissue thermal sensing based on neodymium-doped LaF_3 nanoparticles", ACS Nano. **7** (2013) 1188–1199. doi:10.1021/nn304373q.
12. H. Wang, Y. Liu, M. Li, H. Huang, H.M. Xu, R.J. Hong, H. Shen, "Multifunctional TiO_2 nanowires-modified nanoparticles bilayer film for 3D dye-sensitized solar cells", Optoelectron. Adv. Mater. Rapid Commun. **4** (2010) 1166–1169. doi:10.1039/b000000x.
13. F. Zhang, G.B. Braun, Y. Shi, Y. Zhang, X. Sun, N.O. Reich, D. Zhao, G. Stucky, J. Hao, L.H. Fischer, G.S. Harms, O.S. Wolfbeis, Z.L. Wang, J. Hao, H.L.W. Chan, W.T. Wong, K.L. Wong, "Metal-ion doped luminescent thin films for optoelectronic applications", J. Mater. Chem. C. **8** (2013) 2850–2851. doi:10.1002/smll.201102703.
14. X. Wang, J. Zheng, Y. Xuan, X. Yan, "Optical temperature sensing of $NaYbF_4$: Tm^{3+}@SiO_2 core-shell micro-particles induced by infrared excitation", Opt. Express. **21** (2013) 21596–21606. doi:10.1364/OE.21.021596.
15. H. Zou, X. Wang, Y. Hu, X. Zhu, Y. Sui, Z. Song, "Optical temperature sensing by upconversion luminescence of Er doped $Bi_5TiNbWO_{15}$ ferroelectric materials", AIP Adv. **4** (2014) 1–7. doi:10.1063/1.4905454.
16. L. Xing, Y. Xu, R. Wang, W. Xu, Z. Zhang, "Highly sensitive optical thermometry based on upconversion emissions in Tm^{3+}/Yb^{3+} codoped $LiNbO_3$ single crystal", Opt. Lett. **39** (2014) 454–457. doi:10.1364/OL.39.000454.
17. E.A. Lalla, S.F. León-Luis, V. Monteseguro, C. Pérez-Rodríguez, J.M. Cáceres, V. Lavín, U.R. Rodríguez-Mendoza, "Optical temperature sensor based on the Nd^{3+} infrared thermalized emissions in a fluorotellurite glass", J. Lumin. **166** (2015) 209–214. doi:10.1016/j.jlumin.2015.05.029.
18. R. Dey, A. Kumari, A.K. Soni, V.K. Rai, "$CaMoO_4$:Ho^{3+}-Yb^{3+}-Mg^{2+} upconverting phosphor for application in lighting devices and optical temperature sensing", Sensors Actuators, B Chem. 210 (2015) 581–588. doi:10.1016/j.snb.2015.01.007.
19. A. Benayas, B. Del Rosal, A. Pérez-Delgado, K. Santacruz-Gómez, D. Jaque, G.A. Hirata, F. Vetrone, "Nd:YAG Near-Infrared Luminescent Nanothermometers", Adv. Opt. Mater. **3** (2015) 687–694. doi:10.1002/adom.201400484.
20. S. Wang, H. Zhou, X. Wang, A. Pan, "Up-conversion luminescence and optical temperature-sensing properties of Er^{3+}-doped perovskite $Na_{0.5}Bi_{0.5}TiO_3$ nanocrystals, J. Phys. Chem. Solids. **98** (2016) 28–31. doi:10.1016/j.jpcs.2016.06.002.
21. M.A. Hernández-Rodríguez, A.D. Lozano-Gorrín, I.R. Martín, U.R. Rodríguez-Mendoza, V. Lavín, "Comparison of the sensitivity as optical temperature sensor of nano-perovskite doped with Nd^{3+} ions in the first and second biological windows", Sensors Actuators, B Chem. **255** (2018) 970–976. doi:10.1016/j.snb.2017.08.140.
22. M.A. Hernández-Rodríguez, A.D. Lozano-Gorrín, V. Lavín, U.R. Rodríguez-Mendoza, I.R. Martín, "Yttrium orthoaluminate nanoperovskite doped with Tm^{3+} ions as upconversion optical temperature sensor in the near-infrared region", Opt. Express. **25** (2017) 27845–27856. doi:10.1364/OE.25.027845.
23. P. Du, L. Luo, W. Li, Y. Zhang, H. Chen, "Electrical and luminescence properties of Er-doped $Bi_{0.5}Na_{0.5}TiO_3$ ceramics", Mater. Sci. Eng. B. **178** (2013) 1219–1223. doi:10.1016/j.mseb.2013.08.007.
24. P. Du, L. Luo, W. Li, Q. Yue, H. Chen, "Optical temperature sensor based on upconversion emission in Er-doped ferroelectric $0.5Ba(Zr_{0.2}Ti_{0.8})O_3$-$0.5(Ba_{0.7}Ca_{0.3})TiO_3$ ceramic", Appl. Phys. Lett. **104** (2014) 2–6. doi:10.1063/1.4871378.
25. L.H. Fischer, G.S. Harms, O.S. Wolfbeis, "Upconverting nanoparticles for nanoscale thermometry", Angew. Chemie - Int. Ed. **50** (2011) 4546–4551. doi:10.1002/anie.201006835.
26. A.K. Soni, V.K. Rai, M.K. Mahata, "Yb^{3+} sensitized $Na_2Y_2B_2O_7$:Er^{3+} phosphors in enhanced frequency upconversion, temperature sensing and field emission display", Elsevier Ltd, 2017. doi:10.1016/j.materresbull.2017.01.009.
27. S. Sinha, M.K. Mahata, K. Kumar, S.P. Tiwari, V.K. Rai, "Dualistic temperature sensing in Er^{3+}/Yb^{3+} doped $CaMoO_4$ upconversion phosphor, SAA. (2016). doi:10.1016/j.saa.2016.09.039.
28. F. Vetrone, R. Naccache, A. Zamarrón, A.J. De La Fuente, F. Sanz-Rodríguez, L.M. Maestro, E.M. Rodriguez, D. Jaque, J.G. Sole, J.A. Capobianco, "Temperature sensing using fluorescent nanothermometers", ACS Nano. **4** (2010) 3254–3258. doi:10.1021/nn100244a.
29. A.F. Pereira, K.U. Kumar, W.F. Silva, W.Q. Santos, D. Jaque, C. Jacinto, "Yb^{3+}/Tm^{3+} co-doped $NaNbO_3$ nanocrystals as three-photon-excited luminescent nanothermometers", Sensors Actuators, B Chem. **213** (2015) 65–71. doi:10.1016/j.snb.2015.01.136.
30. V. Lojpur, M. Nikolic, L. Mancic, O. Milosevic, M.D. Dramicanin, "Y_2O_3:Yb,Tm and Y_2O_3:Yb,Ho powders for low-temperature thermometry based on up-conversion fluorescence", Ceram. Int. **39** (2013) 1129–1134. doi:10.1016/j.ceramint.2012.07.036.
31. E. Roduner, "Size matters: why nanomaterials are different", Chem. Soc. Rev. **35** (2006) 583–592. doi:10.1039/b502142c.
32. R. Moncorgé, B. Chambon, J.Y. Rivoire, N. Garnier, E. Descroix, P. Laporte, H. Guillet, S. Roy, J. Mareschal, D. Pelenc, J. Doury, P. Farge, "Nd doped crystals for medical laser applications", Opt. Mater. **8** (1997) 109–119. doi:10.1016/S0925-3467(97)00022-0.
33. C.D.S. Brites, A. Milla, "Lanthanides in Luminescent Thermometry", **49** (2016). doi:10.1016/bs.hpcre.2016.03.005.
34. J. Rodríguez-Carvajal, "Recent advances in magnetic structure determination by neutron powder diffraction", Phys. B Condens. Matter. **192** (1993) 55–69. doi:10.1016/0921-4526(93)90108-I.
35. M.A. Hernández-Rodríguez, A.D. Lozano-Gorrín, I.R. Martín, U.R. Rodríguez-Mendoza, V. Lavín, "Spectroscopic properties of Nd^{3+} ions in YAP nano-perovskites", J. Lumin. **188** (2017) 204–208. doi:10.1016/j.jlumin.2017.04.031.
36. P. Du, L. Luo, W. Li, Q. Yue, "Upconversion emission in Er-doped and Er/Yb-codoped ferroelectric $Na_{0.5}Bi_{0.5}TiO_3$ and its temperature sensing application", J. Alloys Compd. **116** (2014) 014102–014107. doi:10.1063/1.4886575.
37. P. V Santos, M.T. De Araujo, J. a M. Neto, A S.B. Sombra, "Optical Thermometry Through Infrared Excited Upconversion Fluorescence Emission in Er - and Er – Yb -doped Chalcogenide Glasses", Quantum. **35** (1999) 395–399. doi: 10.1109/3.748846.
38. X. Wang, X. Yan. "Ultraviolet and infrared photon-excited synergistic effect in Er^{3+}-doped YbF_3 phosphors, Opt. Lett. **36** (2011) 4353–4355. doi: 10.1364/OL.36.004353.

Acknowledgements

This research was partially supported MINECO (MAT2013-46649-C4-2/4-P, MAT2015-71070-REDC, and MAT2016-75586-C4-2/4-P), and by the EU-FEDER. M.A. Hernández-Rodríguez thanks to MINECO for FPI grant (BES-2014-068666).

6.2. Spectroscopic properties of Ho^{3+} ions in $YAlO_3$ nano-perovskites for bioimaging and energy applications

In this work (pending submission to journal) the structural and spectroscopic properties of Ho^{3+}-doped yttrium orthoaluminate nanoperovskites were studied. First, the structural properties of the sample were studied by X-ray diffraction measurements, confirming the *Pnma* orthorhombic structure for all samples (see Fig. 1), with average grain around of 35-45 nm.

Secondly, the influent of the Ho^{3+} concentration of the samples in the spectroscopic properties was also analyzed. In addition, taking advantage of the 1200 nm emission of the Ho^{3+} ion when it is excited at 895 nm, a sub-tissue penetration depth study was carried out, reaching a penetration depth around 5.4 nm (see Fig. 7), which is quite close to those found in other nanomaterials, suggesting the possible application of $YAlO_3$: Ho^{3+} nano-peroskites in sub-tissue luminescence imaging. On the other hand, the capabilities of $YAlO_3$: Ho^{3+} nano-perovskite in the enhancement of the performance of solar cells were also proven, comparing the upconversion emission of these nano-perovskites with the one obtained by a crystal bulk doped with the same concentration of Ho^{3+} ions. The upconversion emission of Ho^{3+} ions in $YAlO_3$ was sensible higher that the crystal one (see Fig. 8), suggesting that $YAlO_3$: Ho^{3+} nano-perovskite can be used for enhancement of the solar cells performance.

SPECTROSCOPIC PROPERTIES OF Ho^{3+} IONS IN $YAlO_3$ NANO-PEROVSKITES FOR BIOIMAGING AND ENERGY APPLICATIONS

M.A. Hernández-Rodríguez,[a] A.D. Lozano-Gorrín,[a] V. Lavín,[a,b,c] I.R. Martín,[a,b,d] and U.R. Rodríguez-Mendoza [a,b,d]

[a] Departamento de Física, Universidad de La Laguna. E-38200 San Cristóbal de La Laguna, Santa Cruz de Tenerife, Spain.

[b] MALTA Consolider Team, Universidad de La Laguna. E-38200 San Cristóbal de La Laguna, Santa Cruz de Tenerife, Spain

[c] Instituto Universitario de Estudios avanzados en Atómica, Molecular y Fotónica, Universidad de La Laguna. E-38200 San Cristóbal de La Laguna, Santa Cruz de Tenerife, Spain.

[d] Instituto Universitario de Materiales y Nanotecnología, Universidad de La Laguna. E-38200 San Cristóbal de La Laguna, Santa Cruz de Tenerife, Spain.

Keywords:

Abstract: The structural and spectroscopic properties of Ho^{3+}-doped yttrium orthoaluminante nanoperovskites were measured and analyzed. The influent of the Ho^{3+} concentration of the samples in the spectroscopic properties was also analyzed. The potential application of YAP: Ho^{3+} nano-perovskites in sub-tissue luminescence imaging and enhancement of the performance of solar cells were proven.

1. Introduction

In the last decade, several studies have been performed in order to optimize the luminescence properties of trivalent rare-earth (RE^{3+})-doped nanocrystals using their size, shape, phase and concentration dependency [1–3]. The main feature of the nanocrystals is their capacity to keep the luminescence properties compared to bulk counterparts, making them useful as optoelectronic materials, for instance, in the photonic and bioimaging fields [1,4–6]. It is known that luminescence efficiency is generally considered to be low in oxide materials because of noticeable multiphonon relaxation (MPR) rate caused by the high-energy phonons. In spite of this, oxide materials result to

be more efficient for practical applications due to their high chemical durability and thermal stability [7,8]. When the RE^{3+} ions are inserted into the crystals, their conversion efficiencies depend on the RE^{3+} ion concentration, the intra- or inter-energy transfer processes, and the rate of the MPR. Hence, there is a necessity of deep search for RE^{3+}-doped hosts which should accomplish the next features: i) low energy phonons, ii) high quantum efficiencies, and iii) optimum RE^{3+} concentration in order to develop optical devices with efficient luminescence properties [9–11].

Among oxide based materials, perovskites have gained interest because of their technological applications, such as hydrogen sensors, SOFC electrodes, multilayer capacitors, and solar cells [12]. The most used perovskite is the $CaTiO_3$, due to its thermal and chemical stabilities [13]. Futhermore, some of its features make this perovskite a promising candidate as a host material for powder lasers as well as host lattice for efficient luminescence of lanthanide ions [14–17], and biomedical applications [18]. In addition, it is possible to find works focused on others types of perovskites, such as $BaTiO_3$ which it is recognized because its ferroelectric properties [19–21] or $LaAlO_3$ as a host material for RE^{3+} ions [17].

The yttrium orthoaluminate perovskite (YAP) doped with different rare-earths (RE) ions in bulk crystal and nano-powder has been extensively studied due to its optical properties. It has been successfully used as a scintillator [22–24] phosphor [25,26], optical sensor with pressure and temperature [27–30] and for solid-state lasers [31,32]. Due to the spectroscopic properties of the holmium trivalent ion (Ho^{3+}) [ref], several works on of YAP doped with Ho^{3+} can be found, for instance, as phosphors for dosimetry applications [33], lasers [34–36], etc. The present work focuses on the spectroscopic properties of the Ho^{3+}: YAP nanoperovskite and the influence of the Ho^{3+}concentration in its luminescent properties, as well as its potential application energy (solar cells) and biomaging fields.

. Experimental details

Nanocrystalline YAP perovskites of composition $Y_{(1-X)}Ho_XAlO_3$, with x = 0.5, 1.0 and 2.5 (in mol %) were successfully synthesized by the Pechini citrate sol–gel method in an air atmosphere. Stoichiometric molar ratios of high-purity $Y(NO_3)_3{\cdot}4H_2O$ (ALDRICH, 99.9%), $Al(NO_3)_3{\cdot}9H_2O$ (ALDRICH, 99.9%) and $Ho(NO_3)_3{\cdot}5H_2O$ (ALDRICH, 99.9%) materials were dissolved in 25 ml of 1 M HNO3 under stirring at 353 K for 3 h. Afterwards, citric acid, with a molar ratio of metal ions to citric acid of 1:2, was added to the solution, which was stirred and heated at 363 K until reaching the transparency of the solution. Then, 4 mg of polyethylene glycol was added to the solution. The former step created a gel that was fired at 400 ºC for 6 h to remove the residual nitrates and organic compounds and the subsequently obtained powder sample was finally burnt out at 1200º C for 20 h. The second thermal treatment was performed at 1550ºC for 12 h.

X-ray diffraction (XRD) patterns were carried out using a diffractometer (PANalytical X'Pert Pro) using CuKα1 radiation.

The visible and NIR diffuse reflectance spectrum in the range from 400 to 1300 nm was measured using an integrating sphere with a Cary 5000 (Varian).

Emission spectra of YAP: Ho^{3+} nanoperovskites were measured by exciting at 457 nm with a continuous commercial laser. The emission of the samples was focused on the entrance slit of a CCD spectrograph. The luminescence decay curves were measured by exciting the Ho^{3+} ions around 539 nm with a 10 ns pulsed optical parametric oscillator OPO (EKSPLA/NT342/3/UVE) and monitoring the results by using an analogic storage oscilloscope (LeCroy WS424) coupled to the detection system. For the depth penetration studies, a solution of Intralipid® [37] was used as phantom tissue. The excitation wavelength in this experiment was 895 nm, using the laser line of an a Ti:sapphire laser (3900S Spectra Physics) pumped by the Ar+ laser and the emission as a function of the

depth penetration was recorded by using a NIR extended photomultiplier (HAMATSU H10330B-75). All spectra were corrected from the instrument response.

3. Results and discussion

3.1. Structural characterization

All the diffraction patterns of the samples are well indexed to an orthorhombic space group *Pnma*. Thus, XRD confirms the perovskite-type structure of YAP: Ho^{3+}. Crystal structure parameters have been estimated after fitting the profiles of the nanoperovskites by the Rietveld method using the FULLPROF program [38]. The average grains size "*D*" was determined from Scherrer formula:

$$D = \frac{0.89\lambda}{\beta \operatorname{Cos}\theta} \quad (1)$$

where λ= 1.5406 Å, β is the full width at half maximum of the peaks and θ is the angle of diffraction. The average grain size value was around 35-45 nm. No amorphous phase was found in the samples.

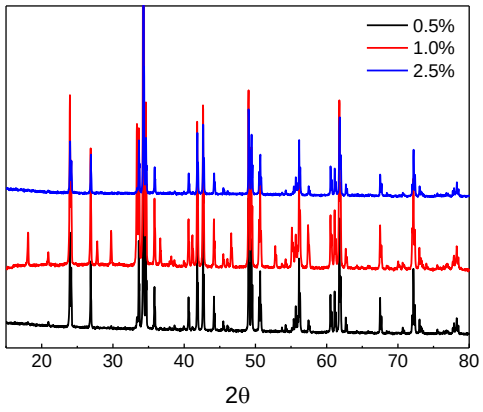

Figure 1. XRD patterns of the YAP: Ho^{3+} nanoperovskite.

3.2. Absorption and luminescence

Knowing the local structure around the RE^{3+} ions inside the host matrix is important, because it gives rise to the fine structure splitting of the free-ion multiplets and the forced intra-configurational 4f-4f electric-dipole transition probabilities in the optical range (UV-VIS-NIR). In the case the of the YAP structure, the RE^{3+} ion enters into the octahedral interstice sites occupied by the Y^{3+} ions [39]. As a result, the crystal field interaction implies a totally breakdown of the degeneracy of the $^{2S+1}L_J$ mutiplets of the free Ho^{3+} ion, resulting in (2J+1)/2 Stark levels, which are labeled according to the irreducible representations obtained from group theory. This crystal field splitting of the electronic levels can be identified from the absorption and emission spectra.

First, the measurement of the diffuse reflectance spectrum of the YAP: Ho^{3+} in the visible-NIR range was performed, and is shown in Fig.2. The sample with the highest concentration was chosen for this measure because it has a greater absorption compared with the other samples. The observed absorption peaks are related to the intra-configurational $4f^{10}$-$4f^{10}$ electronic transitions starting from the $^4I_8$ ground state to the different excited levels of the Ho^{3+}. All the transitions were assumed to be electric-dipole in nature. The sharpness of the peaks of the diffuse reflectance spectrum suggests that the Ho^{3+} ions are incorporated in the nanocrystalline structure of the perovskite. The labels of the electronic transitions of the Ho^{3+} in the yttrium-aluminium nanoperovskites have been assigned according to the Dieke's diagram for this ion.

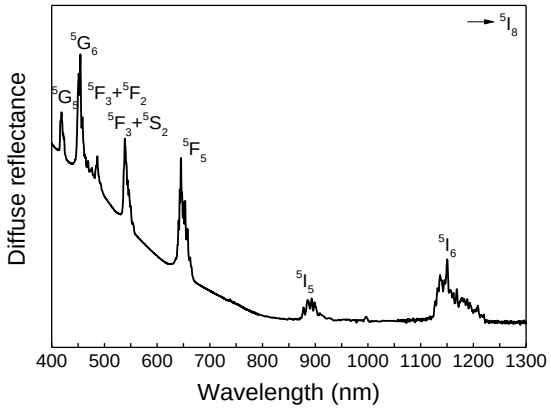

Figure 2. Diffuse reflectance spectrum of the YAP: Ho^{3+} 2.5% nanoperovskite powder in the UV-visible-NIR range at RT. All transitions start from the $^5I_8$ ground state to the indicated levels.

The emission spectra of YAP: Ho^{3+} nanoperovskites for different concentration of doped holmium are shown in Fig.3. Three main emission bands appear in the wavelength measurement range, being the following the most intensive transitions: the $^5S_2(^5F_4) \rightarrow {}^5I_8$ with the maximum about at 550 nm (530-570 nm range), and the $^5S_2(^5F_4) \rightarrow {}^5I_7$ which its maximum centered at 757 nm (740-765 nm range). Transitions from the $^5S_2(^5F_4)$ are more intensive than $^5F_5 \rightarrow {}^5I_8$ transition (640-670 nm range) as can be observed in the Fig. 3.

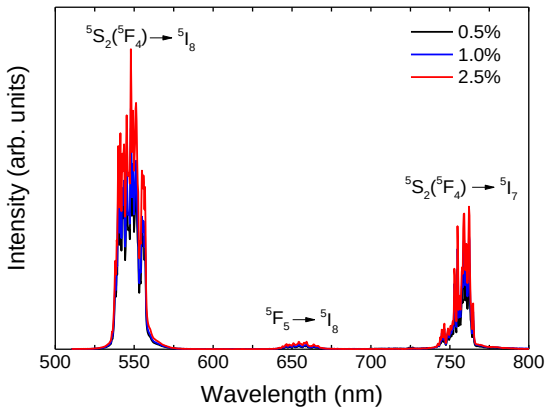

Figure 3. Emission spectra of YAP: Ho^{3+} nanoperovskites for different concentration of doped holmium at room temperature exciting at 457 nm. Transitions are also indicated in the figure.

The emission decay curves for the $^5S_2(^5F_4)$ level of Ho^{3+} ion were obtained by exciting at 539 mm with a pulse laser source and monitoring the $^5S_2(^5F_4) \rightarrow {}^5I_7$ transition at around 757 nm (see Fig. 4). The decay curve for the lowest concentration of Ho^{3+} presented a mono-exponential nature for short times, while the samples with higher concentrations showed non-exponential shapes due to the presence of multipolar interactions between Ho^{3+} ions, which are related with the energy transfer cross-relaxation process [17].

The multipolar interactions mentioned before can be explained by the Inokuti-Hirayama model [40]. According to this model, the luminescence decay intensity *I(t)* after laser pulse excitation can be represented by the following equation:

$$I(t) = I(0) \cdot \exp\left[-\frac{t}{\tau} - Q \cdot \left(\frac{t}{\tau} \right)^{3/S} \right] \quad (2)$$

where *I(0)* is the intensity at time *t=0* (in arbitrary units); τ is the intrinsic lifetime of the engaged donor level; *S* is related to the type of interaction between ions (*S=6* for dipole-dipole interaction); and, in the case of a unique type of acceptor ion, the dimensionless energy transfer parameter, *Q*, is given by the following expression:

$$Q = \frac{4\pi}{3} \cdot \Gamma\left(1 - \frac{3}{S}\right) \cdot C \cdot \left(C_{DA}\tau\right)^{3/S} \quad (3)$$

where Γ is the gamma function, *C* is the concentration of doping ions, and C_{DA} is the donor-acceptor energy transfer parameter [40].

The decay curves of the YAP: Ho^{3+} nanoperovskites have been fitted to the Inokuti-Hirayama with S = 6, confirming the dipole-dipole interaction between the Ho^{3+} ions as main contribution of the energy transfer processes.

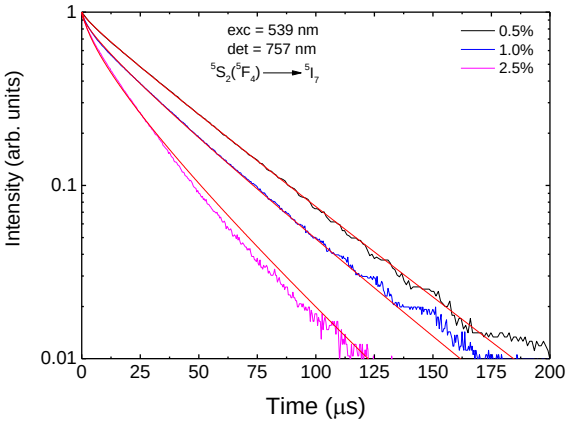

Figure 4. Emission decay curves of the $^5S_2(^5F_4)$ level monitoring the $^5S_2(^5F_4) \rightarrow {}^5I_7$ emission exciting at 539 nm with a pulse laser source. Fitted curves (in red) to the Inokuti-Hirayama model (with S = 6) are also shown.

The lifetime and energy transfer parameters *Q* were estimated from the fitting process. The τ value was found to be 44.46 μs (with an uncertainty of ± 1.0 μs). The *Q* parameters presented a linear dependence (see Fig. 5) with doping concentration of Ho^{3+} ions according to the Eq. 3 (*Q =0.48C*).

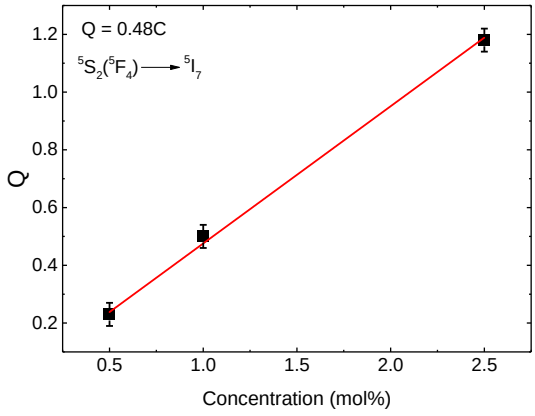

Figure 5. Transfer parameter Q values for the $^5S_2(^5F_4)$ as functions of the Ho^{3+} concentration. Linear fitting is also given (red line).

3.3. Application of YAP: Ho^{3+} nanoperovskites in sub-tissue luminescence imaging

Ho^{3+} ion has remarkable absorptions and emissions in the NIR range, which fall in the well-known "biological windows" of the human skin, composed of two spectral regions, i) the "first biological window" (*I-BW*) that covers the spectral range between 700-950 nm and ii) the "second biological window" (*II-BW*) which spectral range included between 980-1500 nm. In these windows, the optical scattering due to the absorption of water and other compounds present in tissues is notably low, being further decreased in the *II-BW* compared to the *I-BW*, due to the use of longer wavelengths. In fact, Ho^{3+} ions can be excited and emit in the *I-BW* and *II-BW* respectively.

When the YAP: Ho^{3+} nanoperovskite is excited at *I-BW* (895 nm), it exhibits an emission band and its corresponding Stark levels at 1200 nm associated with the $^5I_6 \rightarrow {}^5I_8$ which falls in the *II-BW* (see Fig.6).

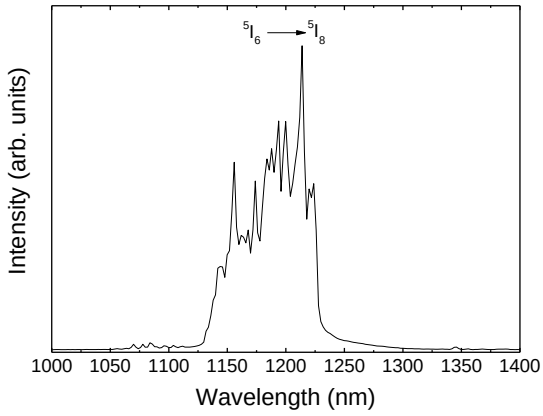

Figure 6. NIR Emission spectrum of YAP: Ho^{3+} 2.5% nanoperovskite at room temperature exciting at 895 nm. Transition is also indicated in the figure.

This feature makes YAP: Ho^{3+} nanoperovskites suitable for applications in the biomaging field. To evaluate this, an experiment was performed using a liquid known as Intralipid, dissolved at 10%, as a phantom tissue. The experimental setup for the determination of the tissue penetration depth of the YAP: Ho^{3+} 2.5% is depicted in Fig.7 (left). Shortly, the sample was placed into a holder which was located under a 1 mm size cuvette filled with a solution of this phantom tissue. The sample was excited with a continuous laser source at 895 nm. The laser beam was partially reflected by a filter and then was focused on the sample. After that, the 1200 nm emission of the sample passed through the former filter and then was focused on the spectrometer by a second lens. With this setup, the YAP: Ho^{3+} 2.5% 1200 nm emission associated with the Ho^{3+} $^5I_6 \rightarrow {}^5I_8$ transition as a function of the tissue thickness by filling the cuvette with a specific volume of the phantom tissue was measured. The phantom tissue used in this experiment was a solution of Intralipid (1.25 mL of Intralipid 20% per 23.6 mL of water) which consists in an absorbing and scattering medium that has been extensively employed in the past to mimic the optical properties of human skin in the *I-BW* and *II-BW* [41–43] .

Fig. 7 (right) shows the emission intensity versus tissue thickness. A decrease of the emission intensity with the thickness can be observed, indicating that the signal is attenuated within the phantom tissue either by absorption and/or scattering processes. However, from the penetration depth results, the use of YAP: Ho^{3+} 2.5% allows for penetration depths into in vitro human skin tissues close to 5.4 mm in the *II*-BW. The penetration depth reported here is in the same order of magnitude as that obtained in the literature [29,44] for Nd^{3+}-doped nanomaterials. This result suggests the possible application of YAP: Ho^{3+} nanoperovskite for subtissue luminescence imaging.

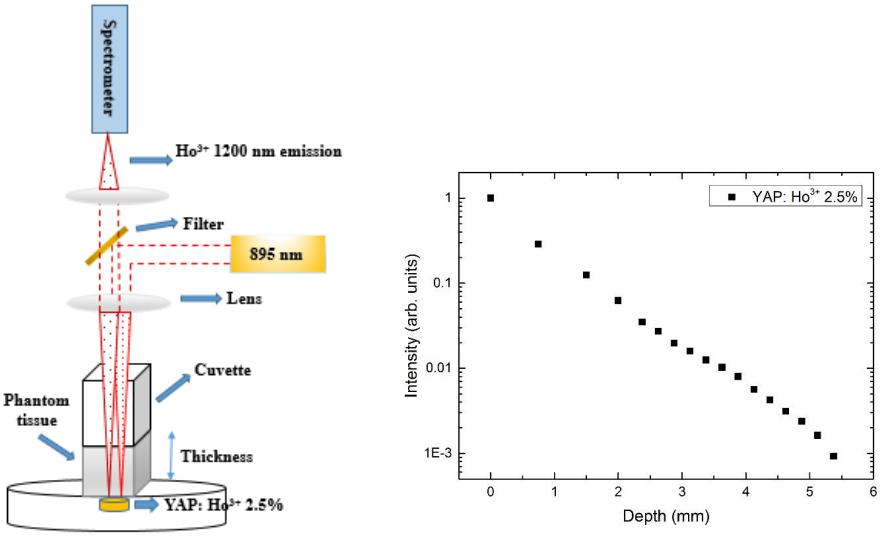

Figure 7. Schematic diagram showing the experimental procedure to determine the penetration depth of YAP: Ho^{3+} 2.5%. (left). Sub-tissue luminescence intensity as a function of the phantom tissue thickness as obtained for the emission of Ho^{3+} associated with $^5I_6 \rightarrow {}^5I_8$ of YAP: Ho^{3+} 2.5% in semilogarithm scale (right).

3.4. Application of YAP: Ho^{3+} in the performance enhancement of solar cells

It is known that upconversion is a luminescence process where two low-energy infrared photons are absorbed by rare-earth ions to generate a high-energy visible photon. The energy transfer upconversion process (ETU), consists in successive transfer processes between excited ions under excitation in the near infrared. Therefore, an excited ion can reach a high energetic level from which de-excites emitting a visible photon. Many works have been focused on improving the performance of the crystalline-silicon based solar cells taking advantage of upconversion processes by using RE^{3+} doped materials [45,46]. Among RE ions, Ho^{3+} could be interesting for hosting upconversion processes to obtain visible emission, mainly due to its energy level scheme. By this way, YAP: Ho^{3+} nano-perovkites could be a suitable candidate for this purpose.

Fig. 8 shows a comparison of the upconversion emission spectra of YAP: Ho^{3+} 2.5% nanoperovskite and glass doped with 2.5 mol% of Ho^{3+} at RT exciting at 1200 nm. The temporal dependence of the upconversion intensities of YAP: Ho^{3+} 2.5% at 550 nm (green) at 660 nm (red) are depicted in insets in the figure. The rise time that can be observed in these curves indicates that the mechanism necessary to produce the upconversion is based in energy transfer processes (ETU) in which an excited ion transfer its excitation energy to a neighbor excited ion.

From the figure, the YAP: Ho^{3+} 2.5% is more efficient than the glass sample doped with the same concentration of Ho^{3+} ions, so the use of YAP: Ho^{3+} nanoperovskites in the improvement of solar cells performance can be considered.

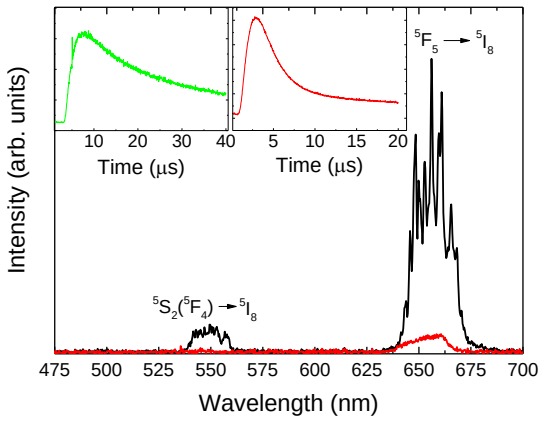

Figure 8. Comparison of the upconversion emission spectra of YAP: Ho^{3+} 2.5 mol% (black line) and glass doped with 2.5 mol% of Ho^{3+} (red line) obtained at RT exciting at 1200 nm. Temporal evolutions of the upconversion emissions associated with $^5S_2(^5F_4) \rightarrow {}^5I_8$ (green) and $^5F_5 \rightarrow {}^5I_8$ (red) are also shown in two insets in the same figure. All the transitions are indicated.

4. Conclusions

Yttrium aluminium nano-perovskite doped with different concentrations of Ho^{3+} ions were properly synthesized by sol-gel method. XRD analysis confirmed the *Pnma* orthorhombic structure of the YAP: Ho^{3+} nano-perovskites. The spectroscopic properties

of these nano-perovskites were measured and analyzed. The influent of the dopant concentration of the samples were also studied. The optical properties depend on the amount of doped ions in the samples, being the most concentrated sample which showed the most intensitive emission. The luminescence dynamics measurements showed a mono-exponential nature for the sample with the lowest concentration of Ho^{3+}, while the samples with higher concentrations of this ion, presented non-exponential profiles due to the energy transfer cross-relaxation process. The potential application of YAP: Ho^{3+} nano-perovskites in sub-tissue luminescence imaging was proven, reaching a penetration depth around of 5.4 mm. In addition, the upconverted emissions of YAP: Ho^{3+} nano-perovskite was compared to a Ho^{3+}-doped glass with the same concentration of Ho^{3+} ions, showing a higher upconverted emission intensities, suggesting the potential use of YAP: Ho^{3+} nano-perovskite to enhance the performance of a solar cell.

References

[1] F. Wang, Y. Han, C.S. Lim, Y. Lu, J. Wang, J. Xu, H. Chen, C. Zhang, M. Hong, X. Liu, Simultaneous phase and size control of upconversion nanocrystals through lanthanide doping, Nature. 463 (2010) 1061–1065. doi:10.1038/nature08777.

[2] X. Bai, H. Song, G. Pan, Y. Lei, T. Wang, X. Ren, S. Lu, B. Dong, Q. Dai, L. Fan, Size-dependent upconversion luminescence in Er3+/Yb 3+-COdOpCd nanocrystalline yttria: Saturation and thermal effects, J. Phys. Chem. C. 111 (2007) 13611–13617. doi:10.1021/jp070122e.

[3] F. Wang, X. Liu, Supporting Information Upconversion Multicolor Fine-Tuning : Visible to Near-Infrared Emission from Lathanide-Doped NaYF 4 nanoparticles, Synthesis (Stuttg). 3 (2008) 1–7. doi:10.1021/ja800868a.

[4] J.C. Boyer, L. a. Cuccia, J. a. Capobianco, Synthesis of colloidal upconverting NaYF4: Er3+/Yb3+ and Tm3+/Yb3+ monodisperse nanocrystals, Nano Lett. 7 (2007) 847–852. doi:10.1021/nl070235+.

[5] P.R. Diamente, M. Raudsepp, F.C.J.M. Van Veggel, Dispersible Tm3+-doped nanoparticles that exhibit strong 1.47 ??m photoluminescence, Adv. Funct. Mater. 17 (2007) 363–368. doi:10.1002/adfm.200600142.

[6] L. Li, C.K. Tsung, Z. Yang, G.D. Stucky, L. Sun, J. Wang, C. Yan, Rare-earth-doped nanocrystalline titania microspheres emitting luminescence via energy transfer, Adv. Mater. 20 (2008) 903–908. doi:10.1002/adma.200701507.

[7] T.R. Hinklin, S.C. Rand, R.M. Laine, Transparent, polycrystalline upconverting nanoceramics: Towards 3-D displays, Adv. Mater. 20 (2008) 1270–1273. doi:10.1002/adma.200701235.

[8] X. Wang, X. Kong, Y. Yu, Y. Sun, H. Zhang, Effect of annealing on upconversion luminescence of ZnO:Er3+ nanocrystals and high thermal sensitivity, J. Phys. Chem. C. 111 (2007) 15119–15124. doi:10.1021/jp0686689.

[9] A. Speghini, F. Piccinelli, M. Bettinelli, Synthesis, characterization and luminescence

spectroscopy of oxide nanopowders activated with trivalent lanthanide ions: The garnet family, Opt. Mater. (Amst). 33 (2011) 247–257. doi:10.1016/j.optmat.2010.10.039.

[10] F. Wang, X. Liu, Recent advances in the chemistry of lanthanide-doped upconversion nanocrystals, Chem. Soc. Rev. 38 (2009) 976–989. doi:10.1039/B809132N.

[11] V. Mahalingam, F. Mangiarini, F. Vetrone, V. Venkatramu, M. Bettinelli, A. Speghini, J. a Capobianco, Bright White Upconversion Emission from Tm 3 + / Yb 3 + / Er 3 + -Doped Lu 3 Ga 5 O 12 Nanocrystals, J. Phys. Chem. C. 112 (2008) 17745–17749. doi:10.1021/jp8076479.

[12] E.C.C. De Souza, R. Muccillo, Properties and applications of perovskite proton conductors, Mater. Res. 13 (2010) 385–394. doi:10.1590/S1516-14392010000300018.

[13] A. Boudali, A. Abada, M. Driss Khodja, B. Amrani, K. Amara, F. Driss Khodja, A. Elias, Calculation of structural, elastic, electronic, and thermal properties of orthorhombic CaTiO3, Phys. B Condens. Matter. 405 (2010) 3879–3884. doi:10.1016/j.physb.2010.06.020.

[14] A. Vecht, D.W. Smith, S.S. Chadha, C.S. Gibbons, J. Koh, D. Morton, New electron excited light emitting materials*, J. Vac. Sci. Technol. B. 12 (1994).

[15] K. Lemański, P.J. Dereń, Spectroscopic properties of Dy3+ ions in CaTiO3 nano-perovskites, J. Lumin. 145 (2014) 661–664. doi:10.1016/j.jlumin.2013.08.048.

[16] K. Lemański, a. Gagor, M. Kurnatowska, R. Pzik, P.J. Dereń, Spectroscopic properties of Nd3 ions in nano-perovskite CaTiO3, J. Solid State Chem. 184 (2011) 2713–2718. doi:10.1016/j.jssc.2011.08.004.

[17] P.J. Dereń, K. Lemański, Cross relaxation in CaTiO3 and LaAlO3 perovskite nanocrystals doped with Ho3+ ions, J. Lumin. 154 (2014) 62–67. doi:10.1016/j.jlumin.2014.04.008.

[18] M. Manso, M. Langlet, J.. Martínez-Duart, Testing sol–gel CaTiO3 coatings for biocompatible applications, Mater. Sci. Eng. C. 23 (2003) 447–450. doi:10.1016/S0928-4931(02)00319-3.

[19] C. Sameera Devi, G.S. Kumar, G. Prasad, Spectroscopic and electrical studies on Nd3+, Zr4+ ions doped nano-sized BaTiO3 ferroelectrics prepared by sol–gel method, Spectrochim. Acta Part A Mol. Biomol. Spectrosc. 136 (2015) 366–372. doi:10.1016/j.saa.2014.09.042.

[20] J.L. and Y.J.W. and M. Kuwabara, Photoluminescence and its Enhancement of Pr3+ -Doped BaTiO3 Phosphor, Jpn. J. Appl. Phys. 44 (2005) L708. http://stacks.iop.org/1347-4065/44/i=5L/a=L708.

[21] Z. Yao, H. Liu, Y. Liu, Z. Wu, Z. Shen, Y. Liu, M. Cao, Structure and dielectric behavior of Nd-doped BaTiO3 perovskites, Mater. Chem. Phys. 109 (2008) 475–481. doi:10.1016/j.matchemphys.2007.12.019.

[22] K. Yasuda, S. Usuda, H. Gunji, Properties of a YAP powder scintillator as alpha-ray detector, Appl. Radiat. Isot. 52 (2000) 365–368. doi:10.1016/S0969-8043(99)00179-7.

[23] M. Tardocchi, A. Pietropaolo, C. Andreani, G. Gorini, S. Imberti, E. Perelli-Cippo, R. Senesi, N. Rhodes, E.M. Schooneveld, Comparison of Cadmium–Zinc–Telluride semiconductor and Yttrium–Aluminum–Perovskite scintillator as photon detectors for epithermal neutron spectroscopy, Nucl. Instruments Methods Phys. Res. Sect. A Accel. Spectrometers, Detect. Assoc. Equip. 567 (2006) 337–340. doi:10.1016/j.nima.2006.05.151.

[24] T.B. De Queiroz, C.R. Ferrari, D. Ulbrich, R. Doyle, a. S.S. De Camargo, Luminescence characteristics of YAP:Ce scintillator powders and composites, Opt. Mater. (Amst). 32 (2010) 1480–1484. doi:10.1016/j.optmat.2010.06.004.

[25] Y. Zhydachevskii, A. Durygin, A. Suchocki, A. Matkovskii, D. Sugak, P. Bilski, S. Warchol, Mn-doped YAlO3 crystal: a new potential TLD phosphor, Nucl. Instruments Methods Phys. Res. Sect. B. 227 (2005) 545–550. doi:10.1016/j.nimb.2004.09.013.

[26] H.B. Premkumar, D.V. Sunitha, H. Nagabhushana, S.C. Sharma, B. Daruka Prasad, B.M. Nagabhushana, C. Shivakumara, J.L. Rao, N.O. Gopal, K.R. Prabhakara, S.-C. Ke, R.P.S. Chakradhar, Synthesis, structural and thermoluminescence properties of YAlO3:Dy3+ nanophosphors, J. Alloys Compd. 591 (2014) 337–345. doi:10.1016/j.jallcom.2013.12.217.

[27] M.A. Hernández-Rodríguez, U.R. Rodríguez-Mendoza, V. Lavín, J.E. Muñoz-Santiuste, I.R. Martín, A.D. Lozano-Gorrín, High pressure sensitivity of anti-Stokes fluorescence in Nd 3+ doped yttrium orthoaluminate nano-perovskites, J. Lumin. 196 (2018) 20–24. doi:10.1016/j.jlumin.2017.12.008.

[28] M.A. Hernández-Rodríguez, J.E. Muñoz-Santiuste, V. Lavín, A.D. Lozano-Gorrín, P. Rodríguez-Hernández, A. Muñoz, V. Venkatramu, I.R. Martín, U.R. Rodríguez-Mendoza, High pressure luminescence of Nd 3+ in YAlO 3 nano-perovskites: A crystal field analysis, (Submitted). (n.d.).

[29] M.A. Hernández-Rodríguez, A.D. Lozano-Gorrín, I.R. Martín, U.R. Rodríguez-Mendoza, V. Lavín, Comparison of the sensitivity as optical temperature sensor of nano-perovskite doped with Nd3+ ions in the first and second biological windows, Sensors Actuators, B Chem. 255 (2018) 970–976. doi:10.1016/j.snb.2017.08.140.

[30] M.A. Hernández-Rodríguez, A.D. Lozano-Gorrín, V. Lavín, U.R. Rodríguez-Mendoza, I.R. Martín, Yttrium orthoaluminate nanoperovskite doped with Tm 3+ ions as upconversion optical temperature sensor in the near-infrared region, Opt. Express. 25 (2017) 27845–27856. doi:10.1364/OE.25.027845.

[31] Y. Wei, G. Zhang, C.-H. Huang, H.-Y. Zhu, L.-X. Huang, X.-J. Ou-Yang, G.-F. Wang, A single wavelength 1339nm Nd:YAP pulsed laser, Opt. Commun. 282 (2009) 4397–4400. doi:10.1016/j.optcom.2009.07.055.

[32] M. Fibrich, T. Hambálek, M. Němec, J. Šulc, H. Jelínková, Multiline generation capabilities of diode-pumped Nd:YAP and Nd:YAG lasers, Laser Phys. 24 (2014) 35803. doi:10.1088/1054-660X/24/3/035803.

[33] H.B. Premkumar, B.S. Ravikumar, D. V. Sunitha, H. Nagabhushana, S.C. Sharma, M.B. Savitha, S. Mohandas Bhat, B.M. Nagabhushana, R.P.S. Chakradhar, Investigation of structural and luminescence properties of Ho3+ doped YAlO3 nanophosphors synthesized through solution combustion route, Spectrochim. Acta - Part A Mol. Biomol. Spectrosc. 115 (2013) 234–243. doi:10.1016/j.saa.2013.06.015.

[34] M. Malinowski, M. Kaczkan, a. Wnuk, M. Szufliñska, Emission from the high lying excited states of Ho3+ ions in YAP and YAG crystals, J. Lumin. 106 (2004) 269–279. doi:10.1016/j.jlumin.2003.10.008.

[35] H. Zhang, D. Sun, J. Luo, J. Chen, H. Yang, J. Xiao, Q. Zhang, S. Yin, Growth, thermal, and spectroscopic properties of a Cr,Yb,Ho,Eu:YAP laser crystal, Opt. Mater. (Amst). 36 (2014) 1361–1365. doi:10.1016/j.optmat.2014.03.029.

[36] H. Zhang, D. Sun, J. Luo, S. Cao, M. Cheng, Q. Zhang, S. Yin, Growth and spectroscopic investigations of Yb,Ho: YAP and Yb,Ho,Pr:YAP laser crystals, J. Lumin. 158 (2015) 215–219. doi:10.1016/j.jlumin.2014.10.003.

[37] S. Flock, S.L. Jacques, S.T. Flock, S.L. Jacques, B.C. Wilson, Optical properties of Intralipid : A phantom medium for light propagation studies, Lasers Surg. Med. 12 (1992) 510–519. doi:10.1002/lsm.1900120510.

[38] J. Rodríguez-Carvajal, Recent advances in magnetic structure determination by neutron powder diffraction, Phys. B Condens. Matter. 192 (1993) 55–69. doi:10.1016/0921-4526(93)90108-I.

[39] M.J. Weber, Optical Transition Probabilities for Trivalent Holmium in LaF3 and YAlO3, J. Chem. Phys. 57 (1972) 562. doi:10.1063/1.1678000.

[40] M. Inokuti, F. Hirayama, Influence of Energy Transfer by the Exchange Mechanism on Donor Luminescence, J. Chem. Phys. 43 (1965) 1978. doi:10.1063/1.1697063.

[41] S. Nagarajan, Y. Zhang, Upconversion fluorescent nanoparticles as a potential tool for in-depth imaging., Nanotechnology. 22 (2011) 395101. doi:10.1088/0957-4484/22/39/395101.

[42] K. Welsher, S.P. Sherlock, H. Dai, Deep-tissue anatomical imaging of mice using carbon nanotube fluorophores in the second near-infrared window., Proc. Natl. Acad. Sci. U. S. A. 108 (2011) 8943–8948. doi:10.1073/pnas.1014501108.

[43] V.M. Kodach, J. Kalkman, D.J. Faber, T.G. van Leeuwen, Quantitative comparison of the OCT imaging depth at 1300 nm and 1600 nm., Biomed. Opt. Express. 1 (2010) 176. doi:10.1364/BOE.1.000176.

[44] U. Rocha, K.U. Kumar, C. Jacinto, I. Villa, F. Sanz-Rodríguez, M. Del Carmen Iglesias De La Cruz, A. Juarranz, E. Carrasco, F.C.J.M. Van Veggel, E. Bovero, J.G. Solé, D. Jaque, Neodymium-doped LaF3 nanoparticles for fluorescence bioimaging in the second biological window, Small. 10 (2014) 1141–1154. doi:10.1002/smll.201301716.

[45] M. a. Hernández-Rodríguez, M.H. Imanieh, L.L. Martín, I.R. Martín, Experimental enhancement

of the photocurrent in a solar cell using upconversion process in fluoroindate glasses exciting at 1480 nm, Sol. Energy Mater. Sol. Cells. 116 (2013) 171–175. doi:10.1016/j.solmat.2013.04.023.

[46] F. Lahoz, C. Pérez-Rodríguez, S.E. Hernández, I.R. Martín, V. Lavín, U.R. Rodríguez-Mendoza, Upconversion mechanisms in rare-earth doped glasses to improve the efficiency of silicon solar cells, Sol. Energy Mater. Sol. Cells. 95 (2011) 1671–1677. doi:10.1016/j.solmat.2011.01.027.

Acknowledgements

This work has been partially supported by MINECO (MAT2013-46649-C4-4-P, MAT2015-71070-REDC, and MAT2016-75586-C4-4-P), and by the EU-FEDER funds.

M.A. Hernández-Rodríguez thanks MINECO for FPI grant (BES-2014-068666).

6.3. Other works

1. **Chemical pressure effects on the spectroscopic properties of Nd^{3+}-doped gallium nano-garnets**

Authors: V. Monteseguro, M. Rathaiah, K. Linganna, A.D. Lozano-Gorrín, M.A. Hernández-Rodríguez, I.R. Martín, P. Babu, U.R. Rodríguez-Mendoza, F.J. Manjón, A. Muñoz, C.K. Jayasankar, V. Venkatramu, V. Lavín

Journal: Optical Material Express 5 (2015) 1661–1673.

2. **Synthesis, structural characterization and optical study of Dy^{3+}-doped langbeinite salts**

Authors: A. Souamti, I.R. Martín, L. Zayani, M.A. Hernández-Rodríguez, K. Soler-Carracedo, A.D. Lozano-Gorrín, E. Lalla, D. Ben Hassen Chehim

Journal: Journal of Luminescence 177 (2016) 160–165.

3. **Blue up-conversion emission of Yb^{3+}-doped langbeinite salts**

Authors: A. Souamti, I.R. Martín, L. Zayani, M. A. Hernández-Rodríguez, K. Soler-Carracedo, A.D. Lozano-Gorrín, D. Ben Hassen Chehimi

Journal: Optical Materials 53 (2016) 190–194.

4. **Synthesis, characterization and spectroscopic properties of a new Nd^{3+}-doped Co-picromerite-type Tutton salt**

Authors: A. Souamti, I.R. Martín, L. Zayani, M.A. Hernández-Rodríguez, K. Soler-Carracedo, A.D. Lozano-Gorrín

Journal: Journal of Luminescence 177 (2016) 93–98.

5. **Liquid whispering-gallery-mode resonator as a humidity sensor**

Authors: L. Labrador-Páez, K. Soler-Carracedo, Miguel Hernández-Rodríguez, I.R. Martín, T. Carmon, L.L. Martin

Journal: Optical Material Express 25 (2017) 1165.

6. Er^{3+}-doped tellurite glasses for enhancing a solar cell photocurrent through photon upconversion upon 1500 nm excitation

Authors: K.V. Krishnaiah, P. Venkatalakshmamma, C. Basavapoornima, I.R. Martín, K. Soler-Carracedo, M.A. Hernández-Rodríguez, V. Venkatramu, C.K. Jayasankar

Journal: Material Chemistry and Physics 199 (2017) 67–72.

7. Carbon dots as temperature nanosensors in the physiological range

Authors: M.A. Hernández-Rodríguez, María M. Afonso, J. Antonio Palenzuela, R. Martín, Soler-Carracedo K

Journal: Journal of Luminescence (accepted).

7. REFERENCES

[1] S.A. Wade, S.F. Collins, G.W. Baxter, Fluorescence intensity ratio technique for optical fiber point temperature sensing, J. Appl. Phys. 94 (2003) 4743–4756. doi:10.1063/1.1606526.

[2] F. Vetrone, R. Naccache, A. Zamarrón, A.J. De La Fuente, F. Sanz-Rodríguez, L.M. Maestro, E.M. Rodriguez, D. Jaque, J.G. Sole, J.A. Capobianco, Temperature sensing using fluorescent nanothermometers, ACS Nano. 4 (2010) 3254–3258. doi:10.1021/nn100244a.

[3] Wilfried B. Holzapfel and Neil S. Isaacs, High Pressure Techniques in Chemistry and Physics, Oxford University Press, Oxford, 1997. http://ukcatalogue.oup.com/product/9780198558118.do.

[4] P.W. Bridgman, The effect of homogeneous mechanical stress on the electrical resistance of crystals, Phys. Rev. 42 (1932) 858–863. doi:10.1103/PhysRev.42.858.

[5] J.D. Barnett, S. Block, G.J. Piermarini, An Optical Fluorescence System for Quantitative Pressure Measurement in the Diamond-Anvil Cell, Rev. Sci. Instrum. 44 (1973) 1–9. doi:10.1063/1.1685943.

[6] J. Saldo, Materia a alta presión. Fundamentos y aplicaciones, (2011) 423–440.

[7] A. Lacam, C. Chateau, High-pressure measurements at moderate temperatures in a diamond anvil cell with a new optical sensor: $SrB_4O_7:Sm^{2+}$, J. Appl. Phys. 66 (1989) 366–372. doi:10.1063/1.343884.

[8] J.M. Leger, C. Chateau, A. Lacam, $SrB_4O_7:Sm^{2+}$ pressure optical sensor: Investigations in the megabar range, J. Appl. Phys. 68 (1990) 2351–2354. doi:10.1063/1.346543.

[9] F. Datchi, R. LeToullec, P. Loubeyre, Improved calibration of the SrB4O7: Sm^{2+} optical pressure gauge: Advantages at very high pressures and high temperatures, J. Appl. Phys. 81 (1997) 3333–3339. doi:10.1063/1.365025.

[10] Q. Jing, Q. Wu, L. Liu, J.A. Xu, Y. Bi, Y. Liu, H. Chen, S. Liu, Y. Zhang, L.

Xiong, Y. Li, J. Liu, An experimental study on $SrB_4O_7:Sm^{2+}$ as a pressure sensor, J. Appl. Phys. 113 (2013) 023507-0235011. doi:10.1063/1.4774113.

[11] J. Liu, Y.K. Vohra, Sm:YAG optical pressure sensor to 180 GPa:Calibration and structural disorder, Appl. Phys. Lett. 64 (1994) 3386–3388. doi:10.1063/1.111283.

[12] N.J. Hess, D. Schiferl, Comparison of the pressure-induced frequency shift of Sm:YAG to the ruby and nitrogen vibron pressure scales from 6 to 820 K and 0 to 25 GPa and suggestions for use as a high-temperature pressure calibrant, J. Appl. Phys. 71 (1992) 2082–2086. doi:10.1063/1.351158.

[13] J. Liu, Y.K. Vohra, Photoluminescence and x-ray-diffraction studies on Sm-doped yttrium aluminum garnet to ultrahigh pressures of 338 GPa, J. Appl. Phys. 79 (1996) 7978-7982. doi:10.1063/1.362348.

[14] A.F. Goncharov, J.M. Zaug, J.C. Crowhurst, E. Gregoryanz, Optical calibration of pressure sensors for high pressures and temperatures, J. Appl. Phys. 97 (2005) 094917-094921. doi:10.1063/1.1895467.

[15] Q. Wei, N. Dubrovinskaia, L. Dubrovinsky, Ruby and Sm:YAG fluorescence pressure gauges up to 120 GPa and 700 K, J. Appl. Phys. 110 (2011) 043513-043516 (2011) (2011). doi:10.1063/1.3624618.

[16] H. Hua, S. Mirov, Y. Vohra, High-pressure and high-temperature studies on oxide garnets, Phys. Rev. B. 54 (1996) 6200–6209. doi:10.1103/PhysRevB.54.6200.

[17] H. Hua, J. Liu, Y.K. Vohra, Pressure-induced amorphization in gadolinium scandium gallium garnet by x-ray diffraction and spectroscopic studies, J. Phys. Condens. Matter. 8 (1999) L139–L145. doi:10.1088/0953-8984/8/10/002.

[18] A. Kamińska, P. Kaczor, A. Durygin, A. Suchocki, M. Grinberg, Low-temperature high-pressure spectroscopy of lanthanum lutetium gallium garnet crystals doped with Cr^{3+} and Nd^{3+}, Phys. Rev. B. 65 (2002) 104106–104113. doi:10.1103/PhysRevB.65.104106.

[19] S. Kobyakov, A. Kamińska, A. Suchocki, D. Galanciak, M. Malinowski, Nd^{3+}-doped yttrium aluminum garnet crystal as a near-infrared pressure sensor for

diamond anvil cells, Appl. Phys. Lett. 88 (2006) 234102–234103. doi:10.1063/1.2210084.

[20] A. Kaminska, R. Buczko, W. Paszkowicz, H. Przybylińska, E. Werner-Malento, A. Suchocki, M. Brik, A. Durygin, V. Drozd, S. Saxena, Merging of the $^4F_{3/2}$ level states of Nd^{3+} ions in the photoluminescence spectra of gadolinium-gallium garnets under high pressure, Phys. Rev. B. 84 (2011) 075483–075488. doi:10.1103/PhysRevB.84.075483.

[21] H. Hua, Y.K. Vohra, Pressure-induced blueshift of Nd^{3+} fluorescence emission in $YAlO_3$: Near infrared pressure sensor, Appl. Phys. Lett. 71 (1997) 2602–2604. doi:10.1063/1.119341.

[22] M.A. Hernández-Rodríguez, U.R. Rodríguez-Mendoza, V. Lavín, J.E. Muñoz-Santiuste, I.R. Martín, A.D. Lozano-Gorrín, High pressure sensitivity of anti-Stokes fluorescence in Nd 3+ doped yttrium orthoaluminate nano-perovskites, J. Lumin. 196 (2018) 20–24. doi:10.1016/j.jlumin.2017.12.008.

[23] M.A. Hernández-Rodríguez, J.E. Muñoz-Santiuste, V. Lavín, A.D. Lozano-Gorrín, P. Rodríguez-Hernández, A. Muñoz, V. Venkatramu, I.R. Martín, U.R. Rodríguez-Mendoza, High pressure luminescence of Nd^{3+} in YAlO3 nano-perovskites: A crystal field analysis, J. Chem. Phys. 148 (2018) (In press).

[24] P.R.N. Childs, J.R. Greenwood, C.A. Long, Review of temperature measurement Review of temperature measurement, 2959-2978 (2012). doi:10.1063/1.1305516.

[25] L. Michalski, K. Eckersdorf, J. Kucharski, J. McGhee, Temperature Measurement, Wiley, Chichester, UK, 2001.

[26] S. Maekawa, T. Tohyama, S.E. Barnes, S. Ishihara, W. Koshibae, G. Khaliullin, Physics of Transition Metal Oxides, Springer, Verlag, 2004.

[27] G. Beheim, Integrated Optics, Microstructures, and Sensors, 1995, pp. 285–313, Springer, 1995.

[28] S.F. Collins, G.W. Baxter, S.A. Wade, T. Sun, K.T. V Grattan, Z.Y. Zhang, A.W. Palmer, Comparison of fluorescence-based temperature sensor schemes: Theoretical analysis and experimental validation, 4649-4654 (2003). doi:10.1063/1.368705.

[29] S.A. Wade, Temperature measurement using rare-earth doped fibre fluorescence, (2003) 220.

[30] V.K. Rai, Temperature sensors and optical sensors, Appl. Phys. B Lasers Opt. 88 (2007) 297–303. doi:10.1007/s00340-007-2717-4.

[31] B.A. Weinstein, B.A. Weinstein, Ruby thermometer for cryobaric diamondanvil cell, 57 (1986) 910-913. doi:10.1063/1.1138833.

[32] V.K. Rai, Sm^{3+} as a fluorescence lifetime temperature sensing, IEEE Sens. J. 7 (2007) 1110–1111. doi:10.1109/JSEN.2007.897939.

[33] S.F. León-Luis, U.R. Rodríguez-Mendoza, P. Haro-González, I.R. Martín, V. Lavín, Role of the host matrix on the thermal sensitivity of Er^{3+} luminescence in optical temperature sensors, Sensors Actuators, B Chem. 174 (2012) 176–186. doi:10.1016/j.snb.2012.08.019.

[34] M. Rodrigues, R. Piñol, G. Antorrena, C.D.S. Brites, N.J.O. Silva, J.L. Murillo, R. Cases, I. Díez, F. Palacio, N. Torras, J.A. Plaza, L. Pérez-García, L.D. Carlos, A. Millán, Implementing Thermometry on Silicon Surfaces Functionalized by Lanthanide-Doped Self-Assembled Polymer Monolayers, Adv. Funct. Mater. 26 (2016) 200–209. doi:10.1002/adfm.201503889.

[35] X. Wang, J. Zheng, Y. Xuan, X. Yan, Optical temperature sensing of $NaYbF_4$: $Tm^{3+}@SiO_2$ core-shell micro-particles induced by infrared excitation, Opt. Express. 21 (2013) 21596–21606. doi:10.1364/OE.21.021596.

[36] M.A. Hernández-Rodríguez, A.D. Lozano-Gorrín, V. Lavín, U.R. Rodríguez-Mendoza, I.R. Martín, Yttrium orthoaluminate nanoperovskite doped with Tm^{3+} ions as upconversion optical temperature sensor in the near-infrared region, Opt. Express. 25 (2017) 27845–27856. doi:10.1364/OE.25.027845.

[37] H. Berthou, Optical-fiber temperature sensor based on upconversion-excited fluorescence, 15 (1990) 1100–1102. doi.org/10.1364/OL.15.001100

[38] G.S. Maciel, L. de S. Menezes, A.S.L. Gomes, C.B. de Araújo, Y. Messaddeq, A. Florez, M.A. Aegerter, Temperature Sensor Based on Frequency Upconversion in Er^{3+}-Doped Fluoroindate Glass, IEEE J. Quantum Elec. (1999) 395–399.

[39] B. Dong, D.P. Liu, X.J. Wang, T. Yang, S.M. Miao, C.R. Li, Optical

thermometry through infrared excited green upconversion emissions in Er^{3+}-Yb^{3+} codoped Al_2O_3, Appl. Phys. Lett. 90 (2007) 23–25. doi:10.1063/1.2735955.

[40] E. Maurice, S.A. Wade, S.F. Collins, G.W. Baxter, Self-referenced point temperature sensor based on a fluorescence intensity ratio in Yb^{3+}-doped silica fiber, App. Opt. (1997) 8264-8269.

[41] F. Sidiroglou, S.A. Wade, N.M. Dragomir, G.W. Baxter, S.F. Collins, Effects of high-temperature heat treatment on Nd^{3+}-doped optical fibers for use in fluorescence intensity ratio based temperature sensing, Rev. Sci. Instrum. 74 (2003) 3524–3530. doi:10.1063/1.1578706.

[42] V.K. Rai, D.K. Rai, S.B. Rai, Pr3+ doped lithium tellurite glass as a temperature sensor, Sensors Actuators, A Phys. 128 (2006) 14–17. doi:10.1016/j.sna.2005.12.030.

[43] V.K. Rai, S.B. Rai, Temperature sensing behaviour of the stark sublevels, Spectrochim. Acta - Part A Mol. Biomol. Spectrosc. 68 (2007) 1406–1409. doi:10.1016/j.saa.2007.02.017.

[44] L. Shi, H. Zhang, Q. Su, Eu^{3+} doped Sr_2CeO_4 phosphors for thermometry: single-color or two-color fluorescence based temperature characterization, RSC Adv. 3 (2011) 298–304. doi:10.1039/c1ra00221j.

[45] S.D. Alaruri, A.J. Brewington, M.A. Thomas, J.A. Miller, High-Temperature Remote Thermometry Using Laser-Induced Fluorescence Decay Lifetime Measurements of Y_2O_3: Eu and YAG: Tb Thermographic Phosphors, IEEE Trans. Instrum. Meas. 42 (1993) 735-739. doi:10.1109/19.231599.

[46] R. Hasegawa, I. Sakata, H. Yanagihara, B. Johansson, A. Omrane, M. Aldén, Two-dimensional gas-phase temperature measurements using phosphor thermometry, Appl. Phys. B Lasers Opt. 88 (2007) 291–296. doi:10.1007/s00340-007-2690-y.

[47] A. Sedlmeier, D.E. Achatz, L.H. Fischer, H.H. Gorris, O.S. Wolfbeis, Photon upconverting nanoparticles for luminescent sensing of temperature, Nanoscale (2012) 7090–7096. doi:10.1039/c2nr32314a.

[48] A.M. Smith, M.C. Mancini, S. Nie, Bioimaging: second window for in vivo

imaging, Nat. Nanotechnol. 4 (2009) 710–711. doi:10.1038/nnano.2009.326.

[49] D. Wawrzynczyk, A. Bednarkiewicz, M. Nyk, W. Strek, M. Samoc, Neodymium(iii) doped fluoride nanoparticles as non-contact optical temperature sensors, Nanoscale 4 (2012) 6959-6961. doi:10.1039/c2nr32203j.

[50] U. Rocha, K. Upendra Kumar, C. Jacinto, J. Ramiro, A.J. Caamaño, J. García Solé, D. Jaque, Nd^{3+} doped LaF_3 nanoparticles as self-monitored photo-thermal agents, Appl. Phys. Lett. 104 (2014) 053703-053707. doi:10.1063/1.4862968.

[51] E.C. Ximendes, U. Rocha, B. del Rosal, A. Vaquero, F. Sanz-Rodríguez, L. Monge, F. Ren, F. Vetrone, D. Ma, J. García-Solé, C. Jacinto, D. Jaque, N. Fernández, In Vivo Ischemia Detection by Luminescent Nanothermometers, Adv. Healthc. Mater. 6 (2017) 1–8. doi:10.1002/adhm.201601195.

[52] A. Benayas, B. Del Rosal, A. Pérez-Delgado, K. Santacruz-Gómez, D. Jaque, G.A. Hirata, F. Vetrone, Nd:YAG Near-Infrared Luminescent Nanothermometers, Adv. Opt. Mater. 3 (2015) 687–694. doi:10.1002/adom.201400484.

[53] I.E. Kolesnikov, E. V. Golyeva, A.A. Kalinichev, M.A. Kurochkin, E. Lähderanta, M.D. Mikhailov, Nd^{3+} single doped YVO_4 nanoparticles for sub-tissue heating and thermal sensing in the second biological window, Sensors Actuators, B Chem. 243 (2017) 338–345. doi:10.1016/j.snb.2016.12.005.

[54] O. Ridge, The classification of tilted octahedra in perovskites, Acta Crystallogr. (1972). doi:10.1107/S0567740872007976.

[55] P.M. Woodward, Octahedral Tilting in Perovskites . I . Geometrical Considerations, Acta Crystallogr. (1997) 32–43. doi:10.1107/S0108768196010713.

[56] P.M. Woodward, Octahedral Tilting in Perovskites. II. Structure Stabilizing Forces, Acta Crystallogr. (1997) 44–66. doi:10.1107/S0108768196012050.

[57] N. A., W. D., Perovskite: A Structure of Great Interest to Geophysics and Materials Science, 1989.

[58] I.P. Kaminow, W.D. Johnston, Quantitative Determination of Sources of the Electro-Optic Effect in $LiNbO_3$ and $LiTaO_3$, Phys. Rev. 160 (1967) 519–522.

doi:10.1103/PhysRev.160.519.

[59] S. Zhu, Y. Zhu, N. Ming, Quasi-Phase-Matched Third-Harmonic Generation in a Quasi-Periodic Optical Superlattice, Science 278 (1997) 843–846. doi:10.1126/science.278.5339.843.

[60] A.J. Wojtowicz, W. Drozdowski, D. Wisniewski, J.L. Lefaucheur, Z. Galazka, Z. Gou, T. Lukasiewicz, J. Kisielewski, Scintillation properties of selected oxide monocrystals activated with Ce and Pr, Opt. Mater. 28 (2006) 85–93. doi:10.1016/j.optmat.2004.09.029.

[61] D. Kan, T. Terashima, R. Kanda, A. Masuno, K. Tanaka, S. Chu, H. Kan, A. Ishizumi, Y. Kanemitsu, Y. Shimakawa, M. Takano, Blue-light emission at room temperature from Ar+-irradiated $SrTiO_3$, Nat. Mater. 4 (2005) 816–819. doi:10.1038/nmat1498.

[62] H. Takashima, K. Shimada, N. Miura, T. Katsumata, Y. Inaguma, K. Ueda, M. Itoh, Low-driving-voltage electroluminescence in perovskite films, Adv. Mater. 21 (2009) 3699–3702. doi:10.1002/adma.200900524.

[63] S.Y. Yang, J. Seidel, S.J. Byrnes, P. Shafer, C.-H. Yang, M.D. Rossell, P. Yu, Y.-H. Chu, J.F. Scott, J.W. Ager, L.W. Martin, R. Ramesh, Above-bandgap voltages from ferroelectric photovoltaic devices., Nat. Nanotechnol. 5 (2010) 143–147. doi:10.1038/nnano.2009.451.

[64] S. Wang, H. Zhou, X. Wang, A. Pan, Up-conversion luminescence and optical temperature-sensing properties of Er^{3+}-doped perovskite $Na_{0.5}Bi_{0.5}TiO_3$ nanocrystals, J. Phys. Chem. Solids. 98 (2016) 28–31. doi:10.1016/j.jpcs.2016.06.002.

[65] P. Du, L. Luo, W. Li, Q. Yue, Upconversion emission in Er-doped and Er/Yb-codoped ferroelectric $Na_{0.5}Bi_{0.5}TiO_3$ and its temperature sensing application, J. Alloys Compd. 116 (2014) 014102–014107. doi:10.1063/1.4886575.

[66] M.J. Weber, M. Bass, K. Andringa, R.R. Monchamp, Comperch.E, Czochralski Growth and Properties of $YAlO_3$ Laser Crystals, Appl. Phys. Lett. 15 (1969) 342–345. doi:10.1063/1.1652851.

[67] G. Neuroth, F. Wallrafen, Czochralski growth and characterisation of pure and

doped $YAlO_3$ single crystals, J. Cryst. Growth. 199 (1999) 435–439. http://www.sciencedirect.com/science/article/pii/S0022024898010732.

[68] W.S. Rabinovich, S.R. Bowman, B.J. Feldman, M.J. Winings, Tunable Laser Pumped 3 μm Ho:$YAlO_3$ Laser, IEEE J. Quantum Elec. 27 (1991) 895–897.

[69] J.J. Romero, E. Montoya, L.E. Bausá, F. Agulló-Rueda, M.R.B. Andreeta, A.C. Hernandes, Multiwavelength laser action of Nd^{3+}:$YAlO_3$ single crystals grown by the laser heated pedestal growth method, Opt. Mater. 24 (2004) 643–650. doi:10.1016/S0925-3467(03)00179-4.

[70] E. Roduner, Size matters: why nanomaterials are different., Chem. Soc. Rev. 35 (2006) 583–592. doi:10.1039/b502142c.

[71] K. Lemański, A. Gagor, M. Kurnatowska, R. Pzik, P.J. Dereń, Spectroscopic properties of Nd^{3+} ions in nano-perovskite $CaTiO_3$, J. Solid State Chem. 184 (2011) 2713–2718. doi:10.1016/j.jssc.2011.08.004.

[72] K. Lemański, P.J. Dereń, Spectroscopic properties of Dy^{3+} ions in $CaTiO_3$ nano-perovskites, J. Lumin. 145 (2014) 661–664. doi:10.1016/j.jlumin.2013.08.048.

[73] P.J. Dereń, R. Mahiou, R. Pązik, K. Lemanski, W. Stręk, P. Boutinaud, Upconversion emission in $CaTiO_3$:Er^{3+} nanocrystals, J. Lumin. 128 (2008) 797–799. doi:10.1016/j.jlumin.2007.11.057.

[74] P.J. Dereń, K. Lemański, A. Gągor, A. Watras, M. Małecka, M. Zawadzki, Symmetry of $LaAlO_3$ nanocrystals as a function of crystallite size, J. Solid State Chem. 183 (2010) 2095–2100. doi:10.1016/j.jssc.2010.07.015.

[75] K. Lemański, P.J. Dereń, Luminescent properties of dysprosium(III) ions in $LaAlO_3$ nanocrystallites, J. Rare Earths. 29 (2011) 1195–1197. doi:10.1016/S1002-0721(10)60625-4.

[76] M.A.R.C. Alencar, G.S. Maciel, C.B. De Araújo, A. Patra, Er^{3+}-doped $BaTiO_3$ nanocrystals for thermometry: Influence of nanoenvironment on the sensitivity of a fluorescence based temperature sensor, Appl. Phys. Lett. 84 (2004) 4753–4755. doi:10.1063/1.1760882.

[77] A.F. Pereira, K.U. Kumar, W.F. Silva, W.Q. Santos, D. Jaque, C. Jacinto, Yb^{3+}/Tm^{3+} co-doped $NaNbO_3$ nanocrystals as three-photon-excited luminescent

nanothermometers, Sensors Actuators, B Chem. 213 (2015) 65–71. doi:10.1016/j.snb.2015.01.136.

[78] C. Shi, H. Qin, M. Zhao, X. Wang, L. Li, J. Hu, Investigation on electrical transport, CO sensing characteristics and mechanism for nanocrystalline La1-xCaxFeO3 sensors, Sensors Actuators, B Chem. 190 (2014) 25–31. doi:10.1016/j.snb.2013.08.029.

[79] F. Hu, H. Zhang, C. Sun, C. Yin, B. Lv, C. Zhang, W.W. Yu, X. Wang, Y. Zhang, M. Xiao, Superior Optical Properties of Perovskite Nanocrystals as Single Photon Emitters, ACS Nano. 9 (2015) 12410–12416. doi:10.1021/acsnano.5b05769.

[80] B. Chr, K. Jorgensen, FFFECTIVE QUANTUM NUMBERS IN d- AND f-SHELLS, J. Inorg. Nucl. Chem. I (1955) 301–308.

[81] A.J. Freeman, R.E. Watson, Theoretical Investigation of Some Magnetic and Spectroscopic Properties of Rare-Earth Ions, Phys. Rev. 127 (1962) 2058-2075.

[82] B.G. Wybourne, Spectroscopic Properties of Rare Earths, 1965. doi:10.1080/715120855.

[83] B. Henderson, G.F. Imbusch, Optical Spectroscopy of Inorganic Solids, J. Mod. Opt. 37 (1990) 1688. doi:10.1080/09500349014551901.

[84] H.D. Gerhard, C. H.M, C. Hannah, Spectra and energy levels of rare earth ions in crystals, New York, 1968.

[85] V.H. Bethe, Termaufspaltung in Kristallen, Ann. Phys. 3 (1929) 133–208.

[86] W.E. Hagston, J.E. Lowther, Multiphonon processes in rare-earth ions, Physica. 70 (1973) 40–61.

[87] M. Inokuti, F. Hirayama, Influence of Energy Transfer by the Exchange Mechanism on Donor Luminescence, J. Chem. Phys. 43 (1965) 1978. doi:10.1063/1.1697063.

[88] M. Yokota, O. Tanimoto, Effects of Diffusion on Energy Transfer by Resonance, J. Phys. Soc. Japan. 22 (1967) 779–784. doi:10.1143/JPSJ.22.779.

[89] A.I. Burshtein, Hopping Mechanism of Energy Transfer, Sov. J. Exp. Theor.

Phys. 35 (1972) 882–885.

[90] P. Company, T. Uniwrsity, DONOR FLUORESCENCE DECAY IN SOLID SOLUTION, Chem. Phys. 64 (1982) 239–248.

[91] C. Li, B. Dong, S. Li, C. Song, Er^{3+}-Yb^{3+} co-doped silicate glass for optical temperature sensor, Chem. Phys. Lett. 443 (2007) 426–429. doi:10.1016/j.cplett.2007.06.081.

[92] G. Tripathi, V.K. Rai, S.B. Rai, Upconversion and temperature sensing behavior of Er^{3+} doped Bi_2O_3-Li_2O-BaO-PbO tertiary glass, Opt. Mater. 30 (2007) 201–206. doi:10.1016/j.optmat.2006.09.021.

[93] M. Hayakawa, T. Hayakawa, X.T. Zhang, M. Nogami, Optical detection of near infrared femtosecond laser-heating of Er^{3+}-doped $ZnONb_2O_5TeO_2$ glass by green up-conversion fluorescence of Er^{3+} ions, J. Lumin. 131 (2011) 843–849. doi:10.1016/j.jlumin.2010.11.023.

[94] Y. Shen, X. Wang, H. He, Y. Lin, C.W. Nan, Temperature sensing with fluorescence intensity ratio technique in epoxy-based nanocomposite filled with Er^{3+}-doped 7YSZ, Compos. Sci. Technol. 72 (2012) 1008–1011. doi:10.1016/j.compscitech.2012.03.012.

[95] I.R. Martín, V.D. Rodríguez, U.R. Rodríguez-Mendoza, V. Lavín, E. Montoya, D. Jaque, Energy transfer with migration. Generalization of the Yokota–Tanimoto model for any kind of multipole interaction, J. Chem. Phys. 111 (1999) 1191–1194. doi:10.1063/1.479304.

[96] Kazuo Nakamoto, Infrared and Raman Spectra of Inorganic and Coordination Compounds, 1986.

[97] J.R. Ferraro, K. Nakamoto, C.W. Brown, Introductory Raman Spectroscopy, 2003. doi:10.1002/jrs.1407.

[98] L.L. Hench, J.O.N.K. West, The Sol-Gel Process, Chem. Rev. 90 (1990) 33–72. doi:10.1021/cr00099a003.

[99] D.A.H. Hanaor, I. Chironi, I. Karatchevtseva, G. Triani, C.C. Sorrell, Single and mixed phase TiO_2 powders prepared by excess hydrolysis of titanium alkoxide, Adv. Appl. Ceram. 111 (2012) 149–158.

doi:10.1179/1743676111Y.0000000059.

[100] R. Diehl, G. Brandt, Crystal structure refinement of $YAlO_3$, a promising laser material, Mater. Res. Bull. 10 (1975) 85–90. doi:10.1016/0025-5408(75)90125-7.

[101] R.A. Forman, G.J. Piermarini, J.D. Barnett, S. Block, Pressure Measurement Made by the Utilization of Ruby Sharp-Line Luminescence, Science 176 (1972) 284–285. doi:10.1126/science.176.4032.284.

[102] G.J. Piermarini, S. Block, J.D. Barnett, Hydrostatic limits in liquids and solids to 100 kbar, J. Appl. Phys. 44 (1973) 5377–5382. doi:10.1063/1.1662159.

[103] G.J. Piermarini, S. Block, Ultrahigh pressure diamond-anvil cell and several semiconductor phase transition pressures in relation to the fixed point pressure scale, Rev. Sci. Instrum. 46 (1975) 973–979. doi:10.1063/1.1134381.

[104] H.K. Mao, P.M. Bell, Cornegia Institution of Washington Year Book, 77, 904 (1978).

[105] W.J. Carter, S.P. Marsh, J.N. Fritz, R.G. McQueen, Accurate Characterization of the High Pressure Environment, in: E.C. Lloyd (Ed.), Washington, DC, 1971: pp. 147–158.

[106] K. Syassen, Ruby under pressure, High Press. Res. 28 (2008) 75–126.

[107] C.D.S. Brites, A. Milla, L.D. Carlos, Lanthanides in Luminescent Thermometry, in: Handb. Phys. Chem. Rare Earths, 2016: pp. 339–427. doi:10.1016/bs.hpcre.2016.03.005

[108] S. Flock, S.L. Jacques, S.T. Flock, S.L. Jacques, B.C. Wilson, Optical properties of Intralipid: A phantom medium for light propagation studies, Lasers Surg. Med. 12 (1992) 510–519. doi:10.1002/lsm.1900120510.

[109] H.J. van Staveren, C.J. Moes, J. van Marie, S.A. Prahl, M.J. van Gemert, Light scattering in Intralipid-10% in the wavelength range of 400-1100 nm., App. Opt. 30 (1991) 4507–4514. doi:10.1364/AO.30.004507.

[110] S. Nagarajan, Y. Zhang, Upconversion fluorescent nanoparticles as a potential tool for in-depth imaging., Nanotechnology. 22 (2011) 395101-395107. doi:10.1088/0957-4484/22/39/395101.

7. REFERENCES

[111] K. Welsher, S.P. Sherlock, H. Dai, Deep-tissue anatomical imaging of mice using carbon nanotube fluorophores in the second near-infrared window., Proc. Natl. Acad. Sci. U. S. A. 108 (2011) 8943–8948. doi:10.1073/pnas.1014501108.

[112] V.M. Kodach, J. Kalkman, D.J. Faber, T.G. van Leeuwen, Quantitative comparison of the OCT imaging depth at 1300 nm and 1600 nm., Biomed. Opt. Express. 1 (2010) 176-185. doi:10.1364/BOE.1.000176